

# transactions of the ASME

Published Quarterly by  
The American Society of  
Mechanical Engineers  
Volume 94 • Series C • Number 1  
FEBRUARY 1972

# journal of heat transfer

## EDITORIAL STAFF

Editor, **J. J. JAKLITSCH, JR.**  
Production, **JIM MOBLEY**

## HEAT TRANSFER DIVISION

Chairman, **W. H. COOK**  
Secretary, **R. W. GRAHAM**  
Senior Technical Editor, **W. H. GIEDT**  
Technical Editor, **L. H. BACK**  
Technical Editor, **J. C. CHEN**  
Technical Editor, **A. E. BERGLES**

## POLICY BOARD, COMMUNICATIONS

Chairman and Vice-President  
**JAMES O. STEPHENS**

### Members-at-Large

**P. G. HODGE, JR.**  
**J. De S. COUTINHO**  
**M. ALTMAN**  
**W. G. CORNELL**

### Policy Board Representatives

Basic, **J. W. HOLL**  
General Engineering, **W. R. LARSON**  
Industry, **G. P. ESCHENBRENNER**  
Power, **G. P. COOPER**  
Research, **E. L. DAMAN**  
Codes and Stds., **W. H. BYRNE**  
Nom. Com. Rep., **H. A. NAYLOR, JR.**  
Business Staff  
345 E. 47th St.  
New York, N. Y. 10017  
212/752-6800

### Dir., Com., **C. O. SANDERSON**

Production Manager,  
**GERTRUDE KELLER**

## OFFICERS OF THE ASME

President, **KENNETH A. ROE**  
Exec. Dir. & Sec'y, **ROGERS B. FINCH**  
Treasurer, **HENRY N. MULLER, JR.**

## CONSULTANT

**O. B. SCHIER, II**

**EDITED and PUBLISHED** quarterly at the offices of *The American Society of Mechanical Engineers*, United Engineering Center, 345 E. 47th St., New York, N. Y. 10017. Cable address, "Mechaneer," New York. Second-class postage paid at New York, N. Y., and at additional mailing offices.

**CHANGES OF ADDRESS** must be received at Society headquarters seven weeks before they are to be effective. Please send old label and new address.

**PRICES:** To members, \$15.00, annually; to nonmembers, \$30.00. Single copies, \$10.00 each. Add \$1.50 for postage to countries outside the United States and Canada.

**STATEMENT from By-Laws.** The Society shall not be responsible for statements or opinions advanced in papers or . . . printed in its publications (B13, Par. 4).

**COPYRIGHT 1972** by The American Society of Mechanical Engineers. Reprints from this publication may be made on condition that full credit be given the TRANSACTIONS OF THE ASME, SERIES C—JOURNAL OF HEAT TRANSFER, and the author and date of publication stated.

- 1 The Effect of Curvature on Heat or Mass Transfer from an Isothermal Sphere (71-HT-7)  
R. G. Watts
- 7 Free-Stream Turbulence Effects on Local Heat Transfer from a Sphere (71-HT-8)  
L. B. Newman, E. M. Sparrow, and E. R. G. Eckert
- 17 Calibration of Constant-Temperature Hot-Wire Anemometers at Low Velocities in Water with Variable Fluid Temperature (71-HT-9)  
K. Hollasch and B. Gebhart
- 23 Heat and Mass Transfer in an Incompressible Turbulent Boundary Layer (71-HT-10)  
E. Brundrett, W. B. Nicoll, and A. B. Strong
- 29 Thermal Recovery Factors in Supersonic Flows of Gas Mixtures (69-WA/HT-27)  
George Maise and John B. Fenn
- 36 Spectral Radiation from Alumina Powder on a Metallic Substrate (70-WA/HT-14)  
J. B. Bergquam and R. A. Seban
- 41 Infrared Radiation of Thin Plastic Films (70-WA/HT-15)  
C. L. Tien, C. K. Chan, and G. R. Cunningham
- 46 Some Experiments on Screen Wick Dry-out Limits (71-WA/HT-6)  
K. R. Chun
- 52 On the Conjugate Problem of Laminar Combined Free and Forced Convection through Vertical Non-Circular Ducts (71-HT-Q)  
M. Iqbal, B. D. Aggarwala, and A. K. Khatry
- 57 Freeze-Drying of Spheres and Cylinders (71-HT-R)  
C. C. Cox and D. F. Dyer
- 64 The Free Convection of Heat from a Vertical Plate to Several Non-Newtonian "Pseudo-plastic" Fluids (71-HT-S)  
J. D. Dale and A. F. Emery
- 73 Thermal Radiation from a Microscopically Roughened Dielectric Surface (71-HT-U)  
R. P. Caren and C. K. Liu
- 80 Laminar Natural Convection under Nonuniform Gravity (71-HT-CC)  
J. Lienhard, R. Eichhorn, and V. Dhir
- 87 Theoretical Distributions of Heat Transfer Downstream of a Backstep in Supersonic Turbulent Flow (71-HT-W)  
J. P. Lamb and C. G. Hood
- 95 Measurement of Free Convection Velocity Field around the Periphery of a Horizontal Torus (71-HT-X)  
T. Aihara and E. Saito
- 99 Steady Two-Dimensional Forced Film Condensation with Pressure Gradients for Fluids of Small Prandtl Numbers (71-HT-Y)  
Ismaila Isa and Ching-Jen Chen
- 105 A Model of Heat Transfer in Fluidized Beds (71-HT-Z)  
Benjamin T. F. Chung, L. T. Fan, and C. L. Hwang
- 111 The Turbulent Boundary Layer on a Porous Plate: Experimental Heat Transfer with Uniform Blowing and Suction, with Moderately Strong Acceleration (71-HT-BB)  
W. H. Thielbahr, W. M. Kays, and R. J. Moffat
- 119 Partially Ionized Gas Flow and Heat Transfer in the Separation, Reattachment, and Re-development Regions Downstream of an Abrupt Circular Channel Expansion (71-HT-DD)  
L. H. Back, P. F. Massier, and E. J. Roschke

R. G. WATTS

Associate Professor,  
Department of Mechanical Engineering,  
Tulane University,  
New Orleans, La.  
Mem. ASME

# The Effect of Curvature on Heat or Mass Transfer from an Isothermal Sphere

Heat or mass transfer from a sphere to a moving fluid at moderate Reynolds and Peclet numbers is governed by an equation of the form

$$\overline{Nu} \text{ or } \overline{Sh} = C_1 Pe^n + C_2$$

All of the parameters  $C_1$ ,  $C_2$ , and  $n$  are functions of the Prandtl number. For the constant-properties case the ranges of the parameters are given in Table 1. The parameter  $C_2$  is not necessarily 2 as is sometimes assumed since the equation cannot be used when  $Pe \rightarrow 0$ .  $C_2$  is shown to be a first-order correction term resulting from the approximate solution of the energy equation including curvature by a perturbation technique.

## Introduction

ANALYSES for the heat or mass transfer from a sphere to a fluid in motion have been published by Boussinesq [1],<sup>1</sup> Ruckenstein [2], Chao [3], Acrivos et al. [4, 5, 6] and others. Boussinesq obtained a solution for the average Nusselt number for the case of potential flow with a thin thermal boundary layer. Ruckenstein and Chao studied similar problems but accounted for flow within the sphere, which was taken to represent a drop or bubble moving in a different fluid. In all of these papers the thermal boundary layer was taken to be very thin. Acrivos et al. have shown how to relax this assumption using a perturbation technique. Acrivos and Goddard [5] have presented the zeroth- and first-order terms in an asymptotic expansion of the average Nusselt number for Stokes flow around an isothermal sphere at very large Peclet numbers as

$$\overline{Nu} = 0.991Pe^{1/3} + 0.922 + o(Pe^{-1/3}) \quad (1)$$

Apparently no similar result exists for the case of potential flow. It is useful and interesting to obtain such a result for several reasons. First of all, the results of Chao and Ruckenstein are applicable mainly in the range of Reynolds numbers between about 10 to  $10^3$ . For the case of a droplet moving through a gas (water-air, water-steam, etc.) this would correspond to a Peclet number in the same range. It is shown in Appendix A that the zeroth-order solution leads to a thermal layer thickness at the stagnation point of

$$\delta_T = 2.04 \frac{R}{\sqrt{Pe}} \quad (2)$$

Clearly, when the Peclet number is  $10^2$  the thermal layer thickness is over 20 percent of the drop radius and the curvature of the drop would be expected to be of some importance.

There is a second important application of the results to be presented here. When the Reynolds number is less than  $10^3$  the heat transfer from the rear of a sphere (the separated region) is of lesser importance than that from the front hemisphere [7]. The average overall Nusselt number for the case of potential flow as reported below is therefore approximately applicable when  $Re < 10^3$  and the Prandtl number is small.

Finally, and perhaps most important of all, since the potential-flow solution is equivalent to the case of  $Pr \rightarrow 0$  without flow separation, the result provides an upper limit for the average Nusselt number in the region of moderate Reynolds numbers. The lower limit is given by equation (1).

## Formulation

**General Assumptions.** The idealized problem to be considered here is that of heat transfer to a constant-temperature sphere in potential flow. All fluid properties are considered to be constants. The Peclet number is large enough that the ratio of the thermal layer thickness to the sphere radius is smaller than unity, but does not necessarily approach zero. The exact nature of this assumption will become clear as the solution unfolds. The local heat-transfer results obtained are applicable to the forward hemisphere for the case of Prandtl number approaching zero while the Peclet number lies between 10 and  $10^3$  approximately. When heat transfer in the wake region is not too large, the average heat-transfer results can be applied for the same conditions.

<sup>1</sup> Numbers in brackets designate References at end of paper.

Contributed by the Heat Transfer Division and presented at the ASME-AIChE Heat Transfer Conference, Tulsa, Okla., August 15-18, 1971. Manuscript received by the Heat Transfer Division July 20, 1970. Paper No. 71-HT-7.

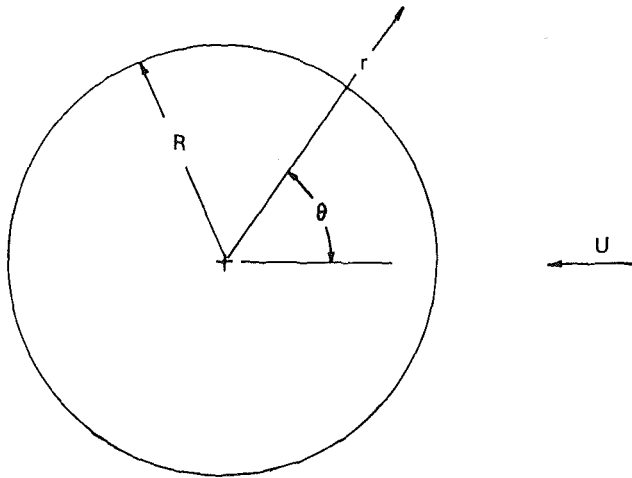


Fig. 1 Coordinate system

If the sphere in question is a bubble or a drop it is assumed to remain spherical. Only steady-state results are given here. Finally, the effects of free-stream turbulence are not included, and the boundary-layer flow is considered to be laminar.

**Equations and Boundary Conditions.** Fig. 1 shows the system to be studied. The angle  $\theta$  is measured from the front stagnation point. When the assumptions above are used the energy equation is

$$u_r \frac{\partial T}{\partial r} + \frac{u_\theta}{r} \frac{\partial T}{\partial \theta} = \kappa \left[ \frac{1}{r} \frac{\partial^2}{\partial r^2} (rT) + \frac{1}{r^2 \sin \theta} \frac{\partial}{\partial \theta} \left( \sin \theta \frac{\partial T}{\partial \theta} \right) \right] \quad (3)$$

If we wish to consider the case of mass transfer,  $T$  represents concentration and  $\kappa$  is the appropriate diffusivity for diffusion of mass. The radial and circumferential velocities for potential flow are

$$u_r = -U \left[ 1 - \frac{R^3}{r^3} \right] \cos \theta \quad (4a)$$

$$u_\theta = U \left[ 1 + \frac{1}{2} \frac{R^3}{r^3} \right] \sin \theta \quad (4b)$$

Boundary conditions are

$$T(R, \theta) = T_s \quad (5a)$$

$$T(\infty, \theta) = T_\infty \quad (5b)$$

$$\frac{\partial T}{\partial \theta} (r, 0) = \frac{\partial T}{\partial \theta} (r, \pi) = 0 \quad (5c)$$

It will be convenient to non-dimensionalize these equations using the following definitions:

$$\Phi = \frac{T - T_\infty}{T_s - T_\infty}$$

$$\xi = \frac{r - R}{R} \cdot \sqrt{\text{Pe}}$$

$$v = u/U$$

where

$$\epsilon = \sqrt{\text{Pe}}/2 \quad \text{and} \quad \text{Pe} = 2UR/\kappa$$

When these substitutions are made in equations (3), (4), and (5) we find

$$\epsilon \left[ (\xi + 2\epsilon)v_r \frac{\partial \Phi}{\partial \xi} + v_\theta \frac{\partial \Phi}{\partial \theta} \right] = \frac{\partial^2}{\partial \xi^2} [(\xi + 2\epsilon)\Phi] + \frac{1}{(\xi + 2\epsilon) \sin \theta} \frac{\partial}{\partial \theta} \left( \sin \theta \frac{\partial \Phi}{\partial \theta} \right) \quad (6)$$

$$v_r = - \left[ 1 - \left( \frac{2\epsilon}{2\epsilon + \xi} \right)^3 \right] \cos \theta \quad (7a)$$

$$v_\theta = \left[ 1 + \frac{1}{2} \left( \frac{2\epsilon}{2\epsilon + \xi} \right)^3 \right] \sin \theta \quad (7b)$$

$$\Phi(0, \theta) = 1 \quad (8a)$$

$$\Phi(\infty, \theta) = 0 \quad (8b)$$

$$\frac{\partial \Phi}{\partial \theta} (\xi, 0) = \frac{\partial \Phi}{\partial \theta} (\xi, \pi) = 0 \quad (8c)$$

## Nomenclature

$C_1$  = constant, equation (29)  
 $C_2$  = constant, equation (29)  
 ${}_1F_1$  = confluent hypergeometric function  
 $f$  = function defined in equation (17a)  
 $g$  = function defined in equation (14a)  
 $I_{1/2}$  = modified Bessel function of the first kind, order  $1/2$   
 $\dot{m}''$  = evaporation rate, mass/time-area  
 $\text{Nu}(\theta)$  = local Nusselt number, equation (20)  
 $\bar{\text{Nu}}$  = average Nusselt number, equation (22)  
 $n$  = exponent, equation (29)  
 $o$  = order of magnitude  
 $\text{Pe}$  = Peclet number,  $2UR/\kappa$   
 $Q_1$  = imaginary source term, defined by equation (17)  
 $R$  = radius of sphere

$R(0)$  = ratio, equation (26)  
 $\bar{R}$  = ratio, equation (25)  
 $r$  = radial position  
 $\bar{\text{Sh}}$  = average Sherwood number, equation (28)  
 $T$  = temperature or mass concentration  
 $U$  = velocity of free stream  
 $u$  = local velocity  
 $v$  = dimensionless local velocity,  $u/U$   
 $\Gamma\left(\frac{3}{2}\right) = \sqrt{\pi}/2$   
 $\delta$  = boundary-layer thickness  
 $\epsilon$  = parameter used for expansion,  $\sqrt{\text{Pe}}/2$   
 $\zeta$  = similarity variable, equation (14b)  
 $\eta$  = similarity variable, equation (14a)  
 $\theta$  = angle measured from front stagnation point  
 $\kappa$  = diffusivity

$\xi$  = dimensionless distance from sphere,  $\frac{r - R}{R} \sqrt{\text{Pe}}$   
 $\pi = 3.14159 \dots$   
 $\rho$  = density of diffusing substance, equation (28)  
 $\tau$  = dummy variable of integration  
 $\Phi$  = dimensionless temperature or concentration  
 $\phi_i$  =  $i$ th term in the expansion, equation (9)

### Subscripts

$L$  = lower limit  
 $r$  = radial direction  
 $s$  = sphere surface  
 $T$  = thermal or concentration  
 $U$  = upper limit  
 $\theta$  = circumferential  
 $0$  = zeroth-order approximation  
 $1$  = first-order correction  
 $2$  = second-order approximation

## Solution

We seek a solution to the above problem in which the parameter  $\epsilon$ , which is proportional to the Peclet number, is large but not necessarily approaching infinity. To obtain such a solution, we assume

$$\Phi(\xi, \theta) = \varphi_0(\xi, \theta) + \left(\frac{1}{2\epsilon}\right) \varphi_1(\xi, \theta) + \left(\frac{1}{2\epsilon}\right)^2 \varphi_2(\xi, \theta) + \dots \quad (9)$$

where  $2\epsilon \gg 1.0$ .

The velocities can be expanded in the same kind of series.

$$v_\theta = \frac{3}{2} \left[ 1 - \frac{\xi}{2\epsilon} + 2 \left(\frac{\xi}{2\epsilon}\right)^2 - \dots \right] \sin \theta, \quad \frac{\xi}{2\epsilon} < 1 \quad (10a)$$

$$v_r = -3 \left[ \frac{\xi}{2\epsilon} - 2 \left(\frac{\xi}{2\epsilon}\right)^2 + \dots \right] \cos \theta, \quad \frac{\xi}{2\epsilon} < 1 \quad (10b)$$

The first few terms of expressions (10a, b) serve as adequate representations of the velocities when  $(\xi/2\epsilon) \ll 1.0$ .

Substituting (9) and (10) into (6) and equating like powers of  $\left(\frac{1}{2\epsilon}\right)$  results in a sequence of partial differential equations for  $\varphi_0, \varphi_1$ , etc. The first two of these are

$$-\frac{3}{2} \xi \cos \theta \frac{\partial \varphi_0}{\partial \xi} + \frac{3}{4} \sin \theta \frac{\partial \varphi_0}{\partial \theta} = \frac{\partial^2 \varphi_0}{\partial \xi^2} \quad (11)$$

and

$$-\frac{3}{2} \xi \cos \theta \frac{\partial \varphi_1}{\partial \xi} + \frac{3}{4} \sin \theta \frac{\partial \varphi_1}{\partial \theta} = \frac{\partial^2 \varphi_1}{\partial \xi^2} + \frac{\partial^2}{\partial \xi^2} (\xi \varphi_0) - \frac{3}{2} \xi^2 \cos \theta \frac{\partial \varphi_0}{\partial \xi} + \frac{3}{4} \xi \sin \theta \frac{\partial \varphi_0}{\partial \theta} \quad (12)$$

By using (11), (12) can be rewritten as

$$-\frac{3}{2} \xi \cos \theta \frac{\partial \varphi_1}{\partial \xi} + \frac{3}{4} \sin \theta \frac{\partial \varphi_1}{\partial \theta} = \frac{\partial^2 \varphi_1}{\partial \xi^2} + 2 \frac{\partial}{\partial \xi} \left( \xi \frac{\partial \varphi_0}{\partial \xi} \right) \quad (12a)$$

The appropriate boundary conditions for (11) and (12a) are

$$\varphi_0(0, \theta) = 1 \quad (13a)$$

$$\varphi_0(\infty, \theta) = 0 \quad (13b)$$

$$\frac{\partial \varphi_0}{\partial \theta}(\xi, 0) = \frac{\partial \varphi_0}{\partial \theta}(\xi, \pi) = 0 \quad (13c)$$

$$\varphi_1(0, \theta) = 0 \quad (13d)$$

$$\varphi_1(\infty, \theta) = 0 \quad (13e)$$

$$\frac{\partial \varphi_1}{\partial \theta}(\xi, 0) = \frac{\partial \varphi_1}{\partial \theta}(\xi, \pi) = 0 \quad (13f)$$

It is interesting to note that the circumferential conduction term does not enter in the first-order correction. It is important only as a second-order correction effect.

Chao [3], Ruckenstein [2] and others have shown that equation (11) can be solved by using the similarity variables

$$\eta = \frac{\sqrt{3}}{2} \xi \sin^2 \theta = g(\theta) \cdot \xi \quad (14a)$$

$$\zeta = 1 - \cos \theta - \frac{1}{3} (1 - \cos^3 \theta) \quad (14b)$$

The solution, as presented by these authors, is

$$\varphi_0(\eta, \zeta) = \operatorname{erfc}(\eta/2\sqrt{\zeta}) \quad (15)$$

Clearly, this is the solution for the case where the Peclet number approaches infinity. For such a case, curvature effects may be considered to be unimportant. On the other hand, as the Peclet number decreases, curvature effects come into play. As the thermal layer thickens the average heat-transfer area becomes larger (somewhere between the area of the sphere and that of the outer edge of the thermal layer) and the heat-transfer coefficient would be expected to be greater than that obtained from equation (15). To get an idea of the effect of decreasing Peclet number we shall find  $\varphi_1(\eta, \zeta)$ .

Substitution of (14) and (15) into (12a) gives

$$\frac{\partial \varphi_1}{\partial \zeta} = \frac{\partial^2 \varphi_1}{\partial \eta^2} + Q_1(\zeta, \eta) \quad (16)$$

where the function  $Q_1(\zeta, \eta)$  is given by

$$Q_1(\zeta, \eta) = \frac{2}{\sqrt{\pi}} f(\zeta) \left[ \frac{\eta^2}{2\zeta} - 1 \right] \exp(-\eta^2/4\zeta) \quad (17)$$

with

$$f(\zeta) = 1/g(\zeta)\sqrt{\zeta} \quad (17a)$$

Sutton [8] has shown that the solution of (16) has the form

$$\varphi_1(\zeta, \eta) = \int_0^\zeta \int_0^\infty \frac{(\eta\eta_1)^{1/2}}{2(\zeta - \zeta_1)} I_{1/2} \left[ \frac{\eta\eta_1}{2(\zeta - \zeta_1)} \right] \times \exp \left[ -\frac{1}{4} \left( \frac{\eta^2 + \eta_1^2}{\zeta - \zeta_1} \right) \right] Q_1(\zeta_1, \eta_1) d\eta_1 d\zeta_1 \quad (18)$$

It is shown in Appendix B that the integration over  $\eta_1$  can be performed with the result

$$\varphi_1(\zeta, \eta) = \frac{\eta}{\sqrt{\pi} \Gamma\left(\frac{3}{2}\right)} \int_0^1 \frac{\sqrt{\zeta\tau}(1-\tau)}{\tau} f[\zeta(1-\tau)] e^{-\eta^2/4\zeta\tau} \times \left\{ -{}_1F_1 \left[ 1; \frac{3}{2}; \frac{\eta^2(1-\tau)}{4\zeta\tau} \right] + 2\tau {}_1F_1 \left[ 2; \frac{3}{2}; \frac{\eta^2(1-\tau)}{4\zeta\tau} \right] \right\} d\tau \quad (19)$$

The functions  ${}_1F_1(\alpha, \beta, \gamma)$  are the confluent hypergeometric functions (see [9], page 96).

Equations (15) and (19) are the first two terms in the series expansion (9) for the temperature. Clearly, the integral is a very difficult one to evaluate analytically. Fortunately the heat flux at the surface, the quantity of primary interest, is somewhat simpler.

We define the local Nusselt number in the usual way.

$$\text{Nu}(\theta) = -2 \left[ \frac{\partial \Phi}{\partial \left( \frac{r}{R} \right)} \right]_{r=R} \quad (20)$$

In terms of the variables  $\eta$  and  $\zeta(\theta)$  we have, from (15) and (19),

$$\text{Nu}(\theta) = -\sqrt{3}\sqrt{\text{Pe}} \sin^2 \theta \left\{ \frac{1}{\sqrt{\pi\zeta}} + \frac{1/\sqrt{\text{Pe}}}{\sqrt{\pi} \Gamma\left(\frac{3}{2}\right)} \times \int_0^1 \frac{\sqrt{\zeta(1-\tau)}}{\sqrt{\tau}} (2\tau - 1) f[\zeta(1-\tau)] d\tau \right\} \quad (21)$$

where  $\zeta = \zeta(\theta)$  as given by equation (14b). The average Nusselt number is obtained from the relation

$$\bar{\text{Nu}} = \frac{1}{2} \int_0^\pi \text{Nu}(\theta) \sin \theta d\theta \quad (22)$$



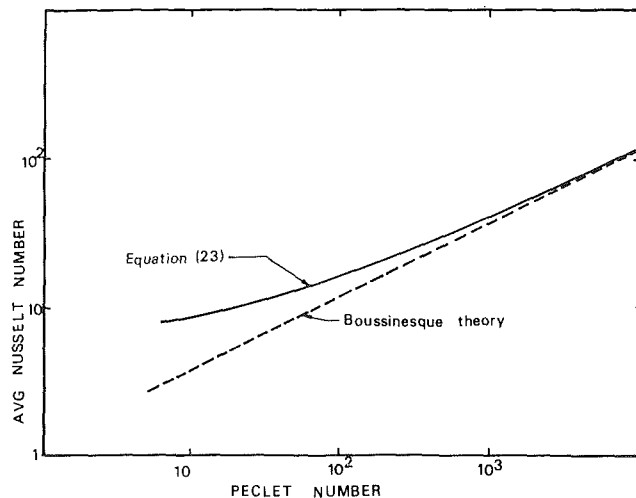


Fig. 2 One- and two-term expansions

## Results

When the indicated integrals (21) and (22) are evaluated we find the following numerical results for the average Nusselt number and for the stagnation-point Nusselt number—two parameters of particular interest:

$$\bar{Nu} = 1.156\sqrt{Pe} + 4.73 + o(Pe^{-1/2}) \quad (23)$$

$$Nu(0) = 1.988\sqrt{Pe} + 8.792 + o(Pe^{-1/2}) \quad (24)$$

The first terms in these two equations represent the asymptotic values for infinite Peclet number. They are in agreement with those previously reported. The second terms represent corrections resulting from the first-order correction term in equation (9). Second-order correction terms are of order  $Pe^{-1/2}$ .

Fig. 2 shows the departure of the two-term expansion from the asymptotic value of the average Nusselt number. The stagnation-point Nusselt number behaves similarly. The departure becomes significant when the Peclet number is less than  $10^3$ . Fig. 3 is a plot of the ratios of the one- and two-term expansions of  $\bar{Nu}$  and  $Nu(0)$ .

$$\bar{R} = \frac{1.156\sqrt{Pe}}{1.156\sqrt{Pe} + 4.73} \quad (25)$$

$$R(0) = \frac{1.988\sqrt{Pe}}{1.988\sqrt{Pe} + 8.792} \quad (26)$$

These ratios are less than 90 percent even when the Peclet number is  $10^3$ . Thus, the first-order correction term is quite significant when the Peclet number is between  $10^2$  and  $10^3$ .

Equations (23) and (24) are complementary to some other analytical results for limiting cases that have appeared in the literature. Acrivos and Taylor [4] obtained a solution for small Reynolds and Peclet numbers assuming Stokes flow. The average Nusselt number for this case is

$$\bar{Nu} = 2 + \frac{1}{2} Pe + o(Pe^2) \quad (27)$$

Acrivos and Goddard [5] obtained a solution for the case of small Reynolds numbers and large or moderate Peclet numbers. Again Stokes flow was assumed. The result was given as equation (1).

$$\bar{Nu} = 0.991Pe^{1/3} + 0.922 + o(Pe^{-1/3}) \quad (1)$$

The first two terms of each of these equations and the first two terms of equation (23) are plotted against Peclet number in Fig. 4. The three curves form an envelope that should contain all

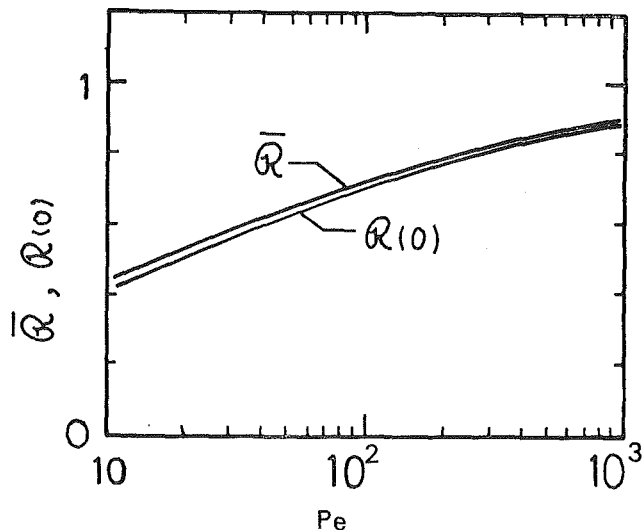


Fig. 3 Ratios of one- and two-term expansions

the low- or moderate-Reynolds-number data (for any Prandtl number) from experiments for which the assumption of constant physical properties is valid.

The experimental data of Kramers [10] for Prandtl numbers ranging from 0.714 (air) to 380 (oil) agree remarkably well with the theory. Kramers measured heat-transfer data at a number of values of  $T_s - T_\infty$  and extrapolated the results to  $T_s - T_\infty = 0$ . His data therefore represent a limiting case for which the assumption of constant properties should be valid; Lee and Ryley [11] and Baxi and Ramachandran [12] have published air data. These represent extensions of the Kramers data to lower and higher Peclet numbers.

Some very interesting data were obtained by Kinzer and Gunn [13] during studies involving the evaporation of raindrops. These data span the Peclet-number range from approximately 0.3 to  $10^3$ . The phenomenon involved was mass transfer (evaporation from water droplets) so the quantity of interest is the Sherwood number, defined as

$$\bar{Sh} = \frac{2\dot{m}R}{\rho_s - \rho_\infty} \quad (28)$$

Judging from the other data, the data of Kinzer and Gunn appear to be somewhat lower than expected for Peclet numbers greater than about 30. The low-Peclet-number data are in excellent agreement with the theory, however. It is interesting to note that when the Peclet number is less than 5 the Nusselt-number data follow equation (27) very accurately, increasing directly with the Peclet number rather than with its square or cube root as is the case at higher Peclet numbers.

It is apparent from Fig. 4 that constant-property heat-transfer data should be correlated by an expression of the form

$$\bar{Nu} = C_1 Pe^n + C_2 \quad (29)$$

when the Peclet number is less than  $10^3$  and greater than some lower limit  $Pe_L$ . Each of the numbers  $C_1$ ,  $C_2$ ,  $n$ , and  $Pe_L$  depends on the Prandtl number. The limiting values that can be deduced for these parameters are given in Table 1. For intermediate Prandtl numbers the parameters should have values between these limits. Many previous correlations have used  $n = 1/2$  exclusively for moderate-Reynolds-number data [7, 10]. There appears also to be a tendency to use  $C_2 = 2$  since this gives the correct value for  $\bar{Nu}$  when  $Pe = 0$  [11, 12]. This is clearly not correct since the constant  $C_2$  results from a curvature correction and since equation (29) is not appropriate for very small Peclet numbers. When the Peclet number is less than  $Pe_L$  equation (27) is probably appropriate for all Prandtl numbers.

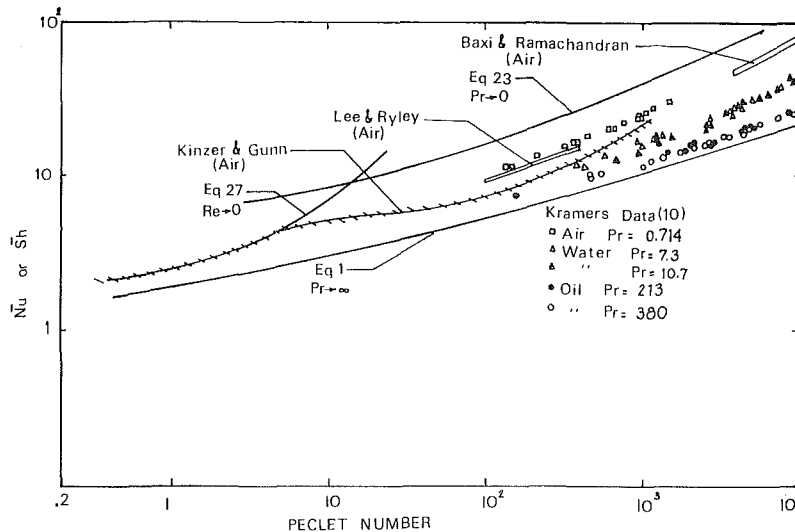


Fig. 4 Heat- and mass-transfer data for spheres at low and moderate Reynolds numbers

Table 1

Pr	Pe <sub>L</sub>	Pe <sub>U</sub>	C <sub>1</sub>	C <sub>2</sub>	n
0	15	>10 <sup>3</sup>	1.156	4.73	1/2
∞	3?	>10 <sup>3</sup>	0.991	0.922	1/3

## Conclusions

1 Curvature effects become quite important in both the local and average Nusselt numbers for heat or mass transfer to spheres at moderate Peclet numbers ( $Pe < 10^3$ ).

2 For moderate Reynolds and Peclet numbers constant-property heat-transfer data should be correlated by the expression

$$\bar{Nu} = C_1 Pe^n + C_2 \quad (29)$$

with  $C_1$ ,  $C_2$ , and  $n$  between the limiting values shown in Table 1.

3 In particular,  $C_2$  is not necessarily equal to 2 since the expression (29) is not expected to be valid when  $Pe \rightarrow 0$ . For very small Peclet numbers

$$\bar{Nu} = 2 + \frac{1}{2} Pe \quad (27)$$

## Acknowledgments

The author is pleased to record the help of Miss Elaine Beede for computational assistance and Miss Carol Butler for typing the manuscript. This work was done while the author was on a N.S.F. Science Faculty Fellowship at Harvard University.

## References

- 1 Boussinesq, M. J., "Calcul du pouvoir refroidissant des courant fluids," *Journal of Mathematics*, Vol. 70, 1905, p. 285.
- 2 Ruckenstein, E., "Mass Transfer between a Single Drop and a Continuous Phase," *International Journal of Heat and Mass Transfer*, Vol. 10, 1967, p. 1785.
- 3 Chao, B. T., "Transient Heat and Mass Transfer to a Translating Droplet," *JOURNAL OF HEAT TRANSFER*, TRANS. ASME, Series C, Vol. 91, No. 2, May 1969, pp. 273-281.
- 4 Acrivos, A., and Taylor, T. D., "Heat and Mass Transfer from Single Spheres in Stokes Flow," *The Physics of Fluids*, Vol. 5, No. 4, 1962, p. 387.
- 5 Acrivos, A., and Goddard, J. D., "Asymptotic Expansions for Laminar Forced-Convection Heat and Mass Transfer: Part I," *Journal of Fluid Mechanics*, Vol. 23, 1965, p. 273.

6 Acrivos, A., and Goddard, J. D., "Asymptotic Expansions for Laminar Forced-Convection Heat and Mass Transfer: Part II," *Journal of Fluid Mechanics*, Vol. 24, 1966, p. 339.

7 Aufdermaur, A. N., "A Wind Tunnel Investigation on the Local Heat Transfer from a Sphere, Including the Influence of Turbulence and Roughness," *ZAMP*, Vol. 18, 1967, p. 852.

8 Sutton, W. G. L., "On the Equation of Diffusion in a Turbulent Medium," *Proc. Roy. Soc. A.*, Vol. 183, p. 48.

9 Irving, J., and Mullineux, N., *Mathematics in Physics and Engineering*, Academic Press, New York, 1959.

10 Kramers, H., "Heat Transfer from Spheres to Flowing Media," *Physica*, Vol. 12, 1946, p. 61.

11 Lee, K., and Ryley, D. J., "The Evaporation of Water Droplets in Superheated Steam," *JOURNAL OF HEAT TRANSFER*, TRANS. ASME, Series C, Vol. 90, No. 4, Nov. 1968, pp. 445-451.

12 Baxi, C. B., and Ramachandran, A., "Effect of Vibration on Heat Transfer From Spheres," *JOURNAL OF HEAT TRANSFER*, TRANS. ASME, Series C, Vol. 91, No. 3, Aug. 1969, pp. 337-344.

13 Kinzer, G. D., and Gunn, R., "The Evaporation, Temperature and Thermal Relaxation Time of Freely Falling Waterdrops," *Journal of Meteorology*, Vol. 8, 1951, p. 71.

## APPENDIX A

The zeroth-order solution for the dimensionless temperature is given by equation (15). When  $\theta \rightarrow 0$

$$\lim_{\theta \rightarrow 0} \frac{\eta}{2\sqrt{\xi}} = \frac{\sqrt{3}}{2} \xi$$

so that at the forward stagnation point

$$\varphi_0 = \operatorname{erfc} \left[ \frac{\sqrt{3}}{2} \xi \right]$$

We take  $\delta_T$  to be the distance from the stagnation point to the point where the temperature reaches 99 percent of the free-stream value. Thus

$$0.01 = \operatorname{erfc} \left[ \frac{\sqrt{3}}{2} \cdot \frac{\delta_T}{R} \cdot \sqrt{Pe} \right]$$

or

$$\delta_T = 2.04 \frac{R}{\sqrt{Pe}}$$

## APPENDIX B

Substitution of (17) into (18) gives

$$\begin{aligned} \varphi_1(\zeta, \eta) &= \frac{1}{\sqrt{\pi}} \int_0^\zeta \frac{\sqrt{\eta} f(\zeta_1) e^{-\eta^2/4(\zeta-\zeta_1)}}{\zeta - \zeta_1} \\ &\times \int_0^\infty \left[ \frac{\eta_1^2}{2\zeta_1} - 1 \right] e^{-\eta_1^2/4\zeta_1} I_{1/2} \left[ \frac{\eta\eta_1}{2(\zeta - \zeta_1)} \right] e^{-\eta^2/4(\zeta - \zeta_1)} \\ &\times \sqrt{\eta_1} d\eta_1 d\zeta_1 \quad (30) \end{aligned}$$

Noting that

$$\int_0^\infty e^{-a^2\eta_1^2} \eta_1^{\nu-1} I_{1/2}(b\eta_1) d\eta_1 = \frac{\Gamma\left[\frac{1}{2}\left(\nu + \frac{1}{2}\right)\right] \sqrt{b/2a}}{2a^\nu \Gamma\left(\frac{3}{2}\right)}$$

$$\times {}_1F_1\left[\frac{1}{2}\left(\nu + \frac{1}{2}\right); \frac{3}{2}; \left(\frac{b}{2a}\right)^2\right] \quad (31)$$

equation (30) becomes

$$\begin{aligned} \varphi_1(\zeta, \eta) &= \frac{1}{\sqrt{\pi}} \int_0^\zeta \frac{\eta f(\zeta_1) \zeta_1 \sqrt{\zeta - \zeta_1} e^{-\eta^2/4(\zeta-\zeta_1)}}{\zeta \Gamma\left(\frac{3}{2}\right)} \\ &\times \left\{ \frac{{}_2F_1\left[2; \frac{3}{2}; \frac{\zeta_1 \eta^2}{4\zeta(\zeta - \zeta_1)}\right]}{\zeta} - \frac{{}_1F_1\left[1; \frac{3}{2}; \frac{\zeta_1 \eta^2}{4\zeta(\zeta - \zeta_1)}\right]}{\zeta - \zeta_1} \right\} d\zeta_1 \quad (32) \end{aligned}$$

The change of variables  $\tau = 1 - \zeta_1/\zeta$  leads directly to equation (19).

L. B. NEWMAN

E. M. SPARROW

Professor,  
Mem. ASME

E. R. G. ECKERT

Professor,  
Mem. ASME

Heat Transfer Laboratory,  
Department of Mechanical Engineering,  
University of Minnesota,  
Minneapolis, Minn.

## Free-Stream Turbulence Effects on Local Heat Transfer from a Sphere

*Experiments involving both heat-transfer and turbulence-field measurements were performed to determine the influence of free-stream turbulence on the local heat transfer from a sphere situated in a forced-convection airflow. The research was facilitated by a miniature heat-flux sensor which could be positioned at any circumferential location on the equator of the sphere. Turbulence grids were employed to generate free-stream turbulence with intensities of up to 9.4 percent. The Reynolds-number range of the experiments was from 20,000 to 62,000. The results indicate that the local heat flux in the forward region of the sphere is uninfluenced by free-stream turbulence levels of up to about 5 percent. For higher turbulence levels, the heat-flux increases with the turbulence intensity, the greatest heat-flux augmentation found here being about 15 percent. Furthermore, at the higher turbulence intensities, there appears to be a departure from the half-power Reynolds-number dependence of the stagnation-point Nusselt number. Turbulent separation occurred at Reynolds numbers of 42,000 and 62,000 for a turbulence level of 9.4 percent, these values being well below the transition Reynolds number of  $2 \times 10^5$  for a sphere situated in a low-turbulence flow.*

### Introduction

THE EFFECT of free-stream turbulence on heat transfer in various external-flow situations has evoked considerable interest in recent years. The present research is concerned with free-stream turbulence effects on local heat transfer from a sphere situated in a forced-convection flow. Local heat-transfer measurements on spheres have been made in a number of investigations, and most of this information is summarized in references [1, 2].<sup>1</sup> In the main, the investigators did not relate their results to the turbulence level in the free stream.

The results of investigations in which trends can be identified in the dependence of stagnation-point heat transfer on free-stream turbulence intensity are summarized in Fig. 1. On the ordinate, both  $Nu$  and  $Re$  are based on the sphere diameter, while  $Re$  contains the velocity of the upstream flow. The turbulence intensity is the ratio of the root-mean-square fluctuating velocity to the mean streamwise velocity. The trend suggested by Fig. 1 is that the heat transfer decreases with turbulence intensity in the range of lower intensities and then increases at higher intensity levels.

It is interesting to briefly consider some aspects of the investigations cited in the figure (a fuller discussion is available in refer-

ence [2]). Short et al. [3, 4] and Venezian et al. [5] did not actually measure turbulence intensity, but used values measured by Davis [6, 7] for a similar, but not identical, wind tunnel. Their heat-flux measurements were accomplished by probing the thin stagnation-region boundary layer of a heated sphere with a small thermocouple, which could have disturbed the air flow. Both of the aforementioned factors might well have affected the reported heat-flux dependence on turbulence. Wadsworth [8] measured the local heat flux with a relatively large, isolated heated element located on the surface of a heated sphere. Inadvertent heat transfer between the element and the sphere could have altered the results. In addition, Wadsworth mentioned difficulties in the measurement of the turbulence intensity.

The present study, based on [2], was motivated by the rather surprising trends exhibited in Fig. 1 and by the evident need for definitive and interrelated heat-transfer and turbulence measurements. The objectives were to measure the local heat flux from a sphere with a minimum disturbance of the temperature fields in the boundary layer and within the sphere, and to correlate the results with carefully measured turbulence parameters. To facilitate the fulfillment of these objectives, a miniature heat meter was designed and fabricated as a modification of an instrument first suggested by Gardon [10, 11]. This sensor, which subtended 4 deg of arc on the surface of the sphere, was capable of being positioned at any angular location on the sphere's equatorial circumference. The turbulence intensity and scale measurements were made with single and paired constant-temperature hot wires.

<sup>1</sup> Numbers in brackets designate References at end of paper.

Contributed by the Heat Transfer Division and presented at the ASME-AIChE Heat Transfer Conference, Tulsa, Okla., August 15-18, 1971. Manuscript received by the Heat Transfer Division September 15, 1970. Paper No. 71-HT-8.



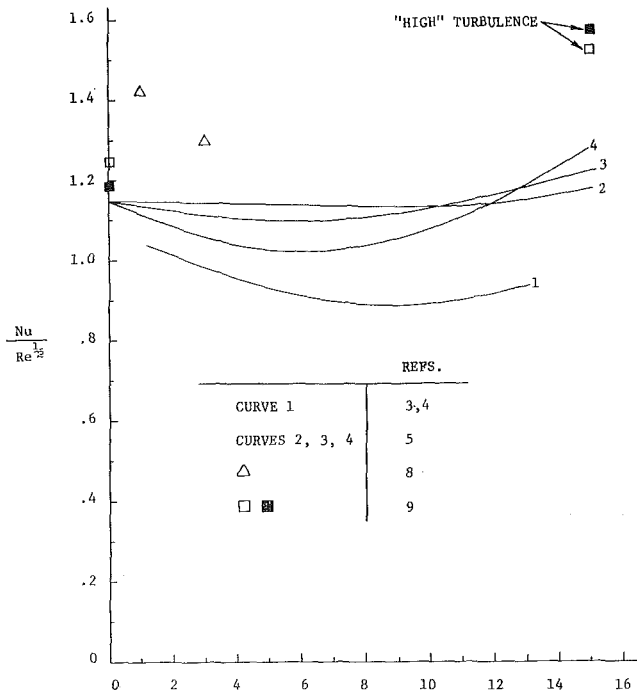


Fig. 1 Summary of available information on the effect of turbulence level on stagnation-point heat transfer

## Experimental Apparatus and Instrumentation

**Turbulence.** The experiments were performed in a low-speed, low-turbulence wind tunnel with a test section 61 cm wide by 30.5 cm high by 244 cm long. The intrinsic turbulence level of the wind tunnel when operated in the open-circuit mode was about 0.2 to 0.3 percent. The turbulence in the test section could be altered by inserting interchangeable grids into a slot at its upstream end. A woven-wire grid having a 0.635-cm square mesh made from 1.27-mm-dia wire and a punched-plate grid having a 2.54-cm square mesh with 6.35-mm bar width were used to generate the turbulence. In addition, for data runs at the basic turbulence level of the wind tunnel, an open frame could be inserted to fill the slot and make it flush with the inlet walls. The velocity range of the experiments was from 5 to 22 m/sec.

A Thermo-Systems constant-temperature, dual-channel hot-wire anemometer system was used for all turbulence measurements. As is customary in studies of free-stream turbulence effects, the turbulence measurements were performed without the spherical test body in place. The hot-wire sensors were of tungsten, with a diameter and active length of 0.0038 mm and 1.25 mm respectively. The details of the instrumentation, experimental technique, and data analysis for the turbulence measurements are available in reference [2].

Fig. 2 shows the turbulence intensities as a function of down-

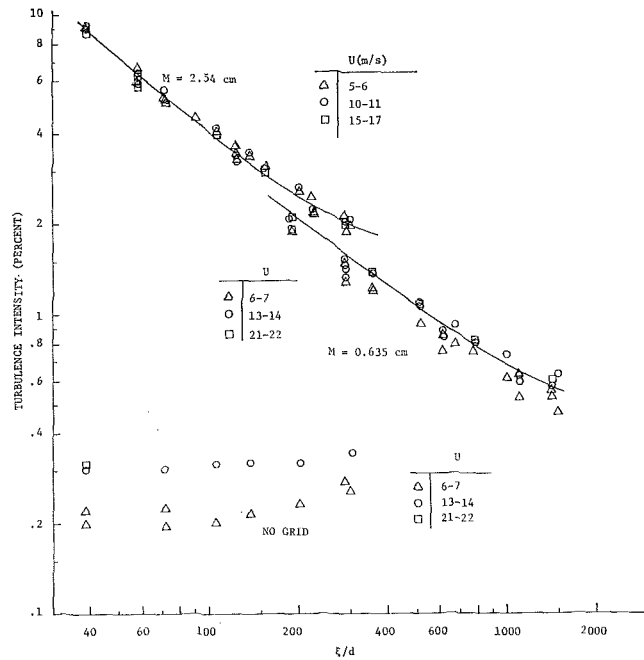


Fig. 2 Turbulence intensity as a function of distance downstream of the grid

stream distance for each grid and for the open frame. The coordinate  $\xi$  is measured from the plane of the downstream face of the turbulence grids, while  $d$  is the diameter of the wire mesh or width of the bars.<sup>2</sup> The data correspond to  $\xi$  locations along the centerline of the wind tunnel. The solid lines are mean representations of the turbulence-intensity data corrected for scale of turbulence effects on the finite length of the hot wire, as suggested by Dryden et al. [12].

The figure shows that the maximum turbulence level attainable with the 2.54-cm mesh grid was 9.4 percent, while the maximum for the 0.635-cm grid was about 2.25 percent. The data for the two grids are nearly continuous when plotted as in Fig. 2. Graphical presentations of measurements of the transverse and longitudinal integral scales of turbulence ( $L_y$  and  $L_x$  respectively) are made in reference [2], but this information is omitted here because of space limitations.

**The Sphere and Its Supports.** The test body itself was a solid copper sphere 5.08 cm in diameter. The blockage of the wind-tunnel cross section by the sphere was 1.1 percent. Heating was accomplished by an electric resistance wire heater placed in the center of the sphere, see Fig. 3. The heater was made small to facilitate a uniform wall-temperature boundary condition. Under operating conditions with wall-to-fluid temperature differ-

<sup>2</sup> For the open frame,  $d$  was evaluated as the bar width of the punched-plate grid.

## Nomenclature

$D$  = diameter of sphere  
 $d$  = characteristic dimension of turbulence grid  
 $E_q$  = output voltage of heat-flux sensor  
 $h$  = local heat-transfer coefficient,  $q/\Delta T$   
 $k$  = thermal conductivity  
 $M$  = mesh of turbulence grid  
 $Nu$  = local Nusselt number,  $hD/k$   
 $Pr$  = Prandtl number

$q$  = local heat transfer per unit time and area  
 $Re$  = Reynolds number,  $UD/\nu$   
 $T$  = temperature  
 $Tu$  = turbulence intensity in stream-wise direction  
 $U$  = streamwise velocity in upstream flow  
 $u$  = local free-stream velocity  
 $x$  = circumferential coordinate on sphere

$\Delta T$  = wall-to-fluid temperature difference  
 $\nu$  = kinematic viscosity  
 $\xi$  = distance downstream of turbulence grid  
 $\phi$  = circumferential angular coordinate on sphere

## Subscript

0 = at the stagnation point in a low-turbulence free-stream flow

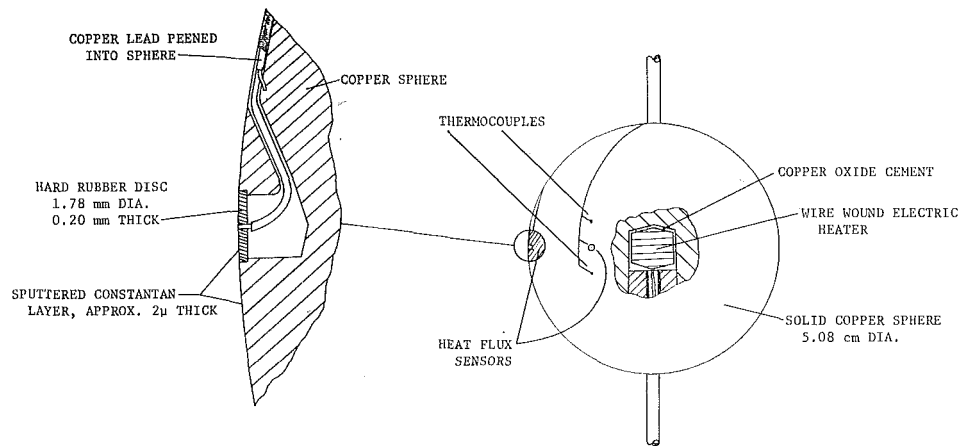


Fig. 3 Schematic of the test body and instrumentation

ences of 6 to 8 deg C, the four thermocouples on the sphere surface agreed within 0.03 deg C. The thermocouples were of calibrated copper-constantan wire, 0.13 mm in diameter.

It was deemed desirable to support the sphere from above and below (that is, side supports) so that a heat-flux sensor located on the sphere's equator could be rotated through 360 deg. To facilitate a rational selection of the diameter of the side-support tubes, an auxiliary flow-visualization study using the lampblack-kerosene technique and a plastic sphere was undertaken. Four pairs of cylindrical side supports with diameters from 2.6 to 10 percent of the sphere diameter were investigated. Photographs of the flow patterns for all of these cases are available in reference [2], but only those corresponding to the supports used in the final design are shown here in Fig. 4. The design supports were made from 2.41-mm stainless steel tubing (4.8 percent of sphere diameter).

The upper photograph of Fig. 4 is a view looking at the forward stagnation point of the sphere from an upstream vantage point; axisymmetric flow paths are clearly visible. The middle photo is a side view showing the separation line, while the lower photo is a top view. Careful study of the photographs showed that there was no deflection of the flow-path lines due to the supports for angular positions of less than 75 deg from the forward stagnation point. Since the forward stagnation region was of primary interest, these side supports were deemed acceptable.

Lead wires from the electrical resistance heater were passed through the lower support tube and were connected to a voltage divider and a 12-v automotive battery via slip rings (to permit rotation of the sphere). Wires from the sphere heat-flux sensor and thermocouples were led out through the upper support tube. To facilitate highly accurate measurements of heat flux and temperature, additional lengths of wire were employed so that the rotation of the sphere could be accommodated without the use of slip rings.

**Heat-Flux Sensor.** The heat-flux sensor was an original adaptation of a design used by Gardon [10, 11]. The sensor is shown schematically in Fig. 3, and its fabrication will now be outlined. A 1.65-mm hole was drilled 2.5 mm deep on the equator of the copper sphere. The hole was counterbored to a diameter of 1.78 mm and a depth of 0.2 mm. A disk of hard rubber was machined to fit onto the counterbored ledge. As seen in the figure, the end of a 0.13-mm-dia copper wire was epoxyed into a hole drilled through the center of the disk, and the disk was then epoxyed in place in the counterbored hole. The upper surface of the rubber disk was sanded and polished to be flush with the surface of the sphere.

The copper wire with its nylon insulation was led through a small aperture in the bottom of the sensor cavity and then to the sphere's surface, see Fig. 3. From there, the wire was laid in a

narrow channel, machined into the surface of the sphere, which conducted it to the upper support tube.

Near the sensor, a second copper wire was peened into a slot to establish good thermal and electrical contact with the sphere. This second wire with its insulation was laid in the same narrow channel as the first wire.

The channel was filled with copper oxide cement and the sphere polished to a mirror-like surface. The assembled sphere was placed in a vacuum chamber and sputtered with a layer of constantan, approximately  $2 \mu$  in thickness.

A completed sensor was effectively a differential thermocouple, with one copper-constantan junction at the center of the sensor and the second junction at the outer rim of the insulated disk. When the sphere was heated, the center of the heat-flux sensor was cooler than the outside edge. This temperature difference, which gave rise to a thermoelectric voltage, was a measure of the heat flux from the sensor surface.

The just-described sensor design minimized several of the objections aimed at other Gardon-type sensors. The sensor surface appeared flush with the sphere surface when viewed under  $20 \times$  magnification. This flushness, combined with the small sensor size, assured a minimum disruption of the boundary layer. The small size also meant that the surface temperature of the sensor was nearly equal to that of the sphere. The maximum temperature depression at the center of the sensor was 0.2 deg C, which corresponded to 3 percent of the sphere-to-air temperature difference (6 to 8 deg C).

Two heat-flux sensors were built into the spherical test body. However, one of the sensors became inoperative soon after the initiation of the data runs, so that all of the data presented herein are from a single sensor.

The voltages generated by the heat-flux sensor and by the thermocouples embedded in the sphere and situated in the air stream were measured by a Leeds and Northrup K-5 potentiometer in conjunction with a 9834 null indicator. The K-5 instrument had a rated accuracy of  $0.1 \mu v$  and could resolve  $0.02 \mu v$ .

## Analysis of Data

To translate the output of the heat-flux sensor into a heat-transfer rate, a calibration relationship is needed. For the calibration, stagnation-point measurements corresponding to the intrinsic turbulence level of the wind tunnel (0.2-0.3 percent) were used in conjunction with the analytical relationship appropriate to negligible-turbulence effects. It should be noted that because of the ratio form of the final presentation of results, the numerical constant appearing in the analytical relationship does not play a decisive role.

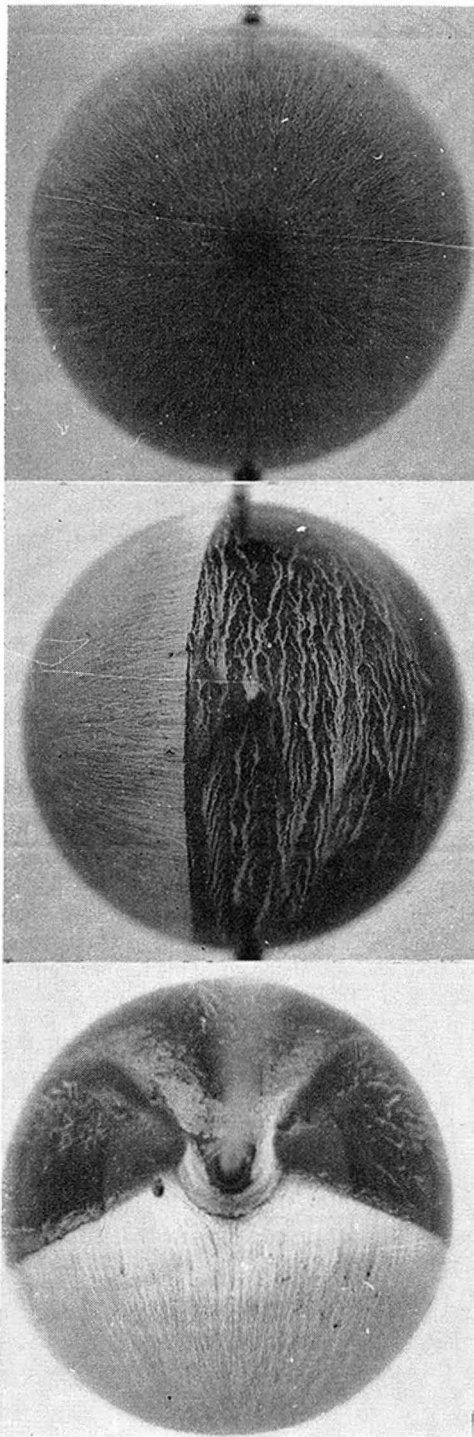


Fig. 4 Flow visualization by lampblack-kerosene technique

At a rotationally symmetric stagnation point, analysis gives [13]:

$$\text{Nu}_x = 0.763 \text{Re}_x^{1/2} \text{Pr}^{2/5} \quad (1)$$

where  $\text{Re}_x = ux/\nu$  and  $\text{Nu}_x = hx/k$ . The coordinate  $x$  measures circumferential distances around the sphere from the forward stagnation point, and  $u = u(x)$  is the local free-stream velocity. The foregoing can be rephrased into the form, with  $\text{Pr} = 0.7$ ,

$$\text{Nu} = 0.662 \text{Re}^{1/2} (uD/xU)^{1/2} \quad (2)$$

in which

$$\text{Nu} = hD/k, \quad \text{Re} = UD/\nu \quad (3)$$

The circumferential distribution of the local free-stream velocity was deduced via Bernoulli's equation from pressure measurements on a 5.71-cm-dia sphere fitted with a 0.5-mm pressure tap on its equator. These data are summarized in Fig. 5, where  $u/U$  is plotted as a function of the angle  $\phi$  which measures angular positions with respect to the forward stagnation point. A least-squares fit for the data corresponding to the tunnel turbulence level has the equation

$$\frac{uD}{xU} = 2.66 - 0.515 \left(\frac{x}{D}\right)^2, \quad 0 \leq \phi \leq 40 \text{ deg} \quad (4)$$

In the stagnation region, only the first term is relevant and, with this, equation (2) becomes

$$\text{Nu} = 1.08 \text{Re}^{1/2} \quad (5)$$

or

$$q = 1.08k\Delta T'(U/\nu D)^{1/2} \quad (6)$$

The right-hand side of equation (6) was evaluated using experimental data, thus providing values of  $q$  which were plotted in Fig. 6 against the output voltage  $E_q$  of the heat-flux sensor. A good least-squares fit of the data was obtained in the form

$$q = AE_q + BE_q^2 \quad (7)$$

where the second-order term was small. Equation (7) was employed to calculate the local heat flux from the measured output voltage of the sensor.

Since the free-stream velocity and the temperatures varied slightly between even nominally identical data runs, a direct comparison of heat-flux values was not appropriate. It was deemed more reasonable to work with the group  $\text{Nu}/\text{Re}^{1/2}$ . Furthermore, to obtain a direct measure of the effects of turbulence on the local heat flux, the ratio

$$\frac{\text{Nu}/\text{Re}^{1/2}}{(\text{Nu}/\text{Re}^{1/2})_0} \quad (8)$$

was evaluated, where the subscript 0 denotes the value of  $\text{Nu}/\text{Re}^{1/2}$  at the stagnation point for the low intrinsic turbulence level of the wind tunnel. In effect, the use of the ratio (8) eliminates the proportionality constant appearing in equation (5).

## Results and Discussion

In the presentation of results, consideration is first given to the effects of free-stream turbulence on the local heat flux at specific circumferential locations on the surface of the sphere. Subsequently, results will be presented for the circumferential distribution of the local Nusselt number.

**Effects of Free-Stream Turbulence.** Values of the ratio  $(\text{Nu}/\text{Re}^{1/2})/(\text{Nu}/\text{Re}^{1/2})_0$ , determined as described in the previous section, are plotted as a function of the free-stream turbulence level in Fig. 7. The upper tier of data points corresponds to the forward stagnation point ( $\phi = 0$  deg), while the lower tier of points corresponds to an angular position 40 deg from the stagnation point. As indicated in the figure, the data at the smaller turbulence intensities are for the  $M = 0.635$ -cm grid, while the higher turbulence data are for the  $M = 2.54$ -cm grid. The turbulence intensities used in plotting the data were taken from Fig. 2, with  $\xi$  being evaluated as the distance between the downstream face of the turbulence grid and the forward stagnation point of the sphere.

Turning first to the stagnation-point results, it is seen that there is no apparent effect of free-stream turbulence for intensities below 5 percent. The data for the  $M = 0.635$ - and  $2.54$ -cm grids overlap and are mutually consistent. There is no evident ordering of the data with free-stream velocity in this range of turbulence intensities ( $\leq 5$  percent).

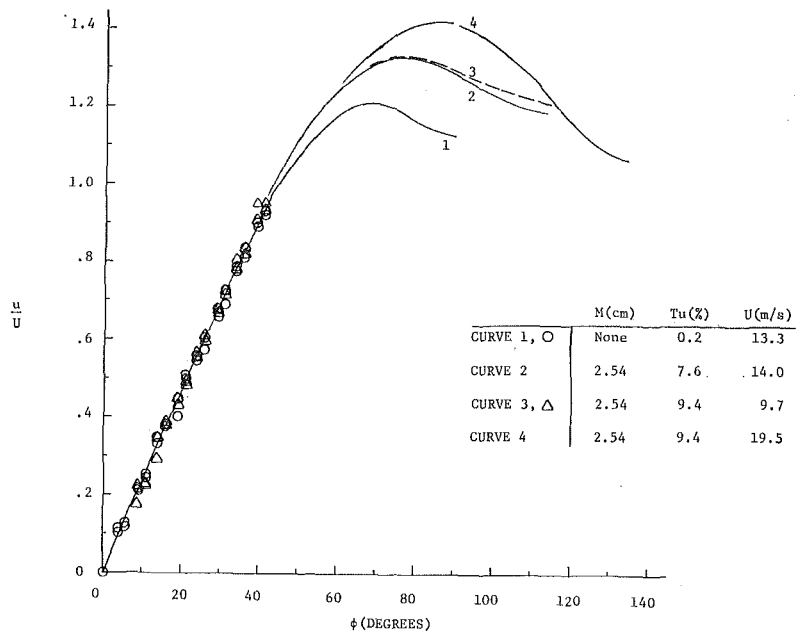


Fig. 5 Circumferential distribution of local free-stream velocity

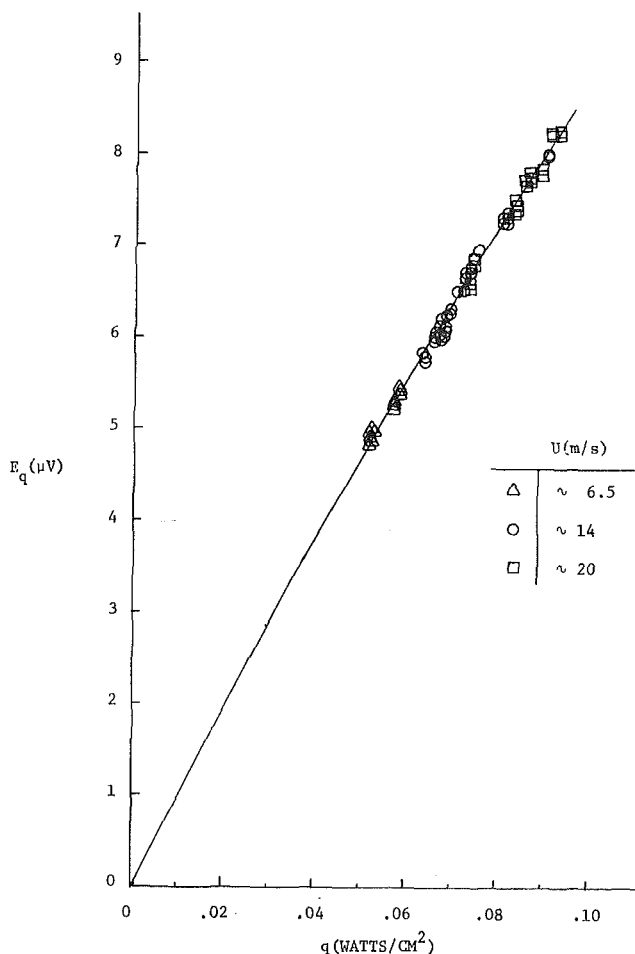


Fig. 6 Calibration curve of the heat-flux sensor

The just-mentioned insensitivity of the stagnation-point heat transfer to intermediate free-stream turbulence intensities is in sharp contrast to experimental findings for the stagnation line of a cylinder in crossflow [14]. There, a twofold increase in the heat-transfer coefficient was induced by turbulence intensities of approximately 2<sup>1/2</sup> percent.

At turbulence levels greater than 5 percent, the stagnation-point heat-transfer results of Fig. 7 are seen to increase with the turbulence intensity. For an intensity level of 9.4 percent, which is the highest of these experiments, the  $(Nu/Re^{1/2})/(Nu/Re^{1/2})_0$  ratio was (on the average) 1.06, 1.12, and 1.14 respectively for the low, middle, and high velocity ranges.<sup>3</sup> This dependence on velocity suggests that the Reynolds-number dependence  $Nu \sim Re^{1/2}$ , which is given by laminar theory for the condition of negligible free-stream turbulence effects, is not universal. That is, the exponent of the Reynolds number in the  $Nu, Re$  relation may well depend on the turbulence level.

The heat-transfer results of Fig. 7 for the angular position  $\phi = 40$  deg show the same general trend as those for the stagnation point. The heat-transfer characteristics appear to be insensitive to the turbulence level for intensities up to 6 percent, whereafter there is an increase in the plotted heat-transfer parameter. In the lower range of intensities, up to 5<sup>1/2</sup> percent, there appears to be some ordering of the data with velocity, but no ordering is in evidence at the highest turbulence level (9.4 percent).

It is of interest to compare the present results relating to the effects of turbulence level with those of prior investigations, and to this end, Fig. 8 has been prepared. The figure, which pertains to the stagnation point, shows lines depicting the findings of Short et al. [3, 4] and of Venezian et al. [5] as well as those of the present work. For turbulence levels greater than 5 percent, the present results and those of Venezian show the same trend. That is,  $Nu/Re^{1/2}$  increases with turbulence intensity, with a more rapid increase for higher Reynolds numbers. Also, for intensities greater than 8 percent, Short's  $Nu/Re^{1/2}$  results also increase with turbulence intensity.

On the other hand, in the range of lower turbulence intensities, the present results do not display the drop-off that is seen in the curves of Short and of Venezian. The fact that the Reynolds numbers of the present experiments are higher than those of the

<sup>3</sup> The significance of the diamond symbol will be discussed later.



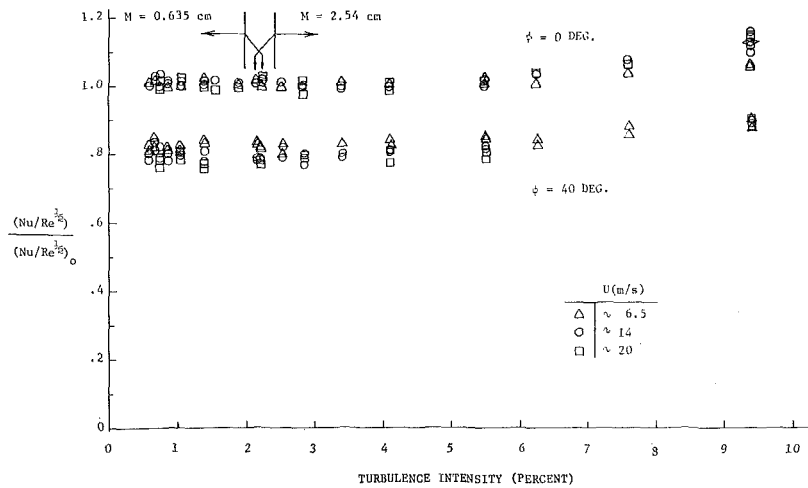


Fig. 7 Effect of turbulence level on local heat flux

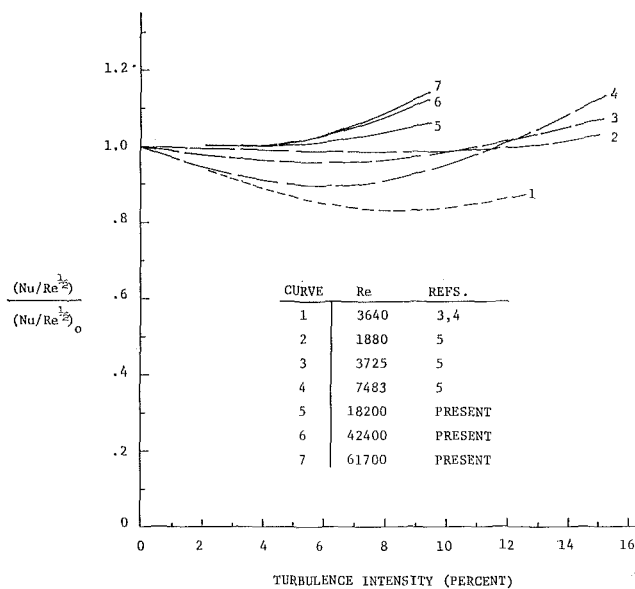


Fig. 8 Comparison of turbulence-level effects on stagnation-point heat transfer

others does not appear to be relevant in explaining the different behavior, since the drop-off in Venezian's curves is accentuated with Reynolds number. The present authors are unable to rationalize the drop-off.

It is also relevant to make mention of the turbulence measurements of Kuethe et al. [17] near the nose of a hemispherical body in a subsonic flow. The hot-wire anemometer used to make the measurements was positioned about 5 boundary-layer thicknesses from the surface. It was found that the rms turbulent fluctuations at the probe location were as much as 2 or 3 times those in the free stream. Furthermore, for a 2-in-dia hemisphere, the turbulence energy was sharply peaked about a frequency of 1 cps. No corresponding measurements were made during the course of the present investigation, so that it is not known whether such selective amplification occurred. In view of the heat-transfer results discussed in connection with Fig. 7, it may be concluded that if there was selective amplification, it was not in a frequency range which significantly affected the heat transfer.

In connection with their measurements, Kuethe et al. postulated the presence of a mechanism causing amplification of vorticity fluctuations in the flow near the stagnation point. Vorticity amplification has also been postulated by Suter, Kestin,

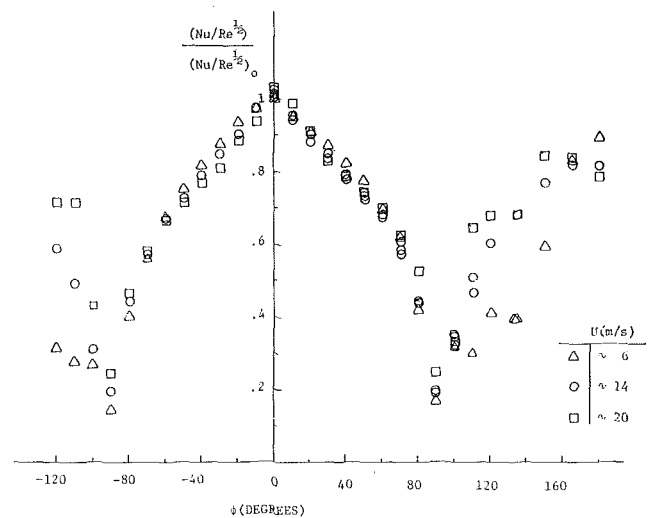


Fig. 9 Typical circumferential distributions of Nusselt number for turbulence levels below 5 percent

and their co-workers to be responsible for the large observed effect of turbulence level on the stagnation-line heat transfer for the cylinder in crossflow, e.g., [18]. The present heat-transfer results do not rule out the occurrence of vorticity amplification, but suggest that such amplification is not a significant factor in the mechanism of heat transfer for a sphere.

**Circumferential Distributions of Nusselt Number.** Rotation of the sphere about its vertical axis permitted the heat-flux sensor to be positioned at any angular location on the sphere's equator. By this means, the circumferential distribution of the  $(Nu/Re^{1/2}) / (Nu/Re^{1/2})_0$  ratio could be determined.

Circumferential distributions that are typical of turbulence-intensity levels below 5 percent are shown in Fig. 9. As before,  $\phi$  is the angular position measured relative to the forward stagnation point. Different data symbols are employed to distinguish the three velocity ranges.

The figure shows that  $Nu/Re^{1/2}$  decreases monotonically with angular position and reaches a minimum in the neighborhood of  $\phi = 90$  deg, whereafter it increases in the separated region. In the forward portion of the sphere, downstream of the stagnation point, there appears to be a tendency for  $Nu/Re^{1/2}$  to be higher at the lower velocities. At the forward stagnation point itself, there is no apparent ordering of the results with velocity.

Fig. 10 shows circumferential distributions of  $(Nu/Re^{1/2}) /$

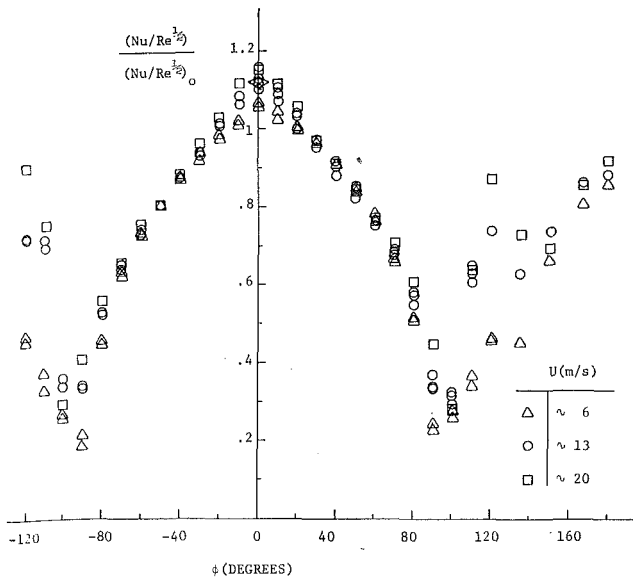


Fig. 10 Circumferential distributions of Nusselt number at a turbulence level of 9.4 percent

$(Nu/Re^{1/2})_0$  corresponding to the highest turbulence level of these tests, 9.4 percent. In the neighborhood of the forward stagnation point,  $Nu/Re^{1/2}$  increases with increasing velocity, whereas just downstream of this region, there is no apparent trend with velocity. It is also interesting to observe that the position of the minimum value of  $Nu/Re^{1/2}$  (i.e., the separation point) is shifted rearward for the middle and high velocity runs, thus indicating turbulent separation.

To explore whether the change in position of separation affected the heat transfer at the forward stagnation point, an auxiliary experiment was performed in which a trip ring was affixed axisymmetrically to the sphere at  $\phi = 75$  deg. The data point taken with this ring in place and for the middle velocity range is depicted by the diamond symbol in Fig. 10 (as well as in Fig. 7). It agrees very well with data from corresponding runs made without the trip ring. Furthermore, with the trip ring in place, no effect on the value of  $(Nu/Re^{1/2})_0$  was observed. In this same connection, it may be noted from Fig. 5 that the shift of the separation point did not affect the distribution of the local free-stream velocity in the range  $0 \leq \phi \leq 40$  deg. In the light of the foregoing discussion, it may be concluded that any measured increases in  $Nu/Re^{1/2}$  on the forward portion of the sphere were not the result of a shift of the separation point.

The circumferential Nusselt-number distributions of the present investigation will now be compared with those of other investigators. The comparison is made in Figs. 11 and 12 respectively for the ranges of low free-stream turbulence and of higher free-stream turbulence.

In preparing Fig. 11, each of the available  $Nu/Re^{1/2}$  distributions was normalized by its own stagnation-point value. In this way, when plotted on a graph of  $(Nu/Re^{1/2})/(Nu/Re^{1/2})_0$  versus  $\phi$ , all curves are in mutual agreement at  $\phi = 0$  deg.<sup>4</sup>

It is seen from Fig. 11 that the present results (solid lines) drop off more rapidly with angle than do those of Venezian et al. [5] and of Aufdermaur and Joss [9]. To examine this matter in more detail, the series solution of Frössling [15] for laminar heat transfer from an isothermal sphere was employed. The governing differential equations for the functions appearing in the series were solved for  $Pr = 0.7$  using the Runge-Kutta technique. In Frössling's notation, the starting values for these solutions were found to be  $(F_0')_0 = -0.4705$ ,  $(G_0')_0 = -0.1897$ , and  $(H_0')_0 = -0.0653$ , accurate within  $\pm 0.0001$ . With these and with the

<sup>4</sup> It is interesting to note that such a normalization may well exaggerate the differences among the curves at other values of  $\phi$ .

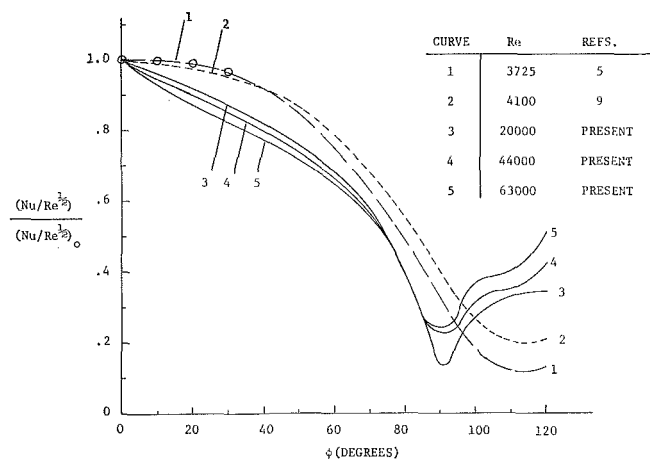


Fig. 11 Comparison of circumferential distributions of Nusselt number, low free-stream turbulence

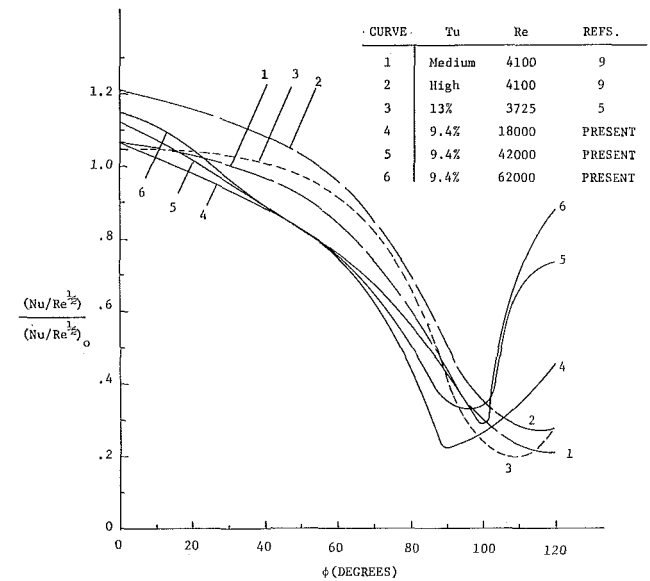


Fig. 12 Comparison of circumferential distributions of Nusselt number, high free-stream turbulence

measured local free-stream velocity distribution expressed by equation (4), the analytical prediction for the local Nusselt-number distribution in the neighborhood of the forward stagnation point is

$$(Nu/Re^{1/2})/(Nu/Re^{1/2})_0 = 1 - 0.249(x/D)^2 \quad (9)$$

Equation (9) is represented in Fig. 11 by the open circles. These predicted values do not show the rapid decrease in  $Nu/Re^{1/2}$  seen in the present experimental results.

Still referring to Fig. 11, a second significant difference between the present results and those of references [5, 9] is seen to be in the nature of the separation. Whereas the separation for the present experiments is subcritical (laminar), that for references [5, 9] appears to be supercritical (turbulent). According to Schlichting [16], the critical Reynolds number for a sphere in a low-turbulence flow is  $2 \times 10^6$ . Therefore, all of the curves appearing in Fig. 11 should have subcritical separations.

Fig. 12 compares available circumferential Nusselt-number distributions for the range of higher free-stream turbulence. As before, the  $(Nu/Re^{1/2})_0$  values are specific to each of the investigations depicted. In the forward region of the sphere, the present results drop off more rapidly than do those of Venezian et al.

[5] and of Aufdermaur and Joss' [9] medium-turbulence run (curve 1), but at about the same rate as Aufdermaur and Joss' high-turbulence run (curve 2).

## Concluding Remarks

The results of the present investigation indicate that the local heat flux in the forward region of a sphere is insensitive to moderate levels of free-stream turbulence. For turbulence levels up to about 5 percent, the heat flux is essentially the same as that prevailing in flows having very low free-stream turbulence. This finding does not confirm the results of prior investigations which show a decrease in heat flux at moderate turbulence levels.<sup>5</sup>

For higher turbulence levels, the heat flux was found to increase with increasing turbulence intensity. The largest increase in heat flux encountered here, at a turbulence intensity of 9.4 percent, was about 15 percent. It also appears that at higher turbulence intensities, the dependence of the stagnation-point Nusselt number on the Reynolds number departs from the relation  $Nu \sim Re^{1/2}$ , which corresponds to a laminar boundary layer in a low-turbulence free stream.

At all turbulence levels below 9.4 percent, subcritical (laminar) separation occurred, suggesting that the available disturbances were not sufficient to promote boundary-layer transition. Supercritical (turbulent) separation appeared to occur at a turbulence intensity of 9.4 percent for Reynolds numbers of 42,000 and 62,000. These Reynolds numbers are well below the value  $2 \times 10^6$  for transition in a low-turbulence flow.

## References

- 1 Galloway, T. R. and Sage, B. H., "Thermal and Material Transport from Spheres. Prediction of Macroscopic Thermal and Material Transport," *International Journal of Heat and Mass Transfer*, Vol. 10, 1967, pp. 1195-1210.
- 2 Newman, L. B., "Effect of Freestream Turbulence on Local Heat Transfer from a Sphere," PhD thesis, Department of Mechanical Engineering, University of Minnesota, Minneapolis, Minn., 1970.
- 3 Short, W. W., Brown, R. A. S., and Sage, B. H., "Thermal Transfer in Turbulent Gas Streams. Effect of Turbulence on Local Transport From Spheres," *Journal of Applied Mechanics*, Vol. 27, TRANS. ASME, Series E, Vol. 82, No. 3, Sept. 1960, pp. 393-402.
- 4 Short, W. W. and Sage, B. H., "Temperature Measurements in a Spherical Field: Transfer Coefficients and Corrections for Thermocouples in Boundary Flows," *AIChE Journal*, Vol. 6, 1960, pp. 163-167.
- 5 Venezian, E., Crespo, M. J., and Sage, B. H., "Thermal and Material Transfer in Turbulent Gas Streams: One-Inch Spheres," *AIChE Journal*, Vol. 8, 1962, pp. 383-388.
- 6 Davis, L., "Measurements of Turbulence Level Behind a Set of Square-Mesh Grids and Correlation with Grid Pressure Loss," Report 3-22, Jet Propulsion Laboratory, Pasadena, Calif., 1950.
- 7 Davis, L., "Measurements of Turbulence Decay and Turbulent Spectra Behind Grids," Report 3-17, Jet Propulsion Laboratory, Pasadena, Calif., 1952.
- 8 Wadsworth, J., "The Experimental Examination of the Local Heat Transfer on the Surface of a Sphere When Subjected to Forced Convection Cooling," Report MT-39, Division of Mechanical Engineering, National Research Council of Canada, 1958.
- 9 Aufdermaur, A. N. and Joss, J., "A Wind Tunnel Investigation on the Local Heat Transfer from a Sphere, Including the Influence of Turbulence and Roughness," *ZAMP*, Vol. 18, 1967, pp. 852-866.
- 10 Gardon, R., "An Instrument for the Direct Measurement of Intense Thermal Radiation," *Review of Scientific Instruments*, Vol. 24, 1953, pp. 366-370.
- 11 Gardon, R., "A Transducer for the Measurement of Heat-Flow Rate," *JOURNAL OF HEAT TRANSFER*, TRANS. ASME, Series C, Vol. 82, No. 4, Nov. 1960, pp. 396-398.
- 12 Dryden, H. L., Schubauer, G. B., Mock, W. C., and Skramstad, H. K., "Measurements of Intensity and Scale of Wind-Tunnel Turbulence and Their Relation to the Critical Reynolds Number of Spheres," NACA Report 581, 1937.

<sup>5</sup> A very recent relevant publication by Gostkowski and Costello [19] came to the authors' attention after the submission of the present paper. The trends of that investigation are in qualitative accord with those found here.

13 Sibulkin, M. S., "Heat Transfer Near the Forward Stagnation Point of a Body of Revolution," *Journal of the Aeronautical Sciences*, Vol. 19, 1952, pp. 570-571.

14 Kestin, J., Maeder, P. F., and Sogin, H. H., "The Influence of Turbulence on the Transfer of Heat to Cylinders Near the Stagnation Point," *ZAMP*, Vol. 12, 1961, pp. 115-132.

15 Frössling, N., "Evaporation, Heat Transfer, and Velocity Distribution in Two-Dimensional and Rotationally Symmetrical Laminar Boundary Layer Flow," NACA TM 1432, 1958.

16 Schlichting, H., *Boundary Layer Theory*, 6th ed., McGraw-Hill, New York, 1968, p. 17.

17 Kuethe, A. M., Willmarth, W. W., and Crocker, G. H., "Stagnation Point Fluctuations on a Body of Revolution," *Physics of Fluids*, Vol. 2, 1959, pp. 714-716.

18 Suter, S. P. and Williams, G., "The Effect of External Vorticity on Stagnation Point Heat Transfer at High Prandtl Numbers," *International Journal of Heat and Mass Transfer*, Vol. 11, 1968, pp. 1795-1806.

19 Gostkowski, V. J., and Costello, F. A., "The Effect of Free Stream Turbulence on the Heat Transfer from the Stagnation Point of a Sphere," *International Journal of Heat and Mass Transfer*, Vol. 13, 1970, pp. 1382-1386.

[5] and of Aufdermaur and Joss' [9] medium-turbulence run (curve 1), but at about the same rate as Aufdermaur and Joss' high-turbulence run (curve 2).

## Concluding Remarks

The results of the present investigation indicate that the local heat flux in the forward region of a sphere is insensitive to moderate levels of free-stream turbulence. For turbulence levels up to about 5 percent, the heat flux is essentially the same as that prevailing in flows having very low free-stream turbulence. This finding does not confirm the results of prior investigations which show a decrease in heat flux at moderate turbulence levels.<sup>5</sup>

For higher turbulence levels, the heat flux was found to increase with increasing turbulence intensity. The largest increase in heat flux encountered here, at a turbulence intensity of 9.4 percent, was about 15 percent. It also appears that at higher turbulence intensities, the dependence of the stagnation-point Nusselt number on the Reynolds number departs from the relation  $Nu \sim Re^{1/2}$ , which corresponds to a laminar boundary layer in a low-turbulence free stream.

At all turbulence levels below 9.4 percent, subcritical (laminar) separation occurred, suggesting that the available disturbances were not sufficient to promote boundary-layer transition. Supercritical (turbulent) separation appeared to occur at a turbulence intensity of 9.4 percent for Reynolds numbers of 42,000 and 62,000. These Reynolds numbers are well below the value  $2 \times 10^6$  for transition in a low-turbulence flow.

## References

- 1 Galloway, T. R. and Sage, B. H., "Thermal and Material Transport from Spheres. Prediction of Macroscopic Thermal and Material Transport," *International Journal of Heat and Mass Transfer*, Vol. 10, 1967, pp. 1195-1210.
- 2 Newman, L. B., "Effect of Freestream Turbulence on Local Heat Transfer from a Sphere," PhD thesis, Department of Mechanical Engineering, University of Minnesota, Minneapolis, Minn., 1970.
- 3 Short, W. W., Brown, R. A. S., and Sage, B. H., "Thermal Transfer in Turbulent Gas Streams. Effect of Turbulence on Local Transport From Spheres," *Journal of Applied Mechanics*, Vol. 27, TRANS. ASME, Series E, Vol. 82, No. 3, Sept. 1960, pp. 393-402.
- 4 Short, W. W. and Sage, B. H., "Temperature Measurements in a Spherical Field: Transfer Coefficients and Corrections for Thermocouples in Boundary Flows," *AIChE Journal*, Vol. 6, 1960, pp. 163-167.
- 5 Venezian, E., Crespo, M. J., and Sage, B. H., "Thermal and Material Transfer in Turbulent Gas Streams: One-Inch Spheres," *AIChE Journal*, Vol. 8, 1962, pp. 383-388.
- 6 Davis, L., "Measurements of Turbulence Level Behind a Set of Square-Mesh Grids and Correlation with Grid Pressure Loss," Report 3-22, Jet Propulsion Laboratory, Pasadena, Calif., 1950.
- 7 Davis, L., "Measurements of Turbulence Decay and Turbulent Spectra Behind Grids," Report 3-17, Jet Propulsion Laboratory, Pasadena, Calif., 1952.
- 8 Wadsworth, J., "The Experimental Examination of the Local Heat Transfer on the Surface of a Sphere When Subjected to Forced Convection Cooling," Report MT-39, Division of Mechanical Engineering, National Research Council of Canada, 1958.
- 9 Aufdermaur, A. N. and Joss, J., "A Wind Tunnel Investigation on the Local Heat Transfer from a Sphere, Including the Influence of Turbulence and Roughness," *ZAMP*, Vol. 18, 1967, pp. 852-866.
- 10 Gardon, R., "An Instrument for the Direct Measurement of Intense Thermal Radiation," *Review of Scientific Instruments*, Vol. 24, 1953, pp. 366-370.
- 11 Gardon, R., "A Transducer for the Measurement of Heat-Flow Rate," *JOURNAL OF HEAT TRANSFER*, TRANS. ASME, Series C, Vol. 82, No. 4, Nov. 1960, pp. 396-398.
- 12 Dryden, H. L., Schubauer, G. B., Mock, W. C., and Skramstad, H. K., "Measurements of Intensity and Scale of Wind-Tunnel Turbulence and Their Relation to the Critical Reynolds Number of Spheres," NACA Report 581, 1937.

<sup>5</sup> A very recent relevant publication by Gostkowski and Costello [19] came to the authors' attention after the submission of the present paper. The trends of that investigation are in qualitative accord with those found here.

13 Sibulkin, M. S., "Heat Transfer Near the Forward Stagnation Point of a Body of Revolution," *Journal of the Aeronautical Sciences*, Vol. 19, 1952, pp. 570-571.

14 Kestin, J., Maeder, P. F., and Sogin, H. H., "The Influence of Turbulence on the Transfer of Heat to Cylinders Near the Stagnation Point," *ZAMP*, Vol. 12, 1961, pp. 115-132.

15 Frössling, N., "Evaporation, Heat Transfer, and Velocity Distribution in Two-Dimensional and Rotationally Symmetrical Laminar Boundary Layer Flow," NACA TM 1432, 1958.

16 Schlichting, H., *Boundary Layer Theory*, 6th ed., McGraw-Hill, New York, 1968, p. 17.

17 Kuethe, A. M., Willmarth, W. W., and Crocker, G. H., "Stagnation Point Fluctuations on a Body of Revolution," *Physics of Fluids*, Vol. 2, 1959, pp. 714-716.

18 Suter, S. P. and Williams, G., "The Effect of External Vorticity on Stagnation Point Heat Transfer at High Prandtl Numbers," *International Journal of Heat and Mass Transfer*, Vol. 11, 1968, pp. 1795-1806.

19 Gostkowski, V. J., and Costello, F. A., "The Effect of Free Stream Turbulence on the Heat Transfer from the Stagnation Point of a Sphere," *International Journal of Heat and Mass Transfer*, Vol. 13, 1970, pp. 1382-1386.

## DISCUSSION

### T. R. Galloway<sup>6</sup>

The augmentation by free-stream turbulence of heat and mass transfer at the forward stagnation point of a bluff body has been conjectural, mainly arising from experimental problems for over 20 years. The authors of this paper are to be commended despite their own experimental difficulties on their demonstration that with a better definition of the free-stream turbulence level the forward stagnation point augmentation is a real phenomenon.

It is unfortunate that the early work of Short et al. and Venezian et al. was used in Fig. 1 to reintroduce the reader to the then puzzling result that their heat transfer decreased with increasing turbulence intensity in the lower range. Both Short and Venezian had great difficulties, especially the former, in obtaining a uniform temperature distribution within the sphere body. Many of the runs involved uncertainties to such an extent that the local measurements did not integrate out to the observed overall heat flux. Also, utilizing the tedious technique of thermocouple traverses, derivatives had to be taken numerically and large corrections for uncertainties in the junction heat loss and position had to be applied. All of these raw experimental data were critically analyzed and the temperature fields surrounding the spheres were refitted with contours that correctly satisfied the observed integral heat flux. Runs were rejected where thermocouple corrections were large. New results based on these reworked early data were published [20] earlier and have been replotted in Fig. 13 here. Short had his  $\frac{1}{2}$ -in. sphere supported at the equator, whereas Venezian had his 1-in. sphere supported at the rear. It is true that the turbulence levels used by Short et al. and Venezian et al. were based on the work of Davis for a slightly larger geometry. Couch [21] critically evaluated the work of Davis in light of more recent measurements and theories and found substantial agreement at the lower turbulence levels up to 8 percent but larger errors for the higher levels.

Galloway [22] redesigned their spheres in order to eliminate the large temperature differences within the sphere body, to provide a small surface heat flux meter and to utilize a temperature-compensated rear stem support. Their measurements were repeated with new turbulence grids and new turbulence correlations and are also shown in Fig. 13 here. In all cases substantial agreement with the present authors is noted. A few small differences can be noted. The threshold effect was not observed at 5 percent, somewhat larger enhancements were obtained with free-stream turbulence, and secondary effects of Reynolds number on stagnation transport were slightly larger.

It is not clear that the equatorial supports used by the author did not have some influence on the forward stagnation point re-

<sup>6</sup> Engineering Research Supervisor, Chemical Engineering Department, Shell Development Co., Oakland, Calif.



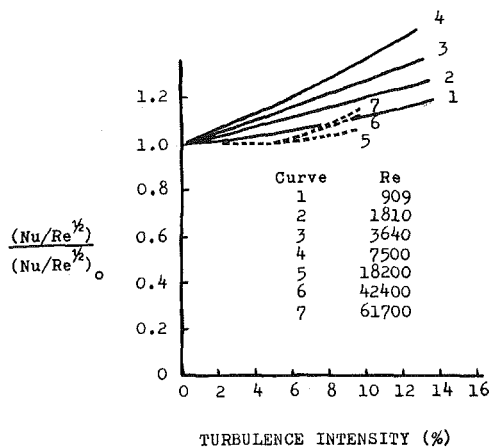


Fig. 13 Comparison of turbulence-level effects on stagnation-point heat transfer

sults. Raithby and Eckert [23] and Galloway [22] have observed such interference (e.g., about a 15 percent increase). Possibly the tripping ring did not alter the outer flow profile because it was already tripped by the equatorial supports. Also in regard to the authors' conclusion that the exponent of the Reynolds number may well depend on the turbulence level, it is also possible that their equation (5) could contain an additive term containing a turbulent Reynolds number to a power above one-half or the product of the turbulence intensity times the ordinary Reynolds number ( $Tu \cdot Re$ ) to a power above one-half.

Figs. 11 and 12 are upsetting. The curves indicate strong cusps at stagnation; these should not exist at a point of symmetry. Around 40 deg the curves are significantly below other experimental or well-established theoretical local heat transfer distributions. It is apparent that in normalization high values at stagnation have artificially depressed this region. It appears that there is a sharp increase in heat flux within a 4.1 deg region on either side of stagnation arising from the cooled center section of the Gardon heat-flux sensor. This effect can be quite significant at stagnation despite the fact that when the sensor is slightly past stagnation the sensor temperature is only depressed 3 percent of the overall  $\Delta T$ . To understand this surprising result let's examine how this sensor functions: When the sphere is heated and the sensor is positioned away from the stagnation point, heat is conducted away into the already developed and growing thermal boundary layer. The larger the resistance in the thermal layer the lower is the heat conducted and therefore the lower is the differential thermocouple voltage output. (There is, incidentally, some residual heat conducted along the central copper wire on the sensor.) However, when the sensor is positioned within its diameter on either side of stagnation (4.1 deg on each side) there is no significant thermal boundary layer developed across the sensor and therefore little thermal resistance to reduce the heat conduction. This results in a large temperature difference and large voltage output, which is in turn interpreted as a large heat transfer coefficient. This phenomenon is analogous to the unheated starting length effect encountered on a flat plate. Indeed, it is an intriguing problem in itself and is worthy of further analysis. However, for this paper it significantly complicates the results, especially when one recognizes that the forward stagnation point position is not completely steady and migrates around depending on the wake process, the Reynolds number, and free-stream turbulence level. And it is the forward stagnation heat flux which was used to normalize the higher turbulence measurements.

### Additional References

- 20 Galloway, T. R., and Sage, B. H., "Thermal and Material

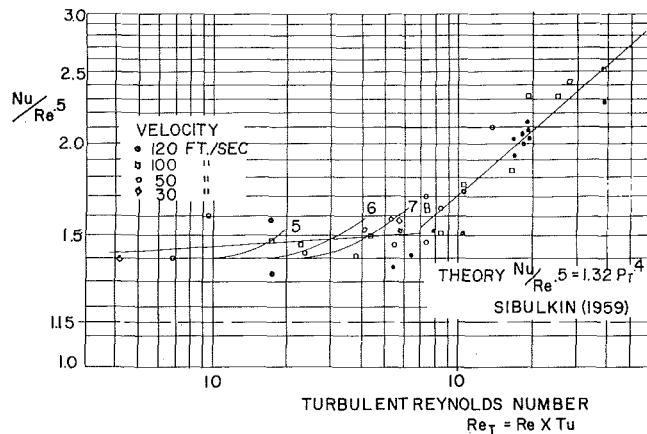


Fig. 14 Correlation of present heat transfer results to turbulent Reynolds number

Transfer from Spheres. Prediction of Local Transport," *International Journal of Heat and Mass Transfer*, Vol. 11, 1968, pp. 539-549.

21 Couch, H. T., "Heat and Mass Transfer from a Cylinder placed in a Turbulent Air Stream—Sherwood and Frössling Numbers as a Function of Free-Stream Turbulence Level and Reynolds Number," Part II, PhD thesis, Department of Chemical Engineering, California Institute of Technology, 1966, University Microfilm 66-11387.

22 Galloway, T. R., and Sage, B. H., "Local and Macroscopic Thermal Transport from a Sphere in a Turbulent Air Stream," to be published in *AIChE Journal*.

23 Raithby, G. D., and Eckert, E. R. G., "The Effect of Turbulence Parameters and Support Position on the Heat Transfer from Spheres," *International Journal of Heat and Mass Transfer*, Vol. 11, 1968, pp. 1233-1252.

### Frederick A. Costello<sup>7</sup>

Fig. 14 shows a comparison between the authors' data and the data and correlation of Gostkowski and Costello [19]. The numbers on the curves correspond to the cases shown in Fig. 8. Both sets of data show an increase in heat transfer with increasing turbulence, but the authors' data shows a Reynolds-number dependence not found in the previous work. Since the authors have used the ratio of  $Nu/Re^{0.5}$  to the same quantity with a clear tunnel (0.2 to 0.3 percent turbulence), the discrepancy might be due to a variation in the reference value; this hypothesis can be tested only if some absolute measurements of the reference value are made. Lacking these, it would be helpful but not conclusive to know the turbulence intensity of the clear tunnel as a function of Reynolds number.

Absolute measurements in a clear tunnel would be useful also in checking Sibulkin's as yet unconfirmed theory [13]. The absolute measurement will be difficult because it will be necessary to show that a small increase in turbulence, from 0 to 0.2 percent, does not cause a significant deviation from the theory. Measurement of the velocity gradient at the stagnation point will also be important. The authors measured a dimensionless gradient of 2.66 as compared to the theoretical value of 3.00.

### Authors' Closure

The discussions submitted by Dr. Galloway and Professor Costello are welcomed as interesting supplements to the paper.

It was good of Dr. Galloway to provide perspective on the work that has been performed over the years by Professor Sage's group at Caltech. As a result, it is now clear that the earlier work published by that group should be discounted.

In spite of all our efforts, we were neither able to follow nor to

<sup>7</sup> Mechanical and Aerospace Engineering Department, University of Delaware, Newark, Del. Mem. ASME.

see the point of Dr. Galloway's discussion of the heat-flux sensor. Notwithstanding what he might have had in mind, there appears to be a basic misconception in his discussion. Dr. Galloway states that the boundary-layer thickness at the stagnation point is essentially zero compared with that at positions away from the stagnation point. It is, on the contrary, well established that the boundary-layer thickness is very little different at the stagnation point and at downstream points, say, up to angles of 40 deg. Another minor point in Dr. Galloway's discussion that warrants correction is the implication that the heat-flux sensor subtended 8.2 deg of arc. The sensor actually subtended 4 deg of arc, as stated in the paper. The matter of the side supports has already been discussed in the paper, where representative results of flow-

visualization studies are given.

In view of Dr. Galloway's concern, it may be well to comment on the possible influence of the temperature depression at the center of the sensor. As noted in the paper, the *maximum* depression was about 3 percent of the sphere-to-air temperature difference. We have estimated that the streamwise temperature gradients induced by the maximum temperature depression were about 1 percent of the transverse temperature gradients. Such induced streamwise gradients should have a negligible influence on the results.

In response to Professor Costello, some information on the variation of the turbulence intensity of the clear tunnel as a function of Reynolds number is given in Fig. 2 of the paper.

K. HOLLASCH<sup>1</sup>

Project Engineer,  
Harrison Radiator Div.,  
General Motors Corp.,  
Lockport, N. Y.

B. GEBHART

Professor,  
Department of Mechanical Engineering,  
Cornell University, Ithaca, N. Y.  
Mem. ASME

# Calibration of Constant-Temperature Hot-Wire Anemometers at Low Velocities in Water with Variable Fluid Temperature

*Calibration of hot-wire probes operated in a constant-temperature mode in water at low velocities is discussed. Operation under circumstances where natural convection effects are important is considered. A method of calibrating a constant-temperature hot-wire probe for variations in fluid temperature is presented. The method consists of varying wire overheat during calibration at a constant fluid temperature. A relation is derived analytically relating anemometer output with a variable overheat resistance to anemometer output with fluid temperature variations. An experimental study to verify the analysis is presented.*

## Introduction

CALIBRATION of hot-wire and film probes in constant-temperature fluids may be carried out by many techniques discussed in the literature. However, anemometer output varies with ambient fluid temperature at constant velocity. Therefore, to measure a fluctuating velocity field when large temperature fluctuations are present in the fluid, calibration at various fluid temperatures must be considered.

A constant-temperature anemometer, in fact, maintains a fixed probe heated or operating resistance. Fluctuating fluid temperature makes it impossible to maintain a constant overheat ratio because  $R_A$ , the unheated resistance, varies as  $T_A$ , the ambient fluid temperature, varies. Hence an independent measure of fluctuating temperature is necessary in order to interpret hot-wire output. An independent temperature measurement, when used with a wire calibrated for various fluid temperatures at fixed overheat resistance, will yield the velocity. The term "fixed overheat resistance" is necessary instead of "fixed overheat ratio," because  $R_A$  (and  $T_A$ ) are now considered variables. Hence the overheat ratio could be considered as maintained at a constant value only by using a fixed reference resistance  $R_0$  at a reference fluid temperature  $T_0$  as the unheated wire resistance in the calculation of overheat ratio.

An example of the above problem is the study of natural convection turbulence. Velocity and temperature fluctuations occur simultaneously. A compact array of two hot-wire probes may be used to determine velocity and temperature instantaneously.

Alternately, a small thermocouple with adequate frequency response might be used in conjunction with a hot-wire probe to yield fluctuating temperature directly and fluid velocity indirectly. The use of two probes is permissible as long as the physical scales of the temperature and velocity fluctuations are large relative to the distance between sensors.

Rose [1]<sup>2</sup>, has considered the response of a linearized hot wire in air to small ambient fluid temperature fluctuations. Sandborn [2] has indicated that fluid temperature fluctuations significantly affect results in many modes of operation. Resch and Coantic [3] and Resch [4] found it necessary to calibrate for fluid temperature variations in water. Newman [5] has calibrated film probes in water at various temperature levels. His results show that fluid temperature variations cause significant variations in hot-wire output. In general, previous experimental work has found the fluid temperature variation effect to be more pronounced in water than in air; one reason is that low overheats are used in water to prevent bubble formation and boiling. Hence a fluid temperature variation in water may significantly alter the temperature difference between wire and fluid. A similar disturbance in air would cause a smaller effect because higher wire temperatures are used. An additional error induced by fluid temperature fluctuation arises from fluid property variations. Property variations with temperature are more rapid in water than in air, causing greater difficulty with water. One successful attempt at this type of calibration is presented by Vliet and Liu [6], using a linearized hot wire.

It is true that calibrating hot wires over adequately large ranges of ambient fluid temperature is experimentally inconvenient and difficult, especially when fluid temperatures differ greatly from ambient laboratory conditions. Large temperature differences induce appreciable natural convection effects in the test fluid. This causes an inaccurate determination of the zero

<sup>1</sup> Formerly NSF Trainee, Department of Mechanical Engineering, Cornell University, Ithaca, N. Y.

Contributed by the Heat Transfer Division and presented at the ASME-AIChE Heat Transfer Conference, Tulsa, Okla., August 15-18, 1971. Manuscript received by the Heat Transfer Division January 18, 1971. Paper No. 71-HT-9.

<sup>2</sup> Numbers in brackets designate References at end of paper.

velocity voltage ( $E_0$ ), which is often used for nondimensionalization of output voltages. In addition, if the flows to be measured have velocities of the same order as any natural convection currents in the calibration vessel, the anemometer output during calibration will be in error. The requirement of a constant fluid temperature greatly different from ambient laboratory conditions also requires the use of regulating equipment. Such regulating equipment complicates apparatus design and increases cost. Vliet and Liu [6] used a heated vessel for their calibration procedure.

The present communication describes a technique of calibrating constant-temperature anemometer probes, accounting for varying ambient fluid temperatures by instead varying overheat resistances at a single reference fluid temperature. Varying overheat resistance is experimentally convenient since modern commercial anemometers usually incorporate decade resistances which expedite setting various overheat resistances.

The motivation behind the proposed technique is as follows. An increase in ambient fluid temperature ( $T_A$ ) decreases the temperature difference between the (constant-temperature) wire at  $T_H$  and the ambient fluid. Heat loss rate from the wire may be represented by:

$$\dot{q} = Ah(U, T_A)(T_H - T_A)$$

where  $h$  is indicated as a function of velocity and fluid temperature. However, a change in overheat resistance from  $R_H$  to  $R_H + r$  may also reduce the temperature difference between the wire and the ambient fluid (if  $r < 0$ ). If  $h$  is a weak function of temperature, the anemometer output characteristics observed when ambient fluid temperature is varied may be approximated by varying the overheat temperature. Of course, account must be taken of the effect of increased probe resistance.

Hence it is proposed to calibrate the output of the hot-wire probe as a function varying ambient of fluid temperature by varying the overheat resistance at a constant reference fluid temperature  $T_0$ .

## Analysis

The heat dissipated in a hot-wire probe by convection processes, neglecting conduction losses to the probe supports, is

$$\dot{q} = hA(T_H - T_A) = \frac{E^2}{R_H}$$

where  $h$  is an average heat transfer coefficient,  $A$  is the area of the wire, and  $T_H - T_A$  is the difference between the constant wire and fluid temperature. Thus

$$E^2 = R_H(T_H - T_A)hA \quad (1)$$

Since  $T_A$  is variable and  $h = h(T_A, U)$ , a hot-wire probe apparently must be calibrated at different fluid temperatures for fixed overheat temperature ( $T_H$ ), i.e., fixed probe overheat resistance.

However, consider the possibility of changing overheat resistance to simulate varying fluid temperature during the calibration of the hot-wire probe. In a small temperature range the probe resistance may be assumed to be a linear function of temperature.

$$R = R_A + (\alpha R_{32})(T - T_A)$$

Consider a small change ( $r$ ) in  $R_H$ , i.e.,  $R_H + r$ , such that the anemometer output voltage, when operated with a variable overheat resistance matches the output voltage that would result when operated at fixed overheat resistance and at an ambient fluid temperature  $T_A$  different from  $T_0$ .

Then, writing the energy balance for calibration when a variable overheat resistance is used and at an ambient temperature equal to the reference temperature  $T_0$ , we have

$$\frac{E_c^2}{R_H + r} = \left( T_H + \frac{r}{\alpha R_{32}} - T_0 \right) h(T_0, U)A \quad (2)$$

where  $h(T_0, U)$  is the film coefficient of heat transfer which is a function of velocity and reference ambient fluid temperature,  $A$  is the area of the wire, and  $\left( T_H + \frac{r}{\alpha R_{32}} - T_0 \right)$  is the temperature difference between the hot wire and the fluid at the reference ambient fluid temperature.

The output voltage with a variable fluid temperature must equal the output voltage with variable overheat resistance.

$$(R_H + r) \left( T_H + \frac{r}{\alpha R_{32}} - T_0 \right) h(T_0, U) = R_H(T_H - T_A)h(T_A, U) \quad (3)$$

For the moment assume  $h(T_0, U) = h(T_A, U)$ , which is equivalent to assuming that fluid property variations are negligible in determining  $h$ . Then

$$T_A - T_0 = \frac{1}{R_H} \left[ \frac{r^2}{\alpha R_{32}} + r \left( T_H - T_0 + \frac{R_H}{\alpha R_{32}} \right) \right] \quad (4)$$

Calibration performed at overheat resistance  $R_H$  with fluid temperature  $T_A$  would produce nearly identical output voltage to a calibration performed at an overheat resistance of  $R_H + r$  with a fluid temperature of  $T_0$ . Equation (4) gives the proper relation for calculating the effective fluid temperature change  $T_A - T_0$  equivalent to a resistance change of  $r$ .

However, a small difference in output should be expected because of fluid property variations. The error is caused because  $h(T_0, U)$  will, in general, be different from  $h(T_A, U)$ .

A correction term to account for fluid property variation may be developed using data which is, in principle, already available from a calibration. Expanding  $h(T_A, U)$  in a Taylor series about  $T_0$ , equation (1) yields

## Nomenclature

$a$ = overheat ratio = $\frac{R_H}{R_A}$	calibration is done with variable $R_H$	$E_c$ = anemometer output with overheat resistance variable
$R_{32}$ = resistance of probe at 32 deg F	$T_H$ = wire temperature when calibration is done with constant $R_H$	$E_0$ = zero velocity voltage = $E_0(T)$ = a function of fluid temperature
$r$ = change in overheat resistance to simulate ambient fluid temperature variations	$T_A$ = ambient fluid temperature	
$R_0$ = reference probe resistance at reference temperature	$\alpha R_{32}$ = resistance coefficient of temperature for probe	$Re_d$ = Reynolds number = $\frac{Vd}{\nu}$
$R_H$ = overheat probe resistance	$A$ = area of wire probe = $\frac{\pi d^2}{4} \cdot l$	$\nu$ = kinematic viscosity
$R_A$ = probe resistance at ambient fluid conditions	$h$ = film coefficient of heat transfer	$d$ = wire diameter
$l$ = length of wire	$\dot{q}$ = rate of heat loss	$B$ = nondimensional voltage parameter = $\frac{E^2}{E_0^2} - 1$
$T_0$ = reference fluid temperature when	$U$ = velocity	
	$E$ = anemometer output with fluid temperature variable	$Gr_d$ = wire Grashof number = $\frac{g\beta}{\nu^2} \Delta t d^3$



$$E^2 = R_H(T_H - T_A)A \left[ h(T_0, U) + \frac{\partial h(T_0, U)}{\partial T} \Big|_U [T_A - T_0] + \frac{\partial^2 h(T_0, U)}{\partial T^2} \Big|_U \frac{[T_A - T_0]^2}{2} + \dots \right] \quad (5)$$

Equations (3) and (4) identify the first term as  $E_c^2$  in equation (2).

$$E^2 = E_c^2 + R_H(T_H - T_A)A \frac{\partial h(T_0, U)}{\partial T} \Big|_U [T_A - T_0] + \dots \quad (6)$$

Using equation (2) to calculate  $\frac{\partial h(T_0, U)}{\partial T} \Big|_U$  and substituting into (6) gives

$$E^2 = E_c^2 + \left[ \frac{R_H(T_H - T_A)}{(R_H + r) \left( T_H + \frac{r}{\alpha R_{32}} - T_0 \right)} \right] \times \frac{\partial E_c^2(T_0, U)}{\partial T} \Big|_U [T_A - T_0] + \dots \quad (7)$$

Noting from (7) that the term in square brackets equals one and substituting (4) into (7) we have

$$E^2 = E_c^2 + \frac{\partial E_c^2(T_0, U)}{\partial T} \Big|_U \times \left[ \frac{r^2}{\alpha R_{32}} + r \left( T_H - T_0 + \frac{R_H}{\alpha R_{32}} \right) \right] \frac{1}{R_H} + \dots \quad (8)$$

Now recalling that  $R$  is a linear function of  $T$ ,

$$\frac{\partial E_c^2(T_0, U)}{\partial T} \Big|_U = \frac{\partial E_c^2}{\partial R} \Big|_U \frac{\partial R}{\partial T} = \alpha R_{32} \frac{\partial E_c^2(R_H, U)}{\partial R} \Big|_U$$

but  $dR = dr$

$$E^2 = E_c^2 + \frac{\partial E_c^2(r = 0, U)}{\partial r} \times \left[ \frac{r^2}{\alpha R_{32}} + r \left( T_H - T_0 + \frac{R_H}{\alpha R_{32}} \right) \right] \frac{\alpha R_{32}}{R_H} + \dots \quad (9)$$

The term  $\partial E_c^2/\partial r$  may be estimated if calibration is performed at two different values of  $r$ . If large property variations occur between the two ambient temperature levels  $T_A$  and  $T_0$  the accuracy requirements of some specific applications may require the retention of more terms in equation (6) as well as calibration at additional  $r$  levels. The second-order correction term to equation (9) is

$$+ \frac{1}{2} \left( \frac{\alpha R_{32}}{R_H} \right)^2 \frac{\partial^2 E_c^2}{\partial r^2} \Big|_U \left[ \frac{r^2}{\alpha R_{32}} + r \left( T_H - T_0 + \frac{R_H}{\alpha R_{32}} \right) \right]^2 \quad (10)$$

The above relation (9) relates the output of the anemometer taken with varying fluid temperature ( $E^2$ ) to the output taken with variable overheat resistance ( $E_c^2$ ) and retains a first-order correction term to account for property variations.

An experimental study to determine the applicability of the above method in a practical situation was undertaken. Wires were first calibrated with variable fluid temperatures. Then the same wires were calibrated at constant reference fluid temperature with variable overheat resistance as calculated from equation (4).

## Experimental Apparatus

The high-accuracy calibration of hot wires at very low velocities in liquids has been described by Dring and Gebhart [7]. The apparatus used in that investigation was modified to allow higher velocities and use with gases as described in Dring and Gebhart

[7], Gebhart, Pera, and Audunson [8], and Gebhart and Pera [9]. The technique consists of holding a probe stationary in a Dewar filled with the fluid of interest. The Dewar is then translated vertically along guides by a counterbalance weight and a synchronous motor. Thus the fluid is translated at a constant velocity over the stationary probe. The fluid used in this study was demineralized degassed water. The temperature of the bath in the Dewar was controlled by circulating the water through a heat exchanger in another identical Dewar. This Dewar contained a high-precision (0.01 deg C) controller which allowed accurate regulation of the fluid temperature.

The anemometers used were DISA model 55D01 used in the constant-temperature mode, operated in the "flat" position to guarantee a constant gain for frequencies down to d-c. The upper limit of frequency response is more than adequate for the relatively low frequencies encountered in turbulent flows of liquids. Anemometer output voltages were measured by voltage-time integration, using a six-digit integrating voltmeter and a seven-digit EPUT meter. In addition, integration distance was measured to 0.0001 in. with a micrometer. Knowing that distance, the timer yielded an independent measure of velocity for every data point taken. Operational details of the switching circuits and hookup of voltage-measuring instruments are described in detail in references [7-9]. The multiple-digit outputs allow high-precision determination of anemometer output voltages. Measured velocities are thought to be accurate to 5 parts in  $10^4$  during the calibration.

The hot-wire prongs and associated supports used were silver-plated. The hot wire used was pure platinum of 0.4-mil diameter. The Dewar was stainless steel. Water used was demineralized, degassed, and filtered. Water resistivity was 1 megohm/cm or higher at all times. Apparently the silver probe supports provide so-called "anodic protection" for the platinum wire in the multi-metal system. This technique is common in design of boilers and ship-building and is discussed in reference [10].

Drift observed from the corrosion process was of the same order as the 0.2 percent/hr quoted by Bankoff and Rosler [11]. The wire was operated only during the actual calibration traverse to further minimize this effect. In addition, no deposits were formed on the wire during operation. Pronounced drift characteristics quoted in references [3, 4, 12, 13] were not observed. Aeration of the water was prevented with a floating plastic cover. Bubble formation was therefore eliminated as a source of drift. For further description of the requirements for stable operation in water see reference [14].

## Procedure

Wire calibrations were first carried out using a variable fluid temperature  $T_A$  and constant wire overheat resistance. For comparison, a calibration with the same probe was performed with variable overheat resistances at a reference fluid temperature  $T_0$ . Resistance-temperature increments were calculated by equation (4).

A single calibration data point consisted of the following steps:

- 1 Waiting for all disturbances to die out, until an approximately stable zero-velocity voltage was observed and recorded (fluctuations of less than 10 mv on a 10-v signal).
- 2 Measuring fluid temperature in the calibration Dewar with mercury in a glass thermometer, accurate to 0.01 deg F.
- 3 Traversing the calibration Dewar in the upward direction; (a) measuring an integrated anemometer voltage; (b) measuring the time interval of integration (yielding velocity).
- 4 Returning Dewar to down position.

Disturbances from a traverse usually were completely dissipated in about 2 min. Wire output was continuously monitored on a strip-chart recorder to assure stable conditions before another data point was taken.

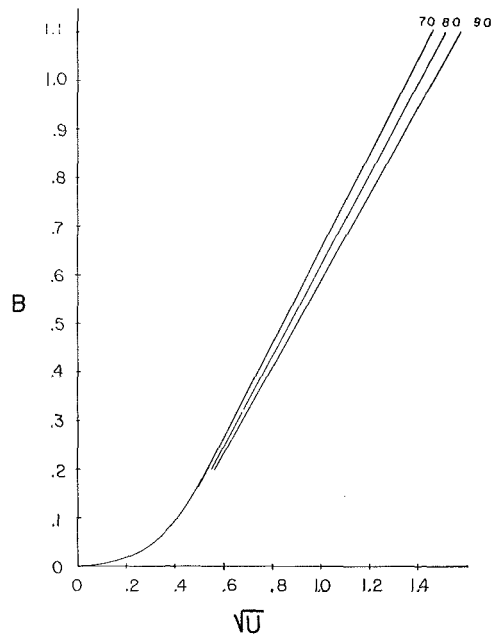


Fig. 1 Plot of regression analysis results for variable temperature data 70, 80, 90 deg F in forced convection region and 70 deg F in mixed convection region;  $[\sqrt{U}] = (\text{in/sec})^{1/2}$

The calibration with variable fluid temperature was performed for six different ambient fluid temperatures from 60 to 100 deg F. The calibration with variable overheat resistance at constant fluid temperature used five different overheat resistances. The different overheat resistances were selected using equation (5). The temperature differences between the wire and fluid were in the same range as those used for the variable fluid temperature calibration.

For the data presented here, which represent one wire only,  $T_H$  was 205 deg F. Fluid temperature variations were up to 30 percent of the wire-fluid temperature difference. The temperature increment calculated using equation (5) was about 2.80 deg F/0.01  $\Omega$ , for a pure platinum wire operated at  $R_H = 2.63 \Omega$ . Overheat ratio based on the cold resistance at 70 deg F was 1.28. Lower overheat ratios would be necessary if an adequate deaeration system were not available.

Data were taken at 8 velocities ranging from 0.01 in/sec to 2.36 in/sec corresponding to  $2.62 \cdot 10^{-2} < Re_d < 6.18$ . Variable fluid temperature data with constant overheat resistance comprised 187 points. Variable overheat resistance data with constant fluid temperature consisted of 155 points. The total test period lasted several days. However, actual wire operating time was only a few hours, to minimize the effect of the 0.2-percent/hr observed drift. Consistent results were obtained from day to day. All of the data discussed herein were obtained with the same hot wire. Other wires have been calibrated with essentially identical results.

## Analysis of Data

The two sets of data obtained (at constant  $R_H$  and variable  $T_A$ , and at variable  $R_H$  and constant  $T_0$ ) were treated separately on a digital computer by the standard statistical technique of regression analysis. This technique calculates a regression function which approximates the data in a least-squares sense. The program used was selected from the UCLA BMD package which is available on many IBM computing machines. (Program designation in BMD02R.) Given a choice of many forms of the specified independent variables, the program selects in a stepwise manner the terms which give the best fit, in a least-squares sense, see reference [15].

The low velocities involved in this work made natural convec-

tion effects appreciable for some of the data. Hence each set of data was broken into two "regions" for purposes of analysis. Some of the data were taken in the mixed convection region. The mixed convection region is defined as the transport region where natural and forced convection effects are of the same order in the transport process from the wire.

The lower velocity limit for appreciable natural convection effect was suspected, from the data of Gebhart et al. [8], to lie within the range of the current calibration. Plotting of anemometer voltage squared,  $E^2$ , versus  $\sqrt{U}$  (see Fig. 1) showed deviations from the straight line expected from King's law for pure forced convection. These deviations from pure forced convection occurred where predicted by the criteria of Gebhart et al. [8]. The mixed convection region was found up to  $\sqrt{U} = (0.5 \text{ in/sec})^{1/2}$ , which corresponds to the point where  $Gr_d^{1/2}/Re_d$  is order 1. For  $Re_d > 0.655$  the wire heat transfer was found to be completely dominated by forced convection cooling. Hence a King's law type variation was used and the region was characterized by linear variation between  $E^2$  and  $\sqrt{U}$ .

The variables used in the statistical treatment of the two sets of data were as follows. The square root of the velocity (or of the Reynolds number) was treated as the dependent variable, since this quantity was known from the calibration. The independent variables were the voltage squared,  $E^2$ , the zero-velocity voltage squared,  $E_0^2$ , and the ambient fluid temperature,  $T_A$ . The two voltages were combined into a single nondimensional independent variable.

$$B = \left( \frac{E^2}{E_0^2} - 1.0 \right)$$

The general formulation attempted was

$$\sqrt{U} = f(B, T) \quad (11)$$

The  $\sqrt{U}$  was expanded in a Taylor series in the independent variables. Here  $B$  is dimensionless and  $T$  has dimensions of deg F.

$$\begin{aligned} \sqrt{U} = f(0, 0) + \frac{\partial f}{\partial B} B + \frac{\partial f}{\partial T} T + \frac{\partial^2 f}{\partial T \partial B} TB \\ + \frac{\partial^2 f}{\partial B^2} \frac{B^2}{2} + \frac{\partial^2 f}{\partial T^2} \frac{T^2}{2} + \dots \quad (12) \end{aligned}$$

All possible combinations of the above terms in equation (12) were tried for the least-squares fit. Many additional higher-order terms were also considered. The two forms found to best describe the data, without significant improvement by the addition of higher-order terms, were

$$\begin{aligned} \sqrt{U} = \text{constant} + \frac{\partial f}{\partial B} B \\ + \frac{\partial^2 f}{\partial T \partial B} TB \quad (\text{forced convection region}) \quad (13a) \end{aligned}$$

$$\begin{aligned} \sqrt{U} = \frac{\partial f}{\partial B} B + \frac{\partial^2 f}{\partial B^2} \frac{B^2}{2} + \frac{\partial f}{\partial T} T \\ + \frac{\partial^2 f}{\partial T^2} \frac{T^2}{2} \quad (\text{mixed convection region}) \quad (13b) \end{aligned}$$

The lack of a constant in the mixed convection region is because  $E = E_0$  for  $\sqrt{U} = 0$ . Hence a zero constant was imposed on the regression analysis for this region. In the two regions of interest, the best forms for the least-squares fit were

$$\begin{aligned} \sqrt{U} = K_1 B + K_2 B \left( \frac{T}{10^2} \right) + K_3 \\ (\text{forced convection region}) \quad (14a) \end{aligned}$$

$$\sqrt{U} = C_1 B + C_2 B^2 + C_3 \left( \frac{T}{10^2} \right) + C_4 \left( \frac{T}{10^2} \right)^2 \quad (\text{mixed convection region}) \quad (14b)$$

These specific forms were used in the analysis of both sets of data. It was desirable to reduce the temperature variable to order 1 for calculating purposes, as shown in (14a) and (14b). Attempts were made to use  $\sqrt{Re_d}$  as the dependent variable with no improvement in correlation.

Evaluation of the data set taken with variable fluid temperature at constant overheat resistance was accomplished as follows. Measured fluid ambient temperature  $T_A$  was used as the  $T$  variable in (14).  $B$  was evaluated using  $E_0 = E_0(T)$ , which was experimentally determined.

The constants for the correlation obtained in this way are given in Table 1a. These results represent the whole data set taken with a variable fluid temperature. Equation (14) with the constants as in Table 1a yields calibration curves shown in Fig. 1.

Data taken with variable overheat resistance at constant fluid temperature were analyzed by the same procedures. However, the temperature used in the regression analysis was  $T = T_0 + \frac{r}{\alpha R_{32}}$ . The experimental value of  $E_0 = E_0(T)$  was replaced by experimental values of  $E_0 = E_0(r)$  in the calculation of the variable  $B$ . The constants obtained for the correlation are given in Table 1b.

The replacement of  $E_0(T)$ , taken when fluid temperature was varied, by  $E_0(r)$ , taken when overheat resistance was varied, is justified by the close agreement between  $E_0(T)$  determined experimentally (187 points) and  $E_0(r)$  (155 points). The above-mentioned  $T = T_0 + \frac{r}{\alpha R_{32}}$  approximation for the variable overheat data set yields an  $E_0[r(T)]$  curve virtually identical to  $E_0(t)$ . The slopes and intercepts of the  $E_0(T)$ 's from the two data sets agree to within 1/2 percent based on separate linear regression analysis of the two data sets.

Equation (9) above shows that a fluid property correction term may be included in the calculations. Since the temperature differences in the data sets were as much as 40 deg F, this correction might be important. An attempt was made to utilize the correction terms presented in equations (9) and (10). Their inclusion in the variable overheat data set was accomplished as follows. The voltages were corrected according to equation (9).

The term  $\left. \frac{\partial E_c^2}{\partial r} \right|_U$  in equation (9) was calculated by fitting  $E_c^2$

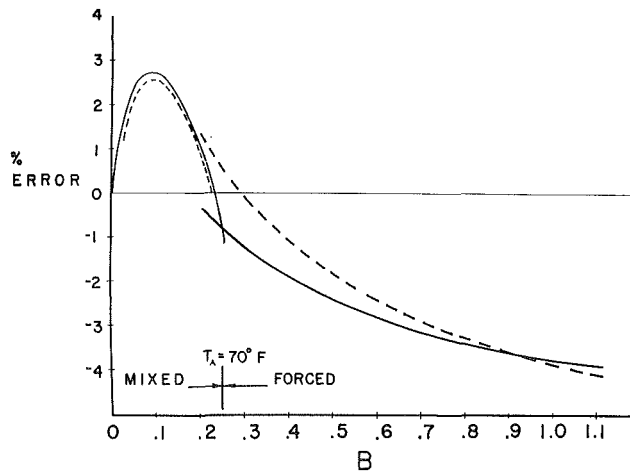


Fig. 2 Plot of percent error in  $\sqrt{U}$  versus  $B$  at 70 deg F; solid line—without fluid property corrections; broken line—with fluid property corrections

versus  $r$  in a least-squares sense. That is, the data were fitted to a linear curve  $E^3 = k_1 + k_2 r$ , which produced the derivative desired, which was  $\left. \frac{\partial E^2}{\partial r} \right|_U = k_2$ . A second-order term was found to

give no improvement over the linear form. The values of  $\left. \frac{\partial E^2}{\partial r} \right|_U$  vary greatly with velocity, and are presented in Table 2. A variable fluid property analysis was then done in exactly the same way as with the variable overheat resistance data set, only using the corrected voltages. The results of that analysis are shown in Table 1c.

## Results

The root-mean-square error in  $\sqrt{U}$ , the standard error, of the data points used in the regression analysis about the generated function is shown in Table 1. The variable overheat resistance conditions allow fluid temperature to be at room ambient temperature, thus reducing the natural convection circulations in the fluid and uncertain fluid temperature. Hence a more precise determination of  $E_0$  (and calibration velocity at low velocities) is possible using this method. This is illustrated in the relatively low standard error of the variable overheat data compared to that taken at variable fluid temperature.

The three generated regression functions shown in Table 1 are compared in Figs. 2, 3, and 4. These figures indicate behavior at ambient fluid temperatures of 70, 80, and 90 deg F, respectively. The solid lines are the percentage difference between the variable fluid temperature regression function and the variable overheat regression function. The difference has been normalized with the value of  $U$  calculated from variable fluid temperature regression function. This percentage error curve is plotted against  $B$ , the nondimensionalized output voltage. The two regions of interest, mixed convection and forced convection (mixed convection for  $B < 0.25$ , forced convection for  $B > 0.25$ ), are seen to have different error characteristics.

In addition, the same comparison was made between the variable fluid temperature regression function and the overheat data which incorporated the fluid property correction term. The corrected data produced error characteristics represented by the

Table 1 Regression coefficients

Dimensions	1a		1b		1c	
	Variable fluid ambient temperature	Variable overheat resistance	Variable overheat resistance	Corrected variable overheat resistance	Corrected variable overheat resistance	Corrected variable overheat resistance
$(\text{in/sec})^{1/2}$	$K_1$	0.67123	1.03266	0.95265	0.95265	0.95265
$(\text{in/sec})^{1/2}/^\circ\text{F}$	$K_2$	0.51215	0.08530	0.21635	0.21635	0.21635
$(\text{in/sec})^{1/2}$	$K_3$	0.32595	0.31536	0.30406	0.30406	0.30406
$(\text{in/sec})^{1/2}$	*	0.0479	0.0072	0.0116	0.0116	0.0116
$(\text{in/sec})^{1/2}$	$C_1$	2.49954	2.29968	2.28472	2.28472	2.28472
$(\text{in/sec})^{1/2}$	$C_2$	-3.83903	-2.95736	-2.91951	-2.91951	-2.91951
$(\text{in/sec})^{1/2}/^\circ\text{F}$	$C_3$	0.49391	-0.49686	0.53586	0.53586	0.53586
$(\text{in/sec})^{1/2}/^\circ\text{F}$	$C_4$	-0.30430	-0.30868	-0.36070	-0.36070	-0.36070
$(\text{in/sec})^{1/2}$	†	0.0191	0.0072	0.0077	0.0077	0.0077

\* Standard error, forced region

† Standard error, mixed region

Table 2  $\left. \frac{\partial E^2}{\partial r} \right|_U$  versus  $\sqrt{U}$

$\sqrt{U}$ (in/sec) <sup>1/2</sup>	1.36	1.01	0.75	0.56	0.47	0.33	0.25	0
$\left. \frac{\partial E^2}{\partial r} \right _U$ volts <sup>2</sup> /ohm	425.8	334.9	286.8	235.4	226.0	209.5	202.5	201.6

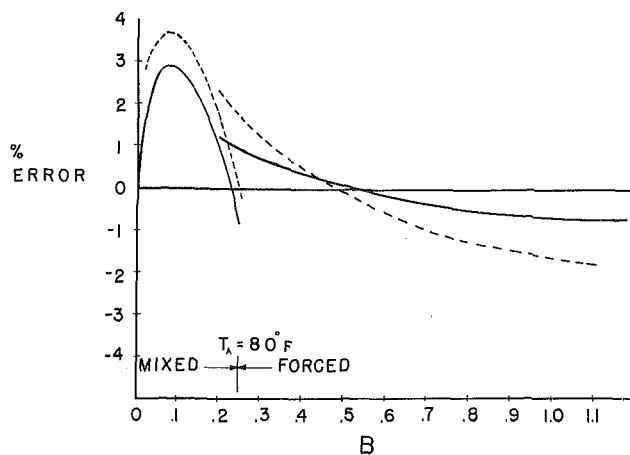


Fig. 3 Plot of percent error in  $\sqrt{U}$  versus  $B$  at 80 deg F; solid line—without fluid property corrections; broken line—with fluid property corrections

dashed curves in Figs. 2, 3, and 4. This correction term appears to reduce error in the forced convection region. The mixed convection region is not significantly improved using the correction term, in fact, the error is greater for the 80 deg F and 90 deg F conditions.

Considering the curves presented in Figs. 2, 3, and 4, a physical explanation even further validates the proposed calibration method. Recall that the variable fluid temperature data were used as the standard of normalization for Figs. 2, 3, and 4. Those data themselves may contain small systematic errors in  $E_0$  as a result of natural convection circulation in the calibration Dewar.

The room temperature was about 80 deg F when these variable fluid temperature data were taken. For fluid temperatures lower than 80 deg F, say 70 deg F as in Fig. 2, natural convection currents go up the wall, and down the center of the Dewar where the wire is located. Thus the circulation opposes natural convection flow generated over the wire and  $E_0$  is decreased. This effect results in a predicted  $\sqrt{U}$  which is lower than the velocity of the Dewar. Hence the standard used for normalization in Fig. 2 is itself low and the error shown by the curve is greater than the actual error in the variable overheat method. The same argument applies to fluid temperatures above room temperatures, say 90 deg F as in Fig. 4. In this case also, the above argument implies a reduction in error between the calibrations produced by the two methods.

## Conclusions

It has been shown that a calibration procedure using variable overheat resistance can provide results which represent hot-wire output response to variations in fluid temperature. Considerable simplifications in experimental calibration equipment and procedures are achieved, at a very small loss in accuracy.

Large errors common to liquid turbulence measurements with high turbulence intensities may justify use of this calibration technique. Hence this method may greatly expedite calibration of hot wires for measurements in turbulent flows where large temperature fluctuations occur.

## Acknowledgments

The authors wish to acknowledge support for this research under National Science Foundation Grant GK 18529. Also acknowledged is fellowship support for the first author from the National Science Foundation under Grant GZ-543 and by the Ford Foundation.

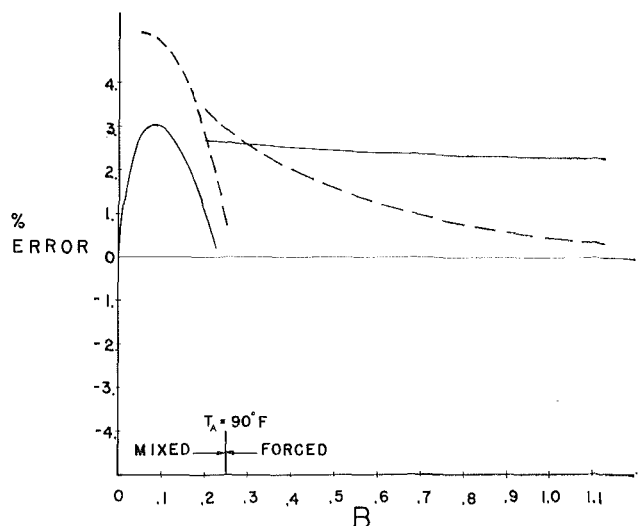


Fig. 4 Plot of percent error in  $\sqrt{U}$  versus  $B$  at 90 deg F; solid line—without fluid property corrections; broken line—with fluid property corrections

## References

- Rose, W. G., "Some Corrections to the Linearized Response of a Constant-Temperature Hot-Wire Anemometer Operated in a Low-Speed Flow," *Journal of Applied Mechanics*, TRANS. ASME, Series E, Vol. 84, No. 3, Sept. 1962, pp. 554-558.
- Sandborn, V. A., "Hot Wire Anemometer Measurements in Large-Scale Boundary Layers," *Advances in Hot Wire Anemometry*, ed. by Melnik and Weske, University of Maryland, 1961.
- Resch, F., and Coantic, M., "Etude sur le fil chaud et le film chaud dans l'eau," *La Houille Blanche*, No. 2, 1969, pp. 151-161.
- Resch, F., "Etudes sur le fil chaud et le film chaud dans l'eau," Rapport CEA-R-3510, Centre d'Etudes Nucléaires de Cadarache, commissariat à l'Energie Atomique, France, 1968.
- Newman, L., "A Survey of the Literature on Transition from Laminar to Turbulent Flow in Natural Convection and Forced Flow," MS thesis, Cornell University, Feb. 1966.
- Vliet, G. C., and Liu, C. K., "An Experimental Study of Turbulent Natural Convection Boundary Layers," *JOURNAL OF HEAT TRANSFER*, TRANS. ASME, Series C, Vol. 91, No. 4, Nov. 1969, pp. 517-531.
- Dring, R. P., and Gebhart, B., "Hot-Wire Anemometer Calibration for Measurements at Very Low Velocity," *JOURNAL OF HEAT TRANSFER*, TRANS. ASME, Series C, Vol. 91, No. 2, May 1969, pp. 241-244.
- Gebhart, B., Pera, L., and Audunson, T., "Forced, Mixed, and Natural Convection from Long Horizontal Wires; Experiments at Various Prandtl Numbers," Paper NC 3.2 presented at Fourth International Heat Transfer Conference, Paris, Sept. 1970.
- Gebhart, B., and Pera, L., "Mixed Convection from Long Horizontal Cylinders," *Journal of Fluid Mechanics*, Vol. 45, 1971, pp. 49-64.
- Perry, J. H., ed., *Chemical Engineers Handbook*, 4th ed., McGraw-Hill, New York.
- Bankoff, S. G., and Rosler, R. D., "Constant Temperature Hot Film Anemometer as a Tool in Liquid Turbulence Measurements," *Review of Scientific Instruments*, Vol. 33, No. 11, 1962, pp. 1209, 1212.
- Bouvard, M., and Dumas, H., "Application de la méthode du file chaud à la mesure de la turbulence dans l'eau," *La Houille Blanche*, No. 3, 1967, pp. 257-270.
- Bouvard, M., and Dumas, H., "Application de la méthode du file chaud à la mesure de la turbulence dans l'eau," *La Houille Blanche*, No. 7, 1967, pp. 723-734.
- Hollasch, K., "A Survey of the Literature, Design, and Experimental Verification of a Measurement Scheme for External Turbulent Natural Convection Flow," MS thesis, Cornell University, Sept. 1970.
- W. J. Dixon, ed., *BMD Biomedical Computer Programs*, 2nd ed., University of California Press, Berkeley, Calif., 1968.
- Collis, D. C., and Williams, M. J., "Two Dimensional Forced Convection from Cylinders at Low Reynolds Number," Aeronautical Research Laboratories (Australia) Report AWS, Nov. 1957.

**E. BRUNDRETT**  
Associate Professor.  
Mem. ASME

**W. B. NICOLL**  
Associate Professor.

**A. B. STRONG**  
Assistant Professor.

Department of Mechanical Engineering,  
University of Waterloo,  
Waterloo, Ontario, Canada

# Heat and Mass Transfer in an Incompressible Turbulent Boundary Layer

*The van Driest damped mixing length has been extended to account for the effects of mass transfer through a porous plate into a turbulent, two-dimensional incompressible boundary layer. The present mixing length is continuous from the wall through to the inner-law region of the flow, and although empirical, has been shown to predict wall shear stress and heat transfer data for a wide range of blowing rates.*

## Introduction

**Objective.** Turbulent boundary layers with mass transfer at the boundary surface are encountered in a variety of engineering situations. For example, such boundary layers are found in transpiration-cooled gas turbine blades, where the mass transfer allows operation with higher-temperature gases and hence higher operating efficiencies. Mass transfer also provides an effective means for the reduction of viscous drag and kinetic heating in high-speed flight.

Little progress has been made to date in solving the time-dependent Navier-Stokes, energy, and continuity equations which govern this phenomenon. This difficulty is usually bypassed with the aid of a phenomenological model with empirical inputs. The efficiency of such a procedure depends upon the generality of the phenomenological structure into which the empirical information is incorporated. Past attempts at the construction of an adequate phenomenological model for turbulent boundary layers with mass injection have suffered from structural limitations which limit their generality, as will be demonstrated below. The objective of the present paper is the presentation of a more general model. The basic structure of the present model is similar to the van Driest [1]<sup>1</sup> damped mixing-length model, the main difference being the incorporation of the implications of the solution to the laminar oscillating plate problem with mass transfer (Stokes, Second Problem [2]) rather than those of the same problem without mass transfer. It will be shown that this modification results in a model which can accurately predict both hydrodynamic quantities such as the drag coefficient and, with the specification of a turbulent Prandtl number, thermal quantities such as the Stanton number for a wide range of flow and temperature conditions.

**Previous Work.** Previous models for turbulent boundary layers with mass transfer may conveniently be classified into two groups: those which provide expressions for the velocity profile in the inner-law region and those which provide instead an "effective" viscosity or mixing-length distribution. Examples of the former are the velocity profile expressions of Black and Sarnecki [3], Stevenson [4], and Spalding [5]. While such expressions are useful in the solution of hydrodynamic problems, they fail to furnish adequate guidance when heat transfer is also involved. In particular, the incorporation of the effects of the laminar sub-layer region in terms of a single empirical function or constant does not allow prediction of the effect of the laminar Prandtl number on the Stanton number, nor does it allow the prediction of the heat transfer characteristics when the thermal boundary layer commences downstream of the hydrodynamic boundary layer; these important phenomena require additional empirical functions for their predictions. For this reason we shall not consider such profile expressions further.

Mixing-length distributions have been proposed by various authors; these distributions typically follow van Driest, who proposed that the Prandtl mixing length should be multiplied by a damping factor which accounts for the effects of viscous damping of the turbulence in the near wall region. The damping function proposed by van Driest was

$$DF = 1 - \exp\left(-\frac{y^+}{A^+}\right) \quad (1)$$

where  $A^+$  is a measure of the mean fluctuation frequency of the turbulent flow. Van Driest assigned  $A^+$  a constant value of 26.0 based on fully developed pipe-flow velocity profile data for the constant shear stress region. Rotta [6] and Patankar [7] independently proposed that this expression, when used in non-constant shear-stress situations, should be modified to:

$$DF = 1 - \exp\left(-\frac{y^+\sqrt{\tau^+}}{A^+}\right) \quad (2)$$

<sup>1</sup> Numbers in brackets designate References at end of paper.

Contributed by the Heat Transfer Division and presented at the ASME-AIChE Heat Transfer Conference, Tulsa, Okla., August 15-18, 1971. Manuscript received by the Heat Transfer Division July 20, 1970. Paper No. 71-HT-10.

where  $\tau^+$  is a dimensionless shear stress based on the wall shear, viz.,

$$\tau^+ = \tau(y) / \tau_s$$

More recently, Cebeci et al. [8] have made use of the same modification. When the Couette-flow approximations apply, the expression for  $\tau^+$  is

$$\tau^+ = 1 + m^+u^+ + p^+y^+ \quad (3)$$

where  $u^+$  is the dimensionless velocity,  $y^+$  the dimensionless distance normal to the wall, and  $m^+$  and  $p^+$  the dimensionless mass transfer parameter and pressure gradient parameter, respectively.

When applying this expression to flows with mass transfer, Rotta found it necessary to empirically relate the quantity  $A^+$  to the mass transfer parameter  $m^+$ . While there is some doubt as to validity of Rotta's relationship between  $A^+$  and  $m^+$  due to the fact that the data he used in its determination, namely, the pioneer data of Mickley and Davis [9], is now questioned, there is no doubt that such a procedure will lead to reasonable hydrodynamic predictions in the fully turbulent region if the empirical  $A^+ \sim m^+$  relation is based on sound data. Since it is based solely on velocity profile data in the inner-law region and on a form for the damping function which was determined for a *no-mass-transfer* flow, however, one may reasonably question its implications when the very near wall region dominates, such as simultaneous heat and mass transfer at large Prandtl numbers and with step wall-temperature changes. This matter will be pursued below in the appropriate section.

## Momentum Transfer

**Mathematical Formulation.** For the moment we shall restrict our attention to flow situations where the velocity field may be regarded as one-dimensional. (This restriction is made in the interest of mathematical clarity and convenience only; it is not a necessary restriction and indeed will be relaxed below when reference is made to problems of a step change in wall temperature and the streamwise distribution of wall shear stress.)<sup>2</sup> The momentum equation for zero pressure gradient combined with Prandtl's mixing-length equation yields:

$$\frac{dz}{dy^*} = \frac{2S_s\tau^+}{1 + \sqrt{1 + 4\tau^+(l^+)^2}} \quad (4)$$

<sup>2</sup> In this latter case a Couette-flow analysis will no longer suffice and the mixing length must then be incorporated into the appropriate two-dimensional boundary layer equations.

## Nomenclature

$A^+$ = the van Driest parameter	$S$ = shear stress parameter $\equiv \tau / \rho U_G^2$	$\rho$ = density (lb <sub>m</sub> /ft <sup>3</sup> )
$C$ = specific heat at constant pressure (Btu/lb <sub>m</sub> -deg F)	$St$ = Stanton number $\equiv h / \rho C U_G$	$\sigma$ = Prandtl number $\equiv \mu C / k$
$h$ = heat transfer coefficient (Btu/sec-ft <sup>2</sup> -deg F)	$T$ = temperature (deg F)	$\sigma_t$ = turbulent Prandtl number
$J$ = diffusional heat flux (Btu/sec-ft <sup>2</sup> )	$u$ = velocity in $x$ direction (ft/sec)	$\sigma_{\text{eff}}$ = effective Prandtl number
$k$ = thermal conductivity (Btu/sec-ft <sup>2</sup> -deg F/ft)	$u^+$ = dimensionless velocity $\equiv (u / U_G) / \sqrt{S_s}$	$\sigma^*$ = Prandtl number ratio $\equiv \sigma / \sigma_t$
$l$ = Prandtl mixing length	$U_G$ = free-stream velocity (ft/sec)	$\tau$ = shear stress (lb <sub>f</sub> /ft <sup>2</sup> )
$l^+$ = dimensionless mixing length $\equiv l \sqrt{\tau_s \rho} / \mu$	$v$ = velocity in $y$ direction (ft/sec)	$\tau^+$ = dimensionless shear stress $\equiv \tau / \tau_s$
$m^+$ = dimensionless mass transfer parameter $\equiv v_s / \sqrt{\tau_s \rho}$	$v^*$ = dimensionless velocity $\equiv v_s / U_G$	$\varphi$ = enthalpy (Btu/lb <sub>m</sub> )
$p$ = pressure (lb <sub>f</sub> /ft <sup>2</sup> )	$x$ = distance along plate (ft)	$\varphi^*$ = dimensionless enthalpy $\equiv (\varphi_s - \varphi) / (\varphi_s - \varphi_G)$
$p^+$ = dimensionless pressure gradient parameter $\equiv \sqrt{\mu^2 / \tau_s^3 \rho} (dp / dx)$	$y$ = distance normal to plate (ft)	
$P$ = function defined by equation (11)	$y^*$ = dimensionless distance $\equiv y U_G / \nu$	
$Re_x$ = Reynolds number $\equiv U_G x / \nu$	$y^+$ = dimensionless distance $\equiv y \sqrt{\tau_s \rho} / \mu$	
	$z$ = dimensionless velocity $\equiv u / U_G$	
	$\epsilon_m$ = eddy diffusivity for momentum (ft <sup>2</sup> /sec)	
	$\kappa$ = a "law of the wall" constant	
	$\mu$ = viscosity (lb <sub>m</sub> /sec-ft)	
	$\nu$ = kinematic viscosity (ft <sup>2</sup> /sec)	
		<b>Subscripts</b>
		$G$ = refers to the free stream
		$0$ = refers to the value of a pertinent variable when the mass transfer rate is zero but all other conditions are equivalent
		$s$ = refers to the wall or porous surface

where

$$z \equiv u / U_G$$

$$y^+ \equiv y U_G / \nu$$

$$S_s \equiv \frac{C_f}{2} \equiv \tau_s / \rho U_G^2$$

$$\tau^+ \equiv 1 + v^* z / S_s$$

and

$$v^* \equiv v_s / U_G$$

The subscripts  $s$  and  $G$  refer to conditions at the surface and free stream respectively. The quantity  $l^+$  is Prandtl's mixing length nondimensionalized in the same fashion as  $y^+$ .

The boundary condition is

$$z = 0 \quad \text{when} \quad y^+ = 0$$

Before equation (4) can be integrated, the  $l^+$  distribution must be specified. We assume

$$l^+ = \kappa y^+ D^+ \quad (5)$$

where

$$D^+ = 1 - \exp \left\{ (y^+ m^+ \sqrt{\tau^+} / 2) (1 \mp 1 / \sqrt{2} [1 + \{1 + 64 / (A^+ m^+)^4\}^{1/2}]^{1/2}) \right\} \quad (6)$$

The  $\mp$  sign is used when  $m^+$  is negative and vice versa.

Several observations concerning the above expression are appropriate. First, since  $D^+$  approaches a finite constant, for any value of  $m^+$ , as  $y^+ \rightarrow \infty$ , the mixing length  $l^+$  is a linear function of  $y^+$  at large values of the latter. This restricts the scope of the present model to situations where relaminarization is not present, i.e., to blowing and moderate suction. In the authors' opinion, the path to the removal of this restriction lies in the relaxation of Prandtl's second assumption, namely that the intensity of turbulence is proportional to the velocity profile gradient, rather than in forcing the length scale to approach zero as the conditions for relaminarization are approached. For the present purposes, however, we will simply retain the restriction. Secondly, the form of  $D^+$  is determined from the solution to Stokes' Second Problem with mass transfer obtained by Nicoll et al. [10]. This is discussed in greater detail by Nicoll and Strong [11], and by Strong [12]. Thirdly, the quantity  $A^+$ , which is the turbulent counterpart of the oscillation frequency



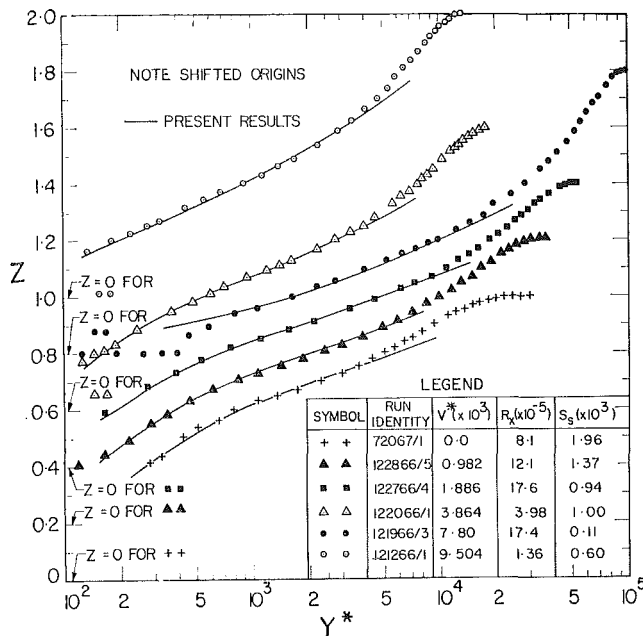


Fig. 1 Comparison of predicted velocity profiles (present model) with representative data of Simpson et al. [13]

$\omega$  in the Stokes problem, may reasonably be anticipated to be dependent on the mass transfer; this simply would mean the turbulent structure itself is modified by the presence of mass transfer. Indeed, this implication could be tested, both grossly and in detail, if suitably accurate data for the spectral characteristics of the turbulent structure were available for such flows as we are presently considering. Unfortunately such data do not at present exist, and we shall have to determine the dependence of  $A^+$  on  $m^+$  from mean velocity profile data. Finally, the dependence of  $D^+$  on the local shear, as suggested by Rotta and Patankar, has been assumed.

**The Determination of  $\kappa$  and  $A^+$ .** Since both  $\kappa$  and  $A^+$  are empirical quantities, their accuracy will be directly proportional to the accuracy of the velocity profile data from which they are obtained. Unfortunately, unexplained inconsistencies exist between the data of various authors. In the authors' opinion, the experiments of Simpson et al. [13] appear to be the most meticulously performed and checked; further, care was taken to both measure and report variations in porosity of the permeable plate. Hence we have adopted their data as our standard, although we will compare our predictions with the data of other authors. Should this opinion turn out to be in error when more accurate experimental techniques are available, it would be a simple matter to correct  $\kappa$  and the  $A^+$  relation.

Having reached this decision we forthwith adopt the value of  $\kappa$  recommended by Simpson et al., namely

$$\kappa = 0.44$$

The determination of  $A^+$  is not as direct. It is reasonable to expect that

$$A^+ = A^+(\tau^+)$$

Further, as  $m^+ \rightarrow 0$  and  $\tau^+ \rightarrow 1$ ,  $A^+ \rightarrow 26$ .

A suitable form for  $A^+$  which satisfies this requirement is:

$$A^+ = 26.0(\tau^+)^a \quad (7)$$

The data of Simpson et al. indicate that the value of  $a$  is<sup>3</sup>

$$a = -1.4$$

<sup>3</sup> For a detailed discussion of the procedure by which  $a$  is determined see Strong [12].

Table 1 Comparison of analytical and experimental values of the wall shear stress for the data of Simpson et al. [13]

Run Identity of Simpson	$Re_x$ ( $\times 10^{-5}$ )	$V^*$ ( $\times 10^3$ )	$S_s$ Experimental ( $\times 10^3$ )			$S_s$ Analytical ( $\times 10^3$ ) K=0.44, a=-1.4
			Simpson - Mon. Int. Equation	Simpson - Sub-Layer Equation	Simpson - Best Estimate	
2367/1	4.04	.0	2.25 (5%)	2.20 (0.2)	2.20 (0.1)	2.25
2367/2	9.44	.0	1.90 (5%)	2.04 (0.2)	1.90 (0.1)	1.90
2367/3	12.2	.0	1.82 (5%)	1.90 (0.2)	1.86 (0.1)	1.86
2367/4	17.6	.0	1.70 (5%)	1.80 (0.2)	1.73 (0.1)	1.68
31067/1	1.31	.0	2.76 (5%)	2.94 (0.2)	2.76 (0.1)	2.71
31067/2	6.56	.0	2.05 (5%)	2.05 (0.2)	2.05 (0.1)	2.05
31067/3	14.5	.0	1.76 (5%)	1.84 (0.2)	1.76 (0.1)	1.76
31067/4	19.9	.0	1.65 (5%)	1.68 (0.2)	1.65 (0.1)	1.65
72067/1	8.10	.0	1.96 (5%)	-	1.96 (0.1)	1.96
72067/2	15.7	.0	1.74 (5%)	-	1.74 (0.1)	1.69
72067/3	21.8	.0	1.63 (5%)	-	1.63 (0.1)	1.63
122866/1	1.32	0.990	2.42 (6%)	2.42 (0.2)	2.42 (0.1)	2.35
122866/2	3.96	0.998	1.89 (6%)	1.92 (0.2)	1.89 (0.1)	1.84
122866/3	6.65	0.993	1.68 (6%)	1.86 (0.2)	1.68 (0.1)	1.63
122866/4	9.27	0.996	1.56 (6%)	1.77 (0.2)	1.56 (0.1)	1.41
122866/5	12.1	0.982	1.47 (6%)	1.63 (0.2)	1.47 (0.1)	1.35
122866/6	14.7	0.984	1.41 (6%)	1.53 (0.2)	1.41 (0.1)	1.31
122866/7	17.4	0.984	1.36 (6%)	1.49 (0.2)	1.36 (0.1)	1.21
122766/1	1.34	1.883	2.00 (7%)	2.20 (0.3)	2.00 (0.1)	2.05
122766/2	6.75	1.916	1.40 (7%)	1.37 (0.3)	1.40 (0.1)	1.32
122766/3	12.2	1.887	1.17 (7%)	1.15 (0.3)	1.17 (0.1)	1.07
122766/4	17.6	1.886	1.04 (7%)	1.03 (0.3)	1.04 (0.1)	0.94
122366/1	4.0	1.944	1.55 (7%)	1.55 (0.3)	1.55 (0.1)	1.50
122366/2	9.35	1.950	1.22 (7%)	1.17 (0.3)	1.22 (0.1)	1.12
122366/3	14.9	1.896	1.13 (7%)	1.20 (0.3)	1.13 (0.1)	1.00
122366/4	20.3	1.869	1.01 (7%)	1.13 (0.3)	1.01 (0.1)	0.91
122066/1	3.98	3.864	1.00 (12%)	1.11 (0.2)	1.00 (0.1)	1.02
122066/2	9.27	3.893	0.74 (12%)	-	0.74 (0.1)	0.68
122066/3	14.7	3.830	0.63 (12%)	0.69 (0.2)	0.63 (0.1)	0.55
122066/4	20.1	3.834	0.57 (12%)	0.62 (0.2)	0.57 (0.1)	0.52
121966/1	3.99	7.836	0.27 (40%)	0.23 (0.4)	0.26 (0.2)	0.33
121966/2	12.0	7.817	0.15 (40%)	0.24 (0.4)	0.18 (0.2)	0.13
121966/3	17.4	7.798	0.12 (40%)	-	0.14 (0.2)	0.115
121966/4	20.2	7.738	0.11 (40%)	-	0.12 (0.2)	0.12
121266/1	1.36	9.504	-	0.63 (0.4)	0.50 (0.2)	0.60
121266/2	4.13	9.482	-	0.18 (0.4)	0.17 (0.2)	0.15
121266/3	6.93	9.405	-	-	0.10 (0.2)	0.10
121266/4	9.72	9.403	-	-	0.05 (0.2)	0.055
121266/5	12.5	9.346	-	-	0.05 (0.2)	0.04
121266/6	15.3	9.376	-	-	0.05 (0.2)	0.04
121266/7	17.9	9.429	-	-	0.05 (0.2)	0.03
121266/8	20.8	9.408	-	-	0.05 (0.2)	0.04

\* Bracketed figures denote error estimates

Table 2 Comparison of analytical and experimental values of the wall shear stress for the data of Mickley and Davis [9], run C-3-50

Run Identity of Mickley and Davis	$Re_x$ ( $\times 10^{-5}$ )	$V^*$ ( $\times 10^3$ )	$S_s$ Experimental ( $\times 10^3$ )		$S_s$ Analytical ( $\times 10^3$ )	
			Mickley and Davis ( $\pm 30\%$ )	Stevenson's Correction <sup>a</sup>	Stevenson's Law of the Wall [4]	Present Analysis ( $\kappa=0.44, a=-1.4$ )
C-3-50/E	2.76	3.04	0.68	-	0.95	1.46
C-3-50/G	5.48	2.95	0.48	-	0.88	1.26
C-3-50/H	7.50	3.00	0.44	-	0.83	1.08
C-3-50/I	9.89	2.90	0.34	0.4	0.8	1.00
C-3-50/J	11.98	2.96	0.33	0.47	0.7	0.88
C-3-50/K	15.16	2.90	0.27	0.43	0.65	0.86
C-3-50/L	18.25	2.86	0.29	0.49	0.7	0.82
C-3-50/M	21.87	2.80	0.25	0.25	0.65	0.80
C-3-50/N	25.30	2.83	0.25	0.25	-	0.74

<sup>a</sup> The letters A and B refer to two  $U_c(x)$  velocity profiles assumed by Stevenson to make the pressure gradient corrections to the Mickley and Davis data. See Reference [4].

With the mixing-length distribution now fixed, equation (4) can now be integrated and its implications compared with experiment.

**Comparison of Prediction and Experiment.** In Fig. 1 are shown comparisons of predicted and experimental velocity profiles for some of the data of Simpson. The agreement of shape in the region  $5 \times 10^2 \lesssim y^* \lesssim 10^4$  confirms the validity of the asymptotic linear variation of  $l^+$  with  $y^+$ . The value of  $S_s$ , which was determined by the Clauser method [14], is compared with the experimental values in Table 1. Again agreement is good. This satisfactory result, however, is no great surprise since the empirical  $A^+$  and  $\kappa$  were chosen so as to obtain such agreement. It should be noted that any of the previously mentioned models have sufficient empirical inputs to lead to similar agreement. A more critical test of the present model will be found in its capacity to predict certain heat transfer phenomena discussed below. Before proceeding to this, however, there are several matters which should be examined.

It is of interest to see how the present model predicts the data of Mickley and Davis, as originally presented and the corrected version by Stevenson [4], and the data of McQuaid [15]. Since these data are also known to conform to the implications of the asymptotic linear variation of  $l^+$  with  $y^+$ , comparisons will only

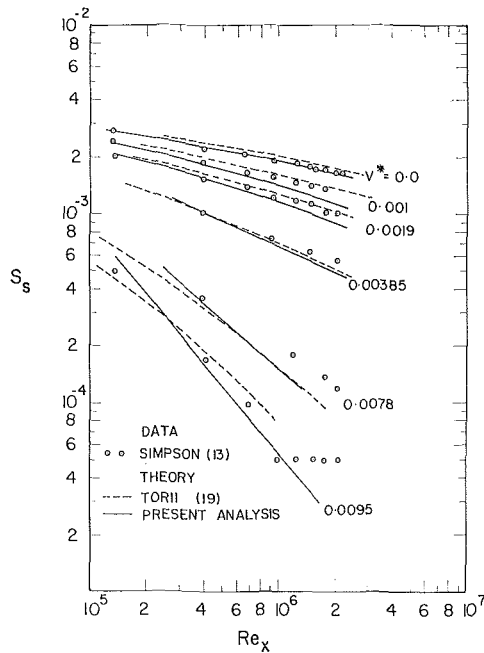


Fig. 2  $S_s$  vs.  $Re_x$  for various values of the mass transfer rate,  $v^*$ ; comparison of the present analysis with the results of Torii et al. and the data of Simpson et al.

be made in terms of wall shear stress. The values of  $S_s$ , determined by the Clauser procedure, are compared with a portion of the data of Mickley and Davis, and with Stevenson's corrected version of the same, in Table 2. It may be seen that while the trends are correctly predicted, the predicted values of  $S_s$  are much higher than those predicted by Mickley and Davis, and also higher than Stevenson's corrected values. A similar comparison for a portion of the data of McQuaid is shown in Table 3. Again the predicted values are higher than the reported experimental values. Possible reasons for these discrepancies have been presented by Simpson [13] and need not be repeated here. What is of relevance is the degree of disagreement between various experimenters, and the demonstration of the need for both more accurate data and methods to evaluate the accuracy of data.

The present analysis has been limited to a Couette analysis in order to focus attention on the physical model. As noted previously, such a restriction is one of convenience, not necessity. A more general analysis, based on a modification of the computational procedure of Spalding and Patankar [16], combined with the present model has been developed by Powell [17] and Powell and Strong [18]. The resultant prediction of the streamwise variation of the drag coefficient,  $S_s$ , with downstream distance is shown in Fig. 2.<sup>4</sup> It may be seen that the agreement is within the experimental uncertainty as computed by Simpson et al. Also shown is the prediction of Torii et al. [19] based on an integral approach. Except for the case of zero mass transfer, their results also agree well with the data. This agreement, as discussed previously, should not be surprising. It is simply confirmation of the fact that all models have sufficient flexibility to reproduce hydrodynamic quantities. A more critical test is the heat transfer implications of any given model; to this matter we now direct our attention.

## Heat Transfer

**Mathematical Formulation.** As in the section on momentum transfer, we shall confine the analysis to the one-dimensional

<sup>4</sup> Values of  $S_s$  were determined by the technique of Clauser plotting. At each station, corresponding to a value of  $Re_x$ , equation (4) is overplotted on the data for values of the parameter  $S_s$ . The  $S_s$  corresponding to the best fit to the data is the plotted value.

Table 3 Comparison of analytical and experimental values of the wall shear stress for the data of McQuaid [15] for  $U_G = 50$  ft/sec

Station Identity by Distance $x$ (inches)	$Re_x$ ( $\times 10^{-5}$ )	$v^*$ ( $\times 10^{-3}$ )	$S_s$ Experimental	$S_s$ Analytical ( $\times 10^{-3}$ )
			McQuaid	Present Analysis $\kappa=0.44, a=-1.4$
			$S_s^*$ ( $\times 10^3$ )	
14.5	3.83	1.71	1.3 (10%)	1.70
21.5	5.61	1.71	1.2 (10%)	1.50
28.4	7.42	1.71	1.1 (10%)	1.30
34.2	9.03	1.71	1.0 (10%)	1.30
14.5	3.82	3.24	0.8 (30%)	1.26
21.5	5.67	3.26	0.7 (30%)	1.04
28.4	7.52	3.26	0.6 (30%)	0.92
34.2	9.02	3.27	0.4 (40%)	0.88
14.5	3.84	4.64	0.5 (30%)	0.92
21.5	5.70	4.63	0.4 (50%)	0.76
28.4	7.53	4.63	0.2 (100%)	0.67
34.2	9.15	4.64	0.3 (70%)	0.66
14.5	3.88	8.09	0.3 (100%)	0.34
21.5	5.70	8.04	0.3 (100%)	0.21
28.4	7.65	8.04	0.3 (100%)	0.15
34.2	9.13	7.99	0.3 (100%)	0.18

\* Bracketed figures denote error estimates.

case for simplicity, although we shall relax this restriction when comparing prediction with experiment.

If  $\varphi = CT$  is the fluid enthalpy, then the distribution of the dimensionless enthalpy  $\varphi^* \equiv (\varphi_s - \varphi)/(\varphi_s - \varphi_G)$  is governed by the equation

$$\frac{d\varphi^*}{dz} = \frac{St}{S_s} \left( 1 + \frac{v^* \varphi^*}{\sigma^*} \right) \frac{\sigma_{eff}}{\tau^+} \quad (8)$$

Here  $St$  is the Stanton number defined by

$$St \equiv h/(\rho C U_G) \\ \equiv J_s/\rho U_G (\varphi_s - \varphi_G) \quad (9)$$

where  $J_s$  is the heat flux at the wall. The effective Prandtl number,  $\sigma_{eff}$ , remains to be specified. We assume that the ratio of the turbulent diffusivities for momentum and heat,  $\sigma_t$ , is constant and equal to unity. There results:

$$\frac{\sigma_{eff}}{\sigma_t} = \left( 1 + \frac{\epsilon_m}{\nu} \right) / \left( \frac{1}{\sigma^*} + \frac{\epsilon_m}{\nu} \right) \quad (10)$$

where  $\sigma^* \equiv \sigma/\sigma_t$  and where  $\sigma$  is the laminar Prandtl number. Equations (4) and (8) can now be integrated to yield an enthalpy profile. Since we shall not compare enthalpy profile predictions with experiment, however, but only Stanton numbers, it is convenient to follow Spalding [20] and introduce the  $P$  function defined by

$$P \equiv \lim_{U_G^+ \rightarrow \infty} \int_0^{U_G^+} \left( \frac{\sigma_{eff}}{\sigma_t} - 1 \right) \frac{du^+}{\tau^+} = P(m^+, \sigma) \quad (11)$$

The  $P$  function may be regarded as a measure of the contribution of the viscous sublayer to the overall heat transfer resistance. The effect of the limiting process is negligible at the Reynolds numbers normally encountered if  $\sigma > 0.5$  since in this situation the integral approaches zero rapidly with increasing  $u^+$ . For very small  $\sigma$  the boundary layer approximations themselves become invalid so we need not consider this case in the present paper.

Equation (8) can be formally integrated and the result can be rearranged to yield:

$$St = \frac{v^*}{\left( 1 + \frac{v^*}{S_s} \right) \sigma_t \exp(v^* \sigma_t P / S_s^{1/2}) - 1} \quad (12)$$

Since the present mixing-length distribution implies an  $\epsilon_m/\nu$  distribution, it is relatively a simple matter to compute  $P$  as a

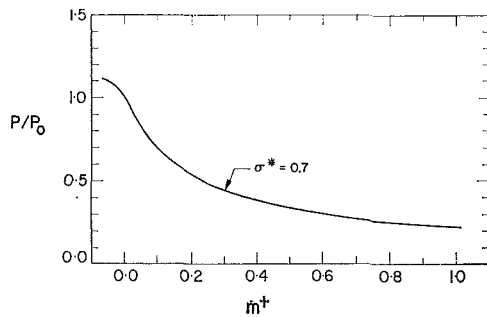


Fig. 3 Distribution of the ratio  $P/P_0$  with  $m^+$  for values of the Prandtl number ratio  $\sigma^* = 0.7$  ( $\sigma_t = 1.0$ )

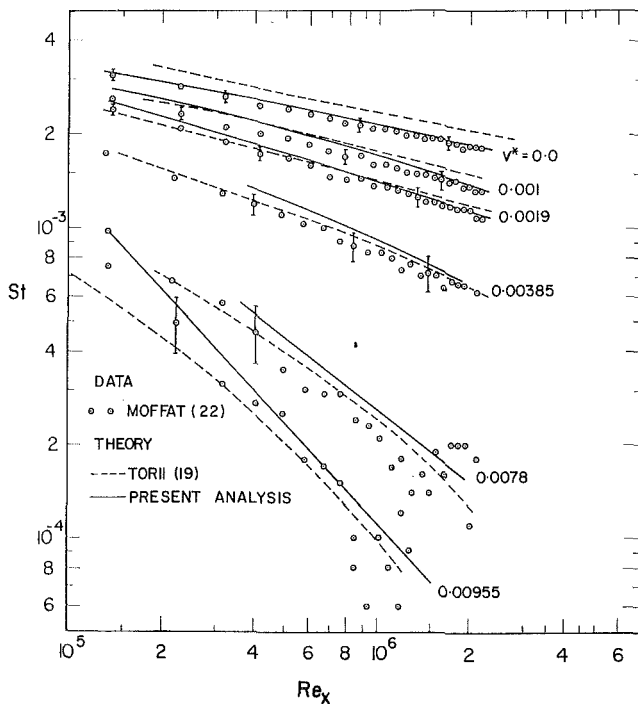


Fig. 4  $St$  vs.  $Re_x$  for various mass transfer rates  $v^*$ ; comparison of the present results with the theory of Torii et al. and the data of Moffat and Kays

function of  $m^+$  and  $\sigma^*$  from equations (10) and (11). The Stanton number can then be determined from equation (12).

For zero mass transfer the present model reduces to that of Patankar [7], and hence his results for  $P$  are identical with the present result when  $m^+ = 0$ . His results have been shown [12] to agree well, within the experimental uncertainty, with the empirical correlation of Jayatilaka [21].

For non-zero mass transfer, the most commonly employed fluid is air for which  $\sigma \approx 0.7$ . For this value of  $\sigma$  the effect of mass transfer on  $P$  is shown in Fig. 3. The ordinate is the ratio  $P/P_0$  where  $P_0$  is the value of  $P$  for  $m^+ = 0$ ,  $\sigma^* = 0.7$  and is equal to  $-2.784$ . It may be observed that mass transfer has a significant effect on the value of  $P$ .

**Comparison with Experiment.** Fig. 4 shows a comparison of the present predictions for Stanton number distribution with the data of Moffat and Kays [22]. The predictions are determined from equation (12) and the calculated local value of  $P$ . The predicted shear-stress distribution shown in Fig. 2 was used to determine the required wall shear-stress values. The data all refer to the region relatively far downstream from a simultaneous step in mass transfer and wall temperature, a region in which the present analysis should be valid. Agreement is seen to be good.

Also shown are the predictions of Torii et al. [19]. The agree-

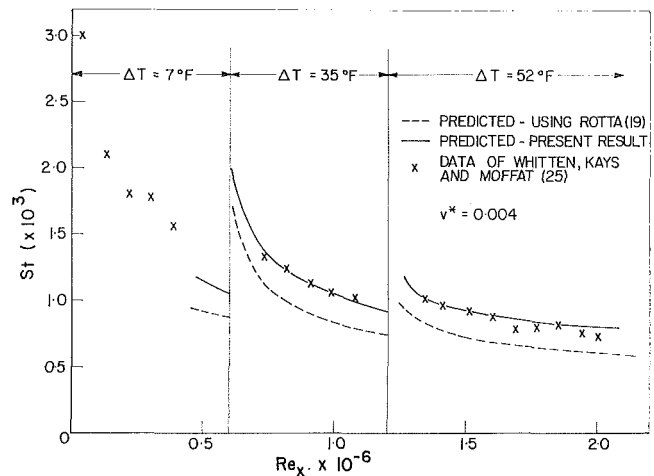


Fig. 5 Hydrodynamic implications of Rotta's model and the present result for the prediction of Stanton number for a step change in wall temperature

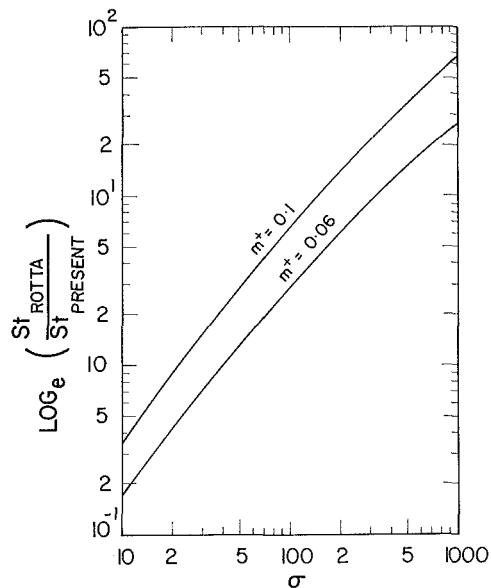


Fig. 6 Comparison of Stanton number between Rotta's model and the present result

ment is also good, with the exception of the zero-mass-transfer case. The implication is that data obtained under these conditions, i.e.,  $\sigma \approx 0.7$ ,  $v^* = \text{constant}$ , and measurement stations far downstream from the start of heat and mass transfer, are insensitive to the precise details of the model being tested. This indeed is consistent with Kays' observation that Spalding's  $B$  theory [23], another Couette analysis, also agrees well with the data of [22].

A far more critical test is the prediction of the Stanton number in the vicinity of a step change in wall temperature. Here, because of the thinner thermal boundary layer, the viscous sublayer and hence the detailed character of the damping function plays a more dominant role. The implications of the present model, as well as those of the Rotta model, for this situation are shown in Fig. 5. The predicted values were obtained by Powell [24] using the method mentioned in the section on momentum transfer.

Two observations are relevant. First, the agreement between the present prediction and the experimental data [25] is excellent. This conclusion is supported by a far more comprehensive comparison between data and experiment by Powell and Strong [18] to be reported elsewhere. Secondly, unlike the previous comparisons, the step wall-temperature change problem *does* provide

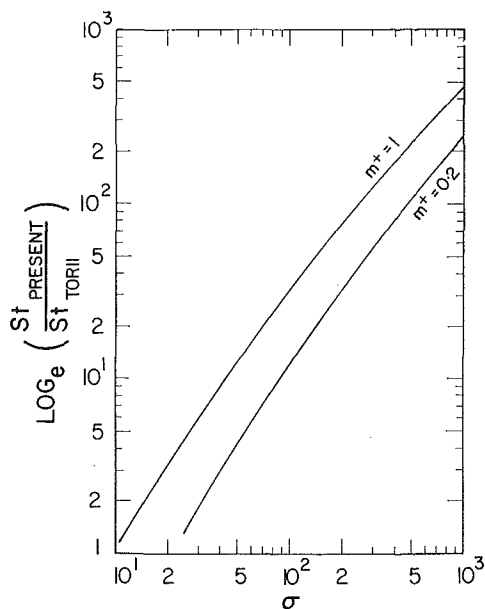


Fig. 7 Comparison of Stanton number predictions between the present model and Torii's result for large Prandtl number

a method of testing the relative merits of various models; for the given experimental conditions the Rotta model leads to a predicted Stanton number development which is well below the experimental development.

This capacity to distinguish between various models is also a characteristic of simultaneous heat and mass transfer at large laminar Prandtl numbers. This is shown in Fig. 6 in which the ratio of the Stanton number predicted with the Rotta model is compared with the implications of the present model. It is seen that this ratio becomes enormous at large Prandtl numbers, with the present model yielding the lower value at large Prandtl numbers. (This is not inconsistent with the results presented for the step change in wall temperature; at low Prandtl number the difference is reversed in sign.) Fig. 7 shows a similar comparison between the implications of the present model and the predictions of the Torii et al. procedure. Again the predicted values of Stanton number differ. While it is true that as the Prandtl number increases the Stanton number decreases, and hence the experimental difficulties in the accurate determination of the Stanton number also increase, it is nonetheless also true that high Prandtl number data would allow the various models to be compared meaningfully. The authors are unaware, however, of suitable data.

## Conclusions

A damped mixing-length model of the van Driest type has been proposed for the transpired turbulent boundary layer. It has been shown that the present proposal agrees with available experimental data for both hydrodynamic and heat transfer quantities; specifically:

1 The model leads to accurate prediction of hydrodynamic quantities such as velocity profiles and wall shear-stress distributions.

2 With the additional assumption of a unity turbulent Prandtl number, the model results in accurate heat transfer predictions for a range of temperature boundary conditions including the step-change-in-wall-temperature problem.

Finally, the need for simultaneous heat and mass transfer data at large laminar Prandtl numbers and the need for turbulence spectra data for transpired turbulent boundary layers has been noted.

## References

- 1 Van Driest, E. R., "On Turbulent Flow Near a Wall," *J. Aero. Sci.*, Vol. 23, 1956, p. 1007.
- 2 Moore, F. K., ed., *Theory of Laminar Flows*, Princeton University Press, Princeton, N. J., 1964, pp. 396-401.
- 3 Black, T. J., and Sarnecki, M. A., "The Turbulent Boundary Layer with Suction or Injection," Cambridge University Engineering Department, Reports and Memoranda No. 3387, 1965.
- 4 Stevenson, T. N., "A Law of the Wall for Turbulent Boundary Layers with Suction or Injection," Cranfield College of Aeronautics Report No. CoA 166, 1963.
- 5 Spalding, D. B., "A Unified Theory of Friction Heat Transfer and Mass Transfer in the Turbulent Boundary Layer and Wall-Jet," ARC Report No. 25 925, 1964.
- 6 Rotta, J. C., "On the Velocity Distribution of Turbulent Flow in the Vicinity of Porous Walls," Aerodynamic Research Institute, Göttingen, Germany, Research Report No. 66-45, DLR FB 66-45, 1966.
- 7 Patankar, S. V., "Wall-Shear-Stress and Heat Flux Laws for Turbulent Boundary Layer with a Pressure Gradient: Use of van Driest's Eddy-Viscosity Hypothesis," Imperial College, London, England, TWF/TN/14, 1966.
- 8 Cebece, T., Smith, A. M. O., and Mosinskis, G., "Solution of the Incompressible Turbulent Boundary-Layer Equations With Heat Transfer," *JOURNAL OF HEAT TRANSFER*, TRANS. ASME, Series C, Vol. 92, No. 1, Feb. 1970, pp. 133-143.
- 9 Mickley, H. S., and Davis, R. S., "Momentum Transfer for Flow Over a Flat Plate with Blowing," NACA TN-4017, 1957.
- 10 Nicoll, W. B., Strong, A. B., and Woolner, K. A., "On the Laminar Motion of a Fluid Near an Oscillating Porous, Infinite Plane," *Journal of Applied Mechanics*, Vol. 35, TRANS. ASME, Series E, Vol. 90, No. 1, March 1968, pp. 164-166.
- 11 Nicoll, W. B., and Strong, A. B., "A Mixing Length Hypothesis for the Turbulent Boundary Layer with Suction and Injection," University of Waterloo, Department of Mechanical Engineering, Report No. 8, 1968.
- 12 Strong, A. B., "Wall Shear Stress and Heat Transfer in a Turbulent Boundary Layer with Wall Transpiration," PhD thesis submitted to the University of Waterloo, 1969.
- 13 Simpson, R. L., Kays, W. M., and Moffat, R. J., "The Turbulent Boundary Layer on a Porous Plate: An Experimental Study of the Fluid Dynamics with Injection and Suction," Stanford University, Department of Mechanical Engineering, Thermosciences Division Report No. HMT-2, 1967.
- 14 Clauser, F., "Turbulent Boundary Layers in Adverse Pressure Gradients," *J. Aero. Sci.*, Vol. 21, 1954, pp. 91-108.
- 15 McQuaid, J., "Experiments on Incompressible Turbulent Boundary Layers with Distributed Injection," ARC 28 735, 1967.
- 16 Spalding, D. B., and Patankar, S. V., *Heat and Mass Transfer in Turbulent Boundary Layers*, Morgan Grampian Press, London, England, 1967.
- 17 Powell, T. E., "Calculation of the Two-Dimensional Turbulent Boundary Layer with Mass Additional Heat Transfer," MASC thesis submitted to the University of Waterloo, Waterloo, Ont., Canada, 1970.
- 18 Powell, T. E., and Strong, A. B., "Calculation of the Two-Dimensional Turbulent Boundary Layer with Mass Addition and Heat Transfer," *Proceedings of the 1970 Heat Transfer and Fluid Mechanics Institute*, Stanford University Press, Palo Alto, Calif.
- 19 Torii, K., Nishiwaki, N., and Hirata, M., "Heat Transfer and Skin Friction in Turbulent Boundary Layer with Mass Injection," *Proceedings Third International Heat Transfer Conference*, AIChE, Vol. 3, 1966.
- 20 Spalding, D. B., "A Unified Theory of Friction, Heat Transfer and Mass Transfer in the Turbulent Boundary Layer and Wall Jet," Imperial College, London, England, 1964 (Formerly published as A.R.C. Report No. 25 925, 1964).
- 21 Jayatilaka, C. L. V., "The Influence of Prandtl Number and Surface Roughness on the Resistance of the Laminar Sub-Layer to Momentum and Heat Transfer," Imperial College, Department of Mechanical Engineering, Report TWF/R/2, 1966.
- 22 Moffat, R. J., and Kays, W. M., "The Turbulent Boundary Layer on a Porous Plate: Experimental Heat Transfer with Uniform Blowing and Suction," Stanford University, Department of Mechanical Engineering, Thermosciences Division Report No. HMT-1, 1967.
- 23 Spalding, D. B., "A Standard Formulation of the Steady Convective Mass Transfer Problem," *International Journal of Heat and Mass Transfer*, Vol. 1, 1960.
- 24 Powell, T. E., private communication.
- 25 Whitten, D. G., Kays, W. M., and Moffat, R. J., "The Turbulent Boundary Layer on a Porous Plate: Experimental Heat Transfer With Variable Suction, Blowing and Surface Temperature," Stanford University, Department of Mechanical Engineering, Thermosciences Division Report HMT-3, 1967.

GEORGE MAISE

Grumman Aircraft Corp.,  
Bethpage, N. Y.

JOHN B. FENN

Department of Engineering and  
Applied Science,  
Yale University,  
New Haven, Conn.

# Thermal Recovery Factors in Supersonic Flows of Gas Mixtures<sup>1</sup>

*Thermal recovery factors were measured at the stagnation point of a hemispheric probe in low-density supersonic jets of helium-argon and hydrogen-nitrogen mixtures. A "guard" heater in the probe made it possible to eliminate conduction losses. Radiation corrections were small. The final values correspond to adiabatic conditions. With jets of mixed gases, experimental recovery factors were as high as 1.6, substantially above the free molecule limit for pure gases. It is suggested that these anomalously high values are due to the species separation which occurs during the stagnation process and which results in concentrations of heavy species in the stagnation zone higher than in the free stream. The results are correlated in terms of the degree of rarefaction and the composition of the jet gas.*

## Introduction

IN AN earlier note we reported the strikingly high thermal recovery factors which we had obtained in some preliminary experiments with argon-helium mixtures in a supersonic jet [1].<sup>2</sup> More recently, Kutateladze et al. have also observed anomalously high recovery temperatures at the stagnation point of a probe immersed in a supersonic flow of nitrogen-hydrogen gas mixtures [2]. There were some essential differences between their experiments and ours but the observed effects in the two cases were related. This communication will present the results of a more complete investigation of the phenomenon. Measurements were made over a range of free-stream densities and compositions at a Mach number of 6.4. A few points were taken at a Mach number of 9.25. In addition, some results were obtained with nitrogen-hydrogen mixtures.

This investigation had its antecedents in the observation, first reported by Becker and his associates, that samples withdrawn through a probe immersed in a supersonic jet of mixed gas were substantially richer in the heavy species than was the original source gas [3]. Similar observations were later reported by Waterman, Stern, and Sinclair [4]. A subsequent investigation in our laboratory showed that under many if not most experimental conditions a large part of the enrichment or separation effect was caused by or occurred during the stagnation process at the probe [5]. Recently, Sherman has provided analytic con-

firmation of the importance of the probe by showing in general that diffusive processes in the free stream could account for only a fraction of the separations that have been observed [6]. Sherman's calculations have been confirmed experimentally by Rothe [7] and in our laboratory by Anderson [8]. Both of these investigators avoided probe-induced separation.

If it is assumed that in a supersonic free jet of a binary gas mixture both species are traveling at the same velocity, it follows that the heavier of the two will have a higher total enthalpy per mole. We reasoned that the stagnation process which results in a higher-than-free-stream concentration of the heavier and more energetic species at the stagnation point of the probe might also result in a stagnation point temperature higher than the total temperature of the gas mixture at the source. Studies in our laboratory of the velocity distributions of molecular beams extracted from supersonic jets of gas mixtures indicated that for a wide range of experimental conditions the assumption of equal species velocity in the jet was sound [9]. Accordingly, we set out to measure the stagnation point temperature on a probe immersed in a supersonic jet of mixed gas.

## Experimental Procedures

The measurement of true adiabatic stagnation temperature in a flowing gas presents some difficulties. The steady-state temperature at the probe tip represents a balance between the heat supplied by the stagnating gas and any heat losses which might occur. There are two primary routes by which heat may be lost from the stagnation point. One is by radiation to the surroundings and the other is by conduction to cooler parts of the probe. We minimized the radiation loss simply by keeping the source gas at room temperature so that surroundings "seen" by the probe were at a temperature lower than the stagnation point only by an amount equal to the excess of stagnation temperature over source temperature. The radiation corrections were thus small and

<sup>1</sup>This research was made possible by support in part from the National Science Foundation under Grant GK 655X and in part from the Office of Naval Research through Project SQUID, Contract Number 3623(00), NR-098-038.

<sup>2</sup>Numbers in brackets designate References at end of paper.

Contributed by the Heat Transfer Division and presented at the Winter Annual Meeting, Los Angeles, Calif., November 16-20, 1969, of THE AMERICAN SOCIETY OF MECHANICAL ENGINEERS. Manuscript received by the Heat Transfer Division June 24, 1969; revised manuscript received February 1, 1971. Paper No. 69-WA/HT-27.

could be readily estimated and applied. They never amounted to more than about 5 percent.

The losses due to conduction in the probe are more serious and less easily circumvented. Because on a hemispheric probe the recovery temperature decreases substantially with distance from the stagnation point the resulting temperature gradient in the probe can cause large errors in stagnation point recovery temperature measurements. Hickman attempted to minimize this conduction error by mounting a thermocouple on a hemispherical shell of thin (0.005 in.) glass [10]. Even so his measured temperatures were always slightly below the true values. We wanted to make measurements under even more rarefied conditions where the lower rate of heat transfer from gas to stagnation point intensifies the problem. After a few vain attempts to construct probes of materials with low thermal conductivity we took a new tack which culminated in a probe whose design is shown in Fig. 1. It comprised a 6.35-mm-dia copper shell, a 1.59-mm-dia fiberglass or plexiglass insert and a 0.64-mm-dia chromel-alumel thermocouple junction in the plastic insert at the stagnation point. Another thermocouple was located in the copper shell at the shoulder of the probe. An 80-ohm electric resistance heater was located aft at a sufficient distance to avoid any aerodynamic interference with the bow flow. (Absence of such interference was established by tests in which it was found that changing the position of the heater made no difference in observed recovery temperature under otherwise identical conditions.) The purpose of the heater was to increase the temperature of the probe shell until it was the same as the stagnation point temperature. At steady state under these conditions there should be no conduction loss and the stagnation point thermocouple should thus reflect the true adiabatic recovery temperature except for the small correction due to radiation. The high thermal conductivity of copper assured uniformity of probe body temperature, at least in the forward section of the probe. Actually there remained a small residual conduction loss from the stagnation point to the plastic insert. Because of its finite size the insert extended away from the stagnation point and was exposed to a region of slightly lower recovery temperature. Because of its relatively low conductivity the plastic was able to support at least part of the small temperature difference between the stagnation point and the part of the plastic exposed to a lower recovery temperature region. Thus, there could have been a small flow of heat from the stagnation point (and also from the copper shell which in the steady state was at the same temperature as the stagnation point) through the plastic to the boundary layer gas in the region of lower recovery temperature. Our most careful estimates of this effect indicated a correction of only 0.4 deg C. Moreover, its magnitude was not much affected by the gas density so we applied the same correction, which amounts to 0.0015 in the recovery factor, to all the data.

In actual practice we did not attempt to adjust the power to the heater so as to achieve coincidence of the tip and shoulder temperatures. The very large time constant of the system precluded this method. Under typical conditions the probe required from 1 to 2 hr to reach a steady state. Consequently, we chose to let the probe come to a steady-state temperature at several power settings and then to plot the tip temperature against the shoulder temperature for each power setting. The intersection of the resulting curve with the 45 deg line representing equal probe and tip temperatures gave the adiabatic stagnation temperature. The curve was in fact always a straight line and we soon learned that two points were sufficient to determine it. Because the intersection of the two lines was at an acute angle it was essential that the tip and shoulder thermocouples be well calibrated with respect to each other. A small error in either temperature could result in a large shift in the point of intersection. For this reason special care was taken to eliminate any spurious effects. The chromel-alumel thermocouple wires were taken from the same spool and cut to the same length. No in-

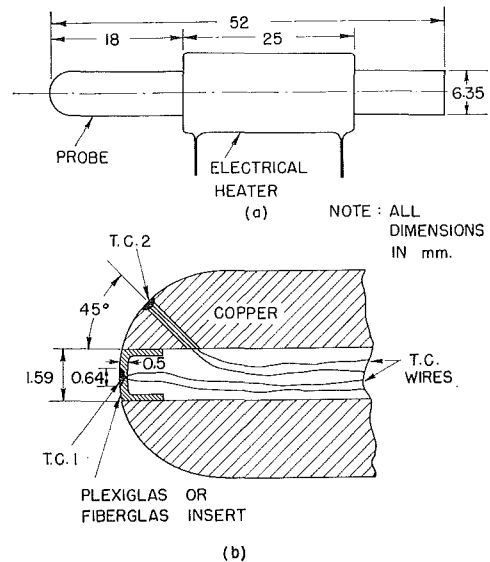


Fig. 1 Schematic diagram of adiabatic probe

intermediate metals were placed in the circuit. At the beginning and end of each test run, when the temperature of the probe became uniform, the temperatures indicated by each thermocouple were read and compared. Differences between the two were tolerated only if they were less than 0.025 deg C. Some probes had to be discarded because they developed small emfs of unknown origin. All emfs were measured on a millivolt potentiometer (Leeds and Northrup, Cat. No. 8686, Range 0-100 mv, L.C. 0.005 mv). No attempt was made to get an absolute calibration of the thermocouples except to ascertain that there was agreement to within less than 1.0 deg C with the NBS tables at the ice point and the steam point.

Unfortunately, there was no way to make absolutely sure that the probe as used gave true values of the adiabatic recovery temperatures under the conditions we studied. We can say that in the low-density continuum regime with pure gases the stagnation temperature measured with the probe matched within 0.5 deg C the temperature in the nozzle plenum chamber. Moreover, in completely free molecule flow at Mach numbers greater than 5 the recovery temperature at the shoulder should equal that at the tip so that no error would be introduced by our technique if in fact it could be applied at such low densities. We simply have to assume that the probe behaved properly in the intermediate regime where we made our measurements. As will emerge presently, the overall consistency of our results and the magnitude of the effects we observed seem to provide some credibility for this assumption. There are no doubt improvements which could be achieved in design and construction of the probe. Accuracy would be increased if the insert between the stagnation thermocouple and the copper shell were made of lower-conductivity material because this would result in a larger initial temperature difference between tip and shoulder and thus in a better definition of the intersection of the curves relating the two temperatures. We used plexiglass because it is easily machined and has a relatively low thermal conductivity. For some of the runs the recovery temperature exceeded 100 deg C and the plexiglass softened. In such cases we used a geometrically similar probe in which the insert was made of an epoxy-based fiberglass. The results with this probe were slightly less accurate because the thermal conductivity of fiberglass is approximately twice that of plexiglass. If one could find a low-conductivity material which could be fabricated and which could withstand high temperatures there seems to be no reason in principle why probes of this general type could not be used at much higher temperatures provided appropriate allowance for or

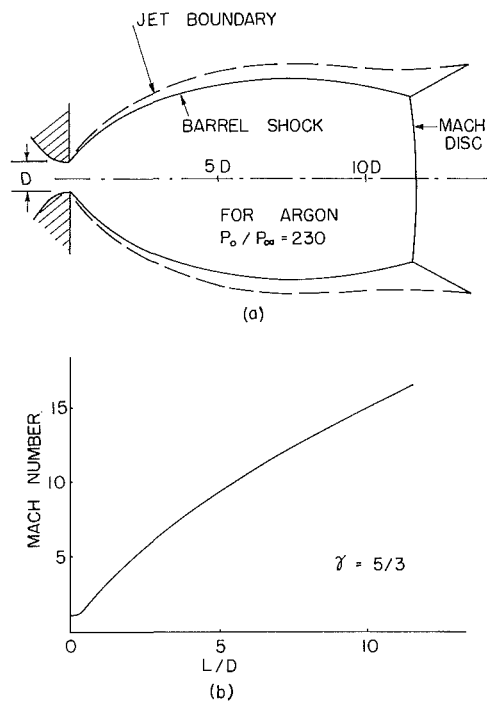


Fig. 2 Structure of a free jet from sonic throat

avoidance of radiation effects could be achieved. It would also be desirable to decrease the thermal capacity of the probe assembly. We found the slow response very costly in terms of both time and materials (gases). It is primarily for this reason that we did not attempt to cover a more comprehensive range of conditions. In this connection one possibility that we did not explore was the use of a time-temperature relation to determine the equal temperature point. It might be that one could follow the time history of each temperature for a given heater power and extrapolate to the intersection point. If this method works it would seem likely to result in substantial economies.

In addition to the probe the other important feature of the apparatus was the flow field in which the probe was immersed. It was produced by expanding gas from a sonic nozzle into a continuously evacuated tank. Fig. 2 shows a schematic diagram of the jet from such a nozzle together with the associated Mach number distribution along the axis. The structure of such jets has been thoroughly documented for continuum conditions by numerous investigators so that one can with some assurance assert the state of the gas at any point along the centerline. Sherman and Ashkenas and Sherman have summarized the state of our knowledge [11, 12]. Suffice it to say that most of our measurements were made with the probe on the axis at a distance of 3 nozzle diameters, i.e., "flow" diameters as determined from actual measurements of nozzle discharge coefficient. This distance corresponds to a Mach number, confirmed by pitot measurement, of 6.4 for the argon-helium mixtures. It should correspond to a Mach number of 4.85 for the nitrogen-hydrogen mixtures if their effective specific heat ratio were  $7/5$ . In actual fact, there is evidence from molecular beam velocity measurements in our laboratory that the rotational energy of hydrogen does not relax completely during the expansion so that the effective Mach number is not 4.85. We will enlarge on this point later. There is also the possibility that the translational temperature might not relax completely during expansion. From the results of Anderson and Fenn we estimate that this was not a problem in most of the data presented here [13]. Only when the source pressure was 5 torr or less would there have been a Mach number "deficit." In the worst case, pure helium at 5 torr, the true Mach number was probably only 5.8. We made no attempt to

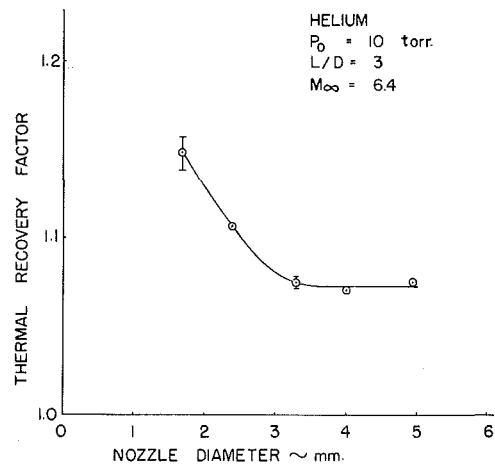


Fig. 3 Effect of nozzle size on recovery factor

allow for this by changing the probe location and we ignored possible corrections in reducing the data for the few points at this low pressure. We will also report some argon-helium results with the probe located at an axial distance of 5 nozzle diameters which corresponds to a Mach number of 9.25. In this case the source pressure was sufficiently high that there was no danger of a Mach number deficit. It should be noted that it is not really the location of the probe body but the front surface of the bow shock which determines the Mach number of the flow entering the shock. The values of shock detachment distance involved in this "correction" to the probe location were obtained from the theoretical analysis of Serbin which has been confirmed by experiment [14].

A more serious problem stems from the divergence of the flow streamlines which results in radial as well as axial Mach number gradients. Because our interest was confined to the stagnation point we were not so concerned with the latter. However, the relatively large diameter of the probe made the former a matter of some apprehension. It is clear that the importance of radial gradients depends directly on the relative size of the probe and the nozzle. The smaller the probe or the bigger the nozzle the less should be any possible effect. Because of fabrication difficulties we could not easily make the probe much smaller than it was. We could, however, vary nozzle diameter and determine directly its effect on the apparent stagnation temperature. In Fig. 3 are shown results obtained with five different nozzles under otherwise comparable conditions. It appears that for our probe at a distance of 3 nozzle diameters the effect of nozzle size becomes negligible for nozzles larger than about 3 mm in diameter. All of the results reported here were obtained with the 3.3-mm nozzle, the smallest one on the flat part of the curve in Fig. 3. It is important to use the smallest nozzle which gives reliable results in order to achieve the largest possible nozzle Reynolds numbers at the highest possible pressure ratios. For a given pumping speed, the smaller the nozzle the smaller is the mass flow and the higher is the pressure ratio for a given Reynolds number.

The test chamber and associated gear were identical with those used by Reis and Fenn [5]. However, additional pumping speed was provided in the form of a 16-in-dia jet booster oil pump (Stokes series 150) backed by three large mechanical pumps (2 Stokes 412 H and 1 Kinney 220 KDH). This system sufficed to maintain a pressure ratio across the nozzle in the range from 380 to 2000 under all conditions of source pressure and gas composition. The pressure ratio was always high enough to insure that the Mach disk was well downstream of the probe and that the background gas did not penetrate the jet [15]. Nozzle-probe distances were measured with a Gaertner cathetometer (L.C. 0.05 mm).



## Results

The data for argon-helium mixtures are summarized in Table 1 in terms of source pressure, composition, and observed stagnation temperature. Also shown are the associated derived quantities including the corrections due to radiation and conduction, the thermal recovery factor  $r$ , and the free-stream probe Knudsen number  $Kn_\infty$ . The recovery factor was computed from the usual relation:

$$r = \frac{T_r - T_\infty}{T_0 - T_\infty} \quad (1)$$

where  $T_r$  is the measured stagnation temperature,  $T_0$  is the source temperature, and  $T_\infty$  is the free-stream static temperature of the gas as it enters the bow shock wave. The last of these quantities was obtained from the standard Mach number relations assuming isentropic expansion from the source. The probe Knudsen number  $Kn_\infty$  was taken as the ratio of the mean free path in the free stream immediately ahead of the bow shock wave to the probe diameter. There are, of course, some conceptual difficulties in connection with the mean free path in a gas mixture, especially at the low static temperature in the high Mach number jet. What we did was to assume the kinetic theory relation:

$$\lambda = \frac{\mu}{0.499\rho u_m} \quad (2)$$

where  $\lambda$  is the mean free path,  $\rho$  the density,  $\mu$  the viscosity, and  $u_m$  the mean thermal velocity. We applied this relation to the gas at the source condition and then multiplied the resulting value of  $\lambda$  by the density ratio  $\rho_0/\rho_\infty$  corresponding to the free-stream condition assuming isentropic expansion. The viscosity was determined for the mixtures from the data of Iwasaki and Kestin [16]. This procedure for computing Knudsen number amounts to assuming that the gas mixture is made up of hard-sphere molecules with a cross section equal to that of a pure gas of the same viscosity having a molecular weight equal to the concentration-weighted mean for the mixture. Such a Knudsen number is a somewhat arbitrary measure of the degree of rarefaction and is defensible mainly because its computation is straightforward and unequivocal even though its physical meaning may

**Table 1 Thermal recovery factor data for argon-helium mixtures ( $T_0 \approx 25$  deg C,  $D_N = 3.31$  mm,  $D_P = 6.35$  mm)**

Comp. (% He)	$P_0$ torr	$P_0/P_B$	$Kn_\infty$	$T_r$ (meas.) °C	$r$ (meas.)	$r$ (corr.)	
$M_\infty = 6.4$ ( $L/D' = 3$ )	0	5	800	34.4	1.032	1.036	
		8	1130	0.058	31.4	1.014	1.016
		10	1220	0.046	28.5	1.012	1.014
		20	1920	0.023	28.2	1.016	1.008
	20	10	1150	0.052	40.5	1.053	1.057
		20	1630	0.026	32.5	1.028	1.030
		30	1880	0.017	30.5	1.017	1.019
	50	7	737	0.093	82.0	1.194	1.204
		10	870	0.065	71.0	1.156	1.164
		20	1110	0.032	50.5	1.086	1.089
		40	1290	0.016	38.0	1.044	1.046
	80	5.5	470	0.159	170.5	1.499	1.525
		10	610	0.088	130.5	1.376	1.388
		20	740	0.044	89.5	1.224	1.229
		40	770	0.022	54.5	1.106	1.108
	90	5.5	420	0.184	189.0	1.567	1.594
		10	540	0.101	150.0	1.436	1.449
		20	610	0.051	105.0	1.270	1.276
		40	650	0.025	60.5	1.125	1.128
	95	5.5	390	0.203	179.0	1.534	1.556
10		500	0.112	138.0	1.407	1.418	
20		570	0.056	101.0	1.260	1.265	
30		590	0.037	77.0	1.174	1.177	
100	5	380	0.252	63.0	1.135	1.139	
	7	430	0.180	53.0	1.097	1.100	
	10	470	0.126	45.5	1.063	1.065	
	15	500	0.084	37.8	1.043	1.045	
	20	520	0.063	31.0	1.025	1.027	
	30	560	0.042	27.5	1.012	1.014	
$M_\infty = 9.25$ ( $L/D' = 5$ )	50	15.3	1040	0.119	78.9	1.178	1.184
	50	30	1220	0.060	57.0	1.102	1.105
	90	24	625	0.119	130.5	1.361	1.367
	100	30	560	0.119	36.5	1.037	1.039

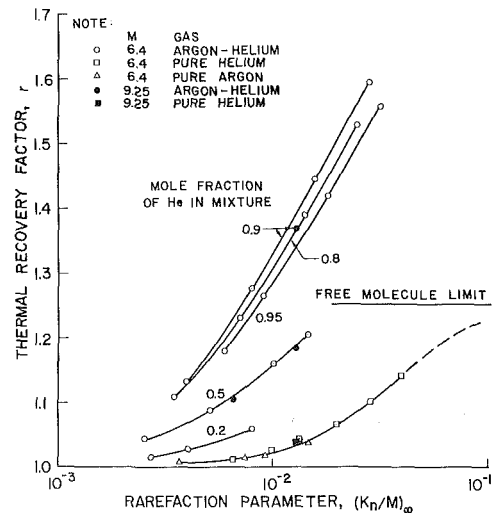


**Fig. 4 Recovery factors for argon-helium mixtures**

not be without ambiguity. The data of Table 1 are displayed in Fig. 4 as plots of observed recovery factor for each source gas composition against the rarefaction parameter  $(Kn/M)_\infty$  which we have found effective and which will be described later. The striking feature of this plot is the marked increase in recovery factors obtained with gas mixtures as compared with pure gases. In some cases values were obtained substantially in excess of the theoretical value at the free molecule limit. Most of the mixtures with low concentrations of argon gave higher values of the recovery factor than the richer mixtures. In order to elucidate the concentration effect we show in Fig. 5 cross-plots at constant Knudsen number of recovery factor against gas composition. These indicate, at each density level, a pronounced peak in recovery factor at an argon concentration of about 12 percent.

The data for nitrogen-hydrogen mixtures are summarized in Table 2. These were all obtained at a single-probe Knudsen number in order that the composition dependence of the recovery factor could be established without the necessity of cross-plotting. In computing Knudsen number Waldmann's data for the viscosity of nitrogen-hydrogen mixtures were used [17]. The results are displayed in Fig. 6 which shows recovery factor against gas composition. The curve is very similar in shape to those for helium-argon mixtures in Fig. 5 but the peak occurs at slightly lower concentrations of the heavy species, i.e., 7 percent as opposed to 12 percent. In connection with the reduction of the hydrogen-nitrogen data there is a problem in choosing the appropriate value of the free-stream static temperature in order to compute the recovery factor. Studies in our laboratory of velocities and velocity distributions in molecular beams extracted from small supersonic free jets at Reynolds numbers in the range of the present experiments have indicated that in hydrogen, and even to some extent in nitrogen, internal energy of rotation does not completely relax during the expansion process [9]. We have found that for hydrogen and hydrogen-rich mixtures the expansion can be reasonably characterized by assuming a  $\gamma$  of  $7/5$  up to Mach number 1, i.e., to the throat of the nozzle, and a  $\gamma$  of  $5/3$  thereafter. On this basis the effective Mach number at 3 nozzle

**Table 2 Thermal recovery factor data for nitrogen-hydrogen mixtures ( $T_0 \approx 25$  deg C,  $D_N = 3.31$  mm,  $D_P = 6.35$  mm)**

Comp. (%H <sub>2</sub> )	$P_0$ torr	$Kn_\infty$	$T_r$ (meas.) °C	$r$ (meas.)	$\Delta r$ (rad.)	$\Delta r$ (cond.)	$r$ (corr.)	$r$ ( $\gamma = 5/3$ , $M_\infty = 6.4$ )
66	10.9	0.0775	96.5	1.292	0.0032	0.0015	1.297	1.335
85	12.5		147.4	1.495	0.0047		1.501	1.575
90	13.2		157.4	1.544	0.0056		1.551	1.625
95	13.8		159.0	1.538	0.0047		1.544	1.631
98	14.3		115.5	1.366	0.0020		1.370	1.426
100	15.0		45.0	1.080	0.0002		1.081	1.095

PROBE WAS LOCATED SO THAT BOW SHOCK WAS AT 3 FLOW DIAMETERS FROM NOZZLE EXIT. IF  $\gamma = 7/5$ , MACH NUMBER IS 4.85. IF  $\gamma = 5/3$ , MACH NUMBER IS 6.4 (LAST COLUMN ON RIGHT).

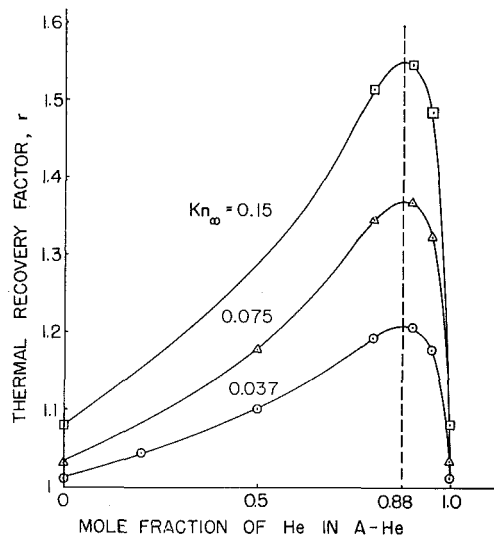


Fig. 5 Composition effects for argon-helium mixtures

diameters is 6.4 rather than 4.85 and the effective translational free-stream static temperature is 22.5 deg K instead of 47.5 deg K. If we further assume that the rotational energy, corresponding to the static temperature at Mach number 1, is "recovered" at the stagnation point then we obtain the apparent recovery factors in the last column of Table 2. This procedure amounts to defining the recovery factor by:

$$r = \frac{h_s - h_\infty}{h_0 - h_\infty} = \frac{(7kT_r/2) - [(5kT_{tr\infty}/2) + kT_{rot}^*]}{(7kT_0/2) - [(5kT_{tr\infty}/2) + kT_{rot}^*]} \quad (3)$$

where subscripts "tr" and "rot" stand for translational and rotational and the other subscripts retain their previous meanings. The asterisk indicates Mach number 1 and  $h$  stands for average enthalpy per molecule. It is clear from the table that this approximation results in slightly higher values of recovery factor than the "equilibrium" values obtained by assuming completely relaxed expansion. (Note that the equilibrium values are the ones shown in Fig. 6.) Our reason for laboring this point will emerge in the discussion.

## Discussion

We now face the problem of trying to explain the high values of recovery factor which we have observed. As we indicated in our preliminary note there are several possible mechanisms which we can contemplate. Prerequisite to all of them is the assumption that the heavy species has more energy per molecule in the free stream than the light species. This assumption is valid if the expansion takes place without "slip" between the heavy and light species, i.e., the free-stream convective velocities and static temperatures of both species are the same. The measurements of velocities in beams extracted from jets indicate that under the conditions of the present experiments there is in fact fairly complete velocity equilibration between the species in the jet [18]. Therefore, we can explore the possible means by which the excess energy of the heavy molecules can be reflected in the realization of higher temperatures at the stagnation point than equilibrium thermodynamic considerations would seem to permit.

If the gas in the stagnation region is sufficiently rarefied the energy transfer to the probe surface will be determined by the nature of the molecule-surface collision process and will not be characterized primarily by bulk gas transport properties, i.e., thermal conductivity. It is well known that the efficiency with which a molecule can exchange energy with a surface depends upon the mass of the molecule. In the case of "engineering" surfaces of the kind which we might expect on our probe Stickney has shown that the thermal accommodation coefficient of argon is

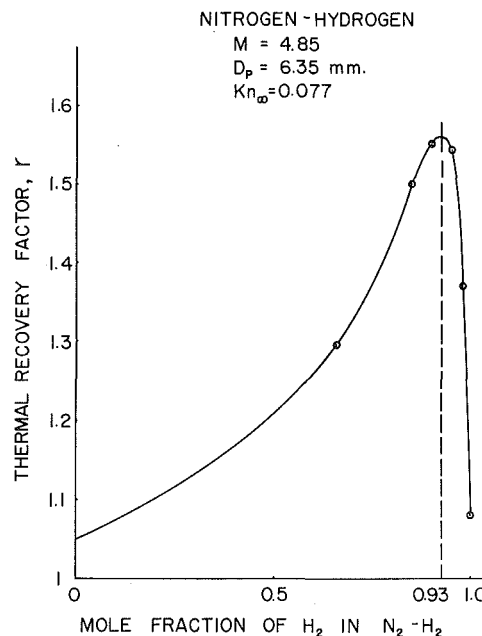


Fig. 6 Composition effects for nitrogen-hydrogen mixtures

almost twice that of helium [19]. Recent measurements by a different technique in our laboratory confirm this relation [20]. Thus, if the stagnation density is low enough so that temperature jump effects can occur or the heat transfer is essentially free molecule in nature the higher accommodation coefficient of the heavier and more energetic species could account for higher than equilibrium values of the recovery temperature even if both species were at the same relative concentrations in the stagnation region as at the source. That is to say, the heavier and hotter species could deposit energy at the probe surface faster than the lighter and cooler species could remove it. There are two reasons for believing that this explanation cannot account completely for the observed effects. In the first place the evidence seems to indicate that the high recovery temperatures occur even when the probe is well into the continuum flow regime. Fig. 4 shows that recovery factors are substantially above 1 for gas mixtures at probe Knudsen numbers for which there is essentially no rarefaction enhancement of the pure gas recovery factor. Moreover, total pressure measurements, by John Chang in our laboratory, with a pitot probe identical with the temperature probe in size and shape, indicate no viscous correction over almost the entire range of composition and density covered in the present work [21]. There was only a slight viscous enhancement of observed stagnation pressure at the highest probe Knudsen numbers which we encountered. These observations imply that the rarefaction was never great enough for heat transfer to the probe surface to be dominated by accommodation efficiency of molecule surface interactions. In the second place, stagnation zone gas under our experimental conditions is definitely and substantially richer in heavy species than the source gas. This conclusion follows from the results of Reis and Fenn [5] and has been confirmed by measurements of stagnation zone composition for mixtures under the present experimental conditions with a probe of the same size and shape as the temperature probe. These latter measurements were also made by Chang in our laboratory [21]. It seems only reasonable to associate the high recovery temperatures with the enrichment in heavy species which occurs during the stagnation process. As we have already mentioned, the velocities of both light and heavy species are essentially the same as they enter the bow shock. If enrichment of the heavy species occurs in the post-shock zone without complete loss of its excess kinetic energy then the stagnation recovery temperature should be higher than the equilibrium value. Collision cross sections for energy exchange between molecules are not markedly different from those for

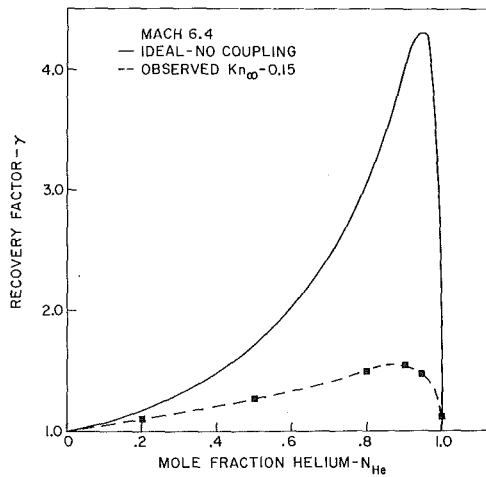


Fig. 7 Comparison of ideal and observed recovery factors

diffusion. Consequently, the occurrence of heavy species enrichment implies also the absence of complete energy exchange between the two species.

It should be recalled that the presence of excess heavy species in the stagnation zone can be due in part to diffusive separation in the free jet. We have already noted that Sherman has provided a theoretical analysis of this separation which has been quantitatively confirmed by the measurements of Rothe [7] and those of Anderson [8]. That this separation can result in high recovery factors is shown in the work of Kutateladze and his co-workers. Indeed, all of their recovery temperature results were obtained at nozzle Reynolds numbers (based on stagnation gas properties and throat diameter) less than 200, low enough for substantial diffusion separation. Our own measurements were for the most part at much higher Reynolds numbers, i.e., in the range of 200 to 2000. Only three of the points were at Reynolds numbers below 400 but in those cases there was some diffusive separation. Therefore, we undertook an estimate of the possible contribution to recovery temperature which might result from diffusive separation in the jet. By Sherman's method we computed the centerline composition in the jet at the probe location [6]. We assumed that the heavy species velocity was equal to the isentropic free-stream velocity. This assumption is, of course, optimistic because there could in fact be no separation in the jet if the species velocities were the same as for the isentropic case. We then computed the centerline total enthalpy and assumed that it was completely recovered at the stagnation point. Even with the heavy bias in favor of increased stagnation temperature incorporated in this calculation only about half of the observed excess recovery temperature could be accounted for under the most favorable condition. In most cases the possible contribution was substantially less.

We are consequently persuaded that at least a large part of the observed excess in recovery factors must be accounted for by the same stagnation process which causes probe-induced enrichment of the heavy species. Unfortunately, there is essentially no theory for probe-induced enrichment which might provide a basis for predicting the recovery factors which have been observed. However, we did have some success in developing an empirical correlation of our results which could be useful in estimating the magnitude of the effect. It may also furnish some clues as to the mechanisms involved.

It is easy to show from the conservation equations that if there is no energy exchange between the two species after they enter the bow shock and before they reach the stagnation point and if they are both at the same velocity and static temperature as they enter the bow shock wave, the following relation holds:

$$r = \frac{h_s - h_\infty}{h_0 - h_\infty} = \frac{\bar{m}_s}{\bar{m}_\infty} \quad (4)$$

where  $r$  is the recovery factor,  $h_s$  is the average total enthalpy per molecule of mixture at the stagnation point,  $h_\infty$  is the average static enthalpy per molecule of mixture in the free stream,  $h_0$  is the average total enthalpy per molecule of mixture in the free stream (for isentropic expansion it is the same as the average molecular enthalpy in the source),  $\bar{m}_s$  is the mean molecular mass at the stagnation point, and  $\bar{m}_\infty$  is the mean molecular mass in the free stream. These average molecular enthalpies can be replaced by their corresponding temperatures for monatomic gases but not for polyatomic gases unless the internal temperatures are at equilibrium with the kinetic or translational temperatures. We assume this is always the case at the stagnation point but, as we have already indicated, it is not necessarily so in the free stream. Moreover, as has been observed by Anderson [22] and Miller [23], the heavy species in a jet of mixed gas may have a static temperature substantially higher than the light species even though velocity equilibration may have occurred. We have not tried to account for this possibility in our considerations but there is little doubt that it is a contributing factor.

We now seek a normalizing factor which will permit comparison and correlation of results for various mixtures under various experimental conditions. By somewhat arbitrary intuition we suggest that the maximum possible recovery factor would result if each component of the mixture were to be stagnated isentropically and separately, i.e., with no energy exchange between components. For this fictitious and presumably ideal stagnation process we can write from the standard Mach number relations

$$\frac{n_{Hs}}{n_{Ls}} = \frac{n_{H\infty} \left(1 + \frac{\gamma-1}{2} M_H^2\right)^{\frac{1}{\gamma-1}}}{n_{L\infty} \left(1 + \frac{\gamma-1}{2} M_L^2\right)^{\frac{1}{\gamma-1}}} = \frac{N_{Hs}}{N_{Ls}} \quad (5)$$

where  $n$  is number density of molecules,  $N$  is mol fraction,  $M$  is Mach number, and  $\gamma$  specific heat ratio. Subscripts H and L identify the heavy and light species and the other subscripts retain their previous meanings. It should be noted that the Mach number for each species is different and is not the same as the mean or equilibrium Mach number in the free stream. If both species are at the same velocity and static temperature in the free stream

$$M_H = \bar{M} \sqrt{\frac{m_H}{\bar{m}}} \quad \text{and} \quad M_L = \bar{M} \sqrt{\frac{m_L}{\bar{m}}} \quad (6)$$

where  $m$  is the molecular mass as before.

From equations (4), (5), and (6) it is straightforward to compute the ideal maximum recovery factor which we identify by  $r_{no}$  where the subscript "no" indicates "no coupling" between the species during this ideal stagnation process. Of course, the stagnation process through the bow shock on a probe in a supersonic stream is far from isentropic. The amount of entropy generation will depend at least upon the free-stream Mach number. Nevertheless, this fictitious ideal stagnation process can serve as a useful reference condition. In Fig. 7 is shown by the solid curve the ideal recovery factor  $r_{no}$  computed by the method we have outlined, as a function of free-stream composition for argon-helium mixtures at a free-stream mean Mach number of 6.4 corresponding to conditions in the experiments we have already reported. Also shown on the dashed curve are the points from a cross-plot of the experimental data corresponding to observed recovery factors for a free-stream Knudsen number of 0.15 as defined earlier. As might be expected the experimental points are far below the "theoretical" ones but the similarity in shape for the two curves is provocative.

We now write:

$$r_{obs} = r_{pg} + x(r_{no} - 1) \quad (7)$$

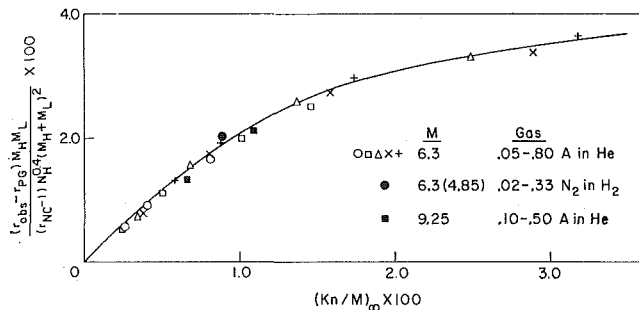


Fig. 8 Correlation of recovery factors

where the subscript "pg" stands for pure gas and "obs" for the observed value. This equation simply states that the observed recovery factor will be equal to the value for a pure gas at the same Knudsen number plus some fraction  $x$  of the increment in recovery factor that could be achieved by the ideal stagnation process we have outlined. Rearrangement of equation (7) gives

$$\frac{r_{\text{obs}} - r_{\text{pg}}}{r_{\text{no}} - 1} = x \quad (8)$$

The question now is what determines the value of  $x$ ? We can be intuitively certain that it will depend primarily on the number and effectiveness of collisions between the two species during stagnation. We therefore expect that it will depend upon the probe Knudsen number, the free-stream Mach number, the molecular mass ratio of the two species, and the composition of the mixture. From the curves obtained by cross-plotting the argon-helium data as shown in Fig. 5 we found that  $x$  was extremely linear in  $N_H^{0.4}$ , the mol fraction of heavy species to the  $1/10$  power. An identical dependence was found for the nitrogen-hydrogen mixtures. We have been unable to rationalize this dependence but we accept it as empirically true over the range of our conditions. We note that  $x$  should be inversely proportional to the efficiency with which energy is exchanged upon a collision between a light and heavy molecule. From mechanics this efficiency is represented by  $m_H m_L / (m_H + m_L)^2$  for simple hard-sphere molecules. In our work with molecular beams and rarefied flows we have found that the parameter  $\text{Kn}/M$ , in this case the probe Knudsen number as previously defined divided by the free-stream mean Mach number, a most useful correlating parameter. It represents a sort of inverse Reynolds number. In view of these observations we plot the group  $(r_{\text{obs}} - r_{\text{pg}}) m_H m_L / (r_{\text{no}} - 1) N_H^{0.4} (m_H + m_L)^2$  against  $\text{Kn}/M$  for all of our experimental data. The results are shown in Fig. 8.

It is apparent that the correlation is quite effective in its ability to collect on a single curve a fairly wide range of experimental observations, of Figs. 4, 5, and 6. We would point out that it is quite sensitive in that it is on a rectilinear and not a logarithmic plot. Moreover, it is in terms of the increment in the recovery factor which is only a fraction of the recovery factor as a whole. It should be noted that the solid circle represents an average of all five of the nitrogen-hydrogen results. They were all obtained at a single value of  $\text{Kn}/M$ . We would point out, however, that four of the five were within about 5 percent of the average. The fifth was about 15 percent off. The explanation may be that the fifth point was for the mixture richest in nitrogen (33 percent). Consequently, rotational relaxation may have been more complete since nitrogen relaxes much more rapidly than hydrogen. In this connection we mention again the fact that for the nitrogen-hydrogen mixtures the computation of all the quantities in the correlation assumed that the specific heat ratio was  $7/5$  to the nozzle throat and  $5/3$  thereafter. These are certainly crude approximations.

It would be risky to put much confidence in the correlation beyond the range of experimental conditions covered in this investigation. Much more data would have to be fed into it before it could be considered even empirically as a reliable means of predicting recovery factors in gas mixtures. Until such additional data become available the correlation represents essentially the only way of estimating recovery factors in the continuum end of the transition flow regime. For such purposes of estimation the following equations are reasonably accurate representations of the curve in Fig. 8:

$$\frac{(r_{\text{obs}} - r_{\text{pg}}) m_H m_L}{(r_{\text{no}} - 1) N_H^{0.4} (m_H + m_L)^2} = 2.10 \text{ Kn}/M_{\infty} \quad \text{Kn}/M_{\infty} < 0.01 \quad (9)$$

$$= 0.081 + 0.031 \log_{10} \left( \frac{\text{Kn}}{M} \right)_{\infty} \quad \text{Kn}/M_{\infty} > 0.01 \quad (10)$$

## Acknowledgment

We would like to record our appreciation for the interest and support of many of our associates in the Beam Kinetics Laboratory. In particular, J. Chang, J. B. Anderson, R. P. Andres, and D. G. H. Marsden have contributed to this work. Without the patient skill of J. Bittner in the design and construction of the probes our efforts would have come to naught.

## References

- 1 Maise, G., and Fenn, J. B., *Phys. Fluids*, Vol. 7, 1964, p. 1080.
- 2 Kutateladze, S. S., Bochkaryou, A. A., Prikhodko, V. G., and Rebrov, A. K., "Diffusive Effects on Recovery Temperature in Supersonic Flow of Rarefied Gas Mixtures," presented at the Fourth International Heat Transfer Conference, Paris, Sept. 1970.
- 3 Becker, E. W., Bier, K., and Burghoff, H., *Z. Naturforsch.*, Vol. 10a, 1955, p. 565.
- 4 Waterman, P. C., and Stern, S. A., *J. Chem. Phys.*, Vol. 31, 1959, p. 405; Stern, S. A., Waterman, P. C., and Sinclair, T. F., *J. Chem. Phys.*, Vol. 33, 1960, p. 805.
- 5 Reis, V. H., and Fenn, J. B., *J. Chem. Phys.*, Vol. 39, 1963, p. 3240.
- 6 Sherman, F. S., *Phys. Fluids*, Vol. 8, 1965, p. 773.
- 7 Rothe, D. E., *Phys. Fluids*, Vol. 9, 1966, p. 1643.
- 8 Anderson, J. B., *AIChE Journal*, Vol. 13, 1967, p. 1188.
- 9 Abuaf, N., Anderson, J. B., Andres, R. P., Fenn, J. B., and Miller, D. R., in: *Rarefied Gas Dynamics*, Vol. 2, Brundin, C. L., ed., Fifth Symposium, Oxford, 1966, Academic Press, New York, N. Y., 1967.
- 10 Hickman, R. S., and Giedt, W. H., "Heat Transfer to Hemisphere-Cylinder at Low Reynolds Numbers," *AIAA Journal*, Vol. 1, No. 3, March 1963, pp. 665-672.
- 11 Sherman, F. S., in: *Rarefied Gas Dynamics*, Vol. 2, Laurmann, J. A., ed., Academic Press, New York, N. Y., 1963, p. 228.
- 12 Ashkenas, H., and Sherman, F. S., in: *Rarefied Gas Dynamics*, Vol. 2, deLeeuw, J. H., ed., Academic Press, New York, N. Y., 1966, p. 84.
- 13 Anderson, J. B., and Fenn, J. B., *Phys. Fluids*, Vol. 8, 1965, p. 780.
- 14 Serbin, H., Rand Corp. Report P1172, 1957.
- 15 Fenn, J. B., and Anderson, J. B., in: *Rarefied Gas Dynamics*, Vol. 2, deLeeuw, J. H., ed., Academic Press, New York, N. Y., 1966, p. 311.
- 16 Iwasaki, H., and Kestin, J., *Physica*, Vol. 29, 1963, p. 1345.
- 17 Waldmann, L., in: *Handbuch der Physik*, Vol. 12, Flügge, S., ed., Springer-Verlag, Berlin, Germany, 1958.
- 18 Abuaf, N., Anderson, J. B., Andres, R. P., Fenn, J. B., and Marsden, D. G. H., *Science*, Vol. 155, 1967, p. 997.
- 19 Stickney, R. E., and Hurlbut, F. C., in: *Rarefied Gas Dynamics*, Talbot, L., ed., Academic Press, New York, N. Y., 1961.
- 20 Kostoff, R. N., Anderson, J. B., and Fenn, J. B., in: *Fundamentals of Gas Surface Interactions*, Saltsburg, H., Smith, J., and Rogers, M., eds., Academic Press, New York, N. Y., 1967.
- 21 Chang, J. H., and Fenn, J. B., in: *Rarefied Gas Dynamics*, Vol. 1, Sixth Symposium, Academic Press, New York, N. Y., 1969, p. 835.
- 22 Anderson, J. B., *Entropie*, No. 18, Dec. 1967, p. 13.
- 23 Miller, D. R., and Andres, R. P., in: *Rarefied Gas Dynamics*, Vol. 2, Sixth Symposium, Academic Press, New York, N. Y., 1969, p. 1385.

**J. B. BERGQUAM**

Associate Professor,  
Department of Mechanical Engineering,  
Sacramento State College,  
Sacramento, Calif.  
Assoc. Mem. ASME

**R. A. SEBAN**

Professor,  
Department of Mechanical Engineering,  
University of California,  
Berkeley, Calif.  
Mem. ASME

## Spectral Radiation from Alumina Powder on a Metallic Substrate

*Normal spectral radiation was measured in the range of 1 to 10  $\mu$  from layers of 0.3- $\mu$  alumina powder of various thicknesses and compactions resting on a platinum substrate. The substrate was heated and the layer lost heat from its upper surface by radiation and free convection. The measurements are compared to the predictions obtained from the two-flux theory applied on a spectral basis, in combination with the equation of conduction. Qualitative correspondence is indicated but the magnitudes of the predicted and measured radiation differ by as much as 40 percent. The inference is that the specification of optical properties is not quite correct and that the thermal conductivity of the powder layer is substantially less than expected.*

### Introduction

THERE IS considered the particular problem of the specification of the radiation emerging from a layer which scatters and absorbs radiation and also conducts heat, one side of this layer being in contact with a hot metal surface and the other losing heat by radiation to the surroundings. Data are presented in the range from 1 to 10  $\mu$  for the radiation emerging normally from a layer of 0.3- $\mu$ -dia alumina powder of a few thicknesses and compactions, situated on a platinum substrate. The size of the particles, combined with the properties of the alumina, produces a large variation in the emergent radiation over the spectral range that is examined.

These results can be used to appraise how well they can be predicted from the optical properties of the alumina, the thermal conductivity of the layer, and the size of the particles. With such information (it turns out that it is probably not well enough known in this case), the problem is to solve the equations of transfer for the radiation field, in conjunction with the conduction equation. The complexity of the equations of transfer has led to a number of simplifications, indicated by Hottel and Sarofim [1]<sup>1</sup>; the one chosen here is the assumption of a diffuse distribution for both the forward and backward radiation and the consequent specification of the familiar two-flux model. This model, though of questionable applicability for small optical thicknesses, does provide for a relatively simple calculation for the spectrally dependent radiation fluxes.

<sup>1</sup> Numbers in brackets designate References at end of paper.

Contributed by the Heat Transfer Division and presented at the Winter Annual Meeting, New York, N. Y., November 29–December 3, 1970, of THE AMERICAN SOCIETY OF MECHANICAL ENGINEERS. Manuscript received by the Heat Transfer Division August 13, 1970; revised manuscript received April 9, 1971. Paper No. 70-WA/HT-14.

### Data

The layer was contained in a 1/8-in-deep 1 1/2-in-dia depression in a stainless steel plate, with a 1-mil-thick platinum sheet placed between the layer and the stainless steel, the steel being heated by irradiation from a furnace, and the temperature  $T_1$  of the platinum being measured by a thermocouple. A 40-gage chromel–alumel thermocouple, stretched across a fork, was used to estimate surface temperatures  $T_2$  by approaching the surface from above. These temperatures are cited, but are probably too low.

Narrow-angle optics gathered radiation in essentially the normal direction from a spot at the center of the disk of powder and directed the energy into a conventional monochromator and detector system. A tilting mirror provided for a reference sight on a cavity maintained at a temperature near that of the platinum. The results are presented as an apparent emittance,  $\epsilon_\lambda = \pi I_N / E_B(T_1)$ , and they are shown in Fig. 1 for the four samples specified in Table 1. The powder was Linde A, 0.3- $\mu$  high-purity alumina abrasive. The emittance of the platinum substrate, which is discussed in the next section, is also shown in Fig. 1.

Because the scattering efficiency of the particles is large at short wavelengths, the emittance is low there. At the long wavelengths, the scattering efficiency is small and the absorption efficiency becomes large, and in consequence the emittance becomes large. The results for sample 1 illustrate this; these results have been connected by a curve to assist in the examination of Fig. 1. The density of sample 2 is the same but it is five times as thick and the increased optical depth decreases the apparent emittance at short wavelengths because of the greater scattering, while at long wavelengths the apparent emittance is reduced primarily because of the lower temperature near the surface of the sample. In sample 3 the compaction is increased and there are more particles in the layer; there is a further decrease in

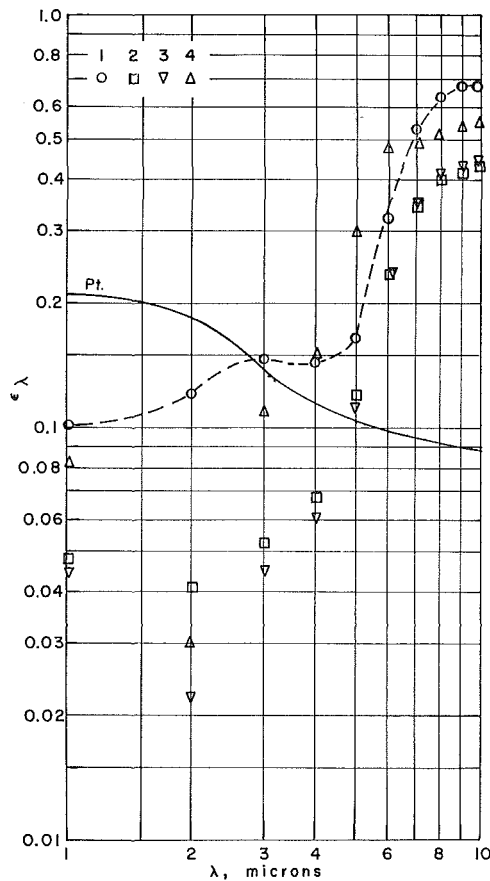


Fig. 1 Experimental values of apparent emittance

emittance at short wavelengths while the emittance is essentially unaltered at the long wavelengths. This trend is not continued in sample 4, where the number of particles is still greater. In this case multiple particle effects apparently occur to diminish the scattering efficiency and the emittance at short wavelengths increases. At long wavelengths there is also an increase in the apparent emittance due to the increased temperatures near the surface of the sample. Finally it is noted that the total emittances are approximately 0.26, 0.16, 0.15, and 0.26 respectively, for the 4 samples, assuming that the spectral emittances are constant for  $\lambda \geq 10 \mu$ .

Table 1 Sample specification and measured temperatures

	Weight, gram	Thickness, in.	$N \times 10^{12}$ particles/cm <sup>3</sup>	$F_S^{(1)}$	$T_1$ , °R	$T_2$ , °R	Compaction
S1	0.2	0.025	5.4	0.07	1840	1500	none
S2	1.0	0.125	5.4	0.07	1800	1150	none
S3	2.0	0.125	10.8	0.14	1800	1200	light
S4	3.5	0.100	24.5	0.31	1770	1300	heavy

(1) Fraction solid.

## Nomenclature

$E_B$  = monochromatic emissive power of a black body, given by Planck function  
 $F_S$  = volume fraction solid  
 $I$  = radiation intensity  
 $k$  = thermal conductivity  
 $K_A, K_S$  = absorption and scattering coefficients  
 $L$  = layer thickness

$N$  = particles per unit volume  
 $n$  = index of refraction  
 $q^+, q^-$  = monochromatic radiant fluxes in positive and negative directions  
 $Q_A, Q_S$  = efficiencies for absorption and scattering  
 $T_1$  = metal substrate temperature  
 $T_2$  = layer surface temperature  
 $T_f$  = adjacent air temperature

$x$  = coordinate normal to layer surfaces, zero at metal surface  
 $\epsilon_\lambda$  = apparent monochromatic emittance  
 $\eta$  = ratio,  $x/L$   
 $\kappa$  = extinction index  
 $\tau_0$  = optical thickness =  $(K_S + K_A)L$   
 $\omega$  = albedo

## Properties

Alumina particles were selected as a material because there exists some information on the optical constants for alumina. Plass [2] has given the values of index of refraction  $n$  and extinction index  $\kappa$  for a temperature of 1800 deg R, as indicated in Table 2. As discussed in reference [8], the extinction indices of Plass appear to be low, particularly for longer wavelengths, and transmission data for alumina given by Olt [3] and Oppenheim [4], together with the index of refraction in Table 2, have been used to obtain the alternative values of extinction index contained in the table. At wavelengths above  $6 \mu$  the transmissivity of alumina is so low that it is no longer possible to calculate the extinction index and the tabulated values of  $n\kappa$ , in this spectral region, have been obtained by extrapolation.

Despite the fact that the particles must actually form a continuous structure, they are idealized as separate, that is as a cloud of individual particles, their number density being calculated from their size and the density of alumina. This number density  $N$  is indicated in Table 1. The  $0.15\text{-}\mu$  radius  $r$  of the particles places them in the Rayleigh regime for the entire range of wavelengths considered here, so that the efficiency factors for scattering and absorption are<sup>2</sup>

$$Q_S = \frac{8}{3} \left( \frac{2\pi r}{\lambda} \right)^4 \left| \frac{n'^2 - 1}{n'^2 + 2} \right|^2 \quad (1)$$

$$Q_A = -4 \left( \frac{2\pi r}{\lambda} \right) \text{Im} \left[ \frac{n'^2 - 1}{n'^2 + 2} \right]$$

Here  $n'$  is the complex index of refraction  $n(1 - i\kappa)$ ; in the present situation  $n \gg n\kappa$  and the efficiency factors can be approximated as

$$Q_S = \frac{8}{3} \left( \frac{2\pi r}{\lambda} \right)^4 \left| \frac{n^2 - 1}{n^2 + 2} \right|^2 \quad (2)$$

$$Q_A = \frac{24 \left( \frac{2\pi r}{\lambda} \right) n^2 \kappa}{(n^2 + 2)^2}$$

These factors and the number density combine to yield the scattering and absorption coefficients

$$K_S = \pi r^2 N Q_S \quad K_A = \pi r^2 N Q_A \quad (3)$$

<sup>2</sup> Reference [1], p. 394.

To account for high number densities, especially as exist for sample 4, there is used the efficiency-concentration function of Harding [5]

$$E = \exp \left[ -4 \left( \frac{2r}{\lambda} \right)^{-3/4} F_S^{1/3} Q_s^{1/2} \right] \quad (4)$$

where  $F_S$  is the volume fraction solid (0.31 for sample 4) and  $E$  is a multiplier for the scattering coefficient to reduce its magnitude to account for multiple particle interaction.

Table 2 contains the values of the absorption and scattering coefficients for the samples, incorporated into the optical depth,  $\tau_0 = (K_S + K_A)L$ , and the albedo for scattering,  $\omega = K_S/(K_A + K_S)$ , and the Harding factor for sample 4.

In addition to the radiation properties of the layer, the prediction of the apparent emissivity requires a specification of the emittance of the platinum substrate and of the thermal conductivity of the layer. The former was evaluated from the normal emittances as specified by Seban [6] and indicated in Table 2 for 1800 deg R, with an approximate adjustment to hemispherical values made by increasing the normal values by 20 percent. Thermal conductivities are uncertain; the values of Godbee and Ziegler [7] obtained for much larger particles with much smaller void fractions were extrapolated to large void fractions so that at unit void fraction the conductivity would be that of air at 1800 deg R. The values so obtained for the four samples were 0.1, 0.1, 0.15, 0.24 Btu/(hr-ft-deg R); these were used in the calculations but the values are probably high.

## Analysis

The radiation field within the medium is specified by the equation of transfer. For the "positive" direction  $0 < \theta < \pi/2$ , this is

$$\cos \theta \frac{dI^+}{dx} = -(K_A + K_S)I^+ + K_A I_B + \frac{K_S}{4\pi} \int_0^{4\pi} I(\theta, \phi) P(\theta, \phi) d\Omega \quad (5)$$

with a similar equation for the "negative" direction.

To simplify the analysis the scattering is assumed to be isotropic,  $P(\theta, \phi) = 1$ , and the intensities  $I^+$  and  $I^-$  are assumed to be independent of  $\theta$ . Integration of equation (5) over the solid angle in the positive direction and the use of  $q^+ = \int_0^{2\pi} I^+ \cos \theta d\Omega$ , which is  $q^+ = \pi I^+$  for the diffuse case considered, gives

$$\frac{dq^+}{dx} = -[2(K_A + K_S) - K_S]q^+ + K_S q^- + 2K_A E_B \quad (6)$$

with a similar equation for the negative direction. The two

equations can also be expressed in the more usual forms for the two-flux model

$$\frac{dq^+}{d\eta} = -\tau_0(2 - \omega)q^+ + \tau_0\omega q^- + 2\tau_0(1 - \omega)E_B; \quad \eta = \frac{x}{L} \quad (7)$$

$$-\frac{dq^-}{d\eta} = -\tau_0(2 - \omega)q^- + \tau_0\omega q^+ + 2\tau_0(1 - \omega)E_B \quad (8)$$

The temperature field needed for the evaluation of the emissive power,  $E_B$ , the Planck function, is obtained from the conduction equation

$$\frac{d}{d\eta} \left[ -\frac{k}{L} \frac{dT}{d\eta} + \int_0^\infty (q^+ - q^-) d\lambda \right] = 0 \quad (9)$$

The solution of the problem involves the simultaneous solution of equations (7), (8), and (9) with the associated boundary conditions. For the system considered here, the boundary conditions are

$$\eta = 0 \quad q^+ = \epsilon_M E_B + (1 - \epsilon_M)q^-$$

where  $\epsilon_M$  is for the metal

$$T = T_1 \quad (10)$$

$$\eta = 1 \quad q^- = 0 \quad (11)$$

$$T = T_2 \quad \text{or}$$

$$-\frac{k}{L} \frac{dT}{d\eta} = h(T_2 - T_f) \quad (11a)$$

where  $h$  is the convective heat transfer coefficient and  $T_f$  is the temperature of the adjacent air.

It should be recalled that for the present analysis the samples are idealized as a cloud of individual particles and therefore the outer boundary condition (11a) does not contain a surface-emission term, inclusion of such a term being inconsistent with the cloud model.

For calculation, reference [8], equations (7) and (8) were solved analytically for  $(q^+ + q^-)$  and  $(q^+ - q^-)$  to obtain advantages in the numerical evaluation of the analytical solutions. Beginning with an assumed linear temperature profile these solutions were evaluated for  $1-\mu$  intervals from 1 to 20  $\mu$ , with layer properties as evaluated for 10  $\mu$  being used for the interval 10 to 20  $\mu$  in which the fraction of the total energy was relatively small. Then the net radiation flux  $(q^+ - q^-)$  for each wavelength interval was summed over the wavelength range at each of the 200 subdivisions of the layer thickness and equation (9) integrated numerically to obtain a new temperature distribu-

Table 2 Optical properties

$\lambda$	$n$	$(1)n_K \times 10^6$	$(2)n_K \times 10^6$	$\omega$	S1 $\tau_0$	S2 $\tau_0$	S3 $\tau_0$	S4 $\tau_0^{(3)}$	$E^{(4)}$	$\epsilon_M^{(5)}$
1	1.75	1	3.44	1.000	<sup>(3)</sup> (5.5)	<sup>(3)</sup> (27.5)	<sup>(3)</sup> (27.5)	24.9	0.019	0.208
2	1.74	1	7.03	0.999	5.18	26.90	51.80	16.9	0.192	0.184
3	1.71	1	11.12	0.998	0.96	4.81	9.63	6.44	0.382	0.138
4	1.68	10	22.70	0.992	0.29	1.43	2.87	2.67	0.522	0.117
5	1.63	100	187	0.870	0.12	0.59	1.19	1.44	0.630	0.104
6	1.54	220	1500	0.260	0.15	0.74	1.49	2.51	0.723	0.097
7	1.42		3160	0.058	0.23	1.16	2.32	4.15	0.806	0.094
8	1.35	330	4110	0.022	0.27	1.33	2.66	4.81	0.856	0.091
9	1.22		4500	0.006	0.28	1.38	2.76	5.01	0.916	0.090
10	1.09	500	4770	0.001	0.28	1.41	2.81	5.09	0.968	0.089

(1) Reference [2].

(2) Used herein.

(3) Includes Harding factor, equation (4).

(4) Harding factor for sample 4.

(5) Normal emittance of platinum at 1800 deg R, reference [6].



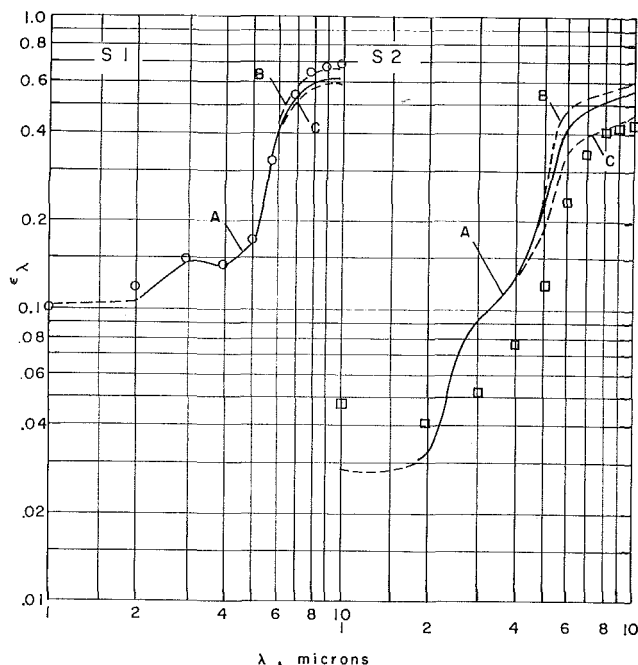


Fig. 2 Experiment and prediction for samples 1 and 2

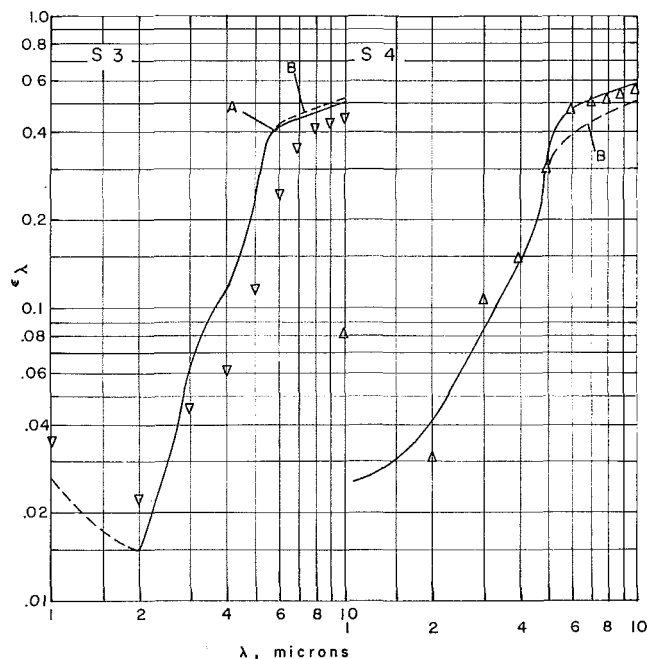


Fig. 3 Experiment and prediction for samples 3 and 4

tion. Iteration was continued until all local absolute temperatures agreed to within 1 percent.

The predicted value of the apparent emittance was then evaluated as  $\epsilon_\lambda = q^+(1)/E_B(T_1)$ .

### Predicted Emittances

In the initial solutions the surface temperature  $T_2$  was prescribed as the measured value indicated in Table 2, and the thermal conductivity was taken at the values already specified. The predictions of apparent emissivity for the four samples are shown as curves A in Figs. 2 and 3, where the experimental points, shown in Fig. 1, are repeated. For samples 1, 2, and 3 the curves are dashed between 1 and 2  $\mu$  to indicate that equation (4) was used to modify the scattering efficiency only at 1  $\mu$ , though it should have been used for the whole range of wavelengths. Had this been done, the effect would have been negligible for wavelengths longer than 3  $\mu$  but the prediction for 2  $\mu$  would have been raised slightly. The comparison of curves A and the data reveals that a qualitative agreement is achieved but that there are still substantial differences between measured and predicted values.

A deficiency in the use of the cited thermal-conductivity values consists in the inference of excessive values of the convective heat transfer coefficient for the sample surface, and for the samples in order, the coefficients are indicated by the solutions to be 12.1, 7.7, 10.7, and 13.3 Btu/(hr-ft<sup>2</sup>-deg R). For the free-convection conditions of the experiment, the coefficient would be expected to have been about 1.5, and certainly not larger than 2 Btu/(hr-ft<sup>2</sup>-deg R). If coefficients of this order did exist, then much lower layer conductivities are needed if there are to be predicted surface temperatures of the order of the measured values. To investigate this matter, predictions were made using the condition (11a) at the surface, with a heat transfer coefficient of 2 Btu/(hr-ft<sup>2</sup>-deg R) and a thermal conductivity of 0.05, about as

low a value as might be expected. Also, to provide further comparison, a conductivity of 0.02 was also used for samples 1 and 2. The results are shown as curves B and C of Fig. 2 and the change in thermal conductivity is revealed to have a discernible effect only at the longer wavelengths where particle absorption becomes important and the apparent emittance changes in the way the predicted surface temperature does. The effect is greater for the thicker sample, S2, because the optical thickness of that sample is great enough to make the emission from the surface primarily that originating in the immediate region of the surface. With a conductivity of 0.05, the surface temperature is raised above the experimental value and the predicted emittance departs further from the data; the abnormally low conductivity of 0.02 is required to lower the surface temperature and improve the agreement with experiment.

Predictions B are also shown in Fig. 3. For sample 3 there is no essential difference from prediction A because the surface temperatures are about the same. There is some reduction in emittance for sample 4 because of the lower predicted surface temperature.

Table 3 specifies the surface temperature for the three cases and also presents the ratio  $(T_1 - T_2)/(T_2 - T_f)$  which can be associated with the conductive-convective energy balance at the surface. If the surface temperature gradient is assumed to be  $(T_1 - T_2)/L$ , then  $(T_1 - T_2)/(T_2 - T_f) = hL/k$ . But the actual temperature gradient is less than this, so that  $hL/k < (T_1 - T_2)/(T_2 - T_f)$  and the ratio of these quantities indicates the reduction in the gradient due to the radiative interaction. The ratio of course increases as the thermal conductivity decreases.

It is clear that to secure predictions which are in agreement with a heat transfer coefficient of 2, it is necessary to assume thermal conductivities at least as low as 0.05, and lower values improve the agreement with the data at the long wavelengths.

Table 3

	S1			S2			S3		S4	
	A	B	C	A	B	C	A	B	A	B
$T_2$	1500	1689	1521	1150	1250	1040	1200	1230	1300	1245
$\frac{T_1 - T_2}{T_2 - T_f}$	0.35	0.13	0.32	1.05	0.76	1.50	0.90	0.81	0.61	0.75
$\frac{hL}{k}$	0.25	0.083	0.208	0.80	0.415	1.04	0.74	0.415	0.46	0.33

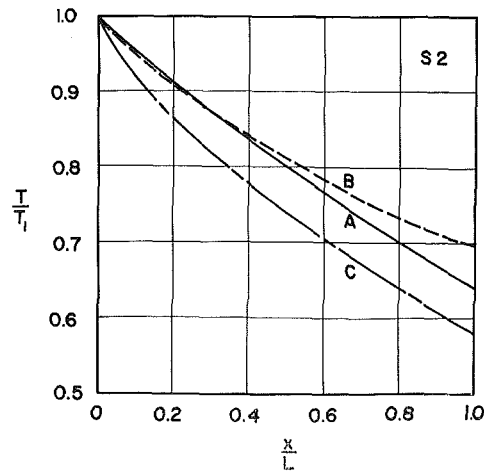


Fig. 4 Predicted temperature distributions for sample 2

It can also be noted that prediction A, which can be approximately construed as being associated with the Biot numbers indicated for that case in Table 3, improves in relative agreement in the long-wavelength region as the optical thickness of the sample increases. With such an increase, the emergent radiation becomes more diffuse and thus the assumption of the two-flux model becomes more agreeable. In this sense the relatively high prediction for sample 2 might be regarded as a consequence of the fact that for this optically thinner sample the normal emittance might be substantially less than  $q^+/\pi$ .

Some insight can be realized from the simple system of an isothermal layer on a perfectly reflecting specular substrate. For this system the ratio of the correct normal intensity to the heat flux  $q^+$  calculated from the two-flux model is

$$\frac{\pi I_N}{q^+} = \frac{1 - e^{-2\tau_0}}{1 - e^{-4\tau_0}}$$

For sample 2 at  $10 \mu$  this ratio is 0.94 and the 20 percent difference between the prediction and the data is not explainable on this basis. At the same wavelength the ratio for sample 1 is 0.64, to imply that the prediction ought to be greater than the data, while actually it is somewhat less.

In the short-wavelength region,  $\lambda < 3$ , the albedo is so high that the radiation field is essentially independent of the temperature field. Here the prediction generally follows the trends of the data which itself is of relatively low accuracy when the apparent emittance becomes as low as 0.05. There is a failure to predict the high emittance of sample 4 at  $1 \mu$ , as though the prediction of  $E$  from equation (4) were not small enough for this wavelength. However, the cloud-of-particles model may as well no longer be applicable for this relatively dense sample, and Bergquam [8] has shown that a model based on a pore-filled solid gives almost an equally acceptable prediction in this case.

An additional result of interest is the temperature distribution in the layer and for the three predictions made for sample 2 the corresponding temperature distributions are shown in Fig. 4. It is noted that as the ratio  $hL/k$  increases the temperature near the outer edge of the layer decreases as does the calculated apparent emittance.

Finally, note is taken of the "hump" in the prediction at  $3 \mu$ , which agrees with the data for sample 1 and appears to a diminishing extent in the predictions for greater optical thickness, but is not apparent in the data for these samples. The albedo for  $3 \mu$  is so large that the problem is still essentially a purely scattering one, and the inference is that the predicted scattering efficiency is not quite large enough for this wavelength. There are no present grounds for a change which would require a larger extinction index in this region, but this is mentioned primarily because at low temperatures Dillenius [9] has shown that alumina powder is so hygroscopic that the appearance of a peak in the index in this region is almost unavoidable. At the temperatures concerned in the present experiments, the existence of any hydrate is considered to be improbable.

## Conclusions

The comparisons of the predictions made with the two-flux model and the experimental data for the apparent normal emittance of an alumina powder layer on a platinum substrate reveal general correspondence in spectral distribution and effect of optical depth. The magnitude correspondence is, however, relatively poor, with discrepancies of up to 40 percent between theory and experiment.

To rationalize the prediction, and the data, in terms of an expected heat transfer coefficient for the free-convection conditions that existed at the surface requires the postulation of a thermal conductivity of the order of that for air, or even somewhat less.

It is important to diminish the single-particle scattering efficiency by a factor such as that of Harding to obtain reasonable results at the low wavelengths where scattering is the predominant radiation effect.

## Acknowledgment

There is acknowledged the assistance to this research of a National Aeronautics and Space Administration traineeship held by one of the authors (J. B. Bergquam).

## References

- Hottel, H. C., and Sarofim, A. F., *Radiative Transfer*, McGraw-Hill, New York, N. Y., 1967.
- Plass, G. N., "Mie Scattering and Absorption Cross Sections for Aluminum Oxide and Magnesium Oxide," *Applied Optics*, Vol. 3, 1964, pp. 867-872.
- Olt, R. D., "Synthetic Sapphire, an Infrared Optical Material," *Industrial Crystals Bulletin F-917-A*, Linde Co., 1958.
- Oppenheim, V. P., and Even, V., "Infrared properties of Sapphire at Elevated Temperatures," *Journal of the Optical Society of America*, Vol. 52, 1962, pp. 1078-1079.
- Harding, R. H., Golding, B., and Morgen, R. A., "Optics of Light Scattering Films. Study of Effects of Pigment Size and Condensation," *Journal of the Optical Society of America*, Vol. 50, 1960, pp. 446-455.
- Seban, R. A., "The Emissivity of Transition Metals in the Infrared," *JOURNAL OF HEAT TRANSFER, TRANS. ASME, Series C*, Vol. 87, No. 2, May 1965, pp. 173-176.
- Godbee, H. W., and Ziegler, W. T., "Thermal Conductivities of MgO, Al<sub>2</sub>O<sub>3</sub>, and ZrO<sub>2</sub> Powders to 850°C," *Journal of Applied Physics*, Vol. 37, 1966, pp. 40-56.
- Bergquam, J. B., "Heat Transfer by Conduction and Radiation in Scattering, Absorbing, and Emitting Materials," PhD thesis, University of California, Berkeley, Calif., 1968.
- Dillenius, M., "Thermal Radiation Properties of Compacted Alumina Powder," PhD thesis, University of California, Berkeley, Calif., 1968.

C. L. TIEN

Professor.  
Mem. ASME

C. K. CHAN

Department of Mechanical Engineering,  
University of California,  
Berkeley, Calif.

G. R. CUNNINGTON

Lockheed Palo Alto Research Laboratory,  
Palo Alto, Calif.

## Infrared Radiation of Thin Plastic Films

*A combined analytical and experimental study is presented for infrared radiation characteristics of thin plastic films with and without a metal substrate. On the basis of the thin-film analysis, a simple analytical technique is developed for determining band-averaged optical constants of thin plastic films from spectral normal transmittance data for two different film thicknesses. Specifically, the band-averaged optical constants of polyethylene terephthalate (Mylar, DuPont Co.) and polyimide (Kapton, DuPont Co.) were obtained from transmittance measurements of films with thicknesses in the range of 0.25 to 3 mil. The spectral normal reflectance and total normal emittance of the film side of singly aluminized films are calculated by use of optical constants; the results compare favorably with measured values.*

### Introduction

Optics and radiation of thin films have long been subjects of considerable fundamental and practical interest. Although the theory of reflection and transmission by thin films has been well developed [1],<sup>1</sup> relatively little information is available for the optical properties of thin-film material. Furthermore, the available information is often restricted to the visible spectral range or to thin-film materials with simple structures such as metals or metallic oxides (see, for instance, references given in [2]). In contrast, infrared optical properties of thin plastic films remain almost unexplored. A series of earlier papers did report investigations of infrared spectra of various high polymers [3], but the major emphasis has been the identification of molecular structure from transmission data. Little information can be extracted from these results regarding optical and thermal radiation properties. The demand for this information, however, is strong and increasing as a result of the extensive use of thin plastic films in optical instruments [4], thermal control coatings [5], and multilayer insulation [6]. In particular, infrared radiation of thin plastic films on a metal substrate, such as singly metallized films, plays a most important role in thermal control and insulation heat transfer calculations.

The purpose of the present paper is to report a combined theoretical and experimental study of infrared radiation of thin plastic films with and without a metal substrate. The key elements of the present study are the introduction of the new concept of band-averaged optical constants, the determination of these constants from thin-film transmittance measurements, and the use of these constants in determining radiation properties of thin plastic films.

<sup>1</sup> Numbers in brackets designate References at end of paper.

Contributed by the Heat Transfer Division and presented at the Winter Annual Meeting, New York, N. Y., November 29–December 3, 1970, of THE AMERICAN SOCIETY OF MECHANICAL ENGINEERS. Manuscript received by the Heat Transfer Division August 10, 1970; revised manuscript received June 24, 1971. Paper No. 70-WA/HT-15.

### Determination of Band-Averaged Optical Constants

In the macroscopic framework of electromagnetic wave theory, radiation phenomena such as reflection, absorption, and transmission can be expressed in terms of certain physical parameters. For solids these parameters are the optical constants  $n$  and  $k$  which form the complex refractive index ( $n - ik$ ). For dielectric materials such as plastics,  $n \gg k$ . Plastics differ from other dielectric solids, however, in that they consist of long-chained polymeric molecules randomly oriented. Radiation in plastics has its origin in the excitation of radical bonds in the large molecule and can be described by a field of randomly distributed excitation centers. As a result, the radiation spectrum of plastics, somewhat analogous to that of radiating gases, contains a larger number of resonances, especially in the infrared. These sharp spectral variations which are noticeably absent in the radiation spectra of metals and metallic oxides would result in cumbersome computations if exact nongray calculations are to be made. In addition, because of the complex plastics structure and radiation mechanisms, it is impossible to predict all these resonances in a quantitative manner.

For the convenience of engineering calculations, it is desirable to devise an approximate technique which is simple but still retains the nongray behavior of the radiation spectrum. In a spirit similar to the band approximations in the calculation of surface radiation [7] and gaseous radiation [8], a technique is to be established to determine band-averaged optical constants from transmittance measurements. Although this technique, with proper modifications, is applicable to all thin films, it is particularly suitable for thin plastic films because of its distinctive absorption band regions as well as its sharp spectral variations in these regions (see, for instance, Figs. 1 and 2). Once the appropriate band-averaged optical constants of the thin-film material are known, all of the radiation properties of the thin film can be calculated.

The analysis given below is based on the premise that the band-averaged optical constants are to be determined from transmittance data for two different thicknesses of thin-film ma-

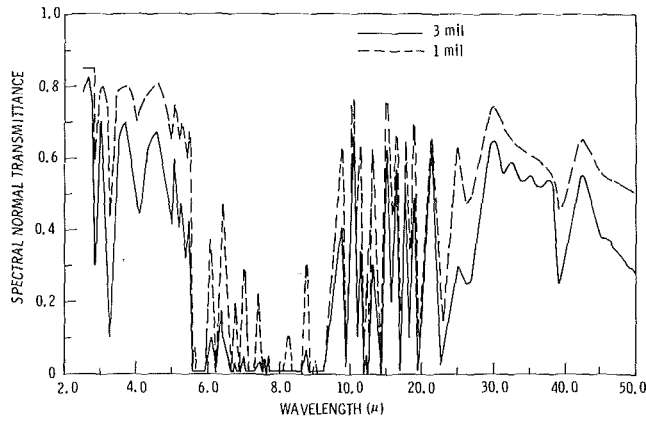


Fig. 1 Spectral normal transmittance of Kapton films

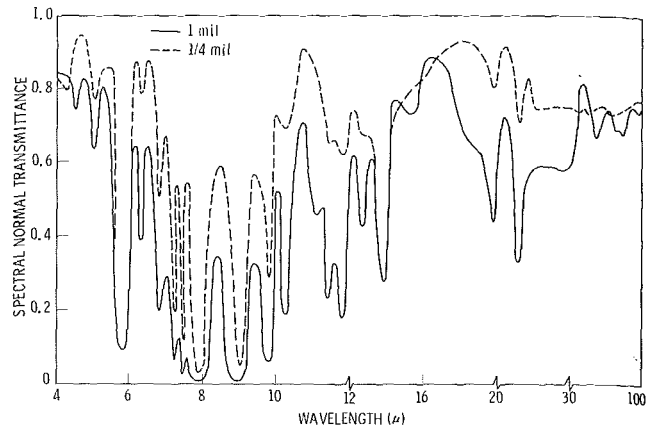


Fig. 2 Spectral normal transmittance of Mylar films

terial. This calculation scheme is fundamentally different from the conventional method which is based on transmittance and reflectance data for one film thickness [1]. The reason for using the two-thickness transmittance data is that considerable simplification can be achieved in the calculation of band-averaged optical constants.

Consider first the transmittance of one single film. For normal incidence, the monochromatic transmittance for an absorbing film of complex refractive index  $(n - ik)$  bounded by a nonabsorbing medium of refractive index of unity is given by [1]

$$T = \frac{t_1^2 t_2^2 \exp(-4\pi k \omega)}{1 + r_1^2 r_2^2 \exp(-8\pi k \omega) + 2r_1 r_2 \cos(\phi_1 + \phi_2 + 4\pi n \omega) \exp(-4\pi k \omega)} \quad (1)$$

where subscripts 1 and 2 denote, respectively, the first and second interface with respect to the incident beam

$$t_1^2 = \frac{4}{(1+n)^2 + k^2} \quad t_2^2 = \frac{4(n^2 + k^2)}{(1+n)^2 + k^2}$$

$$r_1^2 = r_2^2 = \frac{(1-n)^2 + k^2}{(1+n)^2 + k^2} \quad \omega = \frac{d}{\lambda}$$

$$\phi_1 = -\tan^{-1} \left[ \frac{2k}{1-n^2-k^2} \right] \quad \phi_2 = \phi_1 - \pi$$

For dielectric absorbing media ( $n \gg k$ ), equation (1) can be simplified to the following form:

$$T = \frac{\beta \exp(-p\omega)}{1 - 2\alpha [\exp(-p\omega)] \cos q\omega + \alpha^2 \exp(-2p\omega)} \quad (2)$$

where

$$\alpha = r_1^2 = r_2^2 = \frac{(1-n)^2}{(1+n)^2} \quad \beta = t_1^2 t_2^2 = \frac{16n^2}{(1+n)^4}$$

$$p = 4\pi k \quad q = 4\pi n$$

In arriving at equation (2), an approximation has been made on

$$\tan^{-1} \left( \frac{2k}{n^2 - 1} \right) \approx \frac{2k}{n^2 - 1}$$

which is generally valid for weak-absorbing dielectric solids since  $k \ll 1$  and  $n$  is 1.5 or larger.

Equation (2) is still rather complex for mathematical manipulation, especially with the cosine function in the denominator. Since  $|\cos q\omega| < 1$ , the whole denominator could be approximated by unity if  $\alpha \exp(-p\omega) \ll 1$ . This is quite a restrictive condition and is not satisfied in most cases. It is most interesting to note, however, that by making a band average this drastic simplification is indeed generally valid for the end results. This is shown below.

Assume that the sum of the second and third terms in the denominator of equation (2) is less than unity. The assumption is

well justified for the case  $\alpha < 0.4$  or  $n < 4.5$ , which is valid in general for dielectric media. Thus, it is legitimate to express equation (2) in the series form

$$T = \beta \exp(-p\omega) \{ 1 + [2 \exp(-p\omega) \cos q\omega] \alpha + [4 \exp(-2p\omega) \cos^2 q\omega - \exp(-2p\omega)] \alpha^2 + [8 \exp(-3p\omega) \cos^3 q\omega - 4 \exp(-3p\omega) \cos q\omega] \alpha^3 + O(\alpha^4) \} \quad (3)$$

Since  $\omega (= d/\lambda)$  is a logical parameter in all thin-film analyses, and represents a dimensionless frequency or wave number, it is more convenient to integrate over band regions on the basis of  $\omega$ . Integrating equation (3) over a band region  $\Delta\omega$  gives

$$\int_{\Delta\omega} T d\omega \cong -\beta \left[ \left( \frac{1}{p} \right) \exp(-p\omega) - \alpha O \left( \frac{1}{q} \right) \exp(-2p\omega) + \left( \frac{\alpha^2}{3p} \right) \exp(-3p\omega) - \alpha^3 O \left( \frac{1}{q} \right) \exp(-4p\omega) \right]_{\Delta\omega} \quad (4)$$

For dielectric media,  $q \gg p$  and  $\alpha^2 \ll 1$ . Thus, equation (4) can be well approximated by

$$\int_{\Delta\omega} T d\omega = - \left( \frac{\beta}{p} \right) e^{-p\omega} \Big|_{\Delta\omega} \quad (5)$$

As indicated before, although equation (5) can be obtained directly from equation (2) by keeping only the leading term in the denominator, it is under more restrictive conditions than the

## Nomenclature

$d$ = film thickness	$r$ = interface reflection coefficient	$\kappa$ = absorption coefficient
$J$ = band transmittance	$R$ = film reflectance	$\lambda$ = wavelength
$k$ = absorption index	$t$ = interface transmission coefficient	$\mu$ = micron = $10^{-6}$ meter
$n$ = refractive index	$T$ = film transmittance	$\phi$ = phase angle
$p = 4\pi k$	$\alpha = r_1^2 = r_2^2$	$\omega = d/\lambda$
$q = 4\pi n$	$\beta = t_1^2 t_2^2$	

above derivation. The absence of the cosine function in equation (5) also indicates the elimination of the wave interference effect through the band-averaging process, although in the film thickness range ( $\sim 1$  mil) under practical consideration the wave interference effect is very small.

The simple expression of the band transmittance of a film allows a convenient method of determining two band-averaged optical constants from two-band transmittance data. Let  $T_1$  and  $T_2$  be the transmittances of two films of thickness  $d_1$  and  $d_2$ , respectively. The transmittance spectrum is divided into several regions and in each region bounded by  $\lambda_1$  and  $\lambda_2$  the optical constants  $n$  and  $k$  are assumed independent of  $\lambda$ . Defining

$$J_i = \int_{\lambda_1}^{\lambda_2} T_i \frac{d\lambda}{\lambda^2} = \frac{-1}{d_i} \int_{\omega_{i1}}^{\omega_{i2}} T_i d\omega_i$$

$$\omega_i = \frac{d_i}{\lambda} \quad \omega_{ij} = \frac{d_i}{\lambda_j}$$

there follows from equation (5)

$$d_i J_i = (\beta/p) [\exp(-p\omega_{i2}) - \exp(-p\omega_{i1})] \quad (i = 1, 2) \quad (6)$$

or

$$\left(\frac{d_1}{d_2}\right) \left(\frac{J_1}{J_2}\right) = \frac{\exp(-p\omega_{12}) - \exp(-p\omega_{11})}{\exp(-p\omega_{22}) - \exp(-p\omega_{21})} \quad (7)$$

Equation (7) can be used to determine  $k(p = 4\pi k)$  from given values of  $d_1$ ,  $d_2$ ,  $\lambda_1$ , and  $\lambda_2$ , and measured values of  $J_1$  and  $J_2$ . Without much sacrifice in accuracy, a simpler and explicit expression for  $k$  can be obtained by expanding the exponential function and neglecting, if  $p\omega_{ij} < 1$  as in the case of thin plastic films, terms of order  $O(p^3\omega_{ij}^3)$  or higher. The result is

$$k = \frac{2(J_1 - J_2)}{4\pi(\omega_{11} + \omega_{12})[(d_2/d_1)J_1 - J_2]} \quad (8)$$

With  $k$  (or  $p$ ) determined,  $\beta$  and consequently  $n$  can be obtained from equation (6) and the definition of  $\beta$ , respectively. They are

$$\beta = \frac{d_1 J_1 p}{\exp(-p\omega_{12}) - \exp(-p\omega_{11})} \quad (9)$$

and

$$n = \{(2/\sqrt{\beta}) - 1\} + \{[(2/\sqrt{\beta})]^2 - 1\}^{1/2} \quad (10)$$

Equations (8) and (10) represent the end result of the analytical framework in determining the band-averaged optical constants from transmittance measurements of weakly absorbing dielectric films such as thin plastic films. It should be noted that the band-averaged optical constants are defined in terms of the dimensionless wave number  $\omega$ .

## Radiation Properties of Films on a Metal Substrate

If the optical constants of the film as well as the substrate are known, the calculation of radiation properties of the thin film on a substrate is straightforward and can be found in standard texts [1]. For total radiation quantities, the calculation becomes greatly simplified when the concept of band-averaged optical constants is employed. For radiation of films on a metal substrate, two papers have recently appeared. The first [9] concerns radiation of the nonabsorbing film ( $k = 0$ ) on a metal substrate with optical constants described by various theoretical models, notably the Drude single-electron theory and the anomalous skin-effect theory. The second paper [2] presents calculated and measured values of the emittance of oxide layers (with much stronger absorption than plastic material) on a metal substrate. The calculation is based on given values of optical constants in the literature. Since the theoretical formulation for calculating radiation properties of film on a metal substrate is

standard and contained in detail in the given references, it will not be repeated here.

## Experimental Measurements

The experimental measurements performed on the thin-plastic film materials consisted of spectral transmittance of the clear films and spectral reflectance and total hemispherical emittance of the film side of singly aluminized film material. Spectral, normal transmittance measurements were made for  $1/4$ -mil and 1-mil thicknesses of uncoated Mylar and 1-mil and 3-mil thicknesses of uncoated Kapton films. Spectral, near-normal reflectance measurements were also made on the film side of both  $1/4$ -mil Mylar and 1-mil Kapton coated on one surface with vacuum-deposited aluminum ( $600 \pm 100 \text{ \AA}$  metal as reported by supplier and verified by electrical resistance measurements). Calorimetric, total hemispherical emittance measurements were performed on the Mylar surface of the  $1/4$ -mil material having one sided coated with  $600 \text{ \AA}$  of aluminum.

A Beckman Model IR-12 infrared spectrophotometer was used to obtain the normal transmission data for the Kapton film over the wavelength region of 2.0 to  $50 \mu$  [10]. The specimens were held in a frame so that their surfaces were flat and normal to the optical path of the instrument. Transmission data for the Mylar material were measured from 2.5 to  $100 \mu$  using a Perkin-Elmer Model 301 far-infrared spectrophotometer. All data were measured at room temperature.

Spectral, near-normal reflectance measurements on the Kapton film from 2.0 to  $14 \mu$  were performed at room temperature using a Perkin-Elmer heated cavity reflectometer and Model 13 infrared spectrophotometer [10]. The room-temperature measurements of the  $1/4$ -mil Mylar over the wavelength region of 2.0 to  $25 \mu$  were conducted using a Gier-Dunkle Model HC100 heated-cavity reflectometer with a Perkin-Elmer Model 98 monochromator. The specimens of both materials were in the form of 1-in-dia disks cemented to a metal substrate with an epoxy adhesive. The substrate is water-cooled so that the surface is held near room temperature during the measurement process.

The total hemispherical emittance measurements were performed using a calorimetric method described in detail in [11]. The apparatus consists of a  $2^{1/2}$ -in-dia by  $3/16$ -in-thick copper substrate to which the back side of the test surface is cemented with an epoxy adhesive. The substrate is attached to a copper heater block which is thermally connected by a cylindrical-cross-section link to a LN<sub>2</sub>- or LH<sub>2</sub>-cooled vacuum chamber. Sample temperature is controlled from 400 deg K to 60 deg K using a spiral-wound heater embedded in the heater block. Radiated sample energy is collected using a black-body absorber mounted to the cryogenically cooled support structure within the vacuum chamber. The absorber is spaced no more than 30 mil from the test surface.

## Results and Discussion

Measured data of spectral normal transmittance of thin Kapton and Mylar films are shown in Figs. 1 and 2. It is clear that the radiation spectrum of these plastic materials is characterized by a large number of strong resonances. In fact, many of the sharp spectral variations cannot be shown because of the rather compact scale in wavelength. This result demonstrates a need for appropriate mean optical constants over various band regions. On the basis of equations (8) and (10), the band-averaged optical constants were determined from two sets of transmittance data for Kapton in four band regions and for Mylar in five regions. The values, given in Tables 1 and 2, show that in general Mylar has a smaller refractive index than Kapton in each band region, but that Mylar is a stronger absorber. The present results can be compared with the few scattered data in the literature on the refractive index of Mylar. It was given for Mylar that  $n = 1.64$  at  $\lambda = 5.75 \mu$  [12]. In the far infrared, it has been estimated

**Table 1 Band-averaged optical constants of Kapton and band-averaged reflectance of 1-mil Kapton on aluminum**

Wavelength range ( $\mu$ )	Refractive index	Absorption index	Reflectance	
			Theoretical	Experimental
3.0-5.5	1.816	0.00121	0.771	0.73
5.5-9.0	5.047	0.00484	0.501	0.20
9.0-22.5	3.550	0.00579	0.578	0.50
22.5-50.0	2.640	0.01155	0.790	—

**Table 2 Band-averaged optical constants of Mylar and band-averaged reflectance of 1/4-mil Mylar on aluminum**

Wavelength range ( $\mu$ )	Refractive index	Absorption index	Reflectance	
			Theoretical	Experimental
4.0-6.8	1.805	0.00327	0.936	0.88
6.8-9.8	3.648	0.01763	0.651	0.40
9.8-14.3	2.191	0.01700	0.757	0.75
14.3-21.0	1.565	0.01114	0.932	0.91
21.0-100.0	1.955	0.02215	0.800	—

**Table 3 Predicted and measured value of total hemispherical emittance of 1/4-mil Mylar on aluminum**

Temperature ( $^{\circ}$ K)	Total hemispherical emittance		
	Measured for specimen No. 1	No. 2	Predicted
300	—	—	0.45
314	0.37	—	—
305	—	0.39	—
286	0.35	—	—
279	—	0.34	—

that the mean value of  $n$  is 1.85 for the range 10-500  $\mu$  [13]. Both values are in general agreement with the values obtained here. No data are available for comparison of the absorption index, but the calculated values of Kapton and Mylar seem to agree with the general trend for glass (see Fig. 1-16 of [7]) in that the absorption index varies from the order of  $10^{-3}$  to  $10^{-2}$  as wavelength increases (noting that the absorption index is related to the absorption coefficient  $\kappa$  by  $4\pi k = \kappa\lambda$ ).

Fig. 3 shows the measured spectral normal reflectances of the film side of the singly aluminized Kapton and Mylar films. In order to compare with predicted reflectance values based on the band-averaged optical constants, a definition of the band-averaged reflectance must be given. According to the conventional definition of total reflectance [7]

$$R = \int_0^{\infty} R_{\lambda} H_{\lambda} d\lambda / \int_0^{\infty} H_{\lambda} d\lambda$$

the evaluation of  $R$  requires a prescription of spectral irradiation  $H_{\lambda}$ . For the convenience of comparison, it will be assumed here that  $H_{\lambda}$  is independent of wavelength in each band region. Thus, the band-averaged reflectance is

$$R_{\Delta\lambda} = \frac{1}{\Delta\lambda} \int_{\Delta\lambda} R_{\lambda} d\lambda$$

The predicted and measured values of  $R_{\Delta\lambda}$  are presented in Tables 1 and 2. In the theoretical calculation, the optical constants of aluminum are represented according to the Drude single-electron theory with a d-c conductivity of  $3.18 \times 10^{-17}$  sec $^{-1}$  and a relaxation time of  $0.801 \times 10^{-14}$  sec [14]. This description for the actual aluminum coating is of course rather crude as in the case of using other tabulated information [2]; nevertheless, the agreement between calculated and measured reflectances is quite good. Only in the second region where transmittance is low and sharp spectral variations occur does an appreciable discrepancy exist. This is probably due to the combined effect of experimental inaccuracy in measuring low transmittance and theoretical inaccuracy in making band average over sharp variations.

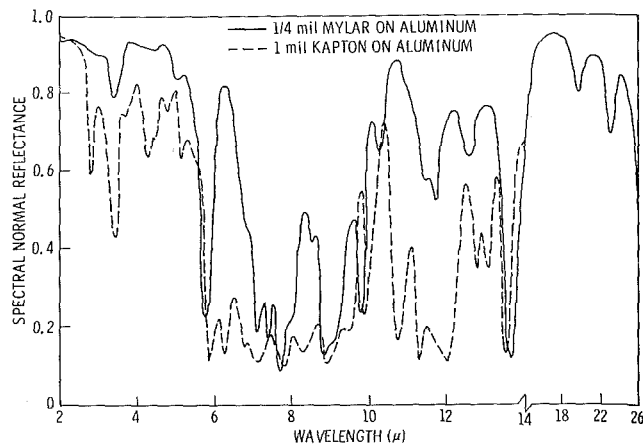


**Fig. 3 Spectral normal reflectance of plastic films on aluminum**

Table 3 presents measured values of total hemispherical emittance of 1/4-mil Mylar coated on one side with aluminum. Two similar samples (Nos. 1 and 2) were used in order to check the consistency of results. For comparison, aluminum-side emittance values are also given. The effect of a weak-absorbing thin film on the emittance of a metal substrate is indeed very large. A change of one order of magnitude in the total hemispherical emittance is indicated in the 1/4-mil Mylar on aluminum. This is in direct contrast with the analytical results obtained for the case of nonabsorbing films on a metal substrate where a very small effect is found [9]. The value of the emittance predicted from the present study for 1/4-mil Mylar film on aluminum is also shown in Table 3. This value is obtained in an approximate manner by first calculating the total normal emittance from the given band-averaged optical constants and then multiplying it by the factor of 1.33 [7]. Only near-room-temperature values are given since the band-averaged optical constants are based on room-temperature measurements. The agreement between the predicted and measured values of emittance is indeed quite satisfactory in view of the many approximations involved in the process of evaluation. The method may be extended to other temperatures if transmission data are obtained as a function of temperature.

### Acknowledgment

The authors wish to acknowledge the contributions of Mr. Ron Alves who assisted in obtaining experimental data. Work at Berkeley was supported by NASA grant NGR-05-003-285.

### References

- 1 Heavens, O. S., *Optical Properties of Thin Solid Films*, Butterworths Scientific Publications, London, England, 1955, Dover edition, 1965, Chapter 4.
- 2 Brannon, R. R., Jr., and Goldstein, R. J., "Emittance of Oxide Layers on a Metal Substrate," *JOURNAL OF HEAT TRANSFER, TRANS. ASME, Series C, Vol. 92, No. 2, May 1970*, pp. 257-263.
- 3 Liang, C. Y., and Krimm, S., "Infrared Spectra of High Polymers," *Journal of Molecular Spectroscopy*, Vol. 3, 1959, p. 554.
- 4 Chamberlain, J. E., et al., "The Spectral Transmission at Infra-red Wavelengths of Michelson Interferometers with Dielectric Film Beam-Dividers," *Infrared Physics*, Vol. 6, 1966, p. 195.
- 5 Cheever, P. R., Miles, J. K., and Romanko, J., "In Situ Measurements of Spectral Reflectance of Thermal Control Coatings Irradiated in Vacuo," in: *Thermophysics of Spacecraft and Planetary Bodies*, G. B. Heller, ed., Academic Press, New York, N. Y., 1967, p. 281.
- 6 Caren, R. P., and Cunningham, G. R., "Heat Transfer in Multi-layer Insulation Systems," *Chemical Engineering Progress Symposium Series*, Vol. 64, No. 87, 1968, p. 67.
- 7 Sparrow, E. M., and Cess, R. D., *Radiation Heat Transfer*, Brooks/Cole Publishing Co., Belmont, Calif., 1966, p. 99.
- 8 Tien, C. L., "Thermal Radiation Properties of Gases," *Advances in Heat Transfer*, Vol. 5, Academic Press, New York, N. Y., 1968, p. 253.

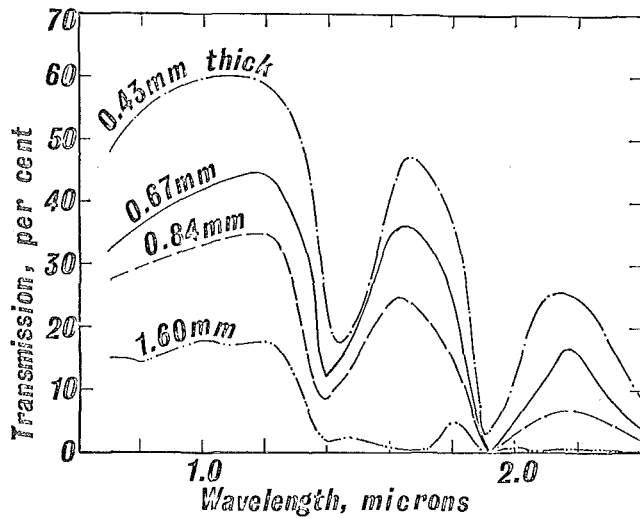


Fig. 4 Spectral transmission of excised white human skin (from reference in footnote 3)

9 Cravalho, E. G., and Coburn, E. L., "The Effect of Thin-Surface Films on the Radiation Properties of Metal Surfaces," in: *Thermophysics: Applications of Thermal Design to Spacecrafts*, J. T. Bevens, ed., Academic Press, New York, N. Y., 1970, p. 363.

10 Cunnington, G. R., et al., "Performance of Multilayer Insulation Systems for Temperatures to 700°K," NASA CR-907, 1967.

11 Cunnington, G. R., et al., "Total Emittance Measurements of Thin Metallic Films at Cryogenic Temperatures," *Journal of Spacecraft and Rockets*, Vol. 7, 1970, p. 1496.

12 Harrick, N. J., *Internal Reflection Spectroscopy*, John Wiley & Sons, New York, N. Y., 1967, p. 81.

13 Gebbie, H. A., and Stone, N. W. B., "A Michelson Interferometer for Far Infrared Spectroscopy of Gases," *Infrared Physics*, Vol. 4, 1964, p. 85.

14 Bennett, H. E., and Bennett, J. M., "Validity of the Drude Theory for Silver, Gold and Aluminum in the Infrared," in: *Optical Properties and Electronic Structure of Metals and Alloys*, F. Abeles, ed., North-Holland Publishing Co., Amsterdam, 1966, p. 175.



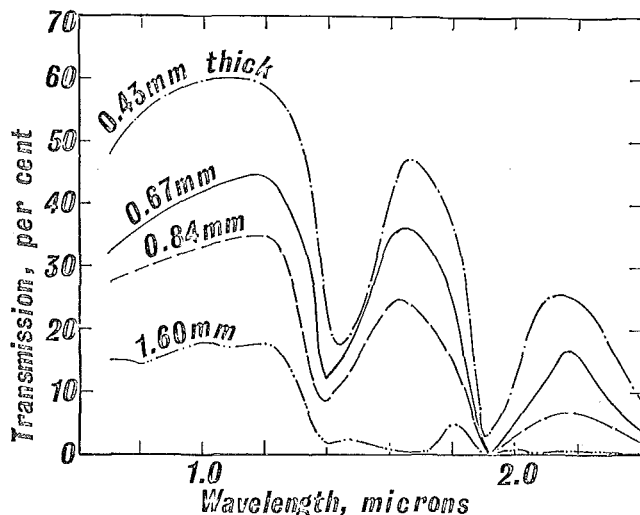


Fig. 4 Spectral transmission of excised white human skin (from reference in footnote 3)

9 Cravalho, E. G., and Coburn, E. L., "The Effect of Thin-Surface Films on the Radiation Properties of Metal Surfaces," in: *Thermophysics: Applications of Thermal Design to Spacecrafts*, J. T. Bevens, ed., Academic Press, New York, N. Y., 1970, p. 363.

10 Cunnington, G. R., et al., "Performance of Multilayer Insulation Systems for Temperatures to 700°K," NASA CR-907, 1967.

11 Cunnington, G. R., et al., "Total Emittance Measurements of Thin Metallic Films at Cryogenic Temperatures," *Journal of Spacecraft and Rockets*, Vol. 7, 1970, p. 1496.

12 Harrick, N. J., *Internal Reflection Spectroscopy*, John Wiley & Sons, New York, N. Y., 1967, p. 81.

13 Gebbie, H. A., and Stone, N. W. B., "A Michelson Interferometer for Far Infrared Spectroscopy of Gases," *Infrared Physics*, Vol. 4, 1964, p. 85.

14 Bennett, H. E., and Bennett, J. M., "Validity of the Drude Theory for Silver, Gold and Aluminum in the Infrared," in: *Optical Properties and Electronic Structure of Metals and Alloys*, F. Abeles, ed., North-Holland Publishing Co., Amsterdam, 1966, p. 175.

## DISCUSSION

### R. F. Boehm<sup>2</sup>

The authors are to be congratulated for an excellent addition to the heat transfer literature. Calculation of optical properties for systems such as those consisting of plastics has indeed been a formidable task prior to the development of this technique. The applications to plastic-coated metals or metal-coated plastics will be of great value in cryogenics as well as other areas.

There are some aspects that I feel could be emphasized in the paper. These deal primarily with the band-averaged theory for determining  $n$  and  $k$  which I feel is an extremely important contribution to the literature. First, the theory should hold for any substance and wavelength region, provided only that  $k \ll 1$  and  $1.5 < n < 4.5$  in addition to the usual ideal optical assumptions such as being homogeneous. The title of the paper might lead

<sup>2</sup> Mechanical Engineering Department, University of Utah, Salt Lake City, Utah.

Table 4 Band-averaged optical properties of skin using the present theory and the data of Fig. 4 (band width of 0.7 to 2.4 micron)

Thickness, mm		Refractive index $n$	Absorption index $k$
$d_1$	$d_2$		
0.43	0.67	2.533	0.00007
0.43	0.84	2.586	0.00006
0.43	1.60	2.876	0.00004
0.84	1.60	4.263	0.00004

one to believe that the theory is more restrictive. Second, the term "band" when applied to polymers is very perplexing to the novice due to the material's complex molecular makeup. The key point with regard to the paper is that the "band" used there is arbitrary. A third point is a suggestion for checking the theory. Have comparisons of  $n$  and  $k$  predicted by this theory been made for other materials (for example, quartz) whose transmission curves as well as  $n$  and  $k$  have previously been determined to a fair degree of accuracy?

As a matter of possible interest, we have applied the theory to the calculation of  $n$  and  $k$  for human skin. Although skin comes far short of being homogeneous, an accurate analysis is bypassed for being nearly hopeless. Some typical low-resolution transmission curves for skin<sup>3</sup> are given in Fig. 4. Preliminary results found by using the present theory are given in Table 4. The variation of  $n$  and  $k$  with thickness can be rationalized by the fact that the skin is comprised of varied layers, a gross inhomogeneity.

### Authors' Closure

The authors appreciate very much the comments by Professor Boehm and his application of the present theory to the calculation of band-averaged optical constants for human skin. Let us first answer the three specific points indicated in the discussion:

1 The theory presented here is indeed a very general one, but it is most useful for materials with distinctive band regions of complex spectral variations such as plastics.

2 The choice of appropriate band regions is not entirely arbitrary. Indeed, the degree of accuracy involved in the predictions by this theory depends on this choice. In the case of plastic materials, rather distinctive band regions are shown in Figs. 1 and 2, and are further indicated in Tables 1 and 2 by the large variations of the band-averaged optical constants over various bands.

3 We did not make any comparison for materials other than plastics, and do not see the need of such a comparison since the theory is on a sound footing and applies successfully to the complex spectrum of plastics.

With regard to the optical properties of human skin, it should be realized that they closely resemble the optical constants of water<sup>4</sup> since water is the major constituent of the skin.

<sup>3</sup> Hardy, J. D., Hammel, H. T., and Murgatroyd, D., "Spectral Transmittance and Reflectance of Excised Human Skin," *Journal of Applied Physiology*, Vol. 9, 1956, p. 261.

<sup>4</sup> Curcio, J. A., Stewart, H. S., and Petty, C. C., "Method for Determination of Flame Temperature from Emission in Ultraviolet OH Band," *Journal of the Optical Society of America*, Vol. 41, No. 3, Mar. 1951, pp. 173-179.

**K. R. CHUN**  
 Member, Senior Technical Staff,  
 Northrop Corporate Laboratories,  
 Hawthorne, Calif.  
 Assoc. Mem. ASME

## Some Experiments on Screen Wick Dry-out Limits

*Dry-out limits of screen wicks vertically pumping against gravity above an acetone pool were determined in evaporation experiments. As the pumping height shortened, the increase in heat input at dry-out became less than that expected from a fully saturated wick layer. The receding of the evaporating boundary into a sublayer of the wick was postulated, based on the fact that the measured thermal resistance across the wick layer decreased as heat input increased. Such a recess seems to terminate at two layers above the heated wall. A new wicking model taking into account the receding of evaporation boundary could predict the experimental dry-out heat inputs within 10 percent.*

### Introduction

ONE OF the limiting factors of heat transport capacity of heat pipes is believed to be bubble nucleation and subsequent drying of the evaporator wick [1, 2].<sup>1</sup> In ordinary pool boiling on a solid surface nucleation starts at the wall since nuclei are distributed on the heated surface and superheat is highest at the wall. In contrast, nucleation in porous media may not be necessarily at the heated wall despite the highest superheat there, since nuclei of a larger size (requiring lower superheat for activation) can exist away from the wall.

Ferrel et al. [3, 4] measured the thermal resistance across liquid-saturated packed beds of granular particles. An analysis of a model of the system led them to conclude that the liquid-vapor interface at which vaporization takes place is located neither at the top of the bed nor at the heated wall, but above a liquid layer approximately of bead radius thickness. In their study, beads of 30 to 50 mesh size were packed inside a container, and the liquid level was above the top layer of beads; the minimum bed thickness tested was  $1/8$  in. It was not conclusively established whether or not the criterion of the liquid film layer of bead radius thickness next to the wall would hold for smaller particles and a thinner bed.

In this paper, screen wicks of 200 mesh and 325 mesh with varying number of layers (2 ~ 12 layers) were tested in the pool boiling mode as well as in the vertical wicking mode with acetone as a working fluid to determine the influence of wall superheat on the maximum pumping capacity of evaporator wicks. The measurement of wall superheat indicates that, for a given wick, the wall superheat in pool boiling mode sets an upper limit to the

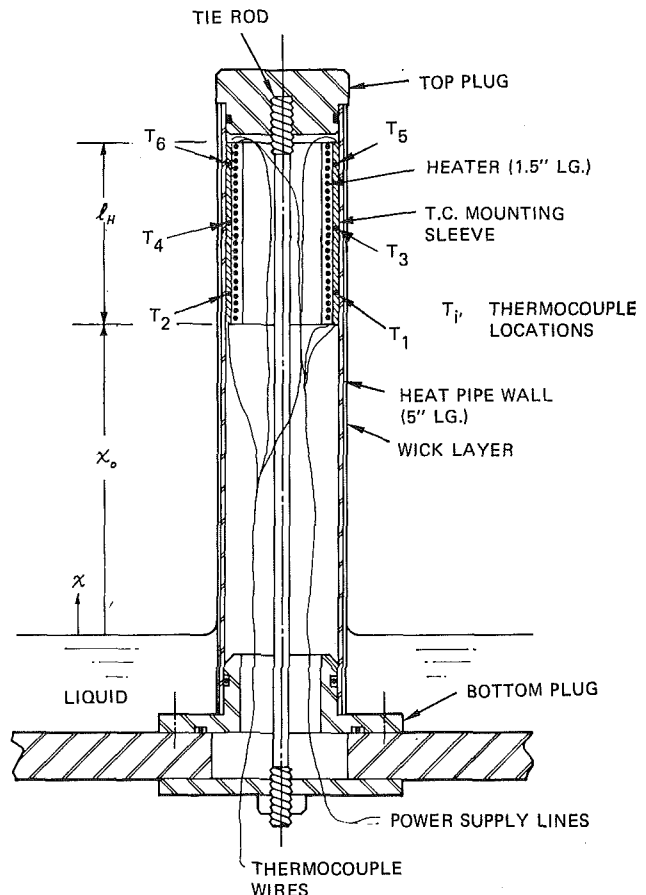


Fig. 1 Cross section of dry-out test rig

<sup>1</sup> Numbers in brackets designate References at end of paper.

Contributed by the Heat Transfer Division and presented at the Winter Annual Meeting, Washington, D. C., November 28-December 2, 1971, of THE AMERICAN SOCIETY OF MECHANICAL ENGINEERS. Manuscript received by the Heat Transfer Division February 28, 1971. Paper No. 71-WA/HT-6.

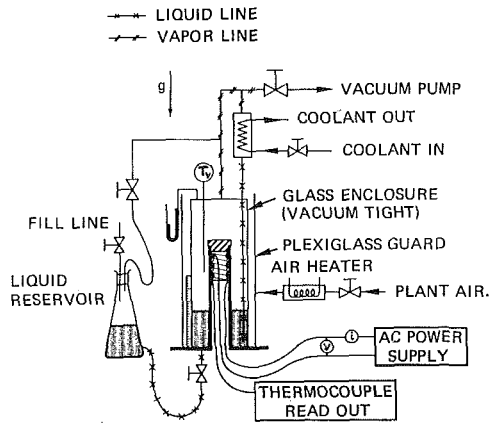


Fig. 2 Flow diagram of dry-out test setup

wall superheat in a wicking mode, and the liquid-vapor boundary recedes progressively to a sublayer of the wick as the heat flux is increased. On the basis of these observations, a new model for wick dry-out is proposed here to take into account the receding of the vapor-liquid boundary; the prediction by the model compares favorably with experimental dry-out limits.

### Experimental Setup and Procedure

A sketch of the test section is shown in Fig. 1. The sample wick is tightly wound outside of 1-in.-OD by 5-in.-long copper tube of 35-mil wall thickness and the wick is spot-welded along the seam. The screen was cleaned in acetone bath before and after winding. A 1.5-in.-long heater is fitted inside the pipe. Heating wire is wound around an oxide-coated, threaded aluminum cylinder. A copper sleeve fits between the heater OD and the pipe ID. The sleeve has vertical grooves in which three pairs of thermocouples (copper-constantan) were mounted flush with the OD of the sleeve. One pair is at the mid-height of the heater and others are at 0.5 in. above and below the middle pair. This assembly is mounted vertically inside a double-walled transparent enclosure with the heater side up. The liquid head  $x_0$  measured from the fluid level to the bottom of the heater is adjustable to any height by draining to the liquid reservoir, or the wick may be completely immersed under the working fluid. Fig. 2 shows the overall test setup.

The heater is turned on after the liquid is purged of non-condensable gas by opening the valve to the vacuum pump. The heat input to the system in the form of latent heat of vaporization is taken out at the condenser and the condensate is drained back to the liquid pool. Meanwhile, the coolant flow rate is adjusted so that the desired steady system pressure is attained. The

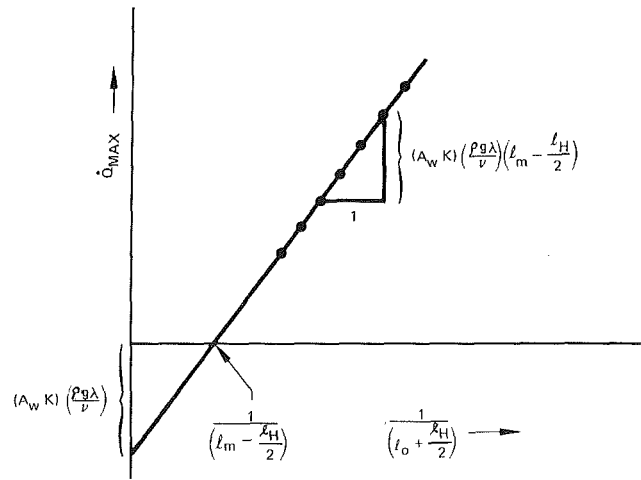


Fig. 3 Wick dry-out behavior based on equation (1)

measured vapor pressure and temperature are compared with the saturation value of acetone, and the saturated state is confirmed. After steady state is reached (at least 1.5 hr were allowed), the wall temperatures are measured at progressively lower liquid levels, first in the pool boiling mode, then the liquid level at the bottom of the heater, and at lower levels at 0.25-in. intervals (at least 30 min were allowed between successive liquid levels). The height  $x_0$  at which the temperature at the top thermocouples begins to rise is noted and designated as  $l_0$ . The same procedure is repeated at higher heat input. Consequently, one obtains for a given wick a series of values of the total wattage input coupled to a maximum pumping height before dry-out,  $l_0$ , and wall superheat.

After removing a few layers from the initial wick, the whole process is repeated.

The assumption of Darcy flow through a homogeneous wick fully saturated with working fluid results in the usual expression for the maximum pumping capability  $\dot{Q}_{max}$  for the wick shown in Fig. 1, where the capillary pumping pressure is just balanced by the sum of hydrostatic pressure drop and frictional pressure drop through the wick; for derivation, see equation (4).

$$\dot{Q}_{max} = (A_w K) \left( \frac{\rho g \lambda}{\nu} \right) \left( l_m - \frac{l_H}{2} \right) \frac{1}{l_0 + (l_H/2)} - (A_w K) \left( \frac{\rho g \lambda}{\nu} \right) \quad (1)$$

where

$A_w$  = wick cross-sectional area

### Nomenclature

$A_w$  = wick nominal cross-sectional area including solid and voids  
 $b$  = tortuosity; for Poiseuille flow,  $b = 8$   
 $D_c$  = equivalent capillary diameter derived from  $l_m$  by  $D_c = \frac{4\sigma}{\rho g l_m}$   
 $D_K$  = equivalent frictional diameter derived from  $K$  by  $D_K = \left( \frac{32K}{\epsilon} \right)^{1/2}$   
 $g$  = gravitational acceleration  
 $K$  = wick permeability as defined in equation (1)  
 $l_H$  = length of the heated zone  
 $l_m$  = static capillary rise height  
 $l_0$  = pumping distance from liquid level to the bottom of the heated zone at incipient dry-out  
 $M$  = constant mass flow rate in adiabatic zone  
 $\dot{m}$  = mass flow rate

$p_{sat}$  = saturation pressure  
 $\dot{Q}$  = heat input rate,  $\dot{Q} = \lambda M$   
 $\dot{Q}_{max}$  =  $\dot{Q}$  at incipient dry-out  
 $R_c$  = equivalent capillary pumping radius,  $\rho g l_m = \frac{2\sigma}{R_c}$   
 $T_w$  = temperature of the heated wall at the heater-wall interface  
 $T_{vap}$  = vapor temperature  
 $x$  = distance from the liquid level  
 $x_0$  =  $x$  to the bottom of the heated zone  
 $Y = (l_0 + 1/2 l_H)^{-1}$   
 $\delta$  = wick thickness  
 $\epsilon$  = porosity  
 $\lambda$  = latent heat of vaporization  
 $\phi$  = contact angle; for perfect wetting  $\phi = 0$   
 $\nu$  = kinematic viscosity  
 $\rho$  = density  
 $\sigma$  = surface tension

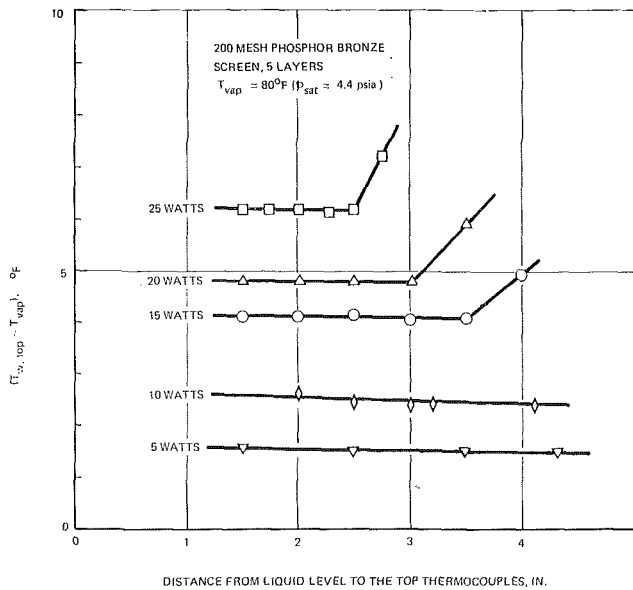


Fig. 4 Criterion of dry-out as indicated by sudden rise in temperature at the top pair of thermocouples

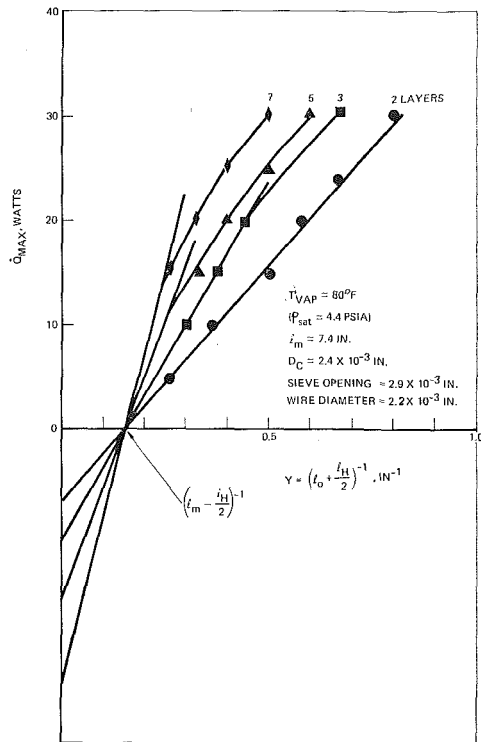


Fig. 5(a) Dry-out limits of 200 mesh phosphor bronze screen wicks in acetone

- $K$  = wick permeability
- $\rho$  = liquid density
- $g$  = gravitational acceleration
- $\lambda$  = latent heat of vaporization
- $\nu$  = kinematic viscosity
- $l_m$  = maximum height of liquid rise without heating

Based on equation (1) one would expect to obtain a linear relationship between  $\dot{Q}_{max}$  and  $[l_0 + (l_H/2)]^{-1}$  for the data as shown in Fig. 3. In fact, one could deduce wick properties such as  $l_m$  and  $K$  from such a plot.

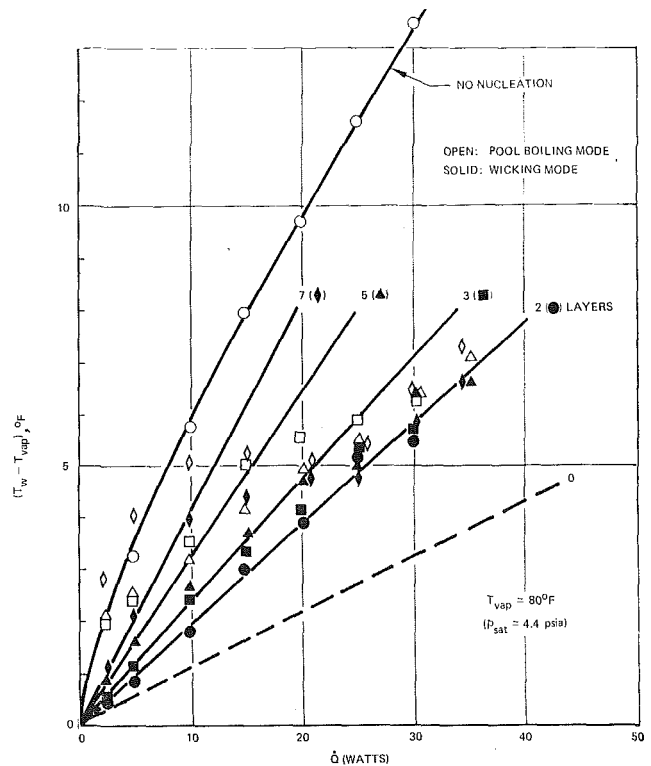


Fig. 5(b) Reduction of thermal resistance with increasing heat input (200 mesh)

## Experimental Results and Discussion

A typical temperature variation at the top pair of thermocouples as the distance from the liquid level is increased is shown in Fig. 4. A slight decrease in wall superheat with increasing pumping height is observable, probably due to the receding of the meniscus at higher pumping requirements. As the wicking height is increased further, the temperature at the top thermocouples rises rather abruptly. The pumping distance just before this rise is taken as the dry-out distance  $l_0$  at the given heat input. It should be mentioned that the indicated rise at the top in temperature is a steady one and seems to result from a partially dry wick rather than a completely dry one. When the test enclosure was completely drained of liquid but maintained at 4 ~ 5 psia vapor pressure, the wall temperature was more than 8.7 deg F above the vapor temperature at only 2 w heat input.

Fig. 5(a) shows the experimental dry-out data for 200 mesh phosphor bronze screen wicks as solid points. Straight lines are drawn through 2- and 3-layer data, and they are consistent with the nature of equation (1). Both lines intercept the  $Y$  axis at about 0.15, indicating the same equivalent capillary size  $R_c = 2\sigma/\rho g l_m$ , and slopes are in the same ratio as the number of wick layers, 2 to 3. The straight lines for 5 and 7 layers are drawn in by assuming the same  $l_m$  as in 2- and 3-layer wicks and increase in slope proportional to the number of layers involved. The actual data for 5- and 7-layer wicks fall below this line and this tendency grows with increasing  $\dot{Q}_{max}$  (or shorter pumping height).

Fig. 5(b) shows the plot of  $(T_w - T_{vap})$  versus total heat input  $\dot{Q}$ . The open points are data for the pool boiling mode (when the heated section is immersed under acetone) and solid points are for the wicking mode (the liquid level at the bottom of the heater). Each point represents the average of 6 thermocouple locations, and the temperature readings were within 10 percent of one another when no dry-out occurred.

A straight line through the solid points for the 2-layer wick indicates that a constant thermal resistance prevailed. When the wick was immersed completely in liquid, no nucleation was

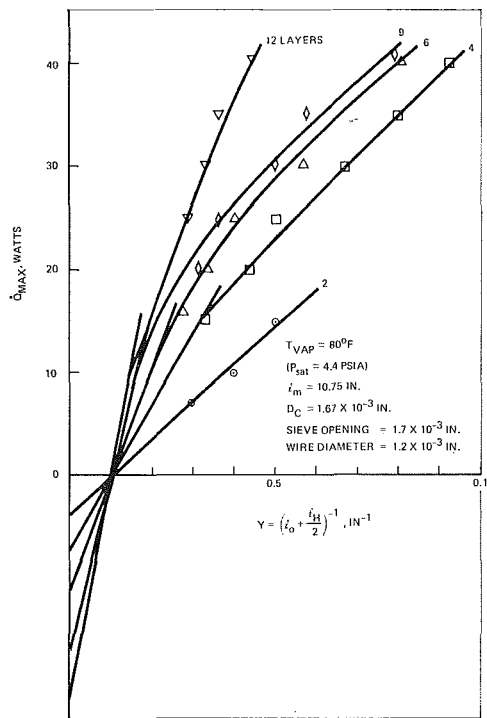


Fig. 6(a) Dry-out limits of 325 mesh phosphor bronze screen wick in acetone

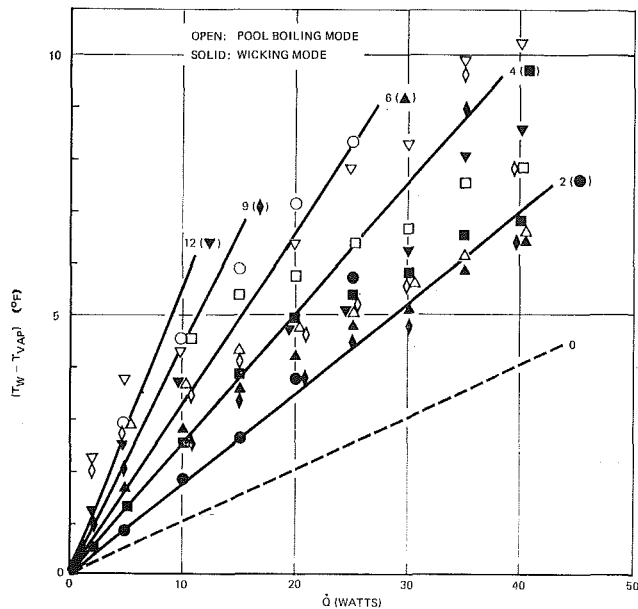


Fig. 6(b) Reduction of thermal resistance with increasing heat input (325 mesh)

observed. Wall superheat at a given heat input was much higher than that in a wicking mode due to the increased thermal layer of natural convection. One can conclude that, for the 2-layer wick in the wicking mode, there could not have been any nucleation. Thus the wick was fully saturated as evidenced by the constant thermal resistance.

Additional lines of constant thermal resistance are drawn in Fig. 5(b) for 3-, 5-, and 7-layer wicks based on wall superheat at low heat inputs; these lines are consistent with one another in relation to the number of layers involved. A dotted line corresponding to the resistance consisting of pipe wall thickness and contact resistance between the ID of the pipe and thermocouple junctions is an extrapolation to the zero layer from the wicking data.

Table 1 Summary of wick properties

Mesh	Sieve opening (mils)	Wire diam. (mils)	Porosity $\epsilon$ (%)	K ( $10^{-10} \text{ft}^2$ )	$D_c$ (mils)	$D_K$ (mils)	Tortuosity $b$
#200 Ph. Brz.	2.9	2.2	67	4.93	2.4	1.85	13.6
#200 Nickel by Kunz, et al. (2)	2.9	2.2	67	8.34	1.97	2.43	5.3
#325 Ph. Brz.	1.7	1.2	67	3.16	1.67	1.48	10.2

When the wick is operating in its wicking mode, wall superheat drops off the constant thermal resistance line as heat input is increased. The corresponding wall superheat in the pool boiling mode also drops off the "no-nucleation" line of the 2-layer wick, and fairly uniform nucleation was observed in almost all cases except at very low wattages. For all wick thicknesses the superheat in the pool boiling mode and the wicking mode both merge to the 2-layer line at higher heat inputs. Similar results for the 325 mesh screen wicks are shown in Figs. 6(a) and 6(b). (Merging to 2-layer temperature drop is not noted in 12- and 9-layer wicks.)

One could explain the dropping of wall superheat with nucleation on a wick layer by the same phenomena as in boiling on a solid surface, namely, cyclic cooling effect caused by bubble formation, departure, and subsequent onrush of cooler liquid to the surface. In wick boiling, however, the location of nuclei may not be necessarily at the wall and the intensity of liquid agitation near nuclei cannot be great due to the high flow friction in capillaries. Therefore, it is postulated here that, in wick boiling, the nucleation site and its density in effect cause the receding of the liquid-vapor boundary to the sublayer of the wick, and the wall superheat thereof is mainly the result of the average conductive resistance from the heated wall to this interface. In the wicking mode, the wall superheat is somewhat lower than that in nucleate pool boiling, presumably due to the absence of a liquid pool in the former; both approach the wall superheat equivalent to the 2-layer conduction path. In conclusion, the upper limit to the wall superheat that can be sustained in the wicking mode is set by the pool boiling mode, and the lower limit is set by the resistance equivalent to the first 2 layers next to the wall. A priori specification of the equivalent conduction layer thickness at a given heat flux is not possible at this time.

Table 1 summarizes the properties of wicks tested in the present work. Also included are the results given by Kunz et al. [2] for 200 mesh sintered nickel screen wick.  $D_K$  is defined as

$$D_K = \left( \frac{32K}{\epsilon} \right)^{1/2} \quad (\epsilon, \text{porosity})$$

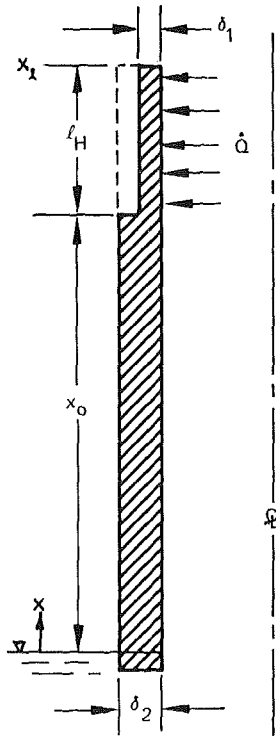
and represents the wick as a bundle of straight parallel tubes of diameter  $D_K$ . If one uses the concept of tortuosity  $b$ ,

$$b = \frac{\epsilon D_c^2}{4K}$$

or

$$b = 8 \left( \frac{D_c}{D_K} \right)^2$$

namely for straight capillary tubes,  $D_c = D_K$  and  $b = 8$  as in Poiseuille flow. Tortuosity should be greater than 8 in porous wicks. The values of  $K$  and  $D_c$  of this work were deduced from Figs. 5(a) and 6(a), while Kunz et al. measured  $D_c$  by mercury intrusion test and  $K$  by "pressure drop versus flow rate" measurement. The results for 200 mesh wick properties in this work indicate larger  $D_c$  and smaller  $K$  than those by Kunz et al. It is somewhat puzzling that the larger capillary size results in smaller permeability, even if one could expect somewhat smaller capillary size for sintered screen than that for a tightly wound wick. How-




 PORTION OF WICK CONTAINING FLUID

Fig. 7 "Step-wick" model with receded evaporation boundary at the heater

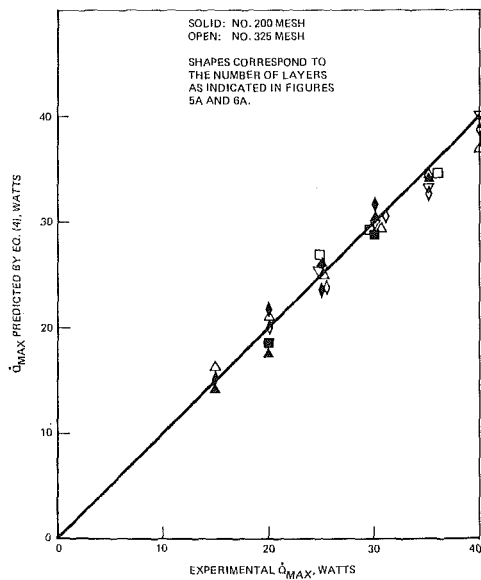


Fig. 8 Prediction by "step-wick" model

ever, the tortuosity values of the present work are larger than 8 and reasonable. The fact that the tortuosity given by Kunz et al. is less than 8 leaves some doubt as to their  $K$  value.

### "Step-Wick" Model

Fig. 7 describes the receding of the effective liquid-vapor boundary into the sublayer of the evaporator wick resulting in a step-shape wet section. The maximum heat input before dry-out based on this model can be estimated as follows.

Assuming Darcy flow in the wick,

Table 2 Prediction by equation (4) compared with experimental data

#200 mesh phosphor bronze screen $\lambda_m \approx 7.4$ in, $l_H = 1.5$ in.						
$\delta_2$ (layers)	$(\pi D \delta_2 K) \left( \frac{\rho g \lambda}{\nu} \right)$ (watts)	$\dot{Q}_{max}$ (watts)	$\delta_1$ (layers)	$\phi_0$ (in)	$\dot{Q}_{max}$ by eq. (4) (watts)	$\dot{Q}_{max}$ by eq. (1) (watts)
7 (23 mils)	24.5	30	2	1.10	32.0	88.3
		25	2	1.75	23.5	41.0
		20	3	2.25	22.0	30.0
		15	4	3.10	15.6	18.0
5 (17 mils)	17.5	35	2	0.75	34.3	60.5
		30	2	0.90	31.5	53.4
		25	2	1.25	26.2	41.0
		20	3	1.75	17.5	29.2
3 (10 mils)	10.5	30	2	0.75	29.0	36.2
		20	2	1.55	18.5	20.0
#325 mesh phosphor bronze screen $\lambda_m \approx 10.75$ in, $l_H = 1.5$ in.						
12 (33 mils)	23	40	3	1.5	40.0	79.2
		35	3	2.0	33.5	60.6
		30	3	2.25	30.3	53.6
		25	3	2.75	25.6	42.8
9 (25 mils)	17.3	40	2	0.5	39.0	121.0
		35	2	1.0	33.0	81.5
		30	2	1.25	30.0	69.1
		25	2	2.0	23.5	45.6
6 (17 mils)	11.5	40	2	0.5	37.0	80.5
		35	2	0.6	34.5	73.6
		30	2	1.0	29.2	54.2
		25	2	1.75	25.2	34.5
4 (12 mils)	7.7	40	2	0.35	37.0	62.3
		35	2	0.5	34.0	54.0
		30	2	0.75	29.0	43.6
		25	3	1.25	27.0	30.8

$$\dot{m} = \frac{\pi D \delta K}{\nu} \left[ \frac{d}{dx} \left( \frac{2\sigma}{R_c} \cos \phi \right) - \rho g \right] \quad (2)$$

where

$\dot{m}$  = total liquid flow rate at a given  $x$

$D$  = wick diameter

$\delta$  = wick thickness

$\sigma$  = surface tension

$R_c$  = capillary pumping radius,  $\rho g l_m = 2\sigma/R_c$

$\phi$  = wetting angle

For the adiabatic zone,  $0 < x < x_0$ ,

$\dot{m} = M$ , constant

$\delta = \delta_2$

For the uniformly heated zone,  $x_0 < x < x_1$ ,

$\dot{m} = M[(x_1 - x)/l_H]$

$\delta = \delta_1$

Integrating equation (2) from  $x = 0$  ( $\phi = \pi/2$ ) to  $x = x_0$  ( $\phi = \phi_0$ ),

$$\cos \phi_0 = \left( M x_0 \frac{\nu}{\pi D \delta_2 K} + \rho g x_0 \right) \frac{R_c}{2\sigma} \quad (3)$$

Integrating equation (2) from  $x_0$  to  $x_1$  ( $\phi = 0$  at maximum pumping)

$$\dot{Q}_{max} = (\pi D \delta_2 K) \left( \frac{\rho g \lambda}{\nu} \right) \left\{ l_m - l_H \left( 1 - \frac{\delta_2}{2\delta_1} \right) \right\} \times \left[ l_0 + \frac{\delta_2}{\delta_1} \frac{l_H}{2} \right]^{-1} - (\pi D \delta_2 K) \left( \frac{\rho g \lambda}{\nu} \right) \quad (4)$$

When  $\delta_2 = \delta_1$ , equation (4) reduces to equation (1).

Taking  $\delta_1$  to be equal to the thermal resistance thickness as indicated in Figs. 5(b) and 6(b), new values of  $\dot{Q}_{\max}$  can be estimated by equation (4), and these predictions are compared with experiments in Table 2 and Fig. 8. The last column of Table 2 shows  $\dot{Q}_{\max}$  by equation (1) if the evaporator wick is assumed fully wet.

## Conclusions

The dropping in thermal resistance across the wick as the heat input is raised led to the "step-wick" model in which the effective liquid-vapor boundary recedes to a sublayer of the wick at the evaporator. The model predicts within 10 percent of the experimental dry-out heat inputs which are far below the values which would be expected if the evaporator wick were fully saturated with liquid. Even though the location of the liquid-vapor boundary within the wick cannot be predicted, it terminated at 2 layers above the wall in most cases of the present work.

The upper limit to the wall superheat that can be sustained in the wicking mode is set by the pool boiling mode and the lower

limit by the thermal resistance equivalent to the first 2 layers next to the wall.

## Acknowledgment

This research was supported by Northrop Corporate Laboratories, Northrop Corporation.

## References

- 1 Cotter, T. P., "Theory of Heat Pipes," LA 3264 MS, Los Alamos Scientific Laboratory, Los Alamos, N. Mex., March 1965.
- 2 Kunz, H. R., Langston, L. S., Hilton, B. H., Wide, S. S., and Nashick, G. H., "Vapor Chamber Fin Studies," NASA CR-812, June 1967.
- 3 Ferrel, J. K., and Alleavitch, J., "Vaporization Heat Transfer in Capillary Wick Structures," AIChE Reprint 6, presented at the Eleventh National Heat Transfer Conference, Minneapolis, Minn., Aug. 3-6, 1969.
- 4 Ferrel, J. K., and Johnson, H. R., "The Mechanism of Heat Transfer in the Evaporator Zone of a Heat Pipe," ASME Paper No. 70 HT/SpT-12, presented at the ASME Space Technology and Heat Transfer Conference, Los Angeles, Calif., June 21-24, 1970.

**M. IQBAL**

Associate Professor,  
Department of Mechanical Engineering,  
University of British Columbia,  
Vancouver, B. C., Canada.  
Mem. ASME

**B. D. AGGARWALA**

Associate Professor,  
Department of Mathematics,  
University of Calgary,  
Calgary, Alb., Canada

**A. K. KHATRY**

Graduate Student,  
Department of Mechanical Engineering,  
University of British Columbia,  
Vancouver, B. C., Canada

## On the Conjugate Problem of Laminar Combined Free and Forced Convection through Vertical Non-Circular Ducts

*The present analysis deals with the conjugate problem of combined free and forced convection through vertical non-circular ducts. The equations coupling heat conduction in the walls with the convection inside the fluid are solved to establish the influence of peripheral wall conduction, using variational technique. Fully developed laminar flow with uniform axial heat input and constant fluid properties, except for the small variation of density in the buoyancy term of the momentum equation, is assumed. The problem has been solved in a generalized way and the results have been presented for rectangular ducts. It is found that large values of the free convection effects and/or of the conduction parameter tend to minimize the asymmetries in circumferential wall temperature.*

### Introduction

IN FLOW and heat transfer through non-circular ducts, two of the thermal boundary conditions applied are (i) uniform wall temperature or (ii) uniform heat input per unit length.

The condition (i) normally implies uniform wall temperature in the flow direction as well as transverse to it. This condition can be achieved by having a condensing fluid on the outside of the duct.

The condition (ii) is achieved in fully developed constant-property flows when the duct wall contains heat sources, for instance. In fully developed constant-property flows, this produces linearly varying wall temperature in the flow direction. In non-circular ducts, as the fluid near the corners is slowed down due to viscous effects, it has inherent ability to pick up less heat from the corner regions and increases temperature levels of those areas. However, it is possible to control the circumferential asymmetries by controlling the wall thickness and its thermal conductivity. Essentially three situations may arise under the condition (ii). The two limiting situations will be: (iia) when the wall thermal conductivity is assumed infinite, the wall temperature becomes uniform circumferentially, and (iib) when the wall thermal conductivity is assumed zero, the heat flux becomes uniform circumferentially. However, a physically realistic situation will be: (iic) when the wall thermal conductivity has a non-zero

finite value, so that neither the heat flux nor the wall temperature will be uniform circumferentially.

Numerous studies of condition (iia) for the fully developed laminar forced convection, as well as laminar combined free and forced convection, are available in the literature, references [1-4]<sup>1</sup> for instance. While some studies [5-7] of fully developed laminar forced convection are available for (iib), very little is known [8, 9] about this problem when free convection effects are superimposed.

In non-circular ducts, when the wall has a non-zero finite thermal conductivity and thickness, the analysis of heat transfer becomes very complex. In this situation, neither the temperature nor the temperature gradients at the wall can be prescribed, and as such it is called the conjugate problem [10-11].

Siegel and Savino [12]<sup>2</sup> have presented an exact solution of fully developed laminar forced convection through rectangular ducts when two parallel sides are under conjugate condition and the two remaining parallel sides are insulated. An exact treatment would become extremely complicated if the conjugate conditions were imposed on all four sides. Additional inclusion of buoyancy effects when the velocity field gets coupled with the temperature field would further complicate the analysis.

In the present report, fully developed combined free and forced convection through vertical ducts is treated for conjugate conditions existing throughout the boundary. A general solution by variational calculus is obtained for arbitrarily shaped ducts and results are presented for rectangular ducts.

Contributed by the Heat Transfer Division for publication (without presentation) in the JOURNAL OF HEAT TRANSFER. Manuscript received by the Heat Transfer Division April 16, 1971. Paper No. 71-HT-Q.

<sup>1</sup> Numbers in brackets designate References at end of paper.

<sup>2</sup> During the review process, one of the reviewers has pointed out that this work has been extended [13] to include the effects of peripheral wall conduction on all four sides.



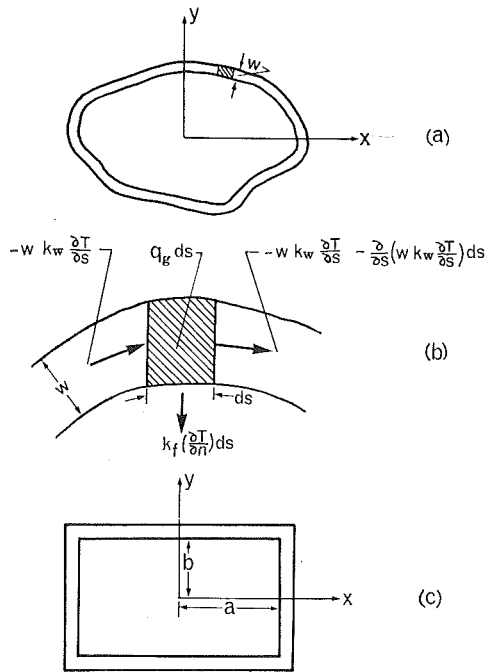


Fig. 1 Coordinate system and analytical model

## Formulation of the Problem

Consider fully developed laminar flow through a straight vertical duct of arbitrary shape but of uniform wall thickness  $w$ , Fig. 1(a). The wall thermal conductivity may vary from zero to infinity. However, the wall conduction effects in the direction parallel to the duct axis are considered negligible. The flow is in the vertical upward direction along the positive  $z$  axis. The duct receives uniform heat input per unit length in the flow direction. This energy input may be considered as through uniformly distributed heat sources in the wall. All fluid properties are assumed constant except for variation of density in the buoyancy term of the momentum equation. Viscous dissipation and pressure work terms in the energy equation are ignored. The fluid may contain uniform heat sources. Under the above idealizations, the governing equations of motion and energy in the non-dimensional form can be written [3, 4] as

$$\nabla^2 V + \text{Ra} \phi = -L, \quad (1)$$

$$\nabla^2 \phi - V = -F. \quad (2)$$

The condition of no-slip at the wall gives

$$V = 0 \quad \text{at the wall.} \quad (3)$$

The buoyancy rates have been evaluated with reference to the

temperature at a point on the wall where the temperature difference is considered zero. Therefore one of the thermal boundary conditions is

$$\phi = 0 \quad \text{on a prescribed point at the wall.} \quad (4)$$

In order to develop the second thermal boundary condition, from Fig. 1(b), we write the thermal energy balance over the small shaded element. Neglecting temperature gradients across the wall thickness, and assuming thermal conductivity of the wall to be invariant with temperature, we get

$$\kappa_f \left( \frac{\partial T}{\partial n} \right) dS = q_g dS + w \kappa_w \frac{\partial}{\partial S} \left( \frac{\partial T}{\partial S} \right) dS. \quad (5)$$

On nondimensionalizing (5), one obtains

$$\frac{\partial \phi}{\partial N} = C_2 + K \frac{\partial^2 \phi}{\partial S^2} \quad \text{at the wall,} \quad (6)$$

where  $C_2 = 0.25(1 - F)$  and the factor 0.25 in it automatically appears after the nondimensionalizing process.

In (3), (4), and (6), by "at the wall," we mean inner side of the wall. In (6),  $K = w \kappa_w / D_h \kappa_f$  is a prescribed constant whose value theoretically may vary from zero to infinity. The constant  $K$  controls the circumferential variation of wall temperature and heat flux. This constant is a ratio of the circumferential conduction along the duct wall to that of normal conduction into the fluid and is in fact the ratio of the local Nusselt number to the Biot number.

Except of a circular duct, an exact solution of (1)–(4) and (6) appears to be extremely complex. For a circular duct, the temperature and heat flux become circumferentially constant and the solutions are available in references [14, 15]. We present a variational solution of the problem at hand.

## Solution

In [4], we have given a variational formulation for the problem of combined free and forced convection with uniform peripheral wall temperature. The problem was to solve equations (1) and (2) of this paper with  $V = \phi = 0$  at the boundary. Without repeating the detailed variational formulation given in [4], we may say that the functional which has to be made stationary for that problem was given by

$$I = \iint \left[ \left( \frac{\partial V}{\partial X} \right)^2 + \left( \frac{\partial V}{\partial Y} \right)^2 \right] dXdY - \text{Ra} \iint \left[ \left( \frac{\partial \phi}{\partial X} \right)^2 + \left( \frac{\partial \phi}{\partial Y} \right)^2 \right] dXdY - \text{Ra} \iint V \phi dXdY + 2\text{Ra} \iint F \phi dXdY - 2L \iint V dXdY. \quad (7)$$

Our interest is now to proceed from (7) to develop a variational expression to take into account the condition (6).

## Nomenclature

$A$  = area of cross section  
 $C_p$  = specific heat of the fluid at constant pressure  
 $C_1$  =  $\partial T / \partial z$ , temperature gradient in flow direction  
 $C_2$  =  $0.25(1 - F)$   
 $D_h$  = hydraulic diameter = (4 · cross-sectional area) / (heat transfer perimeter)  
 $F$  =  $Q / \rho C_p C_1 U$ , heat generation parameter, dimensionless  
 $g$  = gravitational acceleration  
 $K$  =  $w \kappa_w / D_h \kappa_f$ , conduction parameter, dimensionless

$L$  = pressure drop parameter, dimensionless  
 $\text{Nu} = h D_h / \kappa_f$ , Nusselt number, dimensionless  
 $\text{Ra} = (\rho^2 g C_p C_1 \beta D_h^4) / \kappa_f \mu$ , Rayleigh number, dimensionless  
 $Q$  = heat generation rate in the fluid  
 $S$  = circumference of duct  
 $q_g$  = heat generation rate in wall per unit area  
 $T$  = temperature  
 $u$  = axial velocity  
 $U$  = average axial velocity

$V = u / U$ , dimensionless axial velocity  
 $w$  = wall thickness  
 $z$  = axial coordinate in flow direction  
 $\gamma = (T - T_w)$  or  $(T - T_{\text{apex}})$   
 $\phi = \gamma / \left[ \frac{\rho U C_p C_1 D_h^2}{\kappa_f} \right]$ , dimensionless temperature function  
 $\beta, \rho, \mu$  = fluid properties in standard notation  
 $\kappa_f$  = fluid thermal conductivity  
 $\kappa_w$  = wall thermal conductivity

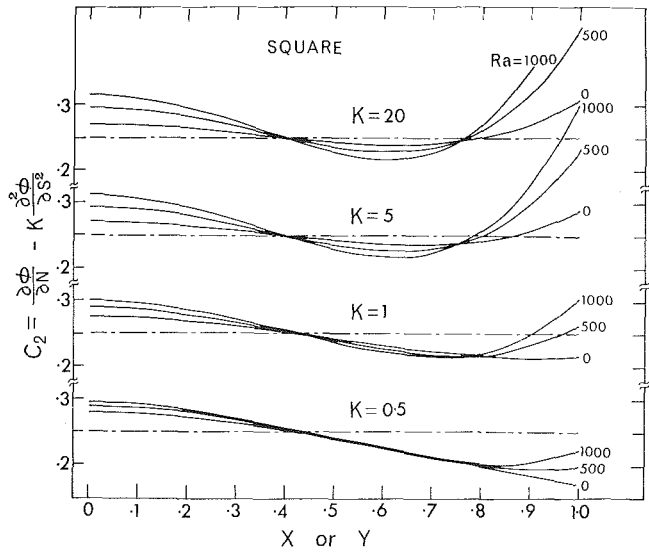


Fig. 2 Variation of  $C_2$  along the boundary of a square duct for different values of  $K$  and  $Ra$

For expression (7) we have

$$\begin{aligned} \delta I = & -2 \iint (\nabla^2 V + Ra\phi + L)\delta V dXdY \\ & + 2Ra \iint (\nabla^2 \phi - V + F)\delta \phi dXdY \\ & + 2 \int_S \delta V \frac{\partial V}{\partial N} dS - 2Ra \int_S \delta \phi \frac{\partial \phi}{\partial N} dS. \end{aligned} \quad (8)$$

For the problem at hand, that is, equations (1), (2), (3), and (6), we assume that the trial functions satisfy equation (3). All terms in  $\delta I$  now vanish except the last. To make this term vanish, we modify  $\delta I$  and write it as

$$\begin{aligned} \delta I = & -2 \iint (\nabla^2 V + Ra\phi + L)\delta V dXdY \\ & + 2Ra \iint (\nabla^2 \phi - V + F)\delta \phi dXdY \\ & + 2 \int_S \delta V \frac{\partial V}{\partial N} dS - 2Ra \int_S \delta \phi \left( \frac{\partial \phi}{\partial N} - C_2 - K \frac{\partial^2 \phi}{\partial S^2} \right) dS. \end{aligned} \quad (9)$$

and correspondingly write  $I$  as

$$\begin{aligned} I = & \iint \left[ \left( \frac{\partial V}{\partial X} \right)^2 + \left( \frac{\partial V}{\partial Y} \right)^2 \right] dXdY \\ & - Ra \iint \left[ \left( \frac{\partial \phi}{\partial X} \right)^2 + \left( \frac{\partial \phi}{\partial Y} \right)^2 \right] dXdY \\ & - 2Ra \iint V \phi dXdY + 2Ra \iint F \phi dXdY - 2L \iint V dXdY \\ & + 2Ra \int_S C_2 \phi dS - Ra \int_S K \left( \frac{\partial \phi}{\partial S} \right)^2 dS. \end{aligned} \quad (10)$$

Functions  $V$  and  $\phi$ , which make  $I$  stationary, will give the solution to our problem.

It is obvious from the form of  $\delta I$ , equation (9), that the trial functions do not have to satisfy exactly condition (6) at the boundary.

Once the velocity and temperature functions are known, the hot spots on the wall can be located. The overall heat transfer to the fluid expressed by the Nusselt number can be evaluated.

Nusselt number in terms of dimensionless velocity and temperature functions can be written as

$$Nu = \frac{1 - F}{4 \left[ \frac{1}{S} \int_S \phi_{wall} dS - \phi_{mx} \right]}, \quad (11)$$

where  $\phi_{mx}$ , the cup-mixing bulk temperature, is given by

$$\phi_{mx} = \frac{\iint V \phi dA}{\iint V dA}. \quad (12)$$

Actual computational process requires selection of functions  $V$  and  $\phi$  with a number of arbitrary coefficients. The form of the function  $V$  has to be chosen in such a way that it vanishes at the boundary to satisfy (3). However, the form of  $\phi$  should be such that in itself it should not vanish at the boundary. For large values of  $K$ , when wall conduction dominates, it is, however, expected that the numerical values of the arbitrary coefficients in  $\phi$  will come out to be such that  $\phi$  might vanish at the boundary. For the rectangular duct, Fig. 1(c), the functions  $V$  and  $\phi$  were chosen in the following form:

$$V = f_b(A_0 + A_1 X^2 + A_2 Y^2 + A_3 X^4 + A_4 Y^4 + A_5 X^2 Y^2), \quad (13)$$

$$\begin{aligned} \phi = & B_0 + B_1 X^2 + B_2 Y^2 + B_3 X^4 + B_4 X^2 Y^2 + B_5 Y^4 \\ & + B_6 X^6 + B_7 X^4 Y^2 + B_8 X^2 Y^4 + B_9 Y^6. \end{aligned} \quad (14)$$

The factor  $f_b$  in (13) is equation of the boundary for a rectangular duct and can be written as

$$f_b = (a^2 - X^2) \cdot (b^2 - Y^2) \quad (15)$$

Equation (15) insures that  $f_b = 0$  and hence  $V = 0$  when  $X = \pm a$ ,  $Y = \pm b$ .

In the present analysis, (13) and (14) were limited to six and ten coefficients respectively. Inserting (13) and (14) in (10) and carrying out the minimization process with respect to these coefficients, one obtains 16 algebraic equations in 17 unknowns,  $L$  being still an unknown. The 17th equation is provided by (4). This completes the solution details. We will now discuss some results of this analysis. In the numerical computations, we have taken  $F = 0$  throughout.

## Discussion

When the conduction parameter  $K$  becomes very large, the wall temperature will tend to become uniform. On the other hand as the value of  $K$  approaches zero, the wall heat flux becomes circumferentially uniform. For the former case ( $K \rightarrow \infty$ ), the results of the present analysis for rectangular ducts should be compared with those of Han [16]. Han has presented an exact solution of (1)-(3) for rectangular ducts under uniform circumferential wall temperature condition. Table 1 contains such a comparison of the Nusselt number values for a square duct. The values of  $K$  used in this table are those which give results close to those of Han. It may be noted in this table that for forced convection,  $Ra = 0$ , a very high value of the conduction parameter ( $K = 100$ ) gives results close to those of Han. As the Rayleigh number is increased, smaller values of  $K$  are required to produce the effect of almost uniform circumferential wall temperature. This last observation is in accordance with the result of [8], where it is shown that high values of the buoyancy parameter tend to produce rotational symmetry of temperature and heat flux in non-circular ducts.

In Table 1, the Nusselt numbers involved the integrated values of the temperature function. Although the Nusselt numbers have come out to be very accurate, it will be interesting to observe how closely the temperature function satisfies the condition (6). In Fig. 2, for a square duct, we have shown the variation of  $C_2$  from the desired value of 0.25. It appears that the calculated values of  $C_2$  fluctuate about its desired value along the duct circumference. At lower values of  $K$ , buoyancy rates have little influence on the variation of  $C_2$ . However, at higher values of  $K$ ,

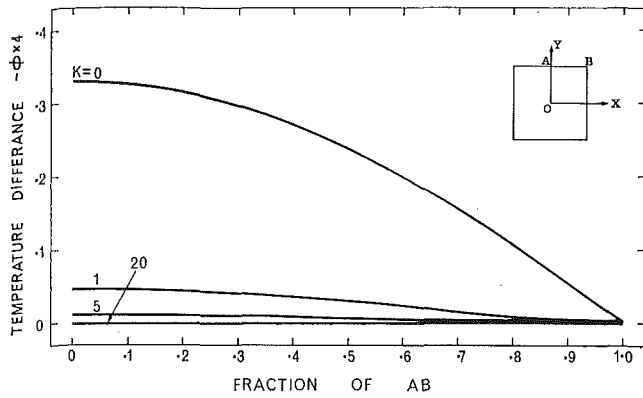


Fig. 3 Temperature difference  $\phi$  for different values of  $K$  along the boundary of a square duct at  $Ra = 1000$

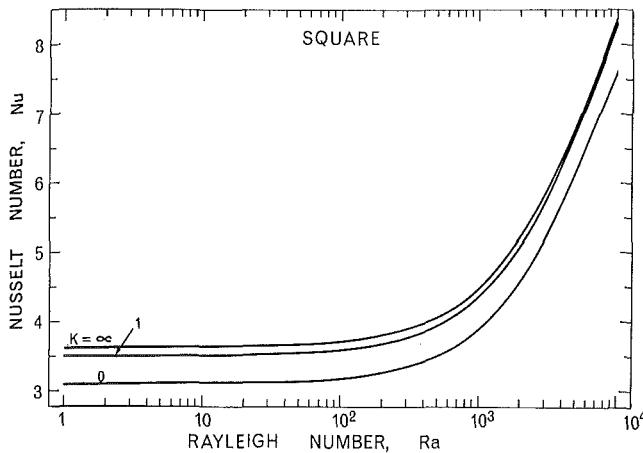


Fig. 4 Nusselt number variations of a square duct for different values of  $K$  against Rayleigh numbers

Table 1 The conduction parameter  $K$  and Rayleigh numbers which give values of Nusselt numbers close to those of Han [16]

Ra	Circumferential Conduction Parameter $K$						Han [16]
	3	4	5	7	20	100	
0						3.6059	3.6078
100						3.6950	3.6986
500						4.0490	4.0491
1000					4.4589		4.4579
2000				5.1822			5.1816
3000			5.7988				5.7943
4000		6.3225					6.3158
5000	6.7632						6.7642
6000	7.1594						7.1547

the buoyancy effects become pronounced and so do the corner effects.

For  $Ra = 0$  and  $K > 0$ , it is also possible to compare the results of the present analysis with those of [13]. Table 2 presents the values of temperature differences for a square duct as obtained from the present analysis and they agree very closely with the values presented in Fig. 6 of reference [13].

In order to demonstrate the effect of  $K$  on circumferential wall temperature, Fig. 3 shows the variation of wall temperature difference  $\phi$  against various values of  $K$ . This figure is for a square duct and  $Ra = 1000$ . It is clearly evident from this diagram that as  $K$  increases, the wall temperature rapidly tends to become uniform. At  $K = 20$ ,  $\phi$  is almost equal to zero throughout the circumference. At values of  $Ra$  greater than 1000,  $\phi$  becomes

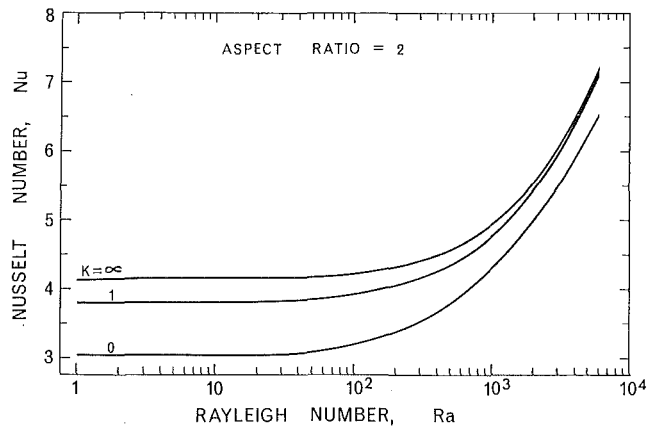


Fig. 5 Nusselt number variations of a rectangular duct with aspect ratio = 2 for different values of  $K$  against Rayleigh number

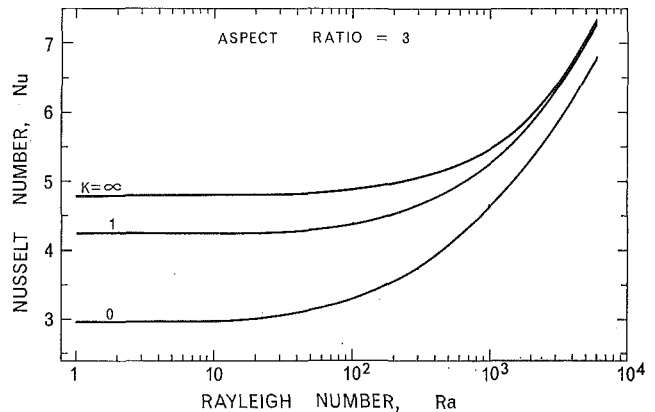


Fig. 6 Nusselt number variations of a rectangular duct with aspect ratio = 3 for different values of  $K$  against Rayleigh number

Table 2 Calculated values of  $(\phi_{wall} - \phi_{mx})/4$  along the boundary of a square duct at  $Ra = 0.0$

X or Y	$(\phi_{wall} - \phi_{mx})/4$					
	$K = 0$	0.1	0.5	1	5	25
0.0	0.20680	0.22560	0.25203	0.26185	0.27349	0.27643
0.1	0.21065	0.22865	0.25359	0.26281	0.27373	0.27648
0.2	0.22216	0.23770	0.25821	0.26565	0.27442	0.27662
0.3	0.24114	0.25241	0.26565	0.27022	0.27553	0.27686
0.4	0.26725	0.27221	0.27554	0.27628	0.27700	0.27716
0.5	0.30003	0.29629	0.28732	0.28348	0.27875	0.27753
0.6	0.33882	0.32356	0.30026	0.29133	0.28065	0.27793
0.7	0.38275	0.35261	0.31340	0.29922	0.28254	0.27832
0.8	0.43069	0.38173	0.32556	0.30637	0.28423	0.27867
0.9	0.48124	0.40880	0.33530	0.31183	0.28544	0.27892
1.0	0.53261	0.43127	0.34086	0.31442	0.28588	0.27900

almost zero on the circumference at values of  $K$  lower than those shown in Fig. 3.

A general variation of Nusselt number against Rayleigh number with  $K$  as a parameter is shown in Figs. 4 to 6. These figures are for aspect ratios 1, 2, and 3 respectively. These figures show that as the aspect ratio increases, the effect of  $K$  parameter on the Nusselt number becomes more important. In these three figures, for  $K \rightarrow \infty$ , the Nusselt number values agree very closely to those of Han. For the situation equivalent to  $K = 0$  (uniform circumferential wall heat flux) published literature contains Nusselt number information only for the square duct, Fig. 4, and these values agree with those given in [8].

In conclusion, it may be added that the variational solution presented here is indeed very accurate. The circumferential wall conduction is more important for low values of the buoyancy parameter and low values of the conduction parameter. Higher values of either of these parameters tend to minimize asymmetries in circumferential wall temperature.

### Acknowledgment

Financial support of the National Research Council of Canada is gratefully acknowledged.

### References

- 1 Eckert, E. R. G., Irvine, T. F., Jr., and Yen, J. T., "Local Laminar Heat Transfer in Wedge-Shaped Passages," *TRANS. ASME*, Vol. 80, 1958, pp. 1433-1438.
- 2 Tao, L. N., "On Some Laminar Forced-Convection Problems," *JOURNAL OF HEAT TRANSFER*, *TRANS. ASME*, Series C, Vol. 83, No. 4, Nov. 1961, pp. 466-472.
- 3 Aggarwala, B. D., and Iqbal, M., "On Limiting Nusselt Number from Membrane Analogy for Combined Free and Forced Convection Through Vertical Ducts," *International Journal of Heat and Mass Transfer*, Vol. 12, 1969, pp. 737-748.
- 4 Iqbal, M., Aggarwala, B. D., and Fowler, A. G., "Laminar Combined Free and Forced Convection in Vertical Non-Circular Ducts Under Uniform Heat Flux," *International Journal of Heat and Mass Transfer*, Vol. 12, 1969, pp. 1123-1139.
- 5 Tao, L. N., "The Second Fundamental Problem in Heat Transfer of Laminar Forced Convection," *Journal of Applied Mechanics*, *TRANS. ASME*, Series E, Vol. 84, No. 2, June 1962, pp. 415-420.
- 6 Yen, J. T., "Exact Solution of Laminar Heat Transfer in

Wedge-Shaped Passages with Various Boundary Conditions," Wright Air Development Center, Technical Report 57-224, July 1957.

7 Sparrow, E. M., and Haji-Sheikh, A., "Flow and Heat Transfer in Ducts of Arbitrary Shape With Arbitrary Thermal Boundary Conditions," *JOURNAL OF HEAT TRANSFER*, *TRANS. ASME*, Series C, Vol. 88, No. 4, Nov. 1966, pp. 351-358.

8 Iqbal, M., Ansari, S. A., and Aggarwala, B. D., "Effect of Buoyancy on Forced Convection in Vertical Regular Polygonal Ducts," *JOURNAL OF HEAT TRANSFER*, *TRANS. ASME*, Series C, Vol. 92, No. 2, May 1970, pp. 237-244.

9 Iqbal, M., Khairy, A. K., and Aggarwala, B. D., "On the Second Fundamental Problem of Laminar Combined Free and Forced Convection through Vertical Non-Circular Ducts," Report No. ME-70-12, Department of Mechanical Engineering, University of British Columbia, Vancouver, B. C., Canada, 1970.

10 Perelman, T. L., "On Conjugated Problems of Heat Transfer," *International Journal of Heat and Mass Transfer*, Vol. 3, 1961, pp. 293-303.

11 Davis, E. J., and Gill, W. N., "The Effects of Axial Conduction in the Wall on Heat Transfer with Laminar Flow," *International Journal of Heat and Mass Transfer*, Vol. 13, 1970, pp. 459-470.

12 Siegel, R., and Savino, J. M., "An Analytical Solution of the Effect of Peripheral Wall Conduction on Laminar Forced Convection in Rectangular Channels," *JOURNAL OF HEAT TRANSFER*, *TRANS. ASME*, Series C, Vol. 87, No. 1, Feb. 1965, pp. 59-66.

13 Savino, J. M., and Siegel, R., "Extension of an Analysis of Peripheral Wall Conduction Effects for Laminar Forced Convection in Thin-Walled Rectangular Channels," NASA TND-2860, June 1965.

14 Hallman, T. M., "Combined Forced and Free-Laminar Heat Transfer in Vertical Tubes With Uniform Internal Heat Generation," *TRANS. ASME*, Vol. 78, 1956, pp. 1831-1841.

15 Morton, B. R., "Laminar Convection in Uniformly Heated Vertical Pipes," *Journal of Fluid Mechanics*, Vol. 8, 1960, pp. 227-240.

16 Han, L. S., "Laminar Heat Transfer in Rectangular Channels," *JOURNAL OF HEAT TRANSFER*, *TRANS. ASME*, Series C, Vol. 81, No. 2, May 1959, pp. 121-128.

C. C. COX  
Professor.

D. F. DYER  
Professor.  
Assoc. Mem. ASME

Department of Mechanical Engineering  
Auburn University,  
Auburn, Ala.

## Freeze-Drying of Spheres and Cylinders

*A quasi-steady analysis is presented for freeze-drying spheres and cylinders of beef, taking into account the diffusional and bulk flow of a binary gas mixture inside the food product. A variation in the interface temperature is accounted for by solving the mass-transfer equations with property data from previous investigations. This analysis involves the solution of the coupled equations of continuity, momentum, energy, and specie concentration. The effects of controllable freeze-drying parameters are considered. Drying times for the two models are compared. The interface position and temperature are calculated. Drying time is predicted as a function of chamber condition and particle size. Typical temperature profiles in the product are given. The diffusional contribution to the total flow is determined. Results indicate that drying time increases with chamber pressure and chamber water concentration, and with the square of the diameter of the particle. The interface temperature increases nonlinearly during drying. More than half the total flow is found to be diffusional under some chamber conditions.*

### Introduction

FREEZE-DRYING is a preservation technique in which the removal of a water substance from its containing matrix is effected by sublimation. The commercial advantages of this method of drying are: long shelf-life, no refrigeration requirement, weight reduction, pleasing market appearance, and good re-hydration properties.

The process is used in the food industry for cooked, fresh, and frozen foods. Freeze-drying is also utilized in preparing drugs and storing whole blood. In addition, this versatile technique is employed in pollution studies, germ-warfare research, and taxidermy. Recently, cut flowers retained their fresh appearance for months when freeze-dried.

Several investigations [1-7]<sup>1</sup> approach the heat- and mass-transfer problems of sublimation dehydration analytically. The emphasis on slab geometries is apparent. The majority of the literature related to particle-bed drying concerns process information. In this category, Cotson and Smith [8] give explicit instructions in the preparation, freeze-drying, and re-hydration of diced chicken, peas, carrots, and minced meats. Blair [9] emphasizes the importance of temperature and pressure control in drying particulate foodstuffs. Smithes [10] makes a similar report for ground beef. Blanching effects on peas to be dried in beds are discussed by Moyer et al. [11], who show that the blanching should be done by steam under pressure. Foda et al. [12] discuss process operation in the freeze-drying of green beans, and Dellamonica and McDowell [13] give a similar experimental

study related to diced carrots. Lusk et al. [14] present the effect of platen temperature, freezing temperature, and chamber pressure on drying beds of shrimp. The storage quality of products such as peas, carrots, and chicken pieces dried in beds is discussed by Swalin [15]. Lawler [16] presents a discussion of accelerating the freeze-drying of diced chicken and gives a survey of European equipment for drying food pieces.

There have been several experimental studies of particulate drying. Seltzer [17] shows that in some cases increasing the number of layers of particulated product only requires a proportionate increase in drying time rather than an increase proportional to the square of the thickness predicted by slab equations. A basic problem in the proper analysis of particulate drying is the determination of the thermal conductivity. Schotte [18] has developed a correlation to predict thermal conductivity of packed beds under various conditions of pressure, temperature, and particle size. Saravacos and Charm [19] give data for the air-drying of particle beds. Although [19] does not deal directly with freeze-drying, the mechanisms discussed in that paper may be relevant to this process. Scotland's Ministry of Agriculture, Fisheries, and Food [20] gives limited data concerning the effect of particle size and tray loading on freeze-drying rates. Forrest [21] elaborates on the data given in [20]. The effects of chamber pressure and platen temperature on freeze-drying of beds of diced carrots, apples, and beef were studied experimentally by Gwinette et al. [22] to gain data on instantaneous drying rates and product temperatures. Hoover and Markantonatos [23] give some experimental data such as temperature, pressure, bed thickness, and drying rates for chopped beef. They give additional data in [24].

King et al. [25-29] have been conducting work on the freeze-drying of particulate beds of turkey meat. Their work includes a model for bed-drying based on the slab-equation analogue for a sphere. The analysis assumes a diffusional flow based on the

<sup>1</sup> Numbers in brackets designate References at end of paper.

Contributed by the Heat Transfer Division for publication (without presentation) in the JOURNAL OF HEAT TRANSFER. Manuscript received by the Heat Transfer Division November 2, 1970. Paper No. 71-HT-R.

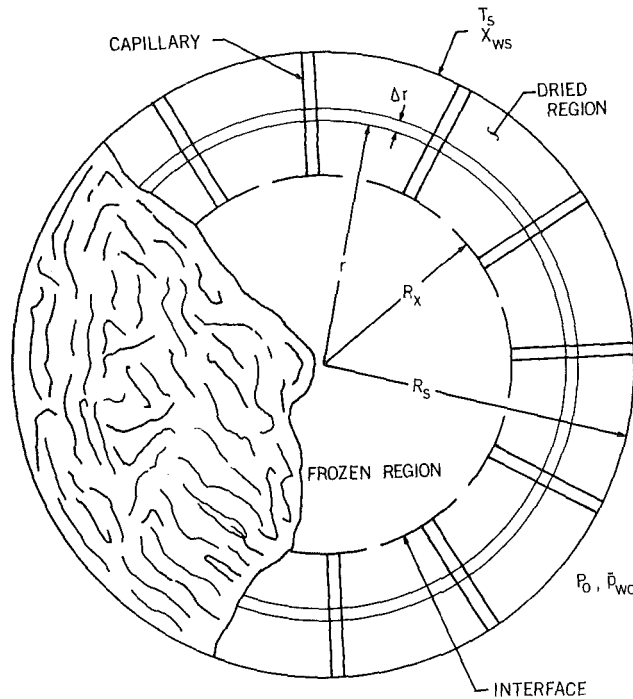


Fig. 1 Analytical model of sublimating product

"dusty gas model," which assumes that the dried food particles are, in effect, large molecules. Flow resulting from a total pressure drop within the product is not considered.

A basic approach for treating bed-drying is needed. An analysis of the freeze-drying process undergone by a generically cylindrical or spherical element is presented in [30], using the simplifying assumption of a constant interface temperature. Complexity is thus avoided, but accuracy in accounting for the interdependency of mass and energy transfer is sacrificed. To reveal this dependence for the sphere and cylinder, the analysis presented herein extends the complete slab analysis of [31] to include these two geometries.

## Analytical Investigation

**Formulation of the Freeze-Drying Process.** Spheres and cylinders of beef undergoing a freeze-drying process are considered. Fig. 1 illustrates, for either case, a typical cross section of the analytical model and its environmental conditions.

Because of the low-pressure surroundings and small void size, the movement of the sublimated vapor through the dried layer is transitional ( $Kn \approx 1$ ). The analysis of this flow path assumes that the void spaces are circular and straight capillaries; to in-

clude deviations from the analytical model, *effective parameters* are used to account for the irregularities.

The interface (distinct separation between the dried and frozen region) is assumed to recede in concentric layers, the mass flux at any point being normal (radially outward) to the interface. The interface motion is assumed to be so slow that the effects of its movement may be neglected with respect to space rates of change in the governing equations. This constitutes a quasi-steady assumption. The driving forces for mass transport are a concentration gradient and total pressure drop. Fick's law of diffusion is used to account for the flow resulting from a concentration gradient. An equation to account for bulk flow in capillaries was developed in [31] and was adopted for this analysis. Thermal transpiration is neglected, this being in agreement with [31].

Energy is transferred by conduction and convection through the dried layer. Conduction to the interface supplies the enthalpy of sublimation to the frozen liquid. The resulting phase change is assumed to occur instantaneously at the infinitely thin interface. This treatment is in accord with the analysis of [32] and [33]. Transfer away from the interface occurs as a result of an increase in the sensible enthalpy of the vapor, its subsequent motion, and conduction through the vapor. Energy storage in the dried product is neglected, an assumption shown to be accurate to within 3 percent by [31]. Effective values of thermal conductivity are used to reduce the form of the transfer equations to those of a pure substance. It is assumed that a one-dimensional treatment of the process is sufficient, and that at any position, the vapor and the dried matrix are in thermal equilibrium. Fourier's law of heat conduction is used to analyze the frozen region for steady conditions and constant properties. Nominal shrinkage during drying is not taken into account, an assumption of [3].

**Governing Equations.** Since the analysis involves a binary gas mixture, each component of the mixture must simultaneously satisfy the conservation equations for mass, momentum, and energy.

**Mass.** A total mass balance for a unit-length differential cylindrical shell requires that the quantities  $rN_w$  and  $rN_a$  be constant. For a sphere, a similar balance shows that  $r^2N_w$  and  $r^2N_a$  are constant. In both cases, the mole flux of air at the interface is zero and the net flux becomes that of water vapor in a stagnant air column.

**Momentum.** An equation which describes the bulk flow through a capillary of length  $L$  is derived in [31]. From the Navier-Stokes equation, considering molecular streaming, the molar flux caused by a pressure gradient is

$$N_w = c\Delta P\epsilon/\mu L \quad (1)$$

For a capillary extending from the interface to the surface of the product, the mole flux per unit total cross-sectional area is

$$N_{wx} = c\Delta P\sigma\epsilon/\mu(R_s - R_x) \quad (2)$$

for the cylinder and sphere.

## Nomenclature

$c$  = molar density (mole/ft<sup>3</sup>)  
 $C_p$  = specific heat (Btu/lb<sub>m</sub>-deg R)  
 $C_1, C_2, \left. \begin{matrix} \\ \\ \end{matrix} \right\}$  = integration constants  
 $D_1, D_2, \left. \begin{matrix} \\ \\ \end{matrix} \right\}$  = integration constants  
 $D_e$  = effective diffusion coefficient (ft<sup>2</sup>/hr)  
 $f(\ )$  = function  
 $H$  = enthalpy of sublimation (Btu/mole)  
 $K$  = effective thermal conductivity (Btu/hr-ft-deg R)  
 $Kn$  = Knudsen number  
 $L$  = length of capillary (ft)  
 $M$  = molecular weight (lb<sub>m</sub>/mole)

$N$  = molar flux (mole/hr-ft<sup>2</sup>)  
 $P$  = total pressure (torr)  
 $\bar{P}$  = partial pressure (torr)  
 $r$  = radial position (ft)  
 $R$  = specific radial position (ft)  
 $t$  = time (hr)  
 $T$  = temperature (deg R)  
 $V$  = mass-average velocity (ft/hr)  
 $X$  = mole fraction  
 $\beta$  = temperature-profile constant  
 $\gamma$  = temperature-profile constant  
 $\epsilon$  = effective permeability (ft<sup>2</sup>)  
 $\mu$  = viscosity (lb<sub>f</sub>-hr/ft<sup>2</sup>)

$\rho$  = mass density (lb<sub>m</sub>/ft<sup>3</sup>)  
 $\sigma$  = porosity (pore volume/total volume)

### Subscripts

$a$  = air  
 $f$  = frozen region  
 $i$  = general specie  
 $m$  = meat matrix  
 $s$  = value at heated surface  
 $v$  = vapor phase  
 $w$  = water  
 $x$  = interface value  
 $0$  = chamber condition

**Energy.** Paralleling the developments of [31] and [33], a shell balance for energy, which assumes no time-dependent quantities and vapor-matrix equilibrium, shows

$$\frac{d}{dr} \left( r \frac{dT}{dr} \right) = \left( \frac{r N_w C_{pv} M_w}{K} \right) \frac{dT}{dr} \quad (3)$$

and

$$\frac{d}{dr} \left( r^2 \frac{dT}{dr} \right) = \left( \frac{r^2 N_w C_{pv} M_w}{K} \right) \frac{dT}{dr} \quad (4)$$

for the cylinder and the sphere, respectively. Under the assumption of constant properties, these equations may be conveniently written as

$$\frac{d}{dr} \left( r \frac{dT}{dr} \right) = \beta \frac{dT}{dr} \quad (5)$$

and

$$\frac{d}{dr} \left( r^2 \frac{dT}{dr} \right) = \gamma \frac{dT}{dr} \quad (6)$$

respectively, where  $\beta$  and  $\gamma$  are constants.

In solving these equations, the temperature profiles become

$$T = C_1 r^\beta + C_2 \quad (7)$$

$$T = D_1 e^{-\gamma/r} + D_2 \quad (8)$$

Subject to the boundary conditions

$$T = T_s \quad \text{at} \quad r = R_s \quad (9)$$

and

$$T = T_x \quad \text{at} \quad r = R_x \quad (10)$$

the constants become

$$C_1 = \frac{T_s - T_x}{R_s^\beta - R_x^\beta} \quad (11)$$

$$C_2 = T_s - C_1 R_s^\beta \quad (12)$$

$$D_1 = \frac{T_s - T_x}{e^{-\gamma/R_s} - e^{-\gamma/R_x}} \quad (13)$$

$$D_2 = T_s - D_1 e^{-\gamma/R_s} \quad (14)$$

**Supporting Equations.** The following equations are used in conjunction with the previous conservation equations:

**Equilibrium Partial Pressure.** The equilibrium partial pressure of the water-like substance of beef, from [34], is

$$\bar{P}_{wx} = \exp(27.7 - 12900/T_x) \quad (15)$$

**Fick's Law.** The diffusional contribution to the total flow is governed by Fick's law. For a capillary with mole fractions specified at its ends, the total mole flux is

$$N_w = -cD_e \frac{dX_w}{dr} + X_w(N_w + N_a) \quad (16)$$

where the first term is the diffusional flow and the second is the bulk contribution to the total flow  $N_w$ . With  $N_a = 0$ , Fick's law may be used in conjunction with the mass balance to find the local molar flux, for the cylinder,

$$N_{wx} = \frac{cD_e \ln[(1 - X_{ws})/(1 - X_{wx})]}{R_x \ln(R_s/R_x)} \quad (17)$$

and for the sphere

$$N_{wx} = \frac{cD_e \ln[(1 - X_{ws})/(1 - X_{wx})]}{(R_x R_s - R_x^2)/R_s} \quad (18)$$

**Table 1 Property values**

$P_0$ (torr)	$K$ (Btu/hr-ft-deg R)	$\sigma\epsilon$ (ft <sup>2</sup> × 10 <sup>8</sup> )	$D_e$ (ft <sup>2</sup> /hr)
1	0.0503	1.529	61.2
2	0.0510	0.530	46.8
3	0.0520	0.270	39.6

The mole fractions may be determined by the relations

$$X_{wx} = \bar{P}_x/P_x \quad (19)$$

$$X_{ws} = \bar{P}_0/P_0 \quad (20)$$

**Interface Energy Balance.** For constant properties, under the quasi-steady assumption, the frozen-region profile must satisfy the Laplace equation. When the interface temperature is matched with the surface temperature of the frozen region,

$$T_f = T_x \quad \text{at} \quad r = R_x \quad (21)$$

By symmetry, the frozen-region profile must also yield

$$\frac{dT_f}{dr_f} = 0 \quad \text{at} \quad r = 0 \quad (22)$$

To fulfill both conditions, the entire frozen region must be at a constant temperature equal to the interface temperature. Since there is no thermal gradient between the frozen region and the interface, an interface energy balance shows that the conduction to the interface supplies the enthalpy of sublimation. This formulation yields

$$K \left. \frac{dT}{dr} \right|_{r=R_x} = N_w H \quad (23)$$

The gradient may be evaluated from the temperature profiles for the cylinder and sphere. Solving for  $N_w$  for each case,

$$N_{wx} = \frac{K C_1 \beta R_x^{\beta-1}}{H} \quad (24)$$

$$N_{wx} = \frac{K D_1 \gamma e^{-\gamma/R_x}}{H R_x^2} \quad (25)$$

**Equation of State.** Each specie of binary gas mixture is assumed to obey the ideal-gas equation of state.

**Variables and Property Data.** The preceding analysis utilizes boundary conditions which are directly controllable in an actual freeze-drying analysis. These controlled variables are chamber pressure, partial chamber pressure, and product surface temperature. This analysis will allow any set of these conditions, provided property data are available.

Effective diffusion coefficient, effective thermal conductivity, and permeability are the properties of primary concern. Values for these properties in the literature vary as much as 100 percent. Each, moreover, is a function of pressure.  $\sigma\epsilon$  and  $D_e$  for beef, shown in Table 1, were obtained from [31]. The values of  $K$  given in Table 1, along with the thermal properties ( $C_{pv} = 0.46$  Btu/lb<sub>m</sub>-deg R and  $H = 1488$  Btu/lb<sub>m</sub>-deg R), were taken from [4].

**Solution Procedure.** The governing equations for the cylindrical or spherical geometry may be combined to reduce the entire set of simultaneous equations to one equation with one unknown. The procedure for the cylinder is as follows:

1 When equations (17), (19), and (20) are combined, the molar flux at the interface becomes

$$N_{wx} = \frac{cD_e \ln[(1 - P_{w0}/P_0)/(1 - P_{wx}/P_x)]}{R_x \ln(R_s/R_x)}$$

2 If equation (2) is solved for  $\Delta P$  and  $P_x = P_0 + \Delta P$  is identified, the molar flux becomes

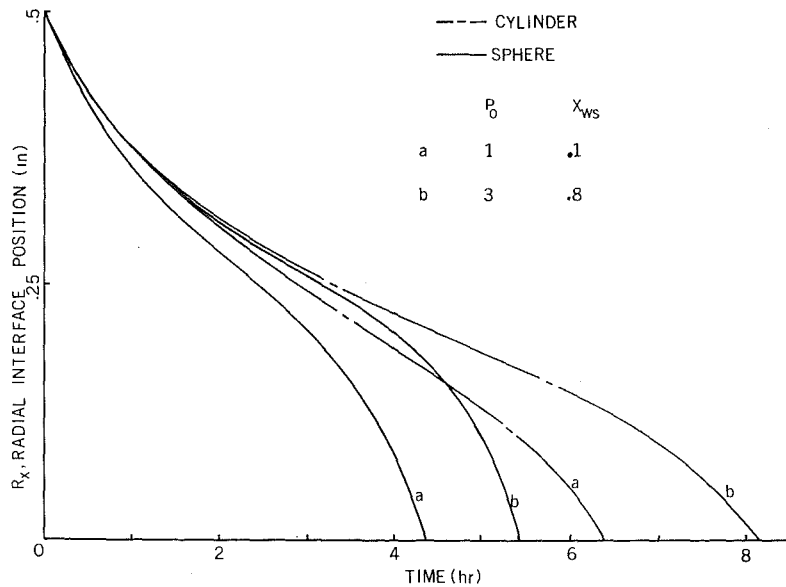


Fig. 2 Interface position as a function of time

$$N_{wx} = \frac{cD_e \ln [(1 - P_{w0}/P_0)/(1 - A)]}{R_x \ln (R_s/R_x)}$$

where

$$A = \frac{\exp (27.7 - 12900/T_x)}{P_0 + N_{wx} \mu (R_s - R_x) / c \sigma \epsilon}$$

3 By combining equations (11) and (24) and solving for  $T_x$ ,

$$T_x = T_s - \frac{N_{wx} H (R_s^\beta - R_x^\beta)}{K \beta R_x^{\beta-1}}$$

4 When this expression for  $T_x$  is used in step 2 above, the equation for the molar flux is of the form

$$N_{wx} = f(N_{wx}, R_x, R_s, P_0, \bar{P}_{w0}, T_s)$$

By specifying the controlled variables  $R_s$ ,  $P_0$ ,  $\bar{P}_{w0}$ , and  $T_s$ , the molar flux at any interface position,  $R_x$ , may be determined by a trial-and-error solution of the above equation, the only unknown being the molar flux  $N_{wx}$ .

5 If the cylinder is broken into layers  $\Delta r$  thick, each layer may be dried, the drying time being deduced from

$$\Delta t = \frac{\Delta r c_j \sigma}{N_{wx}}$$

The cylinder drying time, as well as all other pertinent parameters, is obtained by repetition of this process for the successive layers.

A similar procedure may be used to solve the set of simultaneous equations for the spherical sample. The above procedure was programmed on the IBM 360 digital computer. The particle was incrementally dried in grid steps of  $\Delta r$ . At each grid point, a value disagreement of  $10^{-6}$  was considered acceptable. Grid steps of less than 5 percent of the radius gave drying times which compared within 1 percent.

## Typical Results

This section discusses some typical results from the solution procedures for the following controlled variables:

$$P_0 \text{ (torr)} = 1, 2, 3$$

$$X_{ws} = 0.1, 0.3, 0.5, 0.8$$

$$T_s \text{ (deg R)} = 560$$

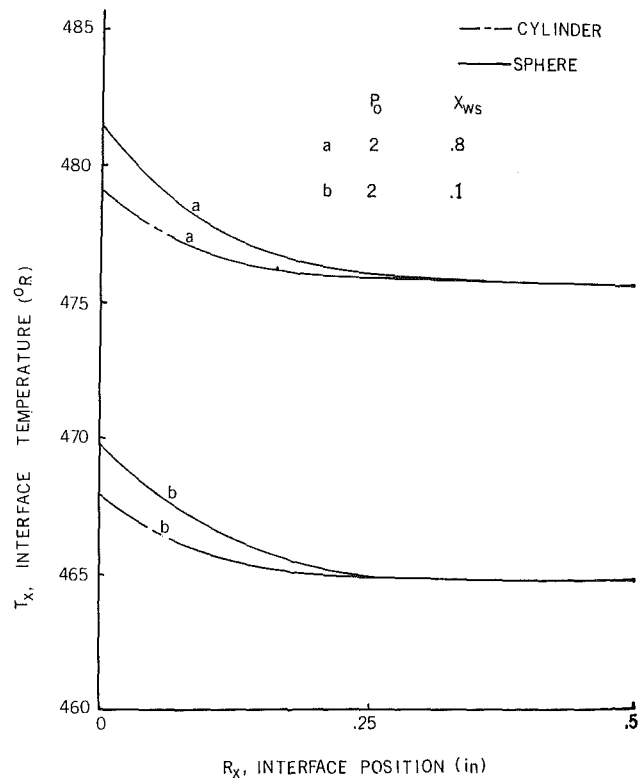


Fig. 3 Variation of interface temperature with position

$$R_s \text{ (in.)} = 1/8, 1/4, 3/8, 1/2$$

**Interface Position as a Function of Time.** Fig. 2 illustrates the interface position as a function of time for the conditions which yield the maximum and minimum drying times. Similar trends are noted for the cylinder and the sphere. The intermediate drying curves indicate an increase in drying time with an increase in mole fraction of water vapor at the surface for a constant chamber pressure. This is explained on the basis of Fick's law which attributes a portion of the total flow to a concentration gradient. An increase in the water concentration in the chamber decreases the concentration gradient from the interface to the surface of the product, and a decrease in flow results.



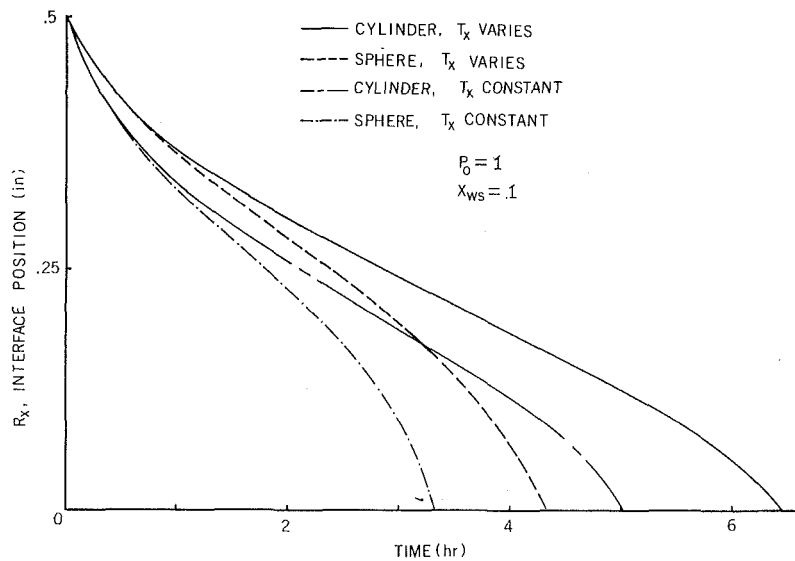


Fig. 4 Comparison with constant-interface solution

For a constant mole fraction of water vapor at the surface of the product, an intermediate drying curve indicates that the drying time increases with an increase in total pressure. This follows from the observation that an increase in the total chamber pressure decreases the total pressure drop from the interface to the product surface. The decreased bulk-flow contribution to the total flow is responsible for the noted decrease in drying speed.

**Interface Temperature as a Function of Position.** Fig. 3 shows the variation of interface temperature with radial position. The increase in temperature indicates that as the interface recedes, more energy is conducted to the interface than can be convected away. The process, therefore, may be considered mass-transfer-limited. (Since the effective thermal conductivity is a function of the conductivity of the gas which surrounds the sample, it may be possible to find a value for thermal conductivity which could make the process heat-transfer-limited.) The decrease in convection is expected since the lengthening of the dried-region flow path affords an increased resistance to the flow. This also necessitates an increased total pressure drop from the interface to the product surface. Since the temperature increases at the interface, the partial pressure must increase at the interface. The mole fraction must decrease at the interface since the flow decreases. This implies that the total pressure must increase more rapidly than the partial pressure. This is in accord with the analytical calculations.

To avoid the difficulties of considering a variable interface temperature, it is common in freeze-drying analysis to assume that the interface temperature either remains constant or varies linearly with position. It is obvious from Fig. 3 that neither assumption is accurate. To examine the effect of a constant-interface solution, Fig. 4 shows that drying times are nearly 10 percent shorter with the constant-interface solution. This more rapid drying is a result of steeper thermal gradients from the surface to the interface. There is, of course, a constant-interface temperature which, if selected, would give drying times in agreement with the analysis of this paper. However, such a selection requires a knowledge of the variable-interface solution to choose a good average interface temperature. The best that may be done in the ordinary situation is to select the equilibrium temperature which corresponds to the chamber partial pressure. This temperature is selected for the comparison of Fig. 4, using Dyer's solution for a constant-interface model [30].

**Typical Temperature Profiles.** Fig. 5 illustrates the typical temperature profiles for the two interface positions,  $R_{x1}$  and  $R_{x2}$ , and the final profiles as the frozen region disappears. It is apparent that

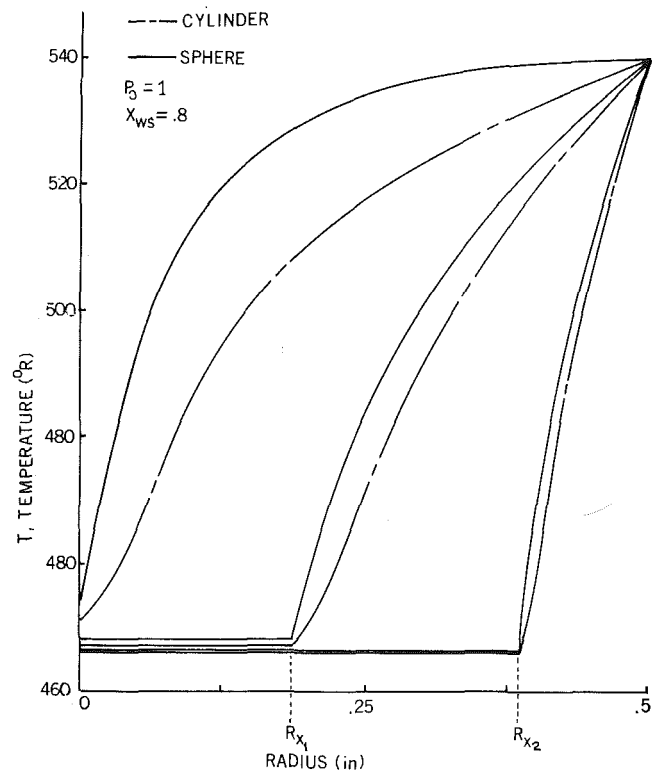


Fig. 5 Typical temperature profiles

the thermal gradients in the sphere are steeper nearer the center than in the cylinder, an observation which accounts for the increased drying time required for the cylinder samples. This typical result marks a significant departure from the slab model. Temperature profiles in the dried region are linear in the slab. Removal of the interior water substance, where resistance to flow is high, is critical in obtaining high drying rates. Because of its sharp thermal gradients in the critical region, the spherical geometry establishes a higher heat flux to the interface. Because the drying time depends strongly on the rate of heat transfer to the interface, the sphere, as opposed to the slab or cylinder, represents an optimum shape for rapid drying.

From Fig. 5, the frozen region is seen to have the temperature of the interface at any position.

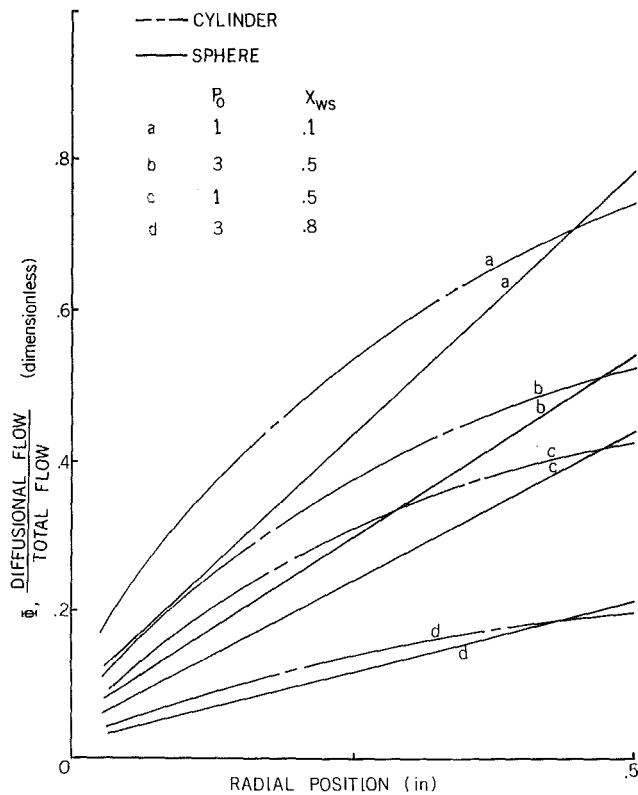


Fig. 6 Diffusional contribution to total flow

**Diffusional Contribution to Total Flow.** To call attention to the necessity for considering diffusional flow, define a parameter  $\Phi$  such that

$$\Phi = \frac{\text{diffusional flow}}{\text{total flow}} \quad (27)$$

This parameter may be evaluated from Fick's law, equation (16), where the first term accounts for the diffusional contribution to the total flow  $N_w$ . Thus,

$$\Phi = \frac{-cD_e dX_w/dr}{N_w} \quad (28)$$

Using  $N_w$  from equation (2),

$$\Phi = \frac{-D_e \mu (R_s - R_x) dX_w}{\Delta P \epsilon \sigma dr} \quad (29)$$

Separating variables and integrating,

$$\int \Phi dr = -D_e \mu (R_s - R_x) \frac{(X_{ws} - X_{wx})}{\Delta P \epsilon \sigma} \quad (30)$$

For a mean value of  $\Phi$ ,

$$\Phi_{avg} = \mu D_e \frac{(X_{wx} - X_{ws})}{\Delta P \epsilon \sigma} \quad (31)$$

This expression was evaluated at each grid position and a plot of  $\Phi_{avg}$  as a function of the interface position is shown in Fig. 6. Since under some conditions the molar flux which results from diffusion constitutes the larger percentage of the flow, diffusion should not be neglected. It is apparent that diffusion plays its most significant role during the initial stages of sublimation. Evidently this is a result of the lack of an appreciable pressure drop at the onset of drying.

## Optimization

The fundamental requirements for an optimum freeze-drying process must be defined with respect to the governing factors: heat supply and moisture removal. Within the framework of this analysis, the factor which controls heat supply is the surface temperature of the product,  $T_s$ . The optimum  $T_s$  is the highest temperature which does not scorch the product. While the optimum surface temperature is a relatively inflexible design parameter, moisture removal offers more versatility. The primary mechanisms involved in mass transfer are those of diffusion and bulk flow. By controlling the driving forces of those mechanisms, one may seek to optimize moisture transfer. The parameters that may be controlled are the concentration gradient and the total pressure drop encountered within the dried region of the product. To alter these parameters, one may change the total and partial pressures at the surface of the food product. Thus, optimization of moisture transfer within the food product reduces to the problem of selecting the most economical set of chamber conditions. While extensive experimental research could eventually establish the best combination, Table 2 indicates the sequence of chamber conditions one should follow in determining the relative effects of a particular combination on drying time. This approach to analytically predicting optimum conditions represents a significant contribution. It may be noted, for instance, that to decrease drying time it may be more economical to change conditions of total pressure and mole fraction from 3.0 and 0.3, respectively, to 2.0 and 0.5, rather than 3.0 and 0.1. Other similar observations may be made. By means of this tabular arrangement of drying times the most economical combination of chamber conditions could be determined by evaluating the relative costs of a particular set of chamber conditions and weighing this against the resultant decrease in drying time. It is interesting to note that, while the drying times for the cylinder and sphere differ, the same progression in chamber conditions is observed as the drying time decreases.

Table 2 Drying times for various chamber conditions

Drying time (hr)	Cylinder*		Drying time (hr)	Sphere*	
	Chamber pressure $P_0$ (torr)	Mole fraction $X_{ws}$		Chamber pressure $P_0$ (torr)	Mole fraction $X_{ws}$
6.46	1	0.1	4.33	1	0.1
6.59	1	0.3	4.42	1	0.3
6.72	1	0.5	4.51	1	0.5
6.79	2	0.1	4.55	2	0.1
6.91	1	0.8	4.63	1	0.8
6.95	3	0.1	4.65	3	0.1
7.06	2	0.3	4.73	2	0.3
7.32	2	0.5	4.90	2	0.5
7.35	3	0.3	4.91	3	0.3
7.67	2	0.8	5.14	2	0.8
7.69	3	0.5	5.14	3	0.5
8.17	3	0.8	5.47	3	0.8

\*  $1/2$ -in. radius.

## References

- 1 Bird, B. R., Stewart, W. E., and Lightfoot, E. N., "Diffusivity and the Mechanisms of Mass Transport," *Transport Phenomena*, John Wiley & Sons, New York, 1960, pp. 495-515.
- 2 Harper, J. C., "Transport Properties of Gases in Porous Media at Reduced Pressures with Reference to Freeze-Drying," *AIChE Journal*, Vol. 8, No. 3, 1962, p. 298.
- 3 Harper, J. C., and Tappel, A. L., "Freeze-Drying of Food Products," *Advances in Food Research*, Vol. 7, Academic Press, New York, 1957, pp. 171-234.
- 4 Massey, W. W., Jr., "Heat and Mass Transfer in Semi-Porous Channels," PhD thesis, Georgia Institute of Technology, 1968.
- 5 Burke, R. F., and Decareov, R. V., "Recent Advances in Freeze-Drying of Food Products," *Advances in Food Research*, Vol. 13, Academic Press, New York, 1964, p. 1.
- 6 Goldblith, S. A., "Freeze-Dehydration of Foods," *Lyophilisation—Freeze-Drying*, (Louis Rey, ed.), Hermann Press, Paris, 1964, p. 581.
- 7 Tease, S. C., "Progress of Food Freeze-Drying in the U.S.A.," *Lyophilisation—Freeze-Drying*, (Louis Rey, ed.), Hermann Press, Paris, 1968, p. 581.
- 8 Cotson, S., and Smith, D. B., eds., *Freeze-Drying of Food-stuffs*, Columbine Press, London, 1963, p. 105.
- 9 Blair, J. M., "Temperature Control in the Freeze-Drying Process," *ASHRAE Journal*, Vol. 8, No. 7, 1966, p. 52.
- 10 Smithes, W. R., "The Influence of Processing Conditions on the Rehydration of Freeze-Dried Foods," *Freeze-Drying of Foods*, National Academy of Science, National Research Council, Washington, D. C., 1962, p. 191.
- 11 Moyer, J. C., Pallesen, H. R., and Shallenberger, R. S., "The Interaction Between Blanching and Drying Rates of Peas," *Food Technology*, Vol. 13, No. 10, 1959, p. 581.
- 12 Foda, H., El-Waraki, A., and Zard, A., "Effect of Dehydration, Freeze-Drying, and Packaging on the Quality of Green Beans," *Food Technology*, Vol. 21, No. 7, 1967, p. 83.
- 13 Dellamonica, E. S., and McDowell, P. E., "Comparison of Beta-Carotene Content of Dried Carrots Prepared by Three Dehydration Processes," *Food Technology*, Vol. 19, No. 10, 1965, p. 188.
- 14 Lusk, G., Karel, M., and Goldblith, S. A., "Effect of Some Processing Parameters on the Rates of Freeze-Dried Shrimp," *Food Technology*, Vol. 19, No. 4, 1965, p. 188.
- 15 Swalin, H., "The Role of Moisture of Deteriorative Reactions of Dehydrated Foods," *Freeze-Drying of Foods*, National Academy of Science, National Research Council, Washington, D. C., 1962, p. 58.
- 16 Lawler, F. K., "Latest in Freeze-Drying," *Food Engineering*, Vol. 33, No. 11, 1961, p. 35.
- 17 Seltzer, E., "Accelerating Freeze-Dehydration," *Freeze-Dehydration of Foods*, Research and Development Associates, Food and Container Institute, Chicago, 1960, p. 38.
- 18 Schotte, W., "Thermal Conductivity of Packed Beds," *AIChE Journal*, Vol. 6, No. 1, 1960, p. 63.
- 19 Saravacos, G. D., and Charm, S. E., "A Study of the Mechanism of Fruit and Vegetable Dehydration," *Food Technology*, Vol. 16, No. 1, p. 78.
- 20 "The Accelerated Freeze-Drying Method of Food Preservation," Ministry of Agriculture, Fisheries, and Food, Aberdeen, Scotland, Her Majesty's Stationery Office, London, 1961.
- 21 Forrest, J. C., "The Accelerated Freeze-Drying Process," *Recent Advances in Food Sciences*, Vol. 2, Butterworths, London, 1962, p. 3.
- 22 Gwinette, L. F., Graham, R. P., and Morgan, A. I., "Freeze-Drying Rates," *Fifth National Symposium on Vacuum Technology Transactions*, Pergamon Press, New York, 1958, p. 268.
- 23 Hoover, M. W., and Markantonatos, A., "UHF Dielectric Heating in Experimental Acceleration of Freeze-Drying of Foods," *Food Technology*, Vol. 20, No. 6, 1966, p. 103.
- 24 Hoover, M. W., and Markantonatos, A., "Engineering Aspects of Using UHF Dielectric Heating to Accelerate the Freeze-Drying of Foods," *Food Technology*, Vol. 20, No. 6, 1966, p. 107.
- 25 Gunn, R. D., "Mass Transport in Porous Media as Applied to Freeze-Drying," PhD thesis, University of California, Berkeley, 1967.
- 26 Gunn, R. D., and King, C. J., "Convective Freeze-Drying in Mixed or Layered Beds," *AIChE Symposium on Cryogenic Food Processing Advances*, Los Angeles, Dec. 1-5, 1968.
- 27 Gunn, R. D., and King, C. J., "Mass Transport Characteristics of Freeze-Dried Foods," *AIChE Annual Meeting*, Los Angeles, Dec. 1-5, 1968.
- 28 Clark, J. P., "Synthesis and Evaluation of an Improved Freeze-Drying Process," PhD thesis, University of California, Berkeley, 1968.
- 29 Clark, J. P., and King, C. J., "Freeze-Drying of Mixed or Layered Beds," *AIChE Annual Meeting*, Los Angeles, Dec. 1-5, 1968.
- 30 Dyer, D. F., "A Model for Freeze-Drying," accepted for presentation and publication in *Transactions of Southeastern Seminar on Thermal Science*, April 1970.
- 31 Dyer, D. F., and Sunderland, J. E., "Heat and Mass Transfer Mechanisms in Sublimation Dehydration," *JOURNAL OF HEAT TRANSFER*, TRANS. ASME, Series C, Vol. 90, No. 4, Nov. 1968, pp. 379-384.
- 32 Dyer, D. F., and Sunderland, J. E., "Bulk and Diffusional Transport in the Region Between Molecular and Viscous Flow," *International Journal of Heat and Mass Transfer*, Vol. 9, 1966, pp. 519-526.
- 33 Dyer, D. F., and Sunderland, J. E., "The Transient Temperature Distribution During Sublimation Dehydration," *JOURNAL OF HEAT TRANSFER*, TRANS. ASME, Series C, Vol. 89, No. 1, Feb. 1967, pp. 109-110.
- 34 Dyer, D. F., Carpenter, D. K., and Sunderland, J. E., "Equilibrium Vapor Pressure of Frozen Bovine Muscle," *Journal of Food Science*, Vol. 31, No. 2, 1966, pp. 196-201.

J. D. DALE

Assistant Professor,  
Department of Mechanical Engineering,  
University of Alberta,  
Edmonton, Alberta, Canada

A. F. EMERY

Professor,  
Department of Mechanical Engineering,  
University of Washington,  
Seattle, Wash.  
Mem. ASME

## The Free Convection of Heat from a Vertical Plate to Several Non-Newtonian "Pseudoplastic" Fluids

The local heat transfer, temperature, and velocity profiles were measured and numerically predicted for the free convection of heat from a vertical constant flux plate to several concentrations of carboxymethylcellulose (CMC) and carboxypolymethylene (Carbopol) powders in water. The fluids were found to have the thermal properties of water and in the shear stress range of interest to follow the power law of Ostwald-de Waele with flow indices varying from 0.395 to 1.0 and with fluid consistencies of 30 to 2300 times that of water. The tests were conducted using either of two plates (12 and 24 in. high) immersed in such a large tank (3000 lb of fluid) that the viscometric properties of the fluid remained unchanged, even for the long test periods used. All fluids, including those with yield stresses and those which suffered free surface effects, were found to transfer heat which could be correlated by the generalized Newtonian correlation

$$Nu_x = C(Gr_x * Pr_x^{*n})^{\frac{1}{3n+2}}$$

which suggests that the precise velocity characteristics of the fluid are of minor importance in determining the heat transfer performance of the system. The numerical solutions, based upon the boundary layer assumptions and the power-law model, were in excellent agreement with the experimental measurements.

### Introduction

ALTHOUGH free convection studies began in 1881 with Lorentz and have continued at a relatively constant rate since then, the basic studies may well be considered to have reached their apogee in the late 1960s when the digital computer was utilized to predict fluid characteristics, to examine variable-property fluid systems, and to co-exist as an equal with the experimental studies. With these twin approaches, minute details of free convection can be studied so efficiently and so completely that one is tempted to query whether any non-turbulent free convection problems remain which are worthy of further study except as routine extensions of this previous work.

However, almost all of these past studies treat only Newtonian fluids and only recently are these methods beginning to be applied to rheologically different materials. With the current awareness of the growing industrial importance of these different fluids—commonly termed “non-Newtonian fluids”—it is apparent that our present powerful experimental and numerical techniques

must be used to investigate these fluids. In particular, the studies must determine in which ways and to what extent the non-Newtonian fluids differ from the Newtonian fluid. These studies must emphasize the differences and the similarities so that the engineer can develop new heat transfer correlations or use those applicable Newtonian fluid relationships with confidence.

In this paper we report the results of a study made to determine the heat transfer rates and temperature and velocity profiles for the steady laminar free convection of non-Newtonian fluids about a vertical flat plate with a uniform wall heat flux. These results were obtained through experimental measurements and through numerical solutions of the partial differential equations.

**Previous Studies.** Prior studies which are germane to this investigation are those of Acrivos [1],<sup>1</sup> Reilly, Tien, and Adelman [2], Emery, Chi, and Dale [3], and Tien [4]. Acrivos studied analytically the free convection of pseudoplastic fluids past several bodies, of which an isothermal vertical flat plate was one. By utilizing the following definitions of generalized Grashof and Prandtl moduli

$$\overline{Gr} = \frac{\rho^2 L^{n+2} [g\beta(T_w - T_\infty)]^{2-n}}{m^2}$$

<sup>1</sup> Numbers in brackets designate References at end of paper.

Contributed by the Heat Transfer Division for publication (without presentation) in the JOURNAL OF HEAT TRANSFER. Manuscript received by the Heat Transfer Division April 2, 1971. Paper No. 71-HT-S.

$$\overline{\text{Pr}} = \frac{\rho c}{k} \left(\frac{m}{\rho}\right)^{\frac{2}{1+n}} L^{\frac{1-n}{1+n}} [Lg\beta(T_w - T_\infty)]^{\frac{3(n-1)}{2(n+1)}}$$

and using Lighthill's assumption that  $\text{Pr} \rightarrow \infty$ , he was able to secure a similar solution. The average Nusselt number was given by

$$\begin{aligned} \text{Nu}_{\text{ave}} &= -\theta'(0) \left(\frac{3n+1}{2n+1}\right)^{\frac{2n+1}{3n+1}} \frac{1}{\overline{\text{Gr}}^{2(n+1)}} \overline{\text{Pr}}^{\frac{n}{3n+1}} \\ &= C \overline{\text{Gr}}^{\frac{1}{2n+1}} \overline{\text{Pr}}^{\frac{n}{3n+1}} \end{aligned}$$

where the characteristic length  $L$  is equal to the length of the plate.  $\theta'(0)$  is the temperature gradient at the wall and is a function of the flow index  $n$ . Because of the term  $\left(\frac{3n+1}{2n+1}\right)^{\frac{2n+1}{3n+1}}$ , the coefficient  $C$  is a very weak function of  $n$ , although it does possess a minimum near  $n = 0.3$ . This minimum has never been experimentally observed and it is doubtful if it will be since Acrivos' solution is valid only for an isothermal wall, a constant fluid temperature far from the wall, constant fluid properties, a power-law fluid, and an infinite Prandtl number. These stringent conditions are unlikely to be met fully in any actual heat transfer system and consequently the solution must be experimentally verified to establish its adequacy and accuracy.

Reilly, Tien, and Adelman reported an experimental study for an electrically heated copper plate immersed in aqueous solutions of Carbopol. Their results were expressed as

$$\text{Nu}_{\text{ave}} = C(n) (\overline{\text{Gr}} \overline{\text{Pr}}^n)^{\frac{1}{3n+1}}$$

where

$$\overline{\text{Gr}} = \frac{g\beta(T_w - T_\infty)L^{\frac{n+2}{2-n}}}{\left(\frac{m}{\rho}\right)^{\frac{2}{2-n}}} \quad \overline{\text{Pr}} = \rho c \left(\frac{m}{\rho}\right)^{\frac{1}{2-n}} L^{\frac{2(1-n)}{2-n}}$$

The product  $(\overline{\text{Gr}} \overline{\text{Pr}}^n)^{\frac{1}{3n+1}}$  can be shown to be equal to Acrivos' product  $\overline{\text{Gr}}^{1/(2n+1)} \overline{\text{Pr}}^{n/(3n+1)}$  and therefore their constant  $C$  to be that of Acrivos. Their measured constant  $C$  agreed with

Acrivos' constant  $C(n)$ , and their slope agreed with  $1/(3n+1)$ .

Emery, Chi, and Dale reported an experimental study of the free convection from a constant flux hot wall to an isothermal cold wall across a narrow layer of either Carbopol or CMC. Since the previous studies of Emery and Chu [5] and MacGregor and Emery [6] had shown that a boundary layer model was adequate to describe the vertical layer's heat transfer characteristics, they applied Acrivos' boundary layer model and demonstrated that the non-Newtonian fluid layer results were well correlated by the generalized Newtonian correlation.

$$\text{Nu}_{\text{ave}} \sim C(\overline{\text{Gr}} \overline{\text{Pr}}^n)^{\frac{1}{3n+1}}$$

where the Grashof numbers were based upon the average temperature across the fluid layer. They also demonstrated that most of the fluids experienced considerable history effects, particularly those portions of the fluid which circulated near the heated and cooled walls.

Tien used the integral method to determine local heat transfer correlation for a constant flux vertical flat plate of the form

$$\text{Nu}_x = C(\text{Gr}_x^* \text{Pr}_x^{*n})^{\frac{1}{3n+2}}$$

In summary the literature reveals only two approximate solutions for the free convection about vertical flat plates. Acrivos' solution is seriously constrained by his assumptions and is mildly substantiated by the overall heat flux measurements reported. No substantiation of Tien's solution exists. Because there are no reported velocity profiles for the non-Newtonian fluids and no local heat transfer measurements, it is not yet possible to determine which of the two definitions for the Grashof and Prandtl numbers is more nearly correct. In addition it is questionable whether the approximations introduced by Acrivos and Tien are valid for a range of flow indices ( $n$ ) and for non-Newtonian fluids under situations where the generalized Prandtl number is not large.

It must be emphasized that both  $\overline{\text{Pr}}$  and  $\overline{\text{Pr}}$  contain a reference length  $L$  and we are faced with the undesirable situation where the Prandtl modulus which is supposed to represent the fluid characteristics contains a reference length which depends upon the experimental system. Thus it appears possible to construct systems with such large reference lengths that the Prandtl modulus is substantially reduced from that based upon an apparent viscosity.

## Nomenclature

$c$  = specific heat capacity (Btu/lb<sub>m</sub>-deg F)

$g$  = acceleration due to gravity (ft/sec<sup>2</sup>)

$\left. \begin{matrix} \overline{\text{Gr}} \\ \overline{\text{Gr}}^* \\ \overline{\text{Gr}}_x^* \end{matrix} \right\}$  = Grashof number,  $\rho^2 L^{n+2} \frac{[g\beta(T_w - T_\infty)]^{2-n}}{m^2}$ ;

$$\frac{g\beta(T_w - T_\infty)L^{\frac{n+2}{2-n}}}{\left(\frac{m}{\rho}\right)^{\frac{2}{2-n}}}; \quad \frac{g\beta q x^{\frac{4}{2-n}}}{k \left(\frac{m}{\rho}\right)^{\frac{2}{2-n}}}$$

$h$  = heat transfer coefficient (Btu/hr-ft<sup>2</sup>-deg F)

$k$  = thermal conductivity (Btu/hr-ft-deg F)

$L$  = length of plate (ft)

$m$  = consistency [lb<sub>m</sub>/ft(sec)<sup>2-n</sup>]

$n$  = flow index

$\text{Nu}_x$  = Nusselt number,  $hx/k$

$\left. \begin{matrix} \overline{\text{Pr}} \\ \overline{\text{Pr}}^* \\ \overline{\text{Pr}}_x^* \end{matrix} \right\}$  = Prandtl number,  $\rho \frac{c}{k} \left(\frac{m}{\rho}\right)^{\frac{2}{1+n}} L^{\frac{1-n}{1+n}}$

$$\times [Lg\beta(T_w - T_\infty)]^{\frac{3(n-1)}{2(n+1)}}; \quad \rho \frac{c}{k} \left(\frac{m}{\rho}\right)^{\frac{1}{2-n}} L^{\frac{2(1-n)}{2-n}};$$

$$\rho \frac{c}{k} \left(\frac{m}{\rho}\right)^{\frac{1}{2-n}} x^{\frac{2(1-n)}{2-n}}$$

$q$  = heat flux (Btu/hr-ft<sup>2</sup>)

$\text{Ra}^*$  = generalized Rayleigh number,  $\text{Gr}_x^* \text{Pr}_x^{*n}$

$T$  = temperature (deg F)

$u, v$  = velocity in the  $x$  and  $y$  directions (ft/sec)

$x$  = distance along the plate (ft)

$y$  = distance normal to the plate (ft)

$\beta$  = coefficient of thermal expansion (1/deg F)

$\dot{\gamma}$  = shear rate (sec<sup>-1</sup>)

$\rho$  = density (lb<sub>m</sub>/ft<sup>3</sup>)

$\sigma$  = surface tension (dyne/cm<sup>2</sup>), standard deviation

$\tau$  = shear stress (lb<sub>f</sub>/ft<sup>2</sup>)

### Subscripts

$w$  = wall

$x$  = local

$\infty$  = ambient fluid

## Numerical Solution

Under the assumptions of steady state, and two-dimensional boundary layer flow, the conservation equations can be expressed as

$$\frac{\partial u}{\partial x} + \frac{\partial v}{\partial y} = 0$$

$$u \frac{\partial u}{\partial x} + v \frac{\partial u}{\partial y} = g\beta(T - T_\infty) + \frac{1}{\rho} \frac{\partial}{\partial y} \left\{ m \left| \frac{\partial u}{\partial y} \right|^{n-1} \frac{\partial u}{\partial y} \right\}$$

$$u \frac{\partial T}{\partial x} + v \frac{\partial T}{\partial y} = \frac{1}{\rho c} \frac{\partial}{\partial y} \left( k \frac{\partial T}{\partial y} \right)$$

with boundary conditions of

$$u = v = 0 \quad -k \frac{\partial T}{\partial y} = q_w \quad \text{at } y = 0$$

$$u = 0 \quad T = T_\infty \quad \text{at } y = \infty$$

where the density and specific heat have been assumed to be constant except in the determination of the buoyancy term. Acrivos [1], Na and Hansen [7], and Lee and Ames [8] have shown that for a power-law fluid the only similarity solutions are for constant wall temperature or for a wall temperature which varies as

$$T_w - T_\infty = Cx^{-1/3}$$

a condition which does not exist for the constant wall heat flux case. Accordingly the conservation equations were expressed in difference form and solved numerically. The appropriate difference forms for constant properties are

$$\frac{u(i, j) - u(i-1, j)}{\Delta x} + \frac{v(i, j) - v(i, j-1)}{\Delta y} = 0$$

$$\begin{aligned} \frac{u'(i, j) - u(i, j)}{\Delta t} + u(i, j) \left( \frac{u(i, j) - u(i-1, j)}{\Delta x} \right) \\ + v(i, j) \left( \frac{u(i, j+1) - u(i, j)}{\Delta y} \right) = g\beta[T(i, j) - T_\infty] \\ + \frac{m/\rho}{\Delta y} \left\{ \left| \frac{u(i, j+1) - u(i, j)}{\Delta y} \right|^{n-1} \left[ \frac{u(i, j+1) - u(i, j)}{\Delta y} \right] \right. \\ \left. - \left| \frac{u(i, j) - u(i, j-1)}{\Delta y} \right|^{n-1} \left[ \frac{u(i, j) - u(i, j-1)}{\Delta y} \right] \right\} \end{aligned}$$

$$\begin{aligned} \frac{T'(i, j) - T(i, j)}{\Delta t} + u(i, j) \left( \frac{T(i, j) - T(i-1, j)}{\Delta x} \right) \\ + v(i, j) \left( \frac{T(i, j+1) - T(i, j)}{\Delta y} \right) \\ = \frac{k}{\rho c} \left( \frac{T(i, j+1) - 2T(i, j) + T(i, j-1)}{\Delta y^2} \right) \end{aligned}$$

where the primed variables indicate the values of the variables at a new time, and  $i$  and  $j$  represent the  $x$  and  $y$  positions of the nodal points. By expressing the conservation equations in an explicit transient form, the equations become parabolic and the solution can be stepped forward in time. Otherwise, the boundary layer assumptions, while permitting the solution to march forward with respect to  $x$ , are elliptic in  $y$  and require a simultaneous solution through the boundary layer. The transient procedure is simple to code and very efficient. Steady state was presumed to exist when no temperature changed by more than 0.001 deg F in 50 time steps.

The time step size utilized in this algorithm was governed by the stability requirements [9] of

$$\begin{aligned} \Delta t \left\{ \frac{m}{\rho} \frac{1}{\Delta y^2} \left[ \left| \max \frac{u(i, j+1) - u(i, j)}{\Delta y} \right|^{n-1} \right. \right. \\ \left. \left. + \left| \max \frac{u(i, j) - u(i, j-1)}{\Delta y} \right|^{n-1} \right] \right. \\ \left. + \frac{|\max u|}{\Delta x} + \frac{|\max v|}{\Delta y} \right\} \leq 1 \end{aligned}$$

and

$$\Delta t \left\{ \frac{2k}{\Delta y^2 \rho c} + \frac{|\max u|}{\Delta x} + \frac{|\max v|}{\Delta y} \right\} \leq 1$$

This formulation of the algorithm in the transient form can be easily converted to the method of successive over-relaxation (the Liebmann iterative method) by simply updating  $u$ ,  $v$ , and  $T$  as each nodal point is calculated. However, this modification only reduces the computation times required by 1.8 to 2 times and since the transient behavior was of interest, it was not used.

A serious problem with the momentum equation stability requirement arises whenever  $\frac{\partial u}{\partial y}$  goes to zero, since for  $n < 1$ ,

$\left| \frac{\partial u}{\partial y} \right|^{n-1}$  tends to infinity. Fortunately most pseudoplastic fluids have a Newtonian fluid behavior below some very low shear rate, thus eliminating the difficulty. However, one must then ascertain this shear rate (henceforth called the departure point) and must evaluate the effect of varying this point.

Of course, a different fluid model could also be used (e.g., the Ellis model), but those models which are not power-law models and which are not subject to this fault require at least one more viscosity term, making the determination of the shear stress-shear rate relationship much more difficult. Although no real non-Newtonian fluid is truly a power-law fluid, or at best can only be classified as a power-law fluid over only a small shear rate range, some practical method must be used to classify the fluid behavior and accordingly the power-law pseudoplastic description was utilized. Without such a description, no convenient heat transfer correlations are possible.

The difference equations were programmed for an IBM-7094 and first run for water to test the accuracy of the method. To simplify these tests only constant properties were considered. For water, the local plate temperature and dimensionless temperature profiles for Prandtl numbers from 1.0 to 10.0 differed from those computed by Sparrow and Gregg [10] by less than 5 percent. The vertical velocity component differed at most by 6 percent for  $Pr = 1.0$  and 0.5 percent for  $Pr = 10.0$ . No explanation for this difference was found. The grid spacing  $\Delta y$  was varied from 0.030 to 0.120 in. with significant effects only near the leading edge of the plate. In general the best results were found when the axial spacing  $\Delta x$  was chosen such that the axial gradients  $\frac{\partial T}{\partial x}$  were approximately equal to the normal gradient  $\frac{\partial T}{\partial y}$ . This was most efficiently done by letting  $\Delta x = 0.125$  in.

from  $x = 0$  to 2.0 in., 0.5 in. from 2.0 to 6.0 in., and 1.0 in. from 6.0 to 24.0 in.

A least-squares fit of the local Nusselt number gave

$$Nu_x = 0.964(Gr_x^*)^{0.1922}$$

compared to Sparrow and Gregg's value of

$$Nu_x = 0.944(Gr_x^*)^{0.20}$$

To assess the effects of varying flow indices upon the temperature and velocity profiles and in particular to determine if the point at which a fluid became Newtonian affected these profiles, a series of numerical tests was made. All fluid properties were

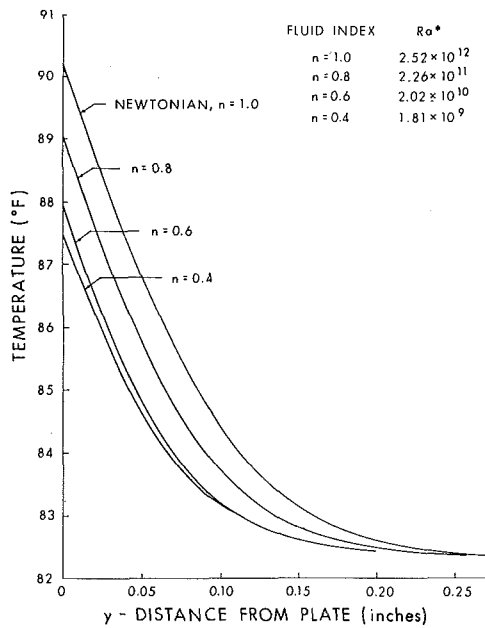


Fig. 1 Temperature distributions for various fluid indexes at 20 in. up-plate

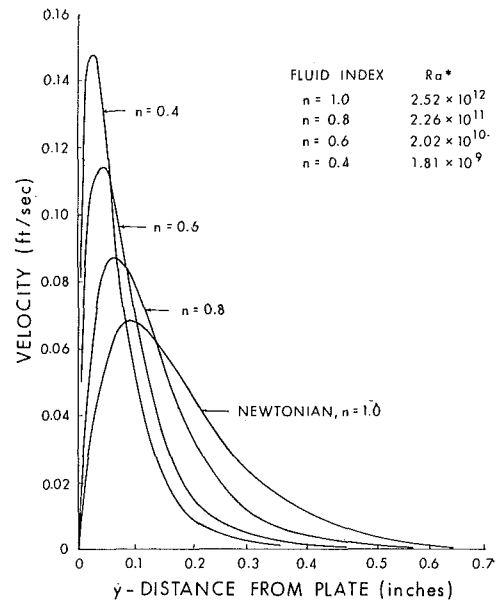


Fig. 2 Velocity distributions for various fluid indexes at 20 in. up-plate

$n$	$C$	$\beta$	$1/(3n + 2)$	$C(\text{Tien})$
1.0	0.610	0.199	0.200	0.682
0.8	0.559	0.227	0.227	0.695
0.6	0.610	0.253	0.263	0.720
0.4	0.569	0.290	0.313	0.75

taken equal to those of water. The fluids were assumed to be Newtonian until  $0.1 \text{ sec}^{-1}$  and their consistency adjusted so that for any  $n$ , the apparent and Newtonian viscosity were equal. The consistency was then held constant and the departure point changed to 0.01, 0.1, 1.0, and  $3.0 \text{ sec}^{-1}$ . Figs. 1 and 2 display the profiles obtained. Decreasing  $n$  is seen to increase the maximum velocity, decrease the plate temperature, and increase the Nusselt number. No significant effect in  $u$  was found when the point of departure was changed. The local Nusselt numbers were found to increase strongly as  $n$  decreased and the values of  $C$  and  $\beta$  for the least-squares fitted correlation  $Nu_x = C(\text{Gr}_x^* \text{Pr}_x^*)^\beta$  are given in Table 1.

The correlation changed, both in terms of  $C$  and  $\beta$ , as the departure point was changed. However, the predicted Nusselt number varied by less than 6 percent as the departure point was changed from  $0.01$  to  $3.0 \text{ sec}^{-1}$ . Consequently it was felt that the precise specification of this point is of marginal concern with respect to both the velocity profiles and the local heat transfer coefficient.

Since the fluids used in the experiments did show some variation in the fluid index with shear rate as shown in Fig. 3, an additional numerical test was made to assess the effects of this variation. The fluid index was taken as 1.0 up to a shear rate of  $1.5 \text{ sec}^{-1}$ , 0.91 from  $1.5 \text{ sec}^{-1}$  to  $3.8 \text{ sec}^{-1}$ , and 0.80 above  $3.8 \text{ sec}^{-1}$ . (These values were chosen by trial and error to insure that  $n$  would change between the plate and the maximum velocity point, between the maximum velocity point and the ambient fluid, and at the plate surface midway up the plate.) The fluid consistency above the latter shear rate was equal to that of the  $n = 0.8$  case mentioned previously, and the consistencies for the other shear rate ranges were evaluated from the power-law model. The results for the velocity and temperature profiles showed differences only in the fourth decimal place from those where the fluid index was held constant. Because of these small differences no discernible variation is evident from the  $n = 0.8$  curves shown in Figs. 1 and 2. The heat transfer correlation was almost identical to the  $n = 0.8$  case in Table 1, the differences being a

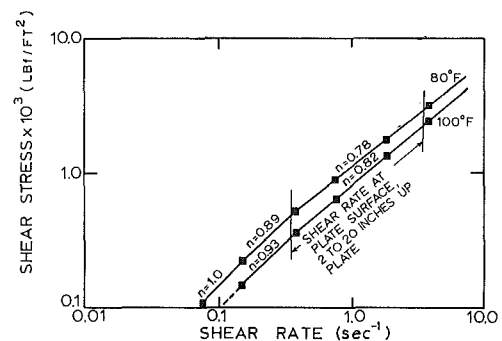


Fig. 3 Rheological behavior of 0.06 percent Carbopol 940, neutralized

2 percent decrease in the value of  $C$  and a 0.2 percent increase in the value of  $\beta$ .

If all the numerically computed values were fitted by curves of the form

$$Nu_x = C(\text{Gr}_x^* \text{Pr}_x^*)^{1/(3n+2)}$$

the curves were all parallel, with values of  $C$  of 0.413, 0.504, 0.568, and 0.615 for  $n = 0.4, 0.6, 0.8,$  and  $1.0$  respectively. The greatest scatter was that of 0.4 data whose standard deviation of  $\log_{10} Nu_x$  was 0.03. The coefficient  $C$  is seen to have a much stronger variation with the flow index  $n$  than that predicted by Acrivos or by Tien.

**The Experiments.** In order to ascertain if the above results are reliable for real non-Newtonian fluids, especially the apparent finding that non-Newtonian fluid correlations can be found by simply replacing the exponent 0.2 in the Newtonian expression by  $1/(3n + 2)$  and that the coefficient  $C$  is that given by the numerical solution, a series of experiments was conducted with two constant heat flux vertical flat plates. These plates were constructed by stretching thin stainless steel (0.004 in.) sheets over a bakelite plate with a sharp leading edge. The plates were  $18 \times 24$  in. and  $6 \times 12$  in. and were suspended in a 3000-lb tank of fluid. The plates were electrically heated by passing a current through the stainless steel. Plate temperatures were measured by copper-constantan thermocouples spot-welded to the back of the steel. The fluid temperatures were measured by chromel-constantan thermocouples mounted on a traversing mechanism which could be moved in 1-in. increments vertically along the plate and moved continuously normal to the plate with an accuracy of 0.001 in.

The velocity measurements were made by photographically tracking small hollow neutrally buoyant glass spheres ( $\sim 30$  microns in diameter). The macromolecules of CMC were of sufficient size that no beads were necessary. Dye streaks were also used for the 0.065 percent Carbopol in which the dye settling velocity was of the order of  $2 \times 10^{-5}$  ft/sec.

The test fluids were:

- (a) water
- (b) 0.05 CMC-water solution<sup>2</sup>
- (c) 0.06 percent and 0.065 percent Carbopol-water solutions, pH = 6.95 and 7.15 respectively<sup>3</sup>
- (d) 0.52, 0.57, 0.68, and 0.75 percent Carbopol-water solutions, pH = 3.2<sup>3</sup>

The water was used as a test fluid to check the system and to evaluate the measuring techniques. The pseudoplastic fluids were mixed by slowly adding the powder to the large tank of water using a high-speed impeller (an outboard motor propeller rotating at 700 rpm,  $\dot{\gamma} \approx 150$ ). After the initial dispersion was complete, two low-speed impellers were used to complete the mixing. The neutralized Carbopol solutions were achieved by adding 10 percent NaOH-H<sub>2</sub>O solution. All fluids tended to gel slightly at the top surface, particularly when the plate was operating, so periodic slow mixing was used to return the gel to the fluid state. Particular care was required in this de-gelling operation, since over-stirring would often cause the fluid to become Newtonian.

Christiansen and Craig [11] and Reilly et al. [2] have measured the density, specific heat capacity, and the coefficient of thermal expansion of CMC and Carbopol solutions respectively, and found them to be those of water. Accordingly these properties were not measured. Since the thermal conductivity and surface tension are delicately related to the molecular construction, these and the viscometric properties were measured for each fluid tested.

The shear stress-shear strain rate relationships were measured using a specially modified Brookfield Synchro-Lectric coaxial cylinder viscometer which was calibrated over the range of shear rate for 0.08 sec<sup>-1</sup> to 74 sec<sup>-1</sup>. Table 2 is a compendium of the viscometric data for the fluids. A shear stress-shear rate relationship for one of the test fluids is shown in Fig. 3. The behavior shown by the 0.06 percent Carbopol is typical in that some variation in the fluid index with shear rate is evident. Note, however, that for the shear rate range of interest the fluid index is essentially constant.

The 0.05 percent CMC was observed to become Newtonian in the shear rate range of 0.175 sec<sup>-1</sup> to 0.440 sec<sup>-1</sup>. Fortunately, as indicated by the numerical results, a precise knowledge of this departure point is not necessary. The fluid also showed a very rapid decay in consistency during the first six days after mixing and slower decay of approximately 1 percent per day thereafter.

The neutralized Carbopol appeared to be tending to a New-

<sup>2</sup> Sodium carboxymethylcellulose type 7435, lot 71284115, Hercules Inc.

<sup>3</sup> Carboxypolyethylene type 940, lot 44113, B. F. Goodrich Chemical Co.

tonian behavior, but at a shear rate below that attainable with the viscometer. The Carbopol solutions gelled slightly at the top surface of the tank. However, when the numerical predictions were compared to the measured velocity distributions, it appeared that the 0.06 percent neutralized solution possessed a yield stress even in the non-gelatinous state. Careful measurements indicate that the yield stress was of the order of  $3 \times 10^{-5}$  lb<sub>f</sub>/ft<sup>2</sup> and in fact no velocity profiles were found with shear stresses less than this.

The 0.065 percent Carbopol did not evidence a yield stress. Since the 0.06 percent was over 100 days old and the 0.065 percent no more than 30 days, aging appears to be responsible for this plastic behavior.

Like the neutralized Carbopol, the acidic Carbopol solutions showed the same tendency to be history-dependent, although the day-to-day variation was of limited concern since each acidic solution was used for a maximum of four days. No yield stress could be found. In contrast to normal fluids, all concentrations of the unneutralized Carbopol showed consistencies which increased with temperature.

The thermal conductivities listed in Table 2 were determined through the comparison technique of Grassmann and Staumann [12]. The values are estimated to be accurate to within 2 percent.

## Experimental Results

The plates were first tested in water and the local Nusselt numbers, temperature profiles, and velocity profiles determined. When plotted according to the similarity variables of Sparrow and Gregg, the temperatures and velocities agreed with both Sparrow and Gregg's results and the numerical computations to within 7 percent for distances up to 14 in. on the plate. The measured and computed local Nusselt numbers agreed with Sparrow and Gregg to within 6 percent at all points along the plate although the wall temperature was approximately 10 percent low at the leading edge. From 2 in. onward, no appreciable difference existed. Turbulence was found to appear at a modified Grashof number of  $10^{11}$ , which is the value reported by Dotson [13] for air.

The 0.05 percent CMC-water solution was then tested. Fig. 4 illustrates the measured velocity data and that determined numerically. The most immediate feature of this graph is the poor agreement in the outer portions of the boundary layer. Initially, no reason could be found, but providentially, a chance visual observation of the macromolecules indicated that some were descending at the outer edge of the layer, rather than being ingested. Consequently a series of dye traces was made, which showed that the boundary layer fluid after rising to the surface of the tank would then descend alongside the boundary layer and form a vortex motion at the upper portion of the plate. A series of experiments and measurements suggested that this descent was caused by the vertical temperature gradient in the ambient fluid. Because of this gradient, the fluid in the outer portion of the boundary layer was frequently colder than the

Table 2 Viscometric properties for the power-law model

Temp., deg F	<i>k</i>	0.05% CMC		0.06% Carbopol, pH = 6.95			0.065% Carbopol, pH = 7.15						
		<i>m</i>	<i>n</i>	<i>k</i>	<i>m</i>	<i>n</i>	<i>k</i>	<i>m</i>	<i>n</i>				
70	0.347	0.008015	0.883	0.347	0.04088	0.780	0.347	0.0704	0.774				
80	0.353	0.007180	0.885	0.353	0.0357	0.788	0.353	0.0623	0.750				
90	0.359	0.006316	0.888	0.359	0.0313	0.796	0.359	0.0532	0.786				
100	0.364	0.005653	0.890	0.364	0.0272	0.810	0.364	0.0413	0.800				
70		$\sigma = 64.4$			$\sigma = 57.6$			$\sigma = 57.0$					
Temp., deg F	<i>k</i>	Carbopol—unneutralized											
		0.52%		0.57%		0.68%		0.75%					
70	0.344	0.01813	0.898	0.338	0.03356	0.863	0.340	0.1264	0.704	0.332	0.1795	0.515	
80	0.351	0.01955	0.885	0.344	0.03987	0.817	0.345	0.1525	0.588	0.338	0.2321	0.403	
90	0.358	0.02181	0.864	0.352	0.04577	0.774	0.348	0.1740	0.494	0.338	0.2809	0.332	
100	0.360	0.02286	0.852	0.354	0.05007	0.726	0.352	0.1950	0.421	0.336	0.3324	0.244	
70		$\sigma = 63.8$			$\sigma = 64.6$			$\sigma = 65.5$			$\sigma = 66.4$		



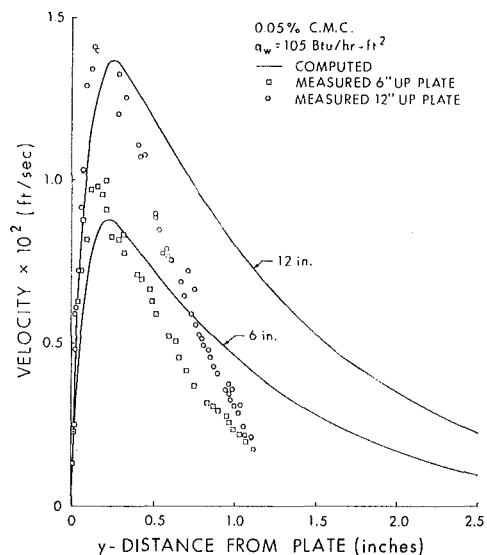


Fig. 4 Measured and calculated velocity distributions across laminar free convection boundary layer for 0.05 percent CMC,  $q_w = 105$  Btu/hr-ft<sup>2</sup>; large plate

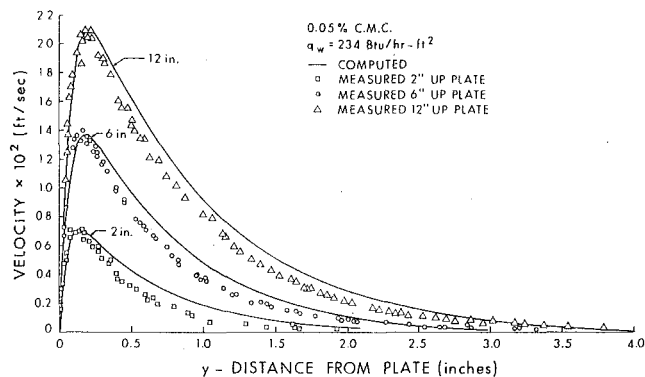


Fig. 5 Measured and calculated velocity distributions across laminar free convection boundary layer for 0.05 percent CMC,  $q_w = 234$  Btu/hr-ft<sup>2</sup>; small plate

ambient fluid. Two procedures were then adopted: (a) the small plate was used; (b) air bubblers were installed. The air bubblers were a sparsely perforated piece of tygon tubing laid on the bottom at each end of the tank. A series of fine screens was interposed between the bubblers and the plate. When the plate was first turned on the heated fluid tended to move over the surface to the ends of the tank, cool partly, and then descend. Since this fluid did not cool to the original fluid temperature, it would eventually heat the mass of fluid and establish a vertical temperature gradient. By using the bubblers, the fluid was adequately cooled before mixing the mass of fluid. The small plate dissipated only  $1/4$  the energy of the large plate and the surface film was easily capable of cooling to the ambient fluid temperature before reaching the ends of the tank and mixing with the main body of fluid. Both the bubblers and the small plate were capable of reducing the vertical gradient to less than 0.5 deg F/ft compared to the gradient of 5 deg F/ft for the large plate. Neither the bubblers nor the small plate tests caused any changes in the local Nusselt numbers or the local plate temperatures as measured on the large plate, indicating that the reverse flow was of no consequence in affecting the heat transfer performance. Fig. 5 shows the velocity distribution on the small plate, and the excellent agreement between the measured and predicted values is apparent.

Dye streak measurements for the small plate and for the large plate with the bubblers on showed that the fluid moved horizontally into the boundary layer, ascended, and did not descend

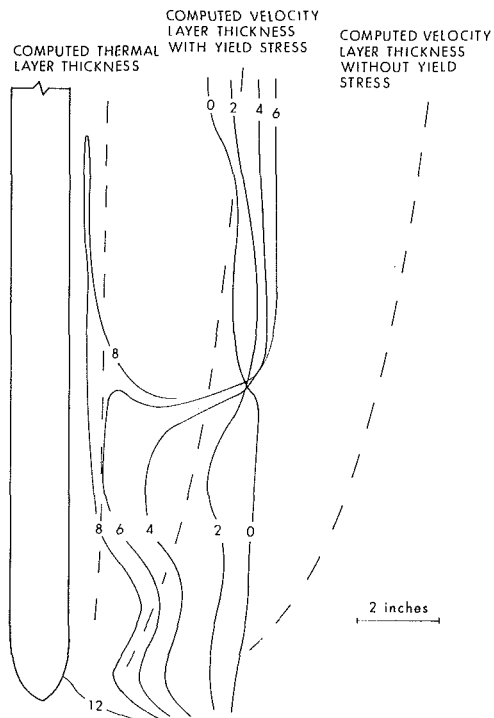


Fig. 6 Flow field for 0.06 percent Carbopol 940, pH = 6.95; large plate

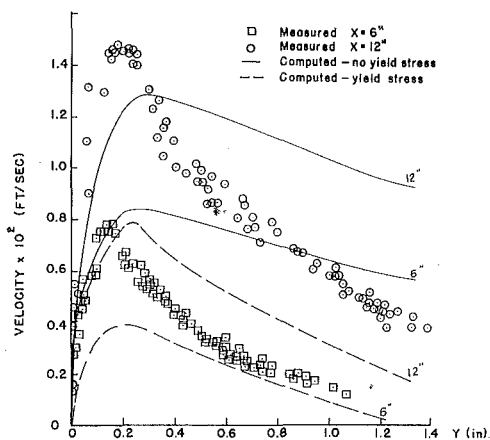


Fig. 7 Velocity distributions for 0.06 percent Carbopol, pH = 6.95,  $q_w = 245$  Btu/hr-ft<sup>2</sup>; large plate

near the plate, but moved across the surface and mixed with the main fluid as desired.

When the 0.06 percent neutralized Carbopol was tested, it too was found to possess a flow reversal. However, when either of the previous remedies was tried, the reversal persisted. Dye streaks showed that this fluid behaved very peculiarly. Fig. 6 is a chronological sketch of the dye streaks with the numbers indicating the time in minutes from a given datum. Note that the fluid is ingested into the layer only over the first portion of the plate. Long-time observations of the dye patterns suggested that the fluid, instead of moving away from the plate on the surface, moved out a short distance and then plumed downward and was again entrapped by the boundary layer. Further viscometric experiments with this fluid showed the presence of a yield stress of  $3 \times 10^{-5}$  lb<sub>f</sub>/ft<sup>2</sup>. Computations based upon the velocities determined from the dye streaks indicated that the ingestion region did in fact end when the shear stress reached this value. Several numerical computations were made using this value for a yield stress. These computations were unable to proceed to the stringent convergence requirements of the non-yielding computations because of stability problems, but did

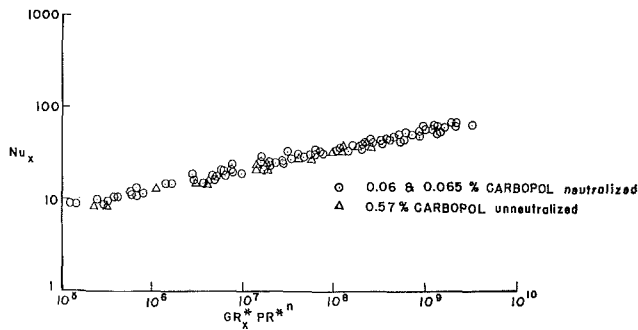


Fig. 8 Local heat transfer Carbowol 940 unneutralized and neutralized,  $n \sim 0.8$

indicate the boundary layer thickness shown in Fig. 6 along with the non-yielding fluid layer thickness. Fig. 7 shows the measured velocity distribution, those computed for no-yield stress, and those computed for the measured yield stress. Although the yield stress computations do not agree with the measured magnitudes, their shape is similar. This similarity of shape and the marked difference between the yielding and non-yielding values emphasizes the importance of the yield stress—even though small. One should especially note that the non-yielding computation and the measured shear stresses at the plate surface are similar (and if the yielding computation magnitudes were similar, the shear stresses would also be equal), demonstrating the insensitivity of the heat transfer to the yield stress behavior of the fluid.

For all tests the local Nusselt numbers were correlated according to

$$Nu_x = C(Gr_x^* Pr_x^n)^\beta$$

with the values of  $C$  and  $\beta$  listed in Table 3.

The standard deviations are those associated with the least-squares fit. To gain some feeling about the accuracy of the fit, the data were analyzed under the assumption that both the  $Nu$  and the  $Ra^*$  moduli were subject to error according to a procedure described by Wald [14]. The variations noted for  $C$  and  $\beta$  for the 0.05 percent CMC are the 95 percent confidence intervals.

Unlike water and CMC, the Carbowol solutions show strong changes of the flow index with temperature, and consequently the average fluid index varied considerably with the applied heat flux. For example, the 0.065 percent Carbowol tests had flow indices of 0.741, 0.744, 0.766, 0.766, 0.811, and 0.821. Consequently, the data were divided into two groups (those with  $n < 0.8$ , and those with  $n > 0.8$ ) and separate correlations made for each.

The exponent  $\beta$  agrees well with the expected value of  $1/(3n + 2)$ , and the coefficients  $C$  are in good agreement with the computed values for all fluids except the 0.68 and 0.75 percent Carbowol. It must be realized that the exponent determined by the least-squares fit is very sensitive to minor displacements of

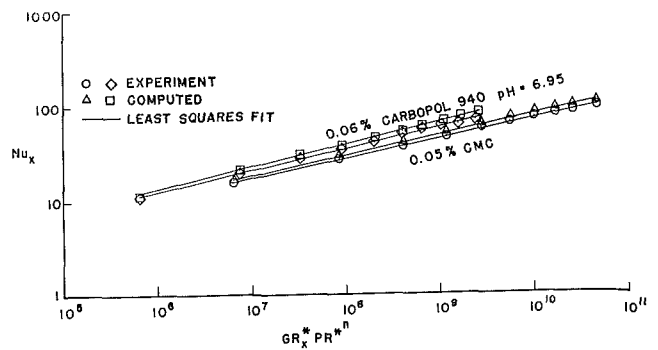


Fig. 9 Local heat transfer for CMC and Carbowol,  $q_w = 250$  Btu/hr-ft<sup>2</sup>

points and if  $\beta$  is changed to  $1/(3n + 2)$ , the coefficients become approximately 0.54 and 0.57. As noted by Schuh [15] and Kubaier and Pei [16], the coefficient increases slightly with the Prandtl modulus and for the 0.068 percent Carbowol, Prandtl number of 7000, the computed value of  $C$  would increase (using Schuh's results) from 0.48 to 0.53, in agreement with the measured data. However, the 0.75 percent computed  $C$  would be approximately 0.47 while the experiment at  $C$  for  $\beta = 1/(3n + 2)$  is 0.57. Whether this discrepancy is due to the low value of  $n$  or the high Prandtl number is not known but it must be recognized that for the very low values of  $n$ , and for very high consistencies, the generalized Rayleigh modulus was in the region of  $10^4$  and here conduction is of equal importance with convection and the form of the correlation given is likely to be inapplicable.

The average values of  $n$  for the 0.06 percent, 0.065 percent Carbowol neutralized and the 0.57 percent Carbowol unneutralized are approximately 0.8 and their correlations are

%	$C$	$\beta$	Pr (ave)	$n$
0.06	0.610	0.219	1052	0.805
0.065	0.649	0.218	1850	0.780
0.57	0.538	0.222	1090	0.807

Within the limits of the experimental errors, these correlations may be regarded as equal. Because of the variation of  $\beta$ , the coefficients  $C$  cannot be directly compared. However, a single plot of all these data (Fig. 8) illustrates the similarity of the data. Of these fluids the 0.06 percent Carbowol was observed to have a yield stress, although its data do not differ significantly from those of the other two fluids.

Similarly the 0.52 percent Carbowol unneutralized and the 0.05 percent CMC had flow indices nearly equal to 0.89 and correlations of

%	$C$	$\beta$	Pr (ave)
0.52	0.570	0.207	368
0.05	0.600	0.210	172

indicating that the flow index  $n$  is the most important rheological property which distinguishes fluids of moderate Prandtl moduli.

Table 3

Fluid	$n$	$C$	$\beta$	$\sigma_{\log Nu_x}$	$\sigma_{\log Ra^*}$	$C$ [Tien]	$C$ [computer]	$1/(3n + 2)$	pH
Water	1.0	0.607	0.200	0.019	0.06	0.682	0.615	0.200	7.0
0.05% CMC	0.888	0.600 $\pm 0.0027$	0.2101 $\pm 0.0003$	0.019	0.06	0.692	0.59	0.214	7.0
0.06% Carbowol	0.823(0.815 - 0.847)*	0.576	0.219	0.019	0.12	0.698	0.57	0.223	6.95
0.06% Carbowol	0.787(0.778 - 0.795)	0.595	0.223	0.03	0.057	0.700	0.56	0.229	6.95
0.065% Carbowol	0.816(0.811 - 0.821)	0.505	0.226	0.018	0.087	0.700	0.57	0.225	7.15
0.065% Carbowol	0.754(0.711 - 0.766)	0.546	0.233	0.023	0.15	0.705	0.55	0.235	7.15
0.52% Carbowol	0.893(0.881 - 0.918)	0.570	0.207	0.021	0.185	0.690	0.59	0.214	3.2
0.57% Carbowol	0.807(0.787 - 0.828)	0.538	0.222	0.023	0.027	0.700	0.56	0.226	3.2
0.68% Carbowol	0.564(0.535 - 0.611)	0.593	0.265	0.013	0.089	0.725	0.48	0.271	3.2
0.75% Carbowol	0.395(0.383 - 0.416)	0.660	0.299	0.013	0.12	0.755	0.41	0.314	3.2

\* Numbers in parentheses indicate the range of flow index  $n$ .

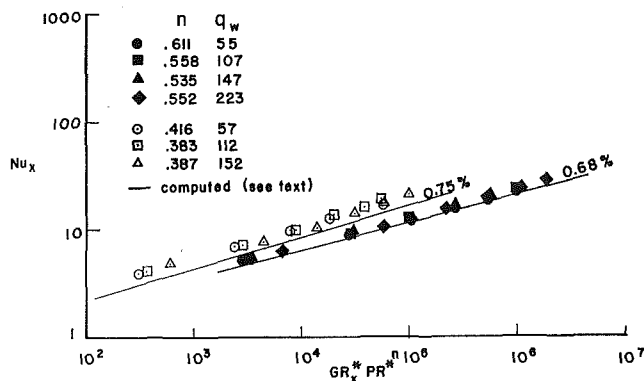


Fig. 10 Local heat transfer, Carbopol 940, pH = 3.2; small plate

### Comparison of Experiment and Computation

Table 4 indicates the correlations determined from the numerical computations and compared to specific experimental measurements. Since the experimental data are for only one specific heat flux, the experimental correlations of Table 4 differ slightly from those of Table 3. Fig. 9 illustrates the agreement between the measured 0.06 percent Carbopol and 0.05 percent CMC data and the numerical prediction based upon the experimental conditions, but incorporating temperature-dependent thermal conductivity and consistency. As a consequence of this agreement, and because of the prohibitively long computation times associated with the highly viscous unneutralized fluids, the other numerical predictions were based upon the computational results given earlier for fluids with Prandtl numbers of water. Fig. 10 indicates the data for the 0.75 percent Carbopol whose viscosity is 2500 times that of water and whose flow index is approximately 0.4, and for 0.68 percent Carbopol whose viscosity is 1500 times that of water with a flow index of 0.6 and the computed heat transfer behavior. The results of the more viscous fluid are seen to be somewhat higher than the computed behavior, in accord with Schuh's findings for Newtonian fluids, and Kubair and Pei's solution for the free-forced convection of non-Newtonian fluids.

Fig. 11 shows a comparison of representative heat transfer data for each of the various fluids tested, plotted as though they were Newtonian fluids. That is, the Rayleigh number used for this figure is the one for Newtonian fluids ( $Gr_x^* Pr_x^n$ ,  $n = 1.0$ ). The viscosities used in reducing the heat transfer data were the apparent viscosities evaluated at the average shear rates at the plate surface for each particular test fluid. For clarity, only one test run was used from each set of heat transfer data for a particular fluid.

While the results show reasonable agreement, it should be noted that as the fluid index decreases from 1.0, the greater the distance the points are from the Newtonian fluid heat transfer correlation. The maximum difference shown here is about 25 percent for the 0.75 percent Carbopol solution which had a fluid index of about 0.4. For the 0.06 percent Carbopol which has a fluid index of about 0.8, the difference is only about 10 percent. In many engineering applications, errors of this magnitude may be acceptable, thus allowing a designer to use heat transfer correlations with which he is familiar.

### Conclusions

Through the use of the finite-difference numerical calculations and the experimental measurements, we draw the following conclusions:

1. The similarity analysis of Acrivos and the integral approach of Tien provide the correct form of the generalized Rayleigh number and the exponent to be used in the local heat transfer coefficient correlation, although the measured coefficient  $C$  does not agree in its dependence upon the flow index  $n$ .

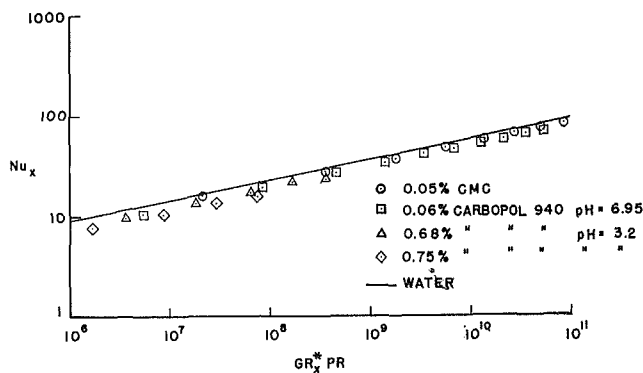


Fig. 11 Comparison of data based upon apparent Newtonian viscosity calculated at average shear rates for test conditions

Table 4

Fluid	$n$	$C$ experimental	$\beta$	$C$ computed	$\beta$	Heat flux (Btu/hr-ft <sup>2</sup> )
0.05% CMC	0.888	0.66	0.208	0.62	0.215	105
0.05% CMC	0.888	0.598	0.209	0.55	0.219	264
0.06% Carbopol	0.795	0.497	0.230	0.52	0.236	245

2 For moderate Prandtl number fluids ( $Pr \leq 10^3$ ), the flow index  $n$  appears to be the primary governing rheological parameter.

3 Free surface effects and small yield stresses substantially affect the velocity profiles in the outer portion of the boundary layer, but have little perceptible effect on the local heat transfer.

4 Viscometric data secured through concentric cylinder viscosities are applicable for correlating free convection data.

5 The finite-difference-power-law algorithms yield accurate predictions of velocities, temperatures, and local heat transfer coefficients for pseudoplastic fluids with Prandtl moduli of 5 to 12,500 and flow indices of 0.4 to 1.0.

6 The apparent viscosity of the non-Newtonian fluids, evaluated at the average shear rates at the plate surface, can be used in the standard Newtonian fluid correlations to give predictions whose error varies with  $n$ , but does not exceed 25 percent for  $n = 0.4$ .

### Acknowledgment

This study was carried out under the sponsorship of the National Science Foundation through Grant GK-567 and represents a portion of the doctoral thesis of J. D. Dale, reference [9]. The authors also wish to acknowledge a grant of computer time from the Computer Research Center of the University of Washington.

### References

- 1 Acrivos, A., "A Theoretical Analysis of Laminar Natural Convection Heat Transfer to Non-Newtonian Fluids," *AIChE Journal*, Vol. 6, 1960, pp. 584-590.
- 2 Reilly, I. G., Tien, C., and Adelman, M., "Experimental Study of Natural Convective Heat Transfer from a Vertical Plate in a Non-Newtonian Fluid," *Can. J. Chem. Eng.*, 1965, pp. 157-160.
- 3 Emery, A. F., Chi, H. W., and Dale, J. D., "Free Convection Through Vertical Plane Layers of Non-Newtonian Power Law Fluids," *JOURNAL OF HEAT TRANSFER, TRANS. ASME, Series C, Vol. 93, No. 2, May 1971, pp. 164-171.*
- 4 Tien, C., "Laminar Natural Convection Heat Transfer from Vertical Plate to Power-Law Fluid," *Appl. Sci. Res.*, Vol. 17, 1967, pp. 233-248.
- 5 Emery, A. F., and Chu, N. C., "Heat Transfer Across Vertical Layers," *JOURNAL OF HEAT TRANSFER, TRANS. ASME, Series C, Vol. 87, No. 1, Feb. 1965, pp. 110-116.*
- 6 MacGregor, R. K., and Emery, A. F., "Free Convection Through Vertical Plane Layers—Moderate and High Prandtl Number Fluids," *JOURNAL OF HEAT TRANSFER, TRANS. ASME, Series C, Vol. 91, No. 3, Aug. 1969, pp. 391-403.*
- 7 Na, T. Y., and Hansen, A. G., "Possible Similarity Solutions

of the Laminar Natural Convection Flow of Non-Newtonian Fluids," *International Journal of Heat and Mass Transfer*, Vol. 9, 1966, pp. 261-262.

8 Lee, S. Y., and Ames, W. F., "Similarity Solutions for Non-Newtonian Fluids," *AIChE Journal*, Vol. 12, No. 4, 1966, pp. 700-708.

9 Dale, J. D., "Laminar Free Convection of Non-Newtonian Fluids from a Vertical Flat Plate with Uniform Surface Heat Flux," PhD thesis, University of Washington, Seattle, Wash., 1969.

10 Sparrow, E. M., and Gregg, J. L., "Laminar Free Convection From a Vertical Plate With Uniform Surface Heat Flux," *TRANS. ASME*, Vol. 78, 1956, pp. 435-440.

11 Christiansen, E. B., and Craig, S. E., Jr., "Heat Transfer to Pseudoplastic Fluids in Laminar Flow," *AIChE Journal*, Vol. 8, No. 2, 1962, pp. 154-160.

12 Grassmann, P., and Staumann, W., "Ein Instationäres Verfahren zur Messung der Wärmeleitfähigkeit von Flüssigkeiten und Gasen," *International Journal of Heat and Mass Transfer*, Vol. 1, No. 1, June 1960, pp. 50-54.

13 Dotson, J. P., "Heat Transfer from a Vertical Flat Plate by Free Convection," MS thesis, Purdue University, May 1954.

14 Wald, A., "The Fitting of Straight Lines if Both Variables are Subject to Error," *Ann. Math. Stat.*, Vol. 11, 1940, pp. 284-300.

15 Schuh, H., "Einige Probleme bei freier Strömung zäher Flüssigkeiten," *Göttinger Monographien*, Bd. B, Grenzschichten, 1946.

16 Kubair, V. G., and Pei, D. C. T., "Combined Laminar Free and Forced Convection Heat Transfer to Non-Newtonian Fluids," *International Journal of Heat and Mass Transfer*, Vol. 11, No. 5, 1968, pp. 885-899.

R. P. CAREN  
Director.

C. K. LIU  
Associate Research Scientist.

Engineering Sciences,  
Lockheed Palo Alto  
Research Laboratory,  
Palo Alto, Calif.

## Thermal Radiation from a Microscopically Roughened Dielectric Surface

*The emission of thermal radiation from a microscopically roughened dielectric surface is treated using a laminar-inhomogeneous layered model for a representation of the effective spatial variation in refractive index associated with a roughened surface layer. The Riccati equation is used to calculate the modification to the spectral angular transmittance of the surface due to the presence of this inhomogeneous surface layer. A consideration of the emission of radiant energy from the bulk dielectric through the surface layer permits the angular emittance to be determined. Total emittance values are obtained using the spectral angular emittance data.*

### Introduction

It is a well-known fact that surface roughness affects to a great extent the magnitude, the angular distribution, and the wavelength dependence of the radiation properties of a surface. For optically smooth surfaces, the monochromatic reflectance in the specular direction can be predicted from electromagnetic theory (the well-known Fresnel laws of reflection). For an optically thick material, the magnitude and the directional distribution of the emittance can then be obtained with the aid of Kirchhoff's law. Although the results obtained are applicable only to the ideal condition of optically smooth surfaces, they can be used for heat-transfer computations on surfaces where the effects of surface roughness, oxidation, and surface strain are insignificant.

However, when the effects of surface roughness exceed the influence of the optical properties of the pure material, the radiation properties can no longer be predicted by classical optics alone. Various investigators have attempted to extend the classical electromagnetic theory to include the effect of surface roughness. A comprehensive review of the major analytical treatments has been carried out by Beckmann and Spizzichino [1].<sup>1</sup> Two basic approaches have been employed in the analysis of the interaction of electromagnetic waves with a randomly rough surface. The first is based on an exact solution by Maxwell's equations involving complex boundary conditions, as done by Rice [2]. The second and less-rigorous approach as reported by Davies [3] is based on an approximation to the exact case, using Fresnel and Fraunhofer diffraction theories. In each case

the surface is assumed to be free of small-scale roughness, i.e., the radius of curvature of the surface is much larger than the wavelength of the incident radiation. In this case the surface is locally smooth and the Fresnel equations apply locally providing the angle of incidence is measured with respect to the local surface normal. Both analyses show that for a slightly rough surface a closed-form solution of the spectral angular reflectance on a stochastically rough surface can be approximated by

$$\rho(\varphi, \lambda) = \rho_{\infty}(\varphi, \lambda) \cdot \exp\{-16\pi^2\sigma_m^2 \cos^2 \varphi / \lambda^2\} \quad (1)$$

where  $\rho_{\infty}$  is the spectral angular reflectance of an optically smooth surface,  $\sigma_m$  is the rms surface roughness,  $\varphi$  is the angle of incidence measured from the surface normal, and  $\lambda$  is the wavelength of incident radiation. Equation (1) has been verified experimentally [4, 5] under the condition

$$\left(\frac{\sigma_m}{\lambda}\right)^2 \cos^2 \varphi \ll 1 \quad (2)$$

In this paper the surface is assumed to be microscopically rough, i.e., there are many surface features on an area of the surface given by  $\lambda^2$ . In this case the previous analyses do not apply. Here we treat the electromagnetic properties of the microscopically rough surface by assuming the transition region, i.e., the roughened layer extending from the bulk material to vacuum, can be represented as a laminar-inhomogeneous layer of equivalent thickness. The index of refraction of this layer at a given value of the  $z$  coordinate, whose axis is along the normal to the surface, is taken to be an average value for the roughened surface over a plane parallel to the surface at the same  $z$  coordinate.

The reflectance of this laminar-inhomogeneous layer is calculated utilizing the Riccati equation as modified by Van Cittert [6] for determining electromagnetic amplitude reflection coefficients. Assuming that the dielectric bulk material is optically thick, a knowledge of the reflectance of the transition layer combined

<sup>1</sup> Numbers in brackets designate References at end of paper.

Contributed by the Heat Transfer Division for publication (without presentation) in the JOURNAL OF HEAT TRANSFER. Manuscript received by the Heat Transfer Division December 29, 1970. Paper No. 71-HT-U.

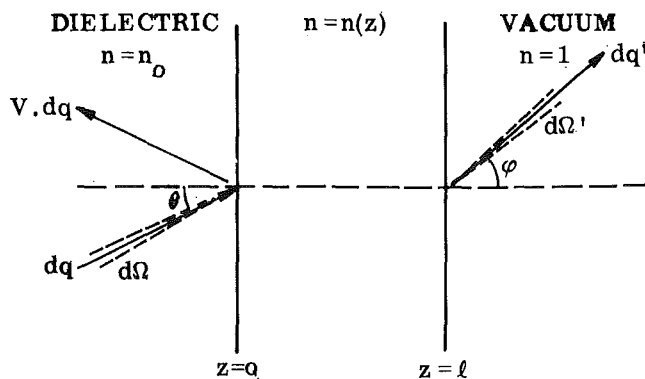


Fig. 1 Reflection and transmission of an electromagnetic wave through a laminar-inhomogeneous layer

with Kirchoff's law provides the emittance of the roughened dielectric surface.

Utilizing this analysis, values of spectral angular emittance, total angular emittance, and total hemispherical emittance are presented for various distributions of the refractive index in the layer, and for various layer thicknesses and temperatures.

## Analysis

Let us consider the geometry shown schematically in Fig. 1. The dielectric is separated from the vacuum by a laminar-inhomogeneous layer of thickness  $l$  in which the variation of the refractive index  $n(z)$  with layer depth is equivalent to that occurring in a microscopically roughened surface layer.

The problem in translating a roughened surface layer into an equivalent inhomogeneous surface layer from the standpoint of radiative properties is to provide an equivalence in the two cases in terms of the variation of refractive index with respect to depth. Landau and Lifshitz [7] have provided a formalism which may be used to establish the effective index with respect to depth for a roughened surface layer. Here the effective dielectric constant  $\epsilon_{\text{mix}}$  of a volume element encompassing the two phases (portions of the roughened dielectric and vacuum) is given through the defining equation

$$\bar{D} = \epsilon_{\text{mix}} \bar{E} \quad (3)$$

where  $\bar{D}$  and  $\bar{E}$  are respectively the average displacement and electric field vectors in the volume element. Landau and Lifshitz have observed that these average field vectors can be defined through the equation

$$\frac{1}{V} \int_V (D - \epsilon_1 E) dV = \bar{D} - \epsilon_1 \bar{E} \quad (4)$$

where, in the present case,  $\epsilon_1$  is the dielectric constant associated with the vacuum phase, i.e.,  $\epsilon_1 = 1$ . Consider an electromagnetic wave at normal incidence to the dielectric. Here, the electric field vector will be continuous across the vacuum-dielectric boundary and thus the displacement vector in the dielectric will be given by  $D = \epsilon_2 E$ ; further,  $\bar{E} = E$ , where  $E$  is the electric field vector in vacuum. Substituting this relationship in equation (4), we find

$$C(\epsilon_2 - \epsilon_1) \bar{E} = \bar{D} - \epsilon_1 \bar{E} \quad (5)$$

where  $C$  is the fractional volume occupied by the dielectric in the volume element of interest. This follows since in the vacuum phase the integral vanishes except in the portions of the volume encompassing the dielectric phase. Thus, we have

$$\bar{D} = [\epsilon_1 + C(\epsilon_2 - \epsilon_1)] \bar{E}$$

or

$$\epsilon_{\text{mix}} = \epsilon_1 + C(\epsilon_2 - \epsilon_1) \quad (6)$$

Utilizing the well-known relationship that the index of refraction of a medium is related to its dielectric constant by  $n^2 = \epsilon$ , we have

$$n_{\text{mix}}^2 = 1 + C(n_0^2 - 1) \quad (7)$$

For any given roughened surface geometry, the average volumetric concentration of the dielectric phase can be defined as a function of depth, i.e.,  $C = C(z)$ . Once this latter quantity has been defined, the effective index of the roughened layer with depth is simply

$$n^2(z) = 1 + C(z)(n_0^2 - 1) \quad (8)$$

## Nomenclature

$c$ = velocity of light in vacuum = $2.998 \times 10^8$ m/sec	$V_s$ = amplitude reflection coefficient of $s$ wave	$\epsilon_H(l)$ = total hemispherical emittance, stochastically rough surface
$e_{\lambda\lambda}(T)$ = spectral blackbody emissive power, $w/m^2$	$V_p$ = amplitude reflection coefficient of $p$ wave	$\epsilon_{H\infty}$ = total hemispherical emittance, smooth surface
$h$ = Planck's constant	$\rho(\varphi, \lambda, l)$ = spectral angular reflectance on a stochastically rough surface	$\theta$ = angle of incidence
$k$ = Boltzmann's constant	$\rho_{\infty}(\varphi, \lambda)$ = spectral angular reflectance of an optically smooth surface	$\theta_c$ = critical angle of incidence
$k_0$ = wave number in vacuum, $2\pi/\lambda$	$\epsilon(\varphi, \lambda, l)$ = spectral angular emittance, stochastically rough surface	$\lambda$ = wavelength of electromagnetic wave
$l$ = thickness of inhomogeneous layer, m	$\epsilon_{\infty}(\varphi, \lambda)$ = spectral angular emittance, smooth surface	$\lambda_m$ = wavelength at which $e_{\lambda\lambda}$ is maximum = $0.2898/T$ cm
$m$ = function of $z$ defined by equation (4)	$\epsilon(\varphi, l)$ = angular emittance, stochastically rough surface	$\rho$ = reflectance = $\frac{1}{2}( V_s ^2 +  V_p ^2)$
$n$ = refractive index; $n_0$ is the value of $n$ at $z = 0$	$\epsilon_{\infty}(\varphi)$ = angular emittance, smooth surface	$\sigma$ = Stefan-Boltzmann constant = $5.668 \times 10^{-8}$ $w/(m^2 \text{ deg } K^4)$
$n_0 l / \lambda_m \cos \varphi$ = dimensionless optical thickness of the inhomogeneous layer	$\epsilon_N(l)$ = normal emittance, stochastically rough surface	$\sigma_m$ = rms roughness
$q$ = time-averaged radiation heat flux defined by equation (13)	$\epsilon_{N\infty}$ = normal emittance, smooth surface	$\tau$ = refractive angle at solid-vacuum surface
$T$ = absolute temperature, deg K		$\Omega$ = solid angle, steradian
$\tau_s$ = transmittance of $s$ wave		$\gamma$ = function of $z$ and $n$ defined by equations (5) and (6)
$\tau_p$ = transmittance of $p$ wave		

This, then, is the proper prescription for the index of refraction of the corresponding inhomogeneous surface layer with depth.

The amplitude reflection coefficient of a plane electromagnetic wave incident at the interface,  $z = 0$ , taking into account the multiple reflections in the layer, is given by Van Cittert's modification of the Riccati equation [6, 8]

$$\frac{dV}{dz} = -2imV + \gamma(1 - V^2) \quad (9)$$

where

$$m(z) = k_0 n(z) \cos \theta(z) \quad (10)$$

For the case in which the electric vector is polarized normal to the plane of incidence (*s* wave),

$$\gamma_s(z) = \frac{m'}{2m} \quad (11)$$

For the case in which the electric vector is polarized parallel to the plane of incidence (*p* wave)

$$\gamma_p(z) = \frac{m'}{2m} - \frac{n'}{n} \quad (12)$$

The quantities  $m'$  and  $n'$  are the derivatives of  $m$  and  $n$  with respect to  $z$ . According to Snell's law, the product  $n(z) \sin \theta(z)$  is a constant. This latter fact can be used to yield a relationship between  $\theta'$  and  $n'$ . Hence, equations (11) and (12) can be rewritten as

$$\gamma_s(z) = \frac{n'}{2n(z) \cos^2 \theta} \quad (11a)$$

$$\gamma_p(z) = \frac{n'}{n(z)} \left( \frac{1}{2 \cos^2 \theta} \right) - 1 \quad (12a)$$

In order to solve equation (3) uniquely, the boundary condition to be used is

$$V \rightarrow 0 \quad \text{as} \quad z \rightarrow l \quad (13)$$

To provide a general solution to equation (9) for all values of  $l/\lambda$  and  $V$ , we let

$$V = X + iY \quad (14)$$

By substituting equation (14) into equation (9) and separating the real and imaginary terms, we obtain

$$\frac{dX}{dz} = 2mY + \gamma(1 + Y^2 - X^2) \quad (15a)$$

$$\frac{dY}{dz} = -2mX - 2\gamma XY \quad (15b)$$

The amplitude reflection coefficient at  $z = l$  is assumed to be zero; using this assumption, the amplitude reflection coefficient at  $z = 0$  is obtained by numerical integration of equation (15) to give

$$|V| = (X^2 + Y^2)^{1/2} \quad (16)$$

This is a function of  $\lambda$  and  $\theta$  for a given  $n(z)$  and  $l$ .

From equations (11) and (12), it is seen that two values of  $|V|$  at  $z = 0$  can be separately evaluated from equation (16), corresponding to the cases in which the electric field vector lies normal or parallel to the plane of incidence. These can be designated  $|V|_s$  and  $|V|_p$ , respectively.

Since the layer is non-absorbing or optically thin, the transmittance at  $z = l$  can then be given by

$$\tau_s = 1 - |V|_s^2 \quad (17a)$$

$$\tau_p = 1 - |V|_p^2 \quad (17b)$$

For thermal radiation which is unpolarized, the above may be combined to give

$$\tau = \frac{1}{2}(\tau_s + \tau_p) \quad (18)$$

Referring to Fig. 1, internally generated thermal radiation flux incident in an element of solid angle  $d\Omega$  at the angle of incidence  $\theta$  and with a wavelength in the range of  $d\lambda$  has a time-average value per unit surface area of

$$dq = \frac{e_{b\lambda}}{\pi} n^2 \cos \theta d\Omega d\lambda \quad (19)$$

The transmitted fraction of the flux is

$$dq' = \tau dq = \tau \frac{e_{b\lambda}}{\pi} n^2 \cos \theta d\Omega d\lambda \quad (20)$$

This flux can be translated into the emergent flux by noting that the angles  $\theta$  and  $\varphi$  shown in Fig. 1 are connected through Snell's law,

$$n \sin \theta = \sin \varphi \quad (21)$$

Hence,

$$\begin{aligned} \cos \theta d\Omega &= 2\pi \sin \theta \cos \theta d\theta \\ &= 2\pi \sin \varphi \cos \varphi d\varphi / n^2 \\ &= \cos \varphi d\Omega' / n^2 \end{aligned} \quad (22)$$

Equations (19) and (20) can now be written as

$$dq = \frac{e_{b\lambda}}{\pi} \cos \varphi d\Omega' d\lambda \quad (19a)$$

$$dq' = \tau \frac{e_{b\lambda}}{\pi} \cos \varphi d\Omega' d\lambda \quad (20a)$$

By use of Krichhoff's law, the spectral angular emittance is defined as the ratio of the transmitted fraction of the flux to the emission of a blackbody per unit time and surface area contained within a solid angle  $d\Omega'$  and a wavelength range  $d\lambda$ , i.e.,

$$\epsilon(\varphi, \lambda, l) = dq'/dq = \tau \quad (23)$$

The total angular emittance is defined by

$$\begin{aligned} \epsilon(\varphi, l) &= \int_{\lambda} dq' / \int_{\lambda} dq \\ &= \int_0^{\infty} \tau e_{b\lambda} d\lambda / (\sigma T^4) \end{aligned} \quad (24)$$

The total hemispherical emittance is defined by

$$\epsilon_H(l) = \frac{2}{\sigma T^4} \int_0^{\infty} \int_0^{\pi/2} \tau e_{b\lambda} \sin \varphi \cos \varphi d\varphi d\lambda \quad (25)$$

## Results

Exact solutions of the amplitude reflection coefficients for normal incidence have been obtained by Rayleigh [9] and Brèkhovskikh [10] where the index of refraction varies according to

$$n(z) = \frac{2l}{l+z} \quad (26)$$

To test the validity of the present method, the amplitude reflection coefficients with the same  $n(z)$  variations as in equation (26) were determined from equations (15) and (16). The results, as shown in Fig. 2(a), are identical to the exact solutions given in [9] and [10]. The results show that as  $k_0 l$  increases, the absolute value of the amplitude reflection coefficients in the direction normal to the surface fall off sharply to zero and then fluctuate. The

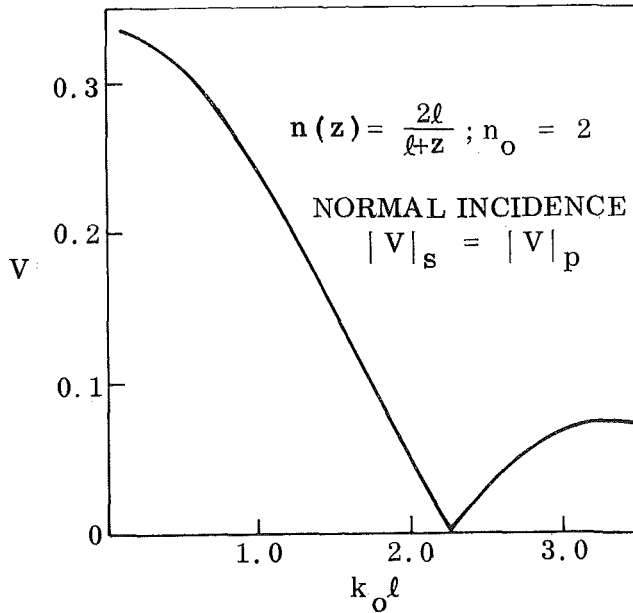


Fig. 2(a) Reflection coefficients;  $|V|$  vs.  $k_0 l$  at normal incidence

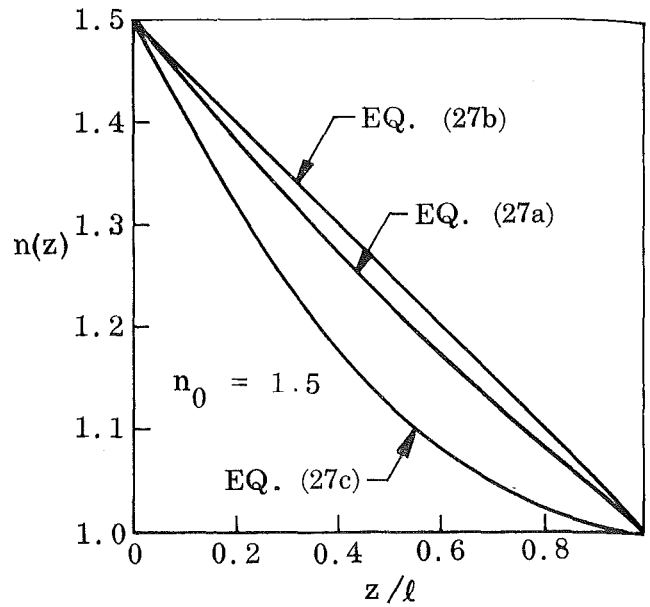


Fig. 2(b) Refractive indices;  $n(z)$  vs.  $z/l$

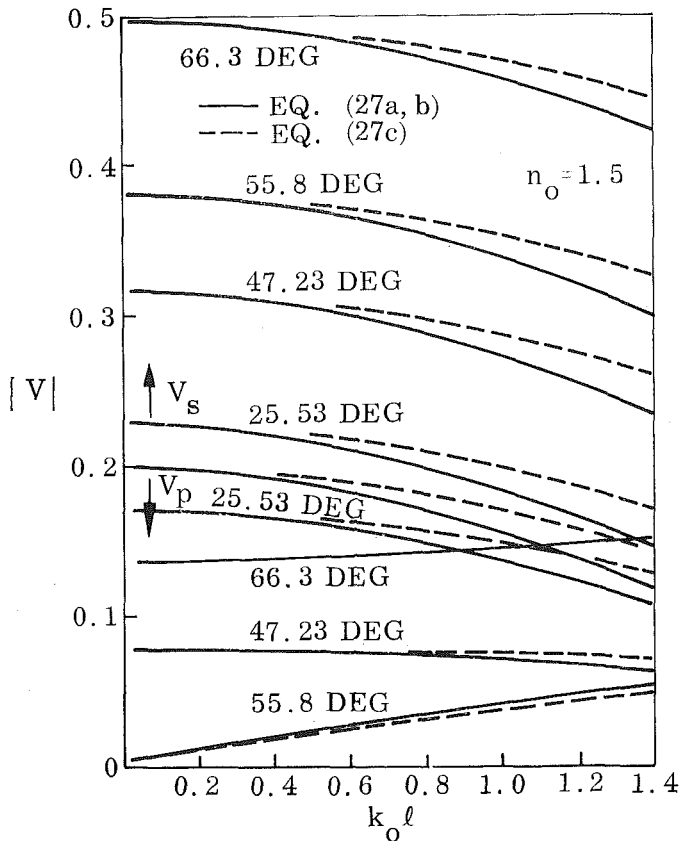


Fig. 2(c) Reflection coefficients;  $|V|_s$  and  $|V|_p$  vs.  $k_0$

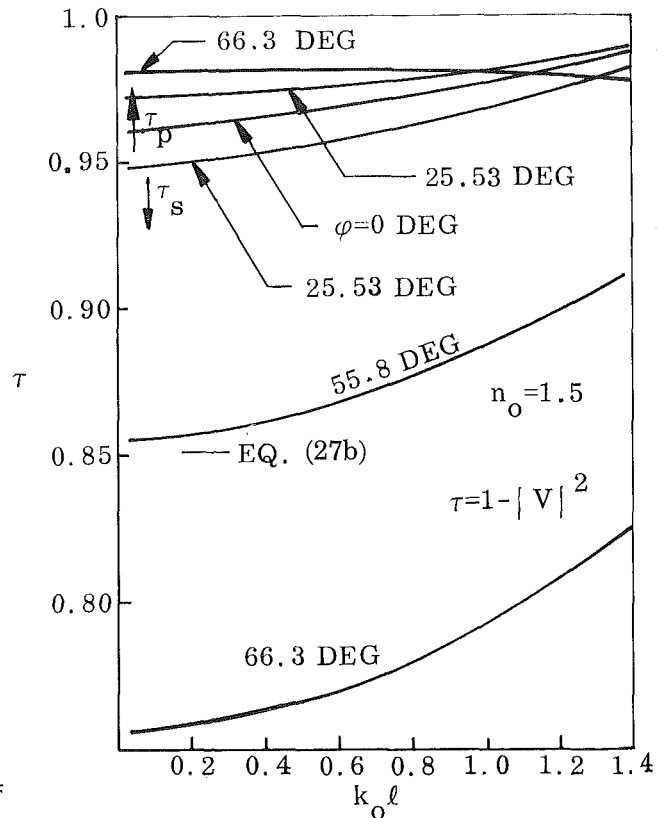


Fig. 2(d) Transmission coefficients;  $\tau_s$  and  $\tau_p$  vs.  $k_0 l$

amplitude coefficient is zero whenever the value of the  $k_0 l$  ( $= 2\pi l/\lambda$ ) is given by  $[(\pi J/\ln n_0)^2 + 1/4]^{1/2}(n_0 - 1)/n_0$ , where  $J$  is any positive integer. As the value of  $k_0 l$  increases, the peak values of  $|V|$  become smaller and smaller. Hence, as  $l/\lambda$  grows large, the values of  $|V|$  become so small that we can approximate the value of transmittance as unity.

One of the prime considerations in the representation of a roughened surface by a laminar-inhomogeneous layer is the sensi-

tivity of the resulting transmission coefficients to the particular spatial variation of the index of refraction of the layer chosen for the representation. Since for a particular roughened surface the surface characteristics are not generally experimentally well-defined, it is highly uncertain just what particular geometry to choose for its mathematical representation. Hence, if the present analyses are to represent a realistic analytical technique, hopefully the results should not depend strongly on the particular dielectric mass distribution chosen to develop  $n(z)$  for the laminar-



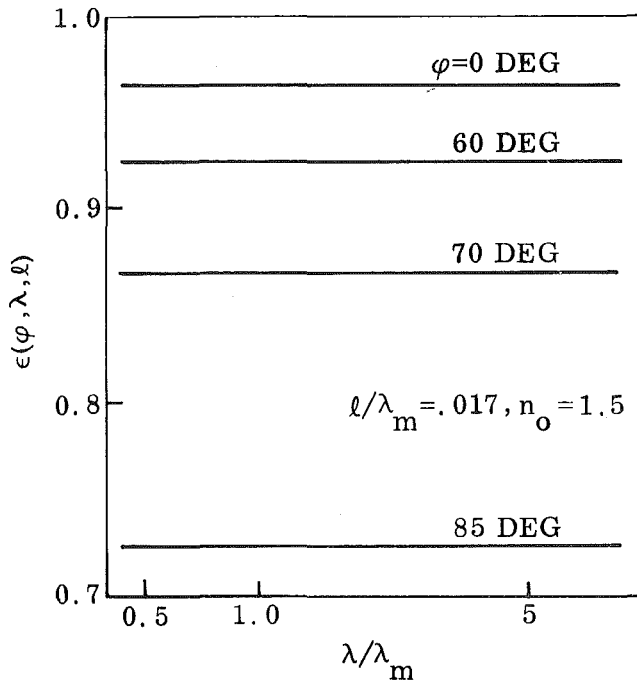


Fig. 3(a) Spectral angular emittance— $n_0 = 1.5$ ,  $\epsilon(\varphi, \lambda, l)$  vs.  $\lambda/\lambda_m$ ,  $l/\lambda_m = 0.017$

inhomogeneous layer. To investigate this question, we will consider several alternative surface mass distributions given by the following geometries:

- (a) Two-dimensional half-sine surfaces
- (b) Two-dimensional triangular surfaces
- (c) Three-dimensional cones

The refractive index  $n(z)$  at each  $z$ ,  $0 \leq z \leq l$ , can be assumed to be given by  $(n^2(z) - 1)/(n_0^2 - 1) = A(z)$  [see equation (8)], where  $A(z)$  is the fractional area occupied by the dielectric material in a plane normal to the  $z$  axis. The distribution of refractive indices for the above geometries are then given respectively by:

$$n(z) = (n_0 - 1) \left[ 1 - \frac{2}{\pi} \sin^{-1}(z/l) \right]^2 + 1 \quad (27a)$$

$$n(z) = (n_0 - 1)(1 - z/l) + 1 \quad (27b)$$

$$n(z) = (n_0 - 1)(1 - z/l)^2 + 1 \quad (27c)$$

where  $n_0$  is the value of  $n$  at  $z = 0$ . The rms roughness  $\sigma_m$  has generally been used to characterize the roughness of a surface. Hence,  $l$  may be replaced by  $\sigma_m$  through its definition.

Equations (27) are plotted in Fig. 2(b) for the case of  $n_0 = 1.5$ .

The angular dependence of the amplitude reflection coefficients is shown in Fig. 2(c). The results as calculated by use of equations (27a) and (27b) for a representation of surface roughness are practically the same (shown as solid lines). For small values of  $k_0 l (\leq 0.5)$ , the values of  $|V|$  as calculated from equation (27c) are also identical to those computed from equations (27a). However, as  $k_0 l$  increases, the amplitude reflection corresponding to equation (27c), shown as dotted lines in Fig. 2(c), is seen to become gradually higher than that for the surface roughness given by equations (27a) and (27b), except for  $|V|_p$  at  $\varphi \geq 55$  deg. The differences are appreciably higher in  $|V|_s$  than in  $|V|_p$ . Nevertheless, the maximum difference in the resulting values of transmittance is less than 1½ percent in all cases. Hence, only the simpler linear distribution of equation (27b) is used for the succeeding calculations.

The transmittances are calculated from equations (17) and (18). Typical results for  $n_0 = 1.5$  are plotted in Fig. 2(d). The spectral angular emittances were calculated from equation (23) and plotted in Fig. 3. The total angular emittances were calculated from equation (24) and plotted in Fig. 4. The total hemispherical emittances were calculated from equation (25) and plotted in Fig. 5. The above results are presented with  $n_0 = 1.5$ , 2.0, and 4.0, and layer thicknesses ranging from  $l/\lambda_m = 0.0017$  to 0.34.

## Discussion

In the present analysis, the value of  $n$  at  $z = l$  is taken to be 1 (the layer is facing vacuum), while the value of  $n_0$  is that of the homogeneous bulk material separated by the layer from the vacuum. Typical values of amplitude reflection coefficients calculated from equations (15) and (16), in which  $n(z)$  varies accord-

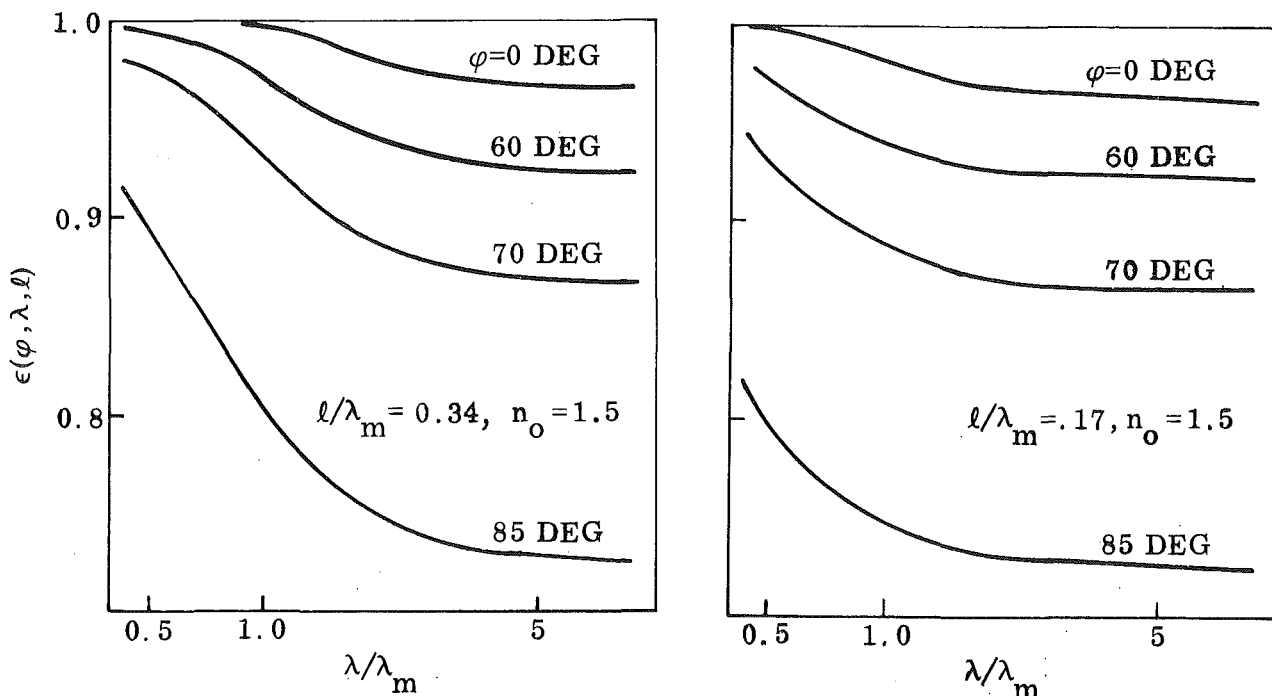


Fig. 3 Spectral angular emittance— $n_0 = 1.5$ ; (b)(right)  $\epsilon(\varphi, \lambda, l)$  vs.  $\lambda/\lambda_m$ ,  $l/\lambda_m = 0.17$ ; (c)(left)  $\epsilon(\varphi, \lambda, l)$  vs.  $\lambda/\lambda_m$ ,  $l/\lambda_m = 0.34$

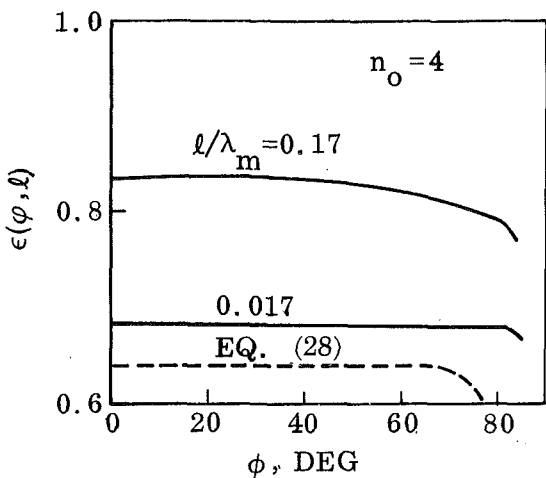
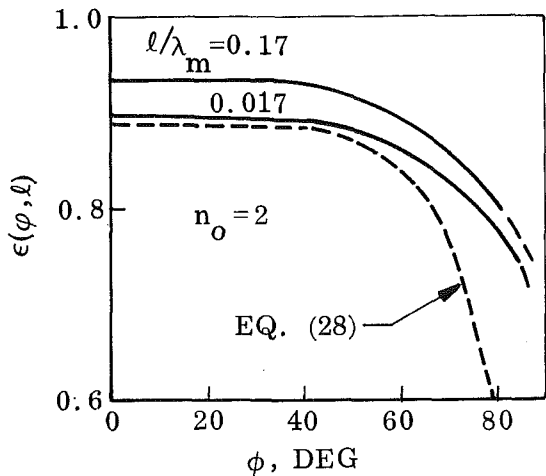
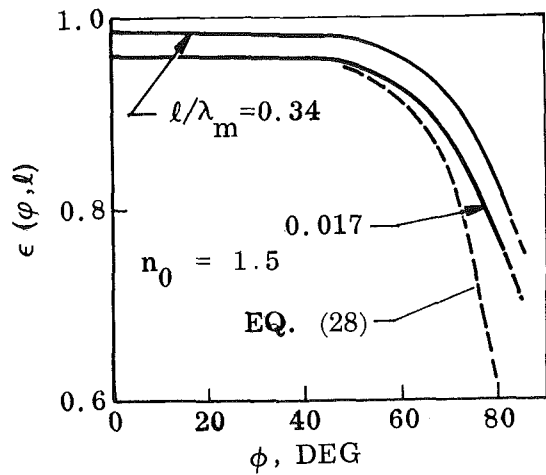


Fig. 4 Total angular emittance; (a) (top)  $\epsilon(\varphi, l)$ , vs.  $\varphi$ ,  $n_0 = 1.5$ ; (b) (middle)  $\epsilon(\varphi, l)$  vs.  $\varphi$ ,  $n_0 = 2$ ; (c) (bottom)  $\epsilon(\varphi, l)$  vs.  $\varphi$ ,  $n_0 = 4$

ing to equation (27), are plotted in Fig. 2(c) for  $n_0 = 1.5$ . The following observations have been made from these results:

(a) For the component of the electromagnetic wave parallel to the plane of incidence, the amplitude reflection coefficient  $|V_p|$  decreases with increasing  $\varphi$  and reaches a minimum at approximately  $\varphi = 55.8$  deg ( $\theta = 33.45$  deg). The values of  $V_p$  then increase rapidly toward 1 at  $\varphi = 90$  deg ( $\theta = \theta_c = 41.81$  deg). The value of  $\theta$  where  $V_p$  is a minimum agrees with the Brewster angle which is given by  $\cot^{-1} n_0$ .

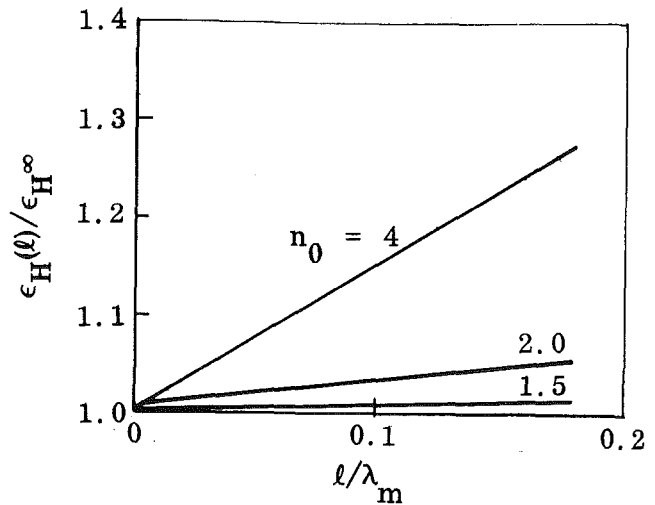
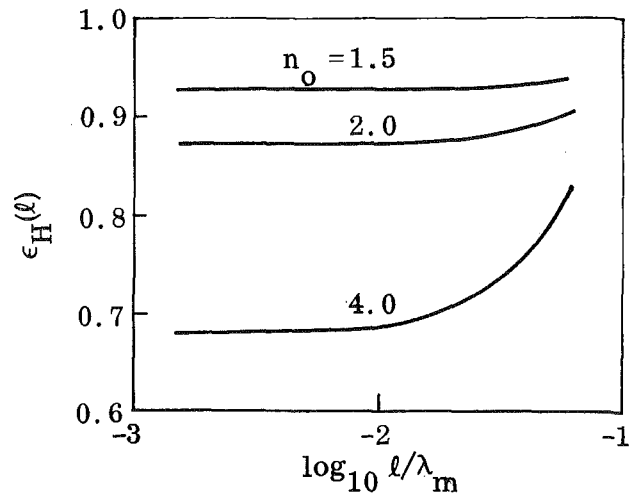


Fig. 5 Total hemispherical emittance; (a) (top)  $\epsilon_H(l)$  vs.  $l/\lambda_m$ ; (b) (bottom)  $\epsilon_H(l)/\epsilon_{H\infty}$  vs.  $l/\lambda_m$

(b) Both  $|V_s|$  and  $|V_p|$  decrease with increasing values of  $k_0 l$  ( $= 2\pi l/\lambda$ ), except for  $|V_p|$  at  $\varphi > 50$  deg. In the latter case,  $|V_p|$  increases slowly with  $k_0 l$ .

(c) At long wavelengths, or for very thin layers such that  $k_0 l \rightarrow 0$ , the amplitude reflection coefficients are relatively insensitive to wavelength. This should be the case since for a smooth dielectric surface the reflectance is independent of wavelength [11]. For the case of normal incidence, as  $k_0 l \rightarrow 0$ , the amplitude reflection coefficient  $|V|$  is seen to approach that of a smooth surface as given by  $(n-1)/(n+1)$ .

(d) The results as calculated by using any one of the equations (27) are practically the same. This implies that the amplitude reflection at  $z = 0$  is not significantly affected by the assumed  $n(z)$  distributions in the layer.

The transmittances calculated from equations (17) and (18) for the case of  $n_0 = 1.5$  are plotted in Fig. 2(d).

These results indicate that the roughness effects on the transmittance become significant at  $k_0 l \gtrsim 0.5$  or  $l/\lambda \gtrsim 0.1$ . If we define  $\lambda_m = 2.898 \times 10^{-3}/T$  m, where  $\lambda_m$  is the wavelength at which the blackbody emissive power is a maximum and  $T$  is in deg K, then the layer thicknesses used in the following calculations are in the range defined by

$$0.0017 \leq l/\lambda_m \leq 0.34$$

Typical values of the spectral angular emittance as calculated from equation (23) are plotted in Fig. 3(a, b, c) for  $l/\lambda_m = 0.017$ ,

0.17, and 0.34. The refracting index  $n(z)$  varies according to equation (27b) with  $n_0 = 1.5$ . At small values of  $l/\lambda_m$  (very thin layers or low temperatures), the effect of  $\lambda/\lambda_m$  is small and the surface can be treated as gray. At higher  $l/\lambda_m$ ,  $\epsilon(\varphi, \lambda, l)$  decreases monotonically with increasing  $\lambda/\lambda_m$ .

The total angular emittance values calculated from equation (24) are plotted in Fig. 4(a, b) for  $n_0 = 1.5$  and 2.0, respectively. At given  $l/\lambda_m$ ,  $\epsilon(\varphi, l)$  remains uniform for  $\varphi$  between zero and an angle which increased with  $n_0$ . Beyond this point,  $\epsilon(\varphi, l)$  falls off rapidly. At  $n_0 = 4$  and  $l/\lambda_m = 0.017$ , Fig. 4(c),  $\epsilon(\varphi, l)$  remains uniform up to very large  $\varphi$  ( $\approx 80$  deg). At a given value of  $\varphi$ , the magnitude of  $\epsilon(\varphi, l)$  decreases with increasing  $n_0$ ; but the value of  $\epsilon(\varphi, l)$  increases with increasing  $l/\lambda_m$  and this increase is rapid for higher values of  $n_0$ . The total angular emittance of a smooth dielectric surface, based on electromagnetic theory, is given by Sparrow and Cess [12] as

$$\epsilon_{\infty}(\varphi) = \frac{2a \cos \varphi}{(a + \cos \varphi)^2} \left[ 1 + \frac{n_0^2}{(a \cos \varphi + \sin^2 \varphi)^2} \right] \quad (28)$$

in which  $a^2 = n_0^2 - \sin^2 \varphi$ . For normal incidence, equation (28) yields

$$\epsilon_{\infty} = 4n_0/(n_0 + 1)^2 \quad (28a)$$

Equation (28) has been used to calculate  $\epsilon_{\infty}$  and the results are plotted in Fig. 4(a, b, c) as dotted lines. As  $l/\lambda_m \rightarrow 0$ , it can be seen that  $\epsilon(l, \varphi) \rightarrow \epsilon_{\infty}(\varphi)$  only at low  $n_0$  and small  $\varphi$ . This is due to the fact that for non-normal emittance the dimensionless optical thickness is approximately given by  $n_0 l/\lambda_m \cos \varphi$ . For example, if  $n_0 = 4$  and  $\varphi = 80$ , then the effective ratio of  $n_0 l/\lambda_m \cos \varphi$  for  $l/\lambda_m = 0.017$  is approximately 0.4, a significant dimensionless film thickness in terms of modification of the optical properties. Therefore, at high  $n_0$  and large  $\varphi$ , the effect of roughness can still be significant for small values of  $l/\lambda_m$ .

Total hemispherical emittances  $\epsilon_H(l)$  as calculated from equation (25) are plotted in Fig. 5(a). It is seen that  $\epsilon_H(l)$  decreases with increasing  $n_0$ . In general,  $\epsilon_H(l)$  increases with  $l/\lambda_m$  more rapidly at higher  $n_0$ . As  $l/\lambda_m$  approaches zero, the values of  $\epsilon_H(l)$  should approach  $\epsilon_{H\infty}$  of a smooth dielectric surface of the same value of  $n_0$ . The latter as given in [12] is

$$\frac{\epsilon_{H\infty}}{\epsilon_n} = \frac{\epsilon_{HS}}{\epsilon_n} = \frac{1}{2} \left[ \frac{2}{3} + \frac{1}{3n_0} + \frac{n_0(n_0 + 1)^2(n_0^2 - 1)^2}{2(n_0^2 + 1)^3} \ln \left( \frac{n_0 + 1}{n_0 - 1} \right) + \frac{n_0^2(n_0 + 1)(n_0^2 + 2n_0 - 1)}{(n_0^2 + 1)^2(n_0 - 1)} - \frac{4n_0^3(n_0^4 + 1)}{(n_0^2 + 1)^3(n_0 - 1)^2} \ln n_0 \right] \quad (29)$$

in which the normal emittance is calculated from equation (28a).

The ratio of  $\epsilon_H(l)$  calculated for a roughened surface using equation (25) and the value of  $\epsilon_{H\infty}$  calculated for a smooth surface using equation (29) is plotted in Fig. 5(b). In general, this ratio increases with both  $n_0$  and  $l/\lambda_m$ . For materials having a relatively low index of refraction, i.e.,  $n_0 \lesssim 2$ , the hemispherical emittance is not altered appreciably from its value for a smooth surface in the presence of microscopic surface roughening. Even for materials such as germanium ( $n_0 = 4$ ) which possess a very high index of refraction, the percentage increase in total hemispherical emittance due to microscopic surface roughness is less than 30 percent for  $l/\lambda_m \leq 0.17$ .

## Conclusion

The emission process of thermal radiation from a microscopically roughened dielectric surface into vacuum has been treated by using a laminar-inhomogeneous layered model for a described surface. The emission process of thermal radiation from the rough surface can then be described by the following observations made from the results obtained in the present analysis.

(a) For given dielectric surfaces, the variation of  $n(z)$  in the layer does not significantly affect  $|V|$  for given  $n_0$ . This implies that the emission process is not strongly dependent on the particulate surface roughness geometry assumed.

(b) The method has been used for values of  $l/\lambda_m$  less than 0.34. At any given  $\lambda_m$ , as the thickness of the layer increases, the values of the reflection coefficient  $|V|$  become smaller and smaller. In the limiting case of  $l/\lambda_m \rightarrow \infty$ , the values of  $|V|$  are zero. The method can be extended to values of  $l/\lambda_m > 0.34$ , but eventually as  $l$  increases, the surface ceases to be microscopically rough from the standpoint of the present criterion that many features should be contained in an area of the surface given by  $\lambda_m^2$ .

(c) The spectral angular emittance,  $\epsilon(\varphi, \lambda, l)$ , decreases with increasing  $\varphi$  and increases with increasing  $l/\lambda_m$ . At small  $l/\lambda_m$ ,  $\epsilon(\varphi, \lambda, l)$  becomes independent of wavelength and is equal to that for a smooth dielectric surface. The roughness effects on  $\epsilon(\varphi, \lambda, l)$  become insignificant at  $l/\lambda \lesssim 0.1$ .

(d) The total angular emittance,  $\epsilon(\varphi, l)$  is generally higher, and remains uniform over a wider range of  $\varphi$ , than  $\epsilon_{\infty}(\varphi)$  for a smooth dielectric surface with the same  $n_0$ .

(e) The total hemispherical emittance,  $\epsilon_H(l)$ , of roughened surfaces is higher than that of smooth surfaces of the same material. The ratio  $\epsilon_H(l)/\epsilon_{H\infty}$  increases with both increasing  $n_0$  and increasing  $l/\lambda_m$ , and for the latter increases more rapidly at higher values of  $n_0$ . However, even for a material of a very high index of refraction such as germanium with  $n_0 = 4$ , the percentage increase in total hemispherical emittance is less than 30 percent for values of  $l/\lambda_m \leq 0.34$ .

## References

- 1 Beckmann, P., and Spizzichino, A., *The Scattering of Electromagnetic Waves from Rough Surfaces*, Macmillan, New York, 1963.
- 2 Rice, S. O., "Reflection of Electromagnetic Waves from Slightly Rough Surfaces," *Pure Appl. Math.*, Vol. 4, 1951, pp. 351-378.
- 3 Davies, H., "The Reflection of Electromagnetic Waves from a Rough Surface," *Proc. Inst. Elec. Eng.*, Vol. 101, 1954, pp. 209-214.
- 4 Bennett, H. E., and Porteus, J. O., "Relation Between Surface Roughness and Specular Reflectance at Normal Incidence," *Journal Opt. Soc. Am.*, Vol. 51, 1961, pp. 123-129.
- 5 Toporetz, A. S., "Specular Reflection from a Rough Surface," *Opt. Spectr.*, Vol. 16, 1964, pp. 54-58.
- 6 Van Cittert, P. H., "On the Propagation of Light in Inhomogeneous Media," *Physica*, Vol. 6, No. 8, Aug. 1939, pp. 840-848.
- 7 Landau, L. D., and Lifshitz, E. M., *Electrodynamics of Continuous Media*, Pergamon, New York, 1960, p. 45.
- 8 Brekhovskikh, L. M., *Waves in Layered Media*, Academic, New York, 1960, p. 218.
- 9 Lord Rayleigh, *Theory of Sound*, Vol. 1, Sec. 148b, Dover, New York, 1945.
- 10 Brekhovskikh, L. M., opt. cit., p. 183, Fig. 78, and p. 226, Fig. 86.
- 11 Ditchburn, R. W., *Light*, Interscience, New York, 1953, pp. 448-452.
- 12 Sparrow, E. M., and Cess, H. D., *Radiation Heat Transfer*, Brooks/Cole, Belmont, Calif., 1966, p. 69.

J. LIENHARD

Professor.  
Mem. ASME

R. EICHHORN

Professor.  
Mem. ASME

V. DHIR

Research Assistant.

Mechanical Engineering Department,  
University of Kentucky,  
Lexington, Ky.

# Laminar Natural Convection under Nonuniform Gravity<sup>1</sup>

*Laminar natural convection is analyzed for cases in which gravity varies with the distance from the leading edge of an isothermal plate. The study includes situations in which gravity varies by virtue of the varying slope of a surface. A general integral solution method which includes certain known integral solutions as special cases is developed to account for arbitrary position-dependence of gravity. A series method of solution is also developed for the full equations. Although it is more cumbersome it provides verification of the integral method.*

## Introduction

NATURAL convection from an isothermal plate subject to a variation of gravity,  $g = g(x)$ , with the distance,  $x$ , from the leading edge, is a fairly common situation. Convection from any body whose slope, measured with respect to an earth-normal gravity field,  $g_n$ , varies with  $x$ , can conveniently be treated as a variable gravity problem if the boundary layer thickness is small enough.

Centrifugal gravity fields commonly arise in many rotating machinery applications. The fact that body forces can play an important role in the cooling of turbine blades is one example. Our particular interest was stimulated by a heat-exchanger design for an experimental centrifuge. Another evocative example is the use of a gravity field created artificially in an orbital space station by rotation. These examples are only a small sampling in comparison with the myriad physical processes that involve convection on rotating and/or curved plates at the earth's surface. Curiously, the problem of treating such convection for cases other than  $g \sim x$  and  $g \sim \sin [(constant)(x)]$  has been virtually untouched.

The first analyses of the nonuniform gravity fields caused by rotation of a plate were apparently those of Lemlich and his co-workers. In a series of papers they considered gravity fields of the form  $g = \omega^2 x$ , where  $\omega$  is the angular speed of rotation and where the leading edge is located on the axis of rotation. They solved the integrated equations of motion for both laminar and turbulent flow [1, 2]<sup>2</sup> and directly integrated the unsteady boundary layer equations [3]. The large time result verified their

earlier integral calculation, but Lemlich later found similar solutions which verified both of the previous calculations [4]. Most recently, Lemlich and Pavri [5] offered experimental verification of their theoretical work using appropriately contoured plates in earth-normal gravity.

The important problem of a rotating plate lying in a radial plane with its leading edge a distance  $x_0$  from the axis was approached in a limited way by Catton [6] in 1968. In this case  $g = \omega^2(x_0 - x)$  and a similar solution cannot be found. Catton employed Braun and Heighway's [7] integral equations for large Prandtl number,  $Pr$ , and obtained a result in series form.

Since the classical work of Ray [8] on horizontal cylinders, several authors have considered convection in the nonuniform gravity fields caused by contoured plates. Herman [9] gave a particularly complete treatment of the horizontal cylinder incorporating his own experimental results with those of Nusselt and Jodlbauer [10]. More recently, Braun, Ostrach, and Heighway [11] developed a series of axisymmetric and two-dimensional body contours which lead to similar solutions. In obtaining numerical results they made use of the integral equations of Braun and Heighway for both high and low  $Pr$ .

Although the integral formulations given by Squire [12] and Eckert [13] are purportedly appropriate to all Prandtl numbers, the method is intended for the moderate  $Pr$  range. Braun and Heighway have given improved versions of the integral equation method appropriate to the high and low  $Pr$  limits, but their method is algebraically cumbersome and it fails near  $Pr = 1$ . The Squire-Eckert method (originally used with the vertical plate) has been applied to the horizontal cylinder by Schuh [14], to the class of surfaces that admit similar solutions and to the horizontal cylinder and sphere by Merk and Prins [15], and to the horizontal plate by Levy [16] and by Singh et al. [17].

Some natural convection problems which do not yield to a similar solution have been solved by series expansion methods. Herman treated convection from horizontal cylinders in this way. Chiang et al. [18] applied such a method to convection from a sphere, and Cremers and Finley [19] confirmed their pre-

<sup>1</sup>This study has received partial support under NASA Grant NGR/18-001-035.

<sup>2</sup>Numbers in brackets designate References at end of paper.

Contributed by the Heat Transfer Division for publication (without presentation) in the JOURNAL OF HEAT TRANSFER. Manuscript received by the Heat Transfer Division October 27, 1970. Paper No. 71-HT-CC.

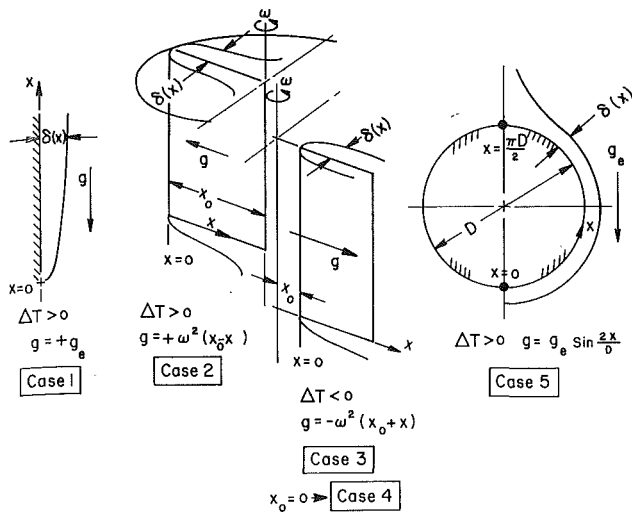


Fig. 1 The five natural convection configurations under consideration

diction experimentally. The method, as we apply it here, is close to that used by Eichhorn [20] in a problem of nonuniform ambient temperature. Chiang and Kaye [21] also applied a series expansion method to the prediction of local natural convection for small  $x$  on nonisothermal cylinders.

Our present objective is to predict the steady natural convection heat transfer from plates subject to a general variation of gravity  $g = g(x)$ . We shall do this by extending the Squire-Eckert integral method for use with a general  $g(x)$ , and by developing a series expansion method for use with a general  $g(x)$ . The integral result can be written in closed form with the help of an accurate simplifying assumption. The series method, though lengthy, provides a check on the application of the integral method.

### Five Specific Problems Involving $g = g(x)$

In developing the methods of solution, we shall refer to five applications. They are shown in Fig. 1 and they include:

- Case 1.** The vertical plate in earth-normal gravity,  $g_e$ .
- Case 2.** The finite hot plate of length  $x_0$ , rotating at  $\omega$  rad/sec in a radial plane about the line  $x = 0$ .
- Case 3.** The infinite cold plate rotating at  $\omega$  rad/sec in a radial

plane with its leading edge beginning a distance  $x_0$  from the axis of rotation.

**Case 4.** Same as Case 3 but with the leading edge located on the axis ( $x_0 = 0$ ).

**Case 5.** The horizontal cylinder in earth-normal gravity,  $g_e$ .

In Cases 2, 3, and 4, the mass of fluid is presumed to be rotating synchronously with the plate. The sign conventions in all five cases are as follows:  $\Delta T$  is the plate temperature minus the ambient temperature (positive for hot plates and negative for cold plates),  $g$  is positive in the negative  $x$  direction.

Case 1 has been solved both by the integral method [12, 13] and exactly [22]; so too have Case 4 [1-5] and Case 5 [8-11]. These solutions will provide points of reference for the present method. Cases 2 and 3 have only been touched upon [6] and they will be developed fairly fully here.

### Integral Method for General $g(x)$

The integral method proceeds as follows: The momentum and energy equations, once integrated across the boundary layer, are<sup>3</sup>

$$\frac{d}{dx} \int_0^\delta \rho u^2 dy = -\mu \left. \frac{\partial u}{\partial y} \right|_{y=0} + \int_0^\delta \rho g \beta (T - T_\infty) dy \quad (1)$$

and

$$\frac{d}{dx} \int_0^\delta u (T - T_\infty) dy = -\alpha \left. \frac{\partial (T - T_\infty)}{\partial y} \right|_{y=0} \quad (2)$$

where  $g$  is a prescribed function of  $x$ . In these equations we take the thermal and hydrodynamic boundary layer thicknesses to be equal, thus suggesting that the results will be most accurate for Prandtl numbers that are not too far from unity.

The temperature and velocity profiles assumed by Eckert are

$$T - T_\infty = \Delta T (1 - \eta)^2 \quad (3)$$

and

$$u = U \eta (1 - \eta)^2 \quad (4)$$

where  $U$  is an as-yet-undetermined characteristic velocity whose form is to be dictated by equations (1) and (2). The magnitude of  $U$  should depend on Pr.

<sup>3</sup> Symbols not defined in the text are ones in common use. They are explained in the Nomenclature section.

### Nomenclature

$C_f$  = local skin friction coefficient  
 $D$  = diameter of a cylinder  
 $f$  = function of  $x$  and Pr defined in the context of equation (5)  
 $F, F_n$  = dimensionless stream functions  
 $Gr$  = Grashof number,  $\beta \Delta T g(x) x^3 / \nu^2$   
 $Gr_x$  = local Grashof number based on a uniform reference gravity, e.g.,  $\beta \Delta T g_e x^3 / \nu^2$  or  $\beta \Delta T (\omega^2 x_0) x^3 / \nu^2$   
 $Gr_{x_0}, Gr_D$  = Gr based on  $x_0$  or  $D$ , respectively, instead of  $x$   
 $g(x)$  = local acceleration in the direction opposite of the  $x$  axis  
 $g_e$  = acceleration of the earth's gravitational field  
 $h$  = local convective heat transfer coefficient

$\bar{h} = \frac{1}{x_0} \int_0^{x_0} h(x) dx$  or  $\frac{2}{\pi D} \int_0^{\pi D/2} h(x) dx$   
 $k$  = thermal conductivity  
 $Nu$  = local Nusselt number,  $hx/k$   
 $\bar{Nu}$  = Nusselt number,  $\bar{h}x_0/k$   
 $\bar{Nu}_D$  = Nusselt number,  $\bar{h}D/k$   
 $Pr$  = Prandtl number  
 $T$  = temperature  
 $T_\infty$  = ambient temperature  
 $U$  = characteristic velocity  
 $u$  = velocity in  $x$  direction  
 $v$  = velocity in  $y$  direction  
 $x$  = axial coordinate  
 $x_0$  = distance of leading edge of the plate from the center of rotation  
 $y$  = coordinate perpendicular to surface

$\alpha$  = thermal diffusivity  
 $\beta$  = bulk coefficient of thermal expansion  
 $\delta$  = boundary layer thickness  
 $\Delta T$  = difference between surface temperature and ambient temperature  
 $\eta$  = nondimensional distance in  $y$  direction,  $y/\delta$ . Also equation (A4) in context of Appendix  
 $\theta, \theta_n$  = nondimensional temperature, equations (A4) and (A9)  
 $\mu$  = viscosity  
 $\nu$  = kinematic viscosity  
 $\xi$  = nondimensional distance in  $x$  direction, equation (A4)  
 $\rho$  = density of fluid  
 $\tau$  = shear stress at the surface  
 $\psi$  = stream function

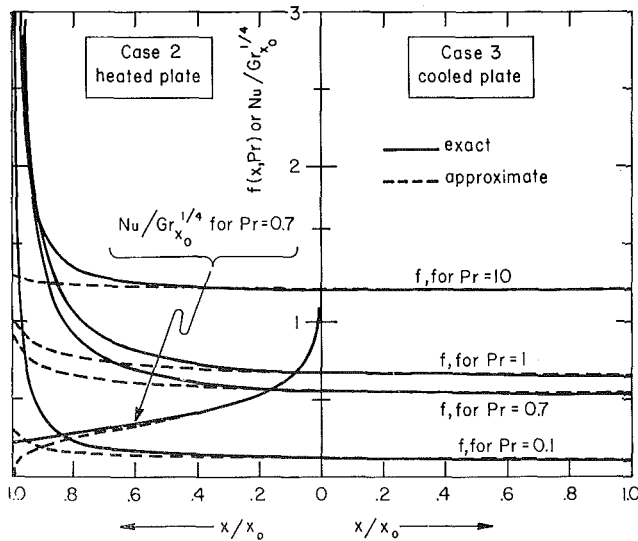


Fig. 2 Comparison of exact and approximate values of  $f$  for rotating plates with leading edge a distance  $x_0$  from the axis

For the vertical plate where  $g = g_0$ ,  $U$  turns out to have the form  $f(\text{Pr})\beta\Delta Tg_0\delta^2/4\nu$ . To treat cases of nonuniform  $g$ , and to satisfy the dimensional requirements of the problem, we will retain this form but will include  $x$  as an independent variable in  $f$ . Thus we generalize the Eckert-Squire method by writing  $U$  as:

$$U = f(x, \text{Pr}) \frac{\beta\Delta T}{4\nu} g(x)\delta^2 \quad (5)$$

If equations (3), (4), and (5) are substituted in equations (1) and (2) and the result rearranged, we obtain two equations for  $f$  and  $\delta$ :

$$\frac{d}{dx} [(fg)^{2/3}\delta]^4 = \frac{448\nu^2}{\beta\Delta T} \left[ \frac{1}{f} - \frac{3}{4} \right] (fg)^{2/3} \quad (6)$$

and

$$\frac{d}{dx} [(fg)^{1/3}\delta]^4 = \frac{320}{\text{Pr}} \frac{\nu^2}{\beta\Delta T} (fg)^{1/3} \quad (7)$$

Let us now eliminate  $\delta(x)$  from this pair of equations and solve for  $f$ . Integrating each with respect to  $x$  and combining the results gives the following integral equation for  $f$ :

$$f(x, \text{Pr}) = \left[ \frac{7\text{Pr} \int_0^x \left[ \frac{1}{f} - \frac{3}{4} \right] (fg)^{2/3} dx}{5g^{4/15} \int_0^x (fg)^{1/3} dx} \right]^{15/4} \quad (8)$$

Equation (8) is a troublesome result. It can of course be integrated numerically but we wish to avoid that. Fortunately, experience with natural convection suggests that the  $x$ -dependence of  $f$  should not be strong. Indeed, as in Cases 1 and 4,  $f$  is  $x$ -independent when the problem admits of a similar solution. In other cases, as we justify below,  $f$  can be approximated by factoring it out of the integrals in equation (8) and solving the result explicitly for  $f$ . This gives

$$f(x, \text{Pr}) \simeq \left[ \frac{3}{4} + \frac{5g^{4/15} \int_0^x g^{1/3} dx}{7\text{Pr} \int_0^x g^{3/5} dx} \right]^{-1} \quad (9)$$

Neglecting the  $x$ -dependence of  $f$  in equation (7) [or equation (6)] as well, we can integrate it and solve the result for  $\delta$ . This gives

$$\delta \simeq \sqrt[4]{\frac{320}{\text{Pr} f} \frac{\nu^2}{\beta\Delta Tg^{4/3}} \int_0^x g^{1/3} dx} \quad (10)$$

Finally with the help of equation (3) we obtain

$$\text{Nu} = - \frac{x}{k\Delta T} k \frac{d(T - T_\infty)}{dy} \Big|_{y=0} = \frac{2x}{\delta} \quad (11)$$

or using equation (10),

$$\text{Nu} \simeq \sqrt[4]{\frac{\text{Pr} f \beta\Delta Tg^{4/3} x^4}{20 \nu^2} \int_0^x g^{1/3} dx} \quad (12)$$

Equations (12) and (9) will meet our objective if we can justify the approximate form of  $f(x, \text{Pr})$  and if we can show that the integral method gives good accuracy.

### On the Effect of Approximating $f$

In using equation (12) to determine  $\text{Nu}$ , we have introduced two approximations. In the first place, equation (9) is an approximation to the true value of  $f$  implied by equation (8). In the second place, when integrating equation (7), we assumed that  $g$  and  $\delta$  were the only  $x$ -dependent functions. We now examine the degree to which these approximations affect the solution.

**Cases 1 and 4.** In both instances, a similar solution is possible so  $f$  is  $x$ -independent. Our results are the same as those of Eckert [13] and Lemlich [1]. For Case 1 specifically

$$\text{Nu} = 0.508 \left[ 1 + \frac{20}{21\text{Pr}} \right]^{-1/4} (\text{Gr}_x \text{Pr})^{1/4} \quad (13)$$

where  $\text{Gr}_x = \beta g_0 \Delta T x^3 / \nu^2$ . For Case 4

$$\text{Nu} = 0.546 \left[ 1 + \frac{8}{7\text{Pr}} \right]^{-1/4} (\text{Gr Pr})^{1/4} \quad (14)$$

where  $\text{Gr} = \beta \omega^2 \Delta T x^4 / \nu^2$ .

**Cases 2 and 3.** Here,  $f$  will be  $x$ -dependent, so using  $g = \pm \omega^2 x_0 (1 \mp x/x_0)$  we find from equation (9) the result

$$f = \frac{4}{3} \left[ 1 + \frac{8}{7\text{Pr}} \left( 1 \mp \frac{x}{x_0} \right)^{4/15} \frac{\left( 1 \mp \frac{x}{x_0} \right)^{4/3} - 1}{\left( 1 \mp \frac{x}{x_0} \right)^{8/5} - 1} \right]^{-1} \quad (15)$$

where the upper sign refers to Case 2 and the lower to Case 3. Equation (15) is plotted for both cases and for several values of  $\text{Pr}$  in Fig. 2 along with the numerical solutions to equation (8). The latter were found by iteration starting from the values given by equation (15).

In Case 3, the error is everywhere less than 3 percent. In Case 2, the error increases with  $x/x_0$  but is less than 10 percent for  $x/x_0 < 0.5$  for all  $\text{Pr}$ . For larger  $x/x_0$  the error becomes very large in Case 2, approaching 100 percent at  $x/x_0 = 1.0$ . This occurs in a region of rapidly increasing  $\delta$  and, indeed, not only the approximation to  $f$ , but the whole concept of a boundary layer deteriorates in this range. The percentage error in the approximation to  $f$  also decreases with increasing  $\text{Pr}$  in both cases.

To illustrate the error in the heat transfer prediction introduced by the approximate  $f$  used with equation (12), we have integrated equation (7) for Case 2 with  $\text{Pr} = 0.7$  using the exact  $f$  from equation (8). The result, included in Fig. 2, indicates that the magnitude of the error in  $\text{Nu}$  is considerably less than that in  $f$ . The approximation underestimates the value of  $\text{Nu}$  by no more than 9 percent up to  $x/x_0 = 0.8$ , then it deteriorates rapidly.

From equation (12) we see that  $\text{Nu}$  varies as  $f^{1/4}$  so errors in the prediction of the heat transfer rate caused by the degree of approximation in equation (9) will be correspondingly diminished. As much as 25 percent error in  $f$  will lead to less than 6 percent

**Table 1 Comparison of Nu for Pr = 0.7 as computed by the integral method, based on both exact and approximate f**

	Case 2 Rotating Hot Plate	Case 3 Rotating Cold Plate	Case 5 Horizontal Cylinder
exact $f$	$\overline{Nu}/Gr_o^{1/4} = 0.430$	$\overline{Nu}/Gr_o^{1/4} = 0.548$	$\overline{Nu}_D/Gr_D^{1/4} = 0.398$
approximate $f$	$\overline{Nu}/Gr_o^{1/4} = 0.411$	$\overline{Nu}/Gr_o^{1/4} = 0.550$	$\overline{Nu}_D/Gr_D^{1/4} = 0.381$
error due to approximation	-4.4%	0.4%	-4.3%

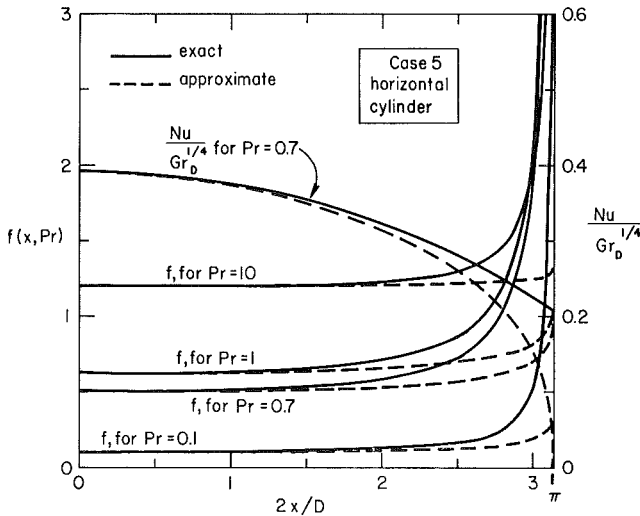


**Fig. 3 Comparison of exact and approximate values of  $f$  for a horizontal cylinder**

error in Nu, for example.

Overall Nusselt numbers,  $\overline{Nu}$ , based on  $\bar{h}$  [where  $\bar{h} = \frac{1}{x_0} \int_0^{x_0} h(x) dx$ ] have been calculated from the integrated equations, using both the exact  $f$  and the approximation, and are given in Table 1 for  $Pr = 0.7$ . The difference is negligible for the cold plate and less than 5 percent for the hot plate.

In both cases, the boundary layer is initially identical to that on a vertical flat plate where  $f$  is independent of  $x$ . As  $x$  increases in Case 3 the boundary layer should pass over to the similar form dictated by  $g = \omega^2 x$  where  $f$  will again be  $x$ -independent. The ratio of the two limiting values of  $f$  is given by

$$\frac{f_{x \rightarrow 0}}{f_{x \rightarrow \infty}} = \frac{\frac{4}{3} / \left[ 1 + \frac{20}{21 Pr} \right]}{\frac{4}{3} / \left[ 1 + \frac{8}{7 Pr} \right]} = \frac{1 + \frac{8}{7 Pr}}{1 + \frac{20}{21 Pr}} \quad (16)$$

which approaches  $6/5$  for small  $Pr$  and unity for large  $Pr$ . Thus the change in  $f$  with  $x$  in Case 3 is not great (even at small  $Pr$ ) and the approximation is quite accurate for all  $x$ .

**Case 5.** The lower half of the horizontal cylinder resembles Case 3 in that  $g$  increases in the direction of flow. Using the same reasoning the upper half of the cylinder resembles Case 2. The details are different of course but the error in  $f$  represented by the approximation of equation (8) displays a similar behavior with the greatest errors occurring in the deceleration region (see Fig. 3).

We also show in Fig. 3 the local heat transfer coefficient for both the approximate  $f$  and the numerical solution of equations (8) and (7). The mean Nusselt number using the approximate  $f$  (see Table 1) turns out to be only 4.3 percent less than that found by numerical integration of equations (8) and (7).

**Table 2 Comparison of similar and integral method solutions**

Pr	$\frac{Nu}{Gr^{1/4}}$					
	Case 1 Vertical Plate in Uniform Gravity			Case 4 Rotating Cold Plate with Leading Edge on Axis		
	Integral	Similar	Percent Error	Integral	Similar	Percent Error
0.1	0.159	0.163	-2.45	0.0984	-----	-----
0.7	0.376	0.353	+6.52	0.392	0.370	+5.95
0.71	0.378	-----	-----	0.395	0.372	+6.2
0.72	0.380	0.356	+6.75	0.398	-----	-----
1.0	0.430	0.40	+7.5	0.452	0.414	+9.2
10.0	0.883	0.825	+7.04	0.945	-----	-----
100.0	1.63	1.55	+5.16	1.72	1.647	+4.44

### Comparison of Integral Method with Exact Solution of Differential Equations

We have shown that the approximate form of  $f$  (which leads to a closed-form solution for Nu) is in most cases sufficiently accurate as a representation of the solution to the integrated equations. We now turn to the question of the accuracy of the integral method itself. In each of the comparisons below we use the approximate form of  $f$  in the integral method.

**Cases 1 and 4.** For Cases 1 and 4, where similar solutions exist, the accuracy is quite easy to check. As shown in Table 2, the integral solution fares quite well even at the extreme values of  $Pr$  represented.

**Cases 2 and 3.** For Cases 2 and 3, the literature contains only the limited results of Catton [6] and these are purported to be appropriate to large  $Pr$  only. Since there are apparently no exact solutions or experimental results with which to compare either our own integral method solution or that of Catton we have developed a series solution valid for small  $x$ . This is essentially new information and we give the development of the method in the Appendix. The heat transfer and skin friction formulae are given by equations (A15) and (A16). Numerical results can be found with the aid of Table 3.

Figs. 4 and 5 show Nu and  $C_f$  for several values of  $Pr$ . In Fig. 4, the local Nusselt number,  $hx/k$ , has been nondimensionalized with the local Nusselt number for a plate subjected to a uniform gravity field,  $g = \omega^2 x_0$ . An equivalent nondimensionalization for the skin friction has been used in Fig. 5. The series solution has only been plotted where the results based on both 3 and 4 terms agree within 1 percent. Since the convergence of the series was fairly rapid, the solid lines in Figs. 4 and 5 are accurate results against which to test the approximate method.

The results of the approximate integral method are plotted in Figs. 4 and 5 for comparison. They show that, in the worst comparison ( $Pr = 0.1$ ), the approximate method is accurate within 2 percent for Case 3 and within 9 percent for Case 2 up to  $x/x_0 = 0.7$ . The integral method based upon an exact  $f$  would have fared better still, of course.

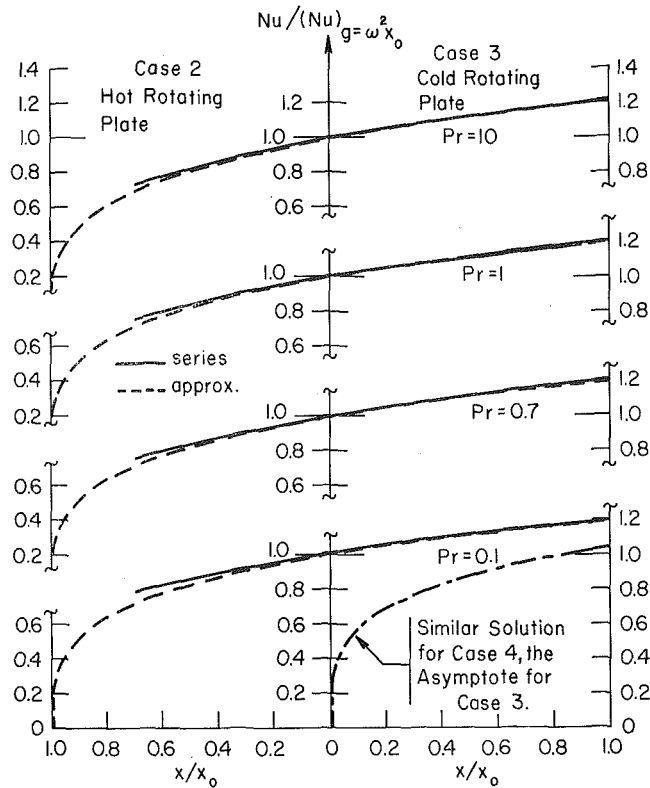


Fig. 4 Comparison of series solution for  $Nu$  with approximate integral method; rotating plate with leading edge a distance  $x_0$  from the axis

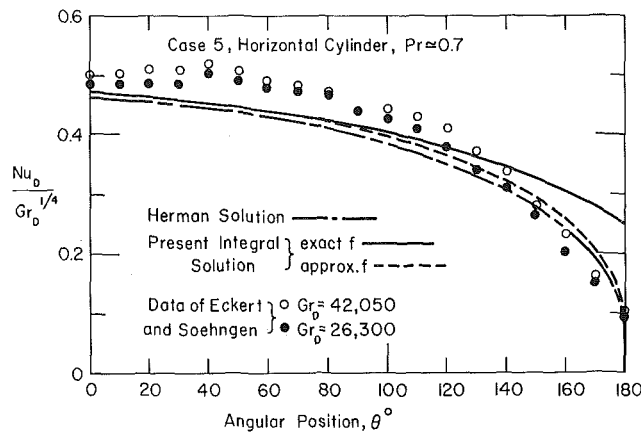


Fig. 6 Comparison of analytical and experimental values of  $Nu$  for a horizontal cylinder

In Case 3, for the cool plate, Lemlich's similarity solution must be approached. The integral method solution does this automatically. Neither solution casts light on the behavior of the heated plate, Case 2, near  $x = x_0$  (the center of rotation), even though the integral method solution gives a result there. None of the methods (in Case 2) predict separation ahead of  $x = x_0$ .

**Case 5.** Fig. 6 displays the results for Case 5, the horizontal cylinder, for  $Pr = 0.7$ . In this case the exact integral result is the same as Merk and Prins' integral result [15], and it represents a slight improvement on Herman's prediction except near the top. In this region the boundary layer theory itself deteriorates and any integral method is doomed to fail. It is thus fortuitous that our approximate integral method predicts the right behavior near the top, and that it also gives the best overall representation of local data among all of the existing predictions. This appears to have been the situation in Case 2, as well.

Our calculations for  $Pr = 0.7$  using the approximate form for  $f$

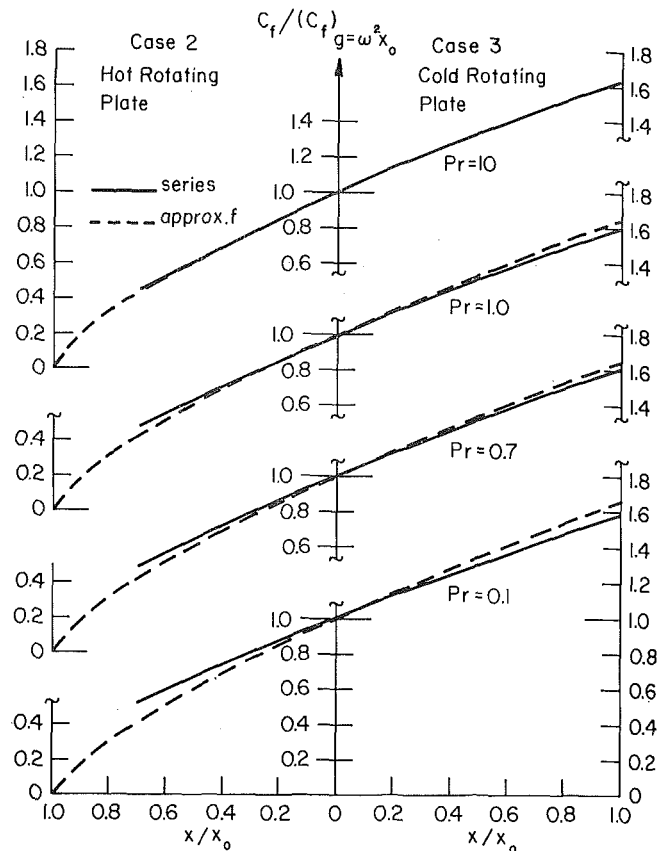


Fig. 5 Comparison of series solution for  $C_f$  with approximate integral method; rotating plate with leading edge a distance  $x_0$  from the axis

give  $\overline{Nu}_D/Gr_D^{1/4} = 0.381$  while the numerical solution based on the exact  $f$  gives 0.398 (see Table 1). For the same  $Pr$ , Herman [9] gave 0.367 and Braun et al. [11] quote Schuh [14] as giving the value 0.386.<sup>4</sup>

The interferometric data of Eckert and Soehngen [23] for air are probably the best measurements of  $Nu$  available and we have included them in Fig. 6. They give an average value  $\overline{Nu}_D/Gr_D^{1/4} \approx 0.42$ . McAdams [24] recommends the highest value, 0.49, as representing the average of several sets of experimental data. Of several other suggested values, Senftleben's [25] value of 0.38 is one of the lowest. Generally, experiments show that  $\overline{Nu}_D/Gr_D^{1/4}$  is not totally independent of  $Gr$ , especially as  $Gr_D$  becomes less than  $10^4$ .

## Conclusions

1 The present series solution (see Appendix) provides a method for predicting the velocity and temperature distributions on a plate subject to general variation of  $g$  with  $x$ . It is somewhat laborious to apply and requires many terms for large  $x$ .

2 A general integral method, which requires the simultaneous numerical integration of equations (7) and (8), has proved to give a good approximation to the series method as long as  $U$  is not slowing toward zero.

3 As long as  $U$  is not slowing toward zero the solution of the problem can be well approximated by:

$$Nu_x = \sqrt[4]{\frac{Pr f \beta \Delta T g^{1/2} x^4}{20 \rho^2}} / \int_0^x g^{1/2} dx \quad (12)$$

where

<sup>4</sup> The literature values cited in this section were referred to  $Pr = 0.7$  (when they were given for slightly higher values of  $Pr$ ) by assuming  $\overline{Nu}_D/Gr_D^{1/4} \sim Pr^{1/4}$ .



$$f(x, \text{Pr}) = \left[ \frac{3}{4} + \frac{5g^{1/15}}{7 \text{Pr}} \frac{\int_0^x g^{1/4} dx}{\int_0^x g^{2/3} dx} \right]^{-1} \quad (9)$$

This approximation to the integral solution is precise if the boundary layer equations admit a similar solution.

4 For Case 3, the cold plate rotating about an axis located a distance  $x_0$  from the leading edge, we can write from equations (12) and (15)

$$\text{Nu} \approx \left[ \frac{\frac{4 \text{Pr}}{45} \text{Gr}_x \frac{x}{x_0} \frac{(1 + x/x_0)^{3/5}}{(1 + x/x_0)^{3/5} - 1}}{1 + \frac{8}{7 \text{Pr}} (1 + x/x_0)^{1/15} \frac{(1 + x/x_0)^{3/5} - 1}{(1 + x/x_0)^{8/5} - 1}} \right]^{1/4} \quad (17)$$

This result is never more than 3 percent away from the exact solution of the integrated equations or 2 percent from the boundary layer solution.

5 For Case 2, the hot plate rotating about an axis located a distance  $x_0$  from the leading edge, we can replace the group  $(1 + x/x_0)$  with  $(1 - x/x_0)$  in equation (17). The result will be valid within 9 percent for  $x/x_0 < 0.7$ .

## References

- Lemlich, R., "Natural Convection to Isothermal Flat Plate with a Spatially Nonuniform Acceleration," *I.E.C. Fundamentals Quart.*, Vol. 2, 1963, pp. 157-158.
- Lemlich, R., and Vardi, J., "Steady Free Convection to a Flat Plate With Uniform Surface Heat Flux and Nonuniform Acceleration," *JOURNAL OF HEAT TRANSFER, TRANS. ASME, Series C*, Vol. 86, No. 4, Nov. 1964, p. 562-563.
- Lemlich, R., and Steinkamp, J. S., "Laminar Natural Convection to an Isothermal Flat Plate with a Spatially Varying Acceleration," *AIChE Journal*, Vol. 10, 1964, pp. 445-447.
- Manoff, M., and Lemlich, R., "Free Convection to a Rotating Central Plate in Synchronously Rotating Surroundings With and Without Consideration of Coriolis Forces," *C.E.P. Symposium Series*, Vol. 66, No. 102, 1970, pp. 118-132.
- Lemlich, R., and Pavri, R. E., "A Thermal Analog for Free Convection with a Gravity Gradient," Paper NC 1.7, International Heat Transfer Conference, Paris-Versailles, Vol. IV, 1970.
- Catton, I., "Effect of a Gravity Gradient on Free Convection From a Vertical Plate," *C.E.P. Symposium Series*, Vol. 64, No. 82, 1968, pp. 146-149.
- Braun, W. H., and Heighway, J. E., "An Integral Method for Natural Convection," NASA TN D-292, June 1960.
- Ray, B., "Free and Forced Convection from Heated Cylinders in Air," *Proc. Indian Assoc. Cultiv. of Sci.*, Vol. 6, 1920, p. 95.
- Herman, R., "Wärmeübergang bei Freier Strömung am wagrechten Zylinder in Zwei-atomik Gasen," *VDI-Forschungsheft*, No. 379, 1936 (translated in NACA TM 1366, Nov. 1954).
- Jodlbauer, K., "Das Temperatur und Geschwindigkeitsfeld um ein Geheiztes Rohr bei Freier Konvektion," *Forsh. Geb. Ing.*, Vol. 4, 1933, pp. 157-172.
- Braun, W. H., Ostrach, S., and Heighway, J. E., "Free-Convection Similarity Flows about Two-dimensional and Axisymmetric Bodies With Closed Lower Ends," *International Journal of Heat and Mass Transfer*, Vol. 2, 1961, pp. 121-135.
- Squire, H. B., in: *Modern Developments in Fluid Dynamics*, Vol. 2 (Goldstein, S., ed.), Oxford University Press, New York, 1938.
- Eckert, E. R. G., and Drake, R. M., Jr., *Heat and Mass Transfer*, 2nd ed., McGraw-Hill, New York, 1959.
- Schuh, H., "Boundary Layers of Temperature," *Reports and Translations*, No. 1007, 1948, Sec. 11.1.
- Merk, H. J., and Prins, J. A., "Thermal Convection in Laminar Boundary Layers. I, II, and III," *App. Sci. Res., Section A*, Vol. 4, 1954, pp. 11-24, 195-206, 207-221.
- Levy, S., "Integral Methods in Natural-Convection Flow," *Journal of Applied Mechanics*, Vol. 22, TRANS. ASME, Vol. 77, No. 4, Dec. 1955, pp. 515-522.
- Singh, S. N., Birkebak, R. C., and Drake, R. M., Jr., "Laminar Free Convection from Downward-Facing Horizontal Surfaces," *Progress in Heat and Mass Transfer*, Vol. 2 (Irvine, T. F., et al., eds.), Pergamon Press, New York, 1969, pp. 87-98.
- Chiang, T., Ossin, A., and Tien, C. L., "Laminar Free Convection From a Sphere," *JOURNAL OF HEAT TRANSFER, TRANS. ASME, Series C*, Vol. 86, No. 4, Nov. 1964, pp. 537-542.
- Cremers, C. J., and Finley, D., "Natural Convection About

Isothermal Spheres," Paper NC 1.5, International Heat Transfer Conference, Paris-Versailles, Vol. IV, 1970.

20 Eichhorn, R., "Natural Convection in a Thermally Stratified Flow," *Progress in Heat and Mass Transfer*, Vol. 2 (Irvine, T. F., et al., eds.), Pergamon Press, New York, 1969, pp. 41-53.

21 Chiang, T., and Kaye, J., "On Laminar Free Convection from a Horizontal Cylinder," *Proceedings Fourth National Congress of Applied Mechanics*, Berkeley, Calif., 1962, pp. 1213-1219.

22 Ostrach, S., "An Analysis of Laminar Free-Convection Flow and Heat Transfer About a Flat Plate Parallel to the Direction of the Generating Body Force," NACA Rept. 1111, 1953.

23 Eckert, E. R. G., and Soehngen, E., "Studies on Heat Transfer in Laminar Free Convection with the Zehnder-Mach Interferometer," USAF Tech. Rept. 5747, 1948.

24 McAdams, W. H., *Heat Transmission*, 3rd ed., McGraw-Hill, New York, 1954, p. 177.

25 Senftleben, H., "Die Wärmeabgabe von Körpern Verschiedener Form in Flüssigkeiten und Gasen bei Freier Strömung," *ZAMP*, Vol. 3, 1951, p. 361.

## APPENDIX

### Series Solution for $g = g(x)$

As the variation of  $g$  with  $x$  becomes sufficiently complicated that a similar solution cannot be obtained, we must either resort to integral methods or power-series methods. For Cases 2 and 3, since the boundary layers first develop as they would on a vertical plate subjected to a uniform gravity field,  $g = \omega^2 x_0$ , our approach to the solution will be to expand the equations of motion in powers of  $x/x_0$ . The leading term in this expansion will be the vertical plate result. In Case 3 the series should approach Lemlich's result as  $x$  increases or as  $x_0$  decreases. More general gravity fields can be handled in a similar way.

Making the usual boundary layer assumptions including the requirement that  $\beta\Delta T \ll 1$  (large Taylor number)<sup>5</sup> the equations of continuity, momentum, and energy are

$$u_x + v_y = 0 \quad (A1)$$

$$uu_x + vv_y = \nu u_{yy} + g(x)\beta(T - T_\infty) \quad (A2)$$

$$uT_x + vT_y = \alpha T_{yy} \quad (A3)$$

Into the equations (A1), (A2), and (A3) we introduce the stream function and the transformations

$$\theta \equiv \frac{T - T_\infty}{\Delta T}$$

$$\psi \equiv (64 \text{Gr}_x)^{1/4} \nu F(\xi, \eta)$$

$$\eta \equiv \frac{y}{x} \left( \frac{\text{Gr}_x}{4} \right)^{1/4} \quad (A4)$$

$$\xi \equiv \frac{x}{x_0}$$

$$\text{Gr}_x \equiv \frac{g_0 \beta \Delta T x^3}{\nu^2}$$

where  $g_0$  is the value of  $g$  at  $x = x_0$ . The equations which result are

$$F_{\eta\eta\eta} + 3FF_{\eta\eta} - 2F_\eta^2 + \theta \left( \frac{g}{g_0} \right) = 4\xi(F_\eta F_{\xi\eta} - F_\xi F_{\eta\eta}) \quad (A5)$$

$$\theta_{\eta\eta} + 3 \text{Pr} F\theta_\eta = 4\xi \text{Pr} (F_\eta \theta_\xi - F_\xi \theta_\eta) \quad (A6)$$

The boundary conditions are

$$\begin{aligned} \theta(\xi, 0) - 1 = \theta(0, \eta) = \theta(\xi, \infty) = F(\xi, 0) = F_\eta(0, \eta) \\ = F_\eta(\xi, \infty) = F_\eta(\xi, 0) = 0. \end{aligned} \quad (A7)$$

<sup>5</sup> Otherwise the vorticity drawn into the boundary layer will not be negligible compared to the vorticity generated by shear [4].

**Table 3 Coefficients for velocity and temperature functions in the series solution for the rotating plate with the edge a distance  $x_0$  from the axis (Cases 2 and 3)**

Pr	n	$F_n''(0)$				$-\theta_n'(0)$			
		0	1	2	3	0	1	2	3
0.1		0.85914	0.54141	-0.12053	0.13355	0.23014	0.05530	-0.03255	0.04291
0.7		0.67891	0.45125	-0.10858	0.12848	0.49951	0.12890	-0.08493	0.12748
1		0.64219	0.43044	-0.10500	0.12583	0.56715	0.14844	-0.09977	0.15289
10		0.41920	0.29101	-0.07559	0.09661	1.16933	0.32736	-0.25938	0.39906

For Case 3,  $g/g_0 = 1 + \xi$ , while for Case 2,  $g/g_0 = 1 - \xi$ . Following the usual procedure of the series expansion method, we next introduce into equations (A5) and (A6) the expressions

$$F(\xi, \eta) = \sum_{n=0}^{\infty} (-1)^n \frac{F_n(\eta) \xi^n}{n!} \quad (A8)$$

and

$$\theta(\xi, \eta) = \sum_{n=0}^{\infty} (-1)^n \frac{\theta_n(\eta) \xi^n}{n!} \quad (A9)$$

where  $l = 0$  for Case 3 and  $l = 1$  for Case 2.

The result, after collecting terms in like powers of  $\xi$  is an infinite set of 5th-order differential equations for  $F_n$  and  $\theta_n$ . The first four sets are, for  $\xi^0$ ,

$$\left. \begin{aligned} F_0'''' + 3F_0 F_0'' - 2F_0'^2 + \theta_0 &= 0 \\ \theta_0'' + 3 \text{Pr } F_0 \theta_0' &= 0 \end{aligned} \right\} \quad (A10)$$

for  $\xi^1$ ,

$$\left. \begin{aligned} F_1'''' + 3F_0 F_1'' - 8F_0' F_1' + 7F_0'' F_1 + \theta_1 &= \theta_0 \\ \theta_1'' + 3 \text{Pr } F_0 \theta_1' - 4 \text{Pr } F_0' \theta_1 - 7 \text{Pr } \theta_0' F_1 &= 0 \end{aligned} \right\} \quad (A11)$$

for  $\xi^2$ ,

$$\left. \begin{aligned} F_2'''' + 3F_0 F_2'' - 12F_0' F_2' + 11F_0'' F_2 + \theta_2 &= -14F_1 F_1'' + 12F_1'^2 + 2\theta_1 \\ \theta_2'' + 3 \text{Pr } F_0 \theta_2' - 8 \text{Pr } F_0' \theta_2 + 11 \text{Pr } \theta_0' F_2 &= -14 \text{Pr } F_1 \theta_1' + 8 \text{Pr } F_1' \theta_1 \end{aligned} \right\} \quad (A12)$$

and for  $\xi^3$ ,

$$\left. \begin{aligned} F_3'''' + 3F_0 F_3'' - 16F_0' F_3' + 15F_0'' F_3 + \theta_3 &= -21F_1 F_2'' + 48F_1' F_2' - 33F_1'' + 3\theta_2 \\ \theta_3'' + 3 \text{Pr } F_0 \theta_3' - 12 \text{Pr } F_0' \theta_3 + 15 \text{Pr } \theta_0' F_3 &= -21 \text{Pr } F_1 \theta_2' + 24 \text{Pr } F_1' \theta_2 \\ &\quad - 33 \text{Pr } F_2 \theta_1' + 12 \text{Pr } F_2' \theta_1 \end{aligned} \right\} \quad (A13)$$

The first set of equations is that for the vertical flat plate. The rest of the equations are linear but have variable coefficients and nonhomogeneous terms. The boundary conditions can be written compactly as

$$\left. \begin{aligned} \theta_n(0) - 1 = F_n(0) = F_n'(0) = F_n''(\infty) &= \theta_n(\infty) = 0, \quad \text{all } n \\ \theta_n(0) = 0, \quad n \geq 1 \end{aligned} \right\} \quad (A14)$$

Equations (A10) through (A12) were solved for Prandtl numbers of 0.1, 0.7, 1, and 10 by forward numerical integration. Double precision was used throughout and the results are believed accurate to 5 significant figures.

Numerical results are given in Table 3. They can be converted to heat transfer and shear stress information by the formulas

$$\text{Nu} = \frac{hx}{k} = \left(\frac{\text{Gr}_x}{4}\right)^{1/4} \left\{ - \sum_{n=0}^{\infty} (-1)^n \frac{\theta_n'(0) \xi^n}{n!} \right\} \quad (A15)$$

and

$$C_f = \frac{\tau}{\rho \left(\frac{v}{x}\right)^2} = 4 \left(\frac{\text{Gr}_x}{4}\right)^{3/4} \left\{ \sum_{n=0}^{\infty} (-1)^n \frac{F_n''(0) \xi^n}{n!} \right\} \quad (A16)$$

The graphical results given in Figs. 4 and 5 were found in this way.

**J. P. LAMB**  
 Professor and Chairman,  
 Mechanical Engineering Department,  
 University of Texas, Austin, Texas.  
 Mem. ASME

**C. G. HOOD**  
 Research Engineer,  
 Collins Radio Co., Dallas, Texas

# Theoretical Distributions of Heat Transfer Downstream of a Backstep in Supersonic Turbulent Flow

*A physically perceptive model is presented for the flow field and convective transport processes in the vicinity of reattachment of a planar, supersonic, turbulent flow. Control volume methods are utilized extensively in the analysis and the resulting integral equations are solved by various numerical search techniques. The analysis enables one to determine significant parameters in the flow field as well as the heat transfer distribution and associated wall temperature of the reattachment surface. Also presented is a general correlation of predicted results for the convection process in terms of pertinent independent variables. The correlated results are shown to agree with measurements for a wide range of test conditions.*

## Introduction

THERE IS continuing interest in the dynamics and thermodynamics of separated flow regions because of requirements for accurate determination of pressure and thermal environments for contemporary flow devices. A fundamental process of considerable importance is that associated with the reattachment of a supersonic turbulent flow onto a plane surface. The geometry most often used to elucidate this type of flow is the backward-facing step shown schematically in Fig. 1.

Experimental studies of diabatic turbulent reattachment in supersonic flow have shown that, in relation to the heat transfer rate of the attached flow upstream of the corner, the convective transfer rate in the low-speed recirculating flow region is considerably lower, whereas that in the immediate vicinity of reattachment is of the same order of magnitude.

In addition, most investigators have concluded that there is a local maximum in the heat transfer rate near reattachment, although there have been no systematic measurements of both dividing streamline reattachment and heat transfer in one series of tests. It has also been found that, while the flow field is largely unaffected by heat transfer, there is a considerable influence of the flow pattern on convection. This is manifested in the observation that the wall heat flux variation is of the same form as the static pressure distribution.

The pioneering analyses of Chapman [1]<sup>1</sup> and Korst [2] have

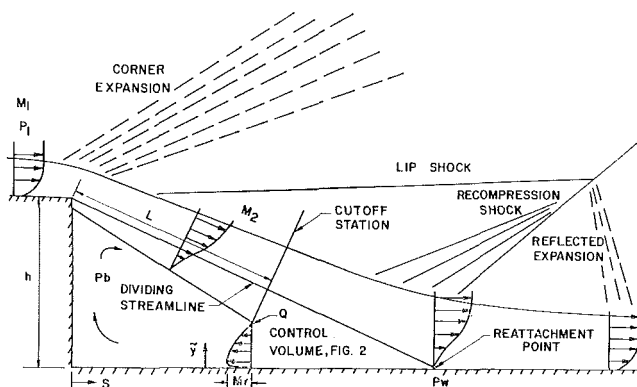


Fig. 1 Some features of the backstep flow field

provided the basis for most subsequent attempts to predict convective transport in separated regions. Both of these early theories incorporated a quiescent wake. The later experimental results of Larson [3] exhibited favorable agreement with the Chapman theory for the laminar range but indicated an order of magnitude discrepancy in the turbulent regime.

These significant differences have been attributed [4] to the omission of finite wake velocities which inherently requires that the bulk temperature and the wall temperature be nearly equal. In fact, these temperatures are substantially different in turbulent flows so that the resistance to heat transfer provided by the free shear layer is only a portion of the total resistance, which also includes that due to the wall layer in the recirculating region (Fig. 1).

<sup>1</sup> Numbers in brackets designate References at end of paper.

Contributed by the Heat Transfer Division for publication (without presentation) in the JOURNAL OF HEAT TRANSFER. Manuscript received by the Heat Transfer Division October 30, 1970. Paper No. 71-HT-W.

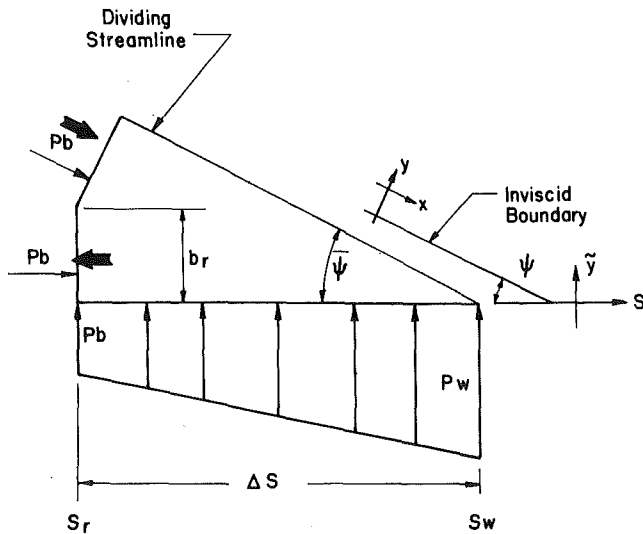


Fig. 2 Control volume for reattachment analysis

An earlier attempt to include an additional resistance to heat transfer was the "reflected image" method of Page and Dixon [5] in which the stagnation temperature ratio across the lower portion of the free layer was "reflected" to the wall and equated to the ratio of bulk to wall temperatures. Although this model has been demonstrated to yield reasonable estimates, it can provide only limited information on the pertinent parameters of the energy transport process.

The current analysis is based on a flow model presented earlier [6] by the present authors. This initial formulation, which yielded realistic results for adiabatic reattachment, has also been utilized [7] to predict convective heat transfer on a blunt trailing edge (i.e., a planar base).

In the next section, the diabatic reattachment analysis of [7] is reviewed. Following this, energy balance relations for the backstep field are developed using a multi-stage control volume approach. With this background, it is possible to determine the distribution of heat transfer rate along an isothermal reattachment surface. Finally, a general correlation of some numerical results in terms of appropriate independent variables is presented and compared with recent test data.

## Flow Field Analysis

The reverse flow is formed at the point where the free layer interacts with the downstream wall (Fig. 1). The point of initial interaction marks the end of the base pressure region (denoted as the cutoff station); it also indicates the onset of the recompression process in which the flow is turned back to the axial direction.

The location of the cutoff station, as well as parameters associated with the point of dividing streamline impingement, were determined in [6] with a conceptually simple control volume analysis. The appropriate control volume is depicted schematically in Figs. 1 and 2.

Conditions which must be satisfied at the cutoff station are: (a) the zero-velocity edges of the mixing zone and reverse flow must coincide (point Q in Fig. 1), and (b) the mass flow rate in the free layer below the dividing streamline must equal that in the reverse flow. The former condition determines the relative magnitudes of momentum fluxes and pressure forces on the control volume.

The reverse flow can be characterized by the plane jet velocity profile which is given by [8]

$$\tilde{\varphi}_r = u/u_r = 1 - \tanh^2(K\tilde{\xi}_r) \quad (1)$$

while the corresponding profile for the free shear layer is

$$\varphi = u/u_2 = 1/2(1 + \operatorname{erf} \eta) \quad (2)$$

where  $\eta$  is proportional to the spread rate parameter  $\sigma$ . Implicit in the use of this profile is the assumption of a relatively thin approaching boundary layer (i.e.,  $\delta_1/h$ ) which was discussed in [6]. Some consequences of this assumption in relation to backstep heat transfer will be mentioned later.

Because both of these profiles approach zero asymptotically, some judgment must be exercised in locating the effective edges of the layers so that the foregoing condition (a) is properly satisfied. The two profile parameters which must be selected are  $\eta_L$ , which determines  $\varphi_L$  from equation (2), and  $K$ , which determines  $\tilde{\varphi}_r(1) = \tilde{\varphi}_r(\tilde{\xi}_r = 1)$ . As noted in [6] it was found, after consideration of a number of methods of profile truncation, that  $\eta_L$  is best identified with a constant percentage of the total mass flux in the free layer and that  $\varphi_L = \tilde{\varphi}_r(1)$ . The particular relation used in the present calculations is

$$I_1(\eta_L) = 0.0025[I_1(\eta_R) - I_1(-\eta_R)]$$

where  $\eta_R = 4.5$ .

## Nomenclature

$b$  = width of reverse flow  
 $c$  = sonic velocity  $(\gamma RT)^{1/2}$   
 $C$  = Crocco number,  $u(2c_p T_0)^{-1/2}$   
 $F_3 = (1 - \lambda_b)I_{2j}L/\sigma$   
 $F_6 = C_r b_r \lambda_r R_3 / C_2 - \lambda_b I_{1j} L / \sigma$   
 $h$  = backstep height  
 $H$  = convective heat transfer coefficient  
 $I_n = \int_{\eta_L}^{\eta} \varphi^n (\Lambda - C_2^2 \varphi^2)^{-1} d\eta$ ,  
 $n = 1, 2$   
 $I_3 = \lambda_b I_1 + (1 - \lambda_b) I_2$   
 $k_t$  = eddy thermal conductivity  
 $K$  = profile constant, equation (1)  
 $L$  = length of free shear layer  
 $M$  = Mach number,  $u/c$   
 $\bar{q}$  = heat flux parameter, equation (21)  
 $R_n = \int_0^1 \tilde{\varphi}_r^n (\tilde{\Lambda}_r - C_r^2 \tilde{\varphi}_r^2)^{-1} d\tilde{\xi}_r$ ,  
 $n = 1, 2$

$R_3 = \lambda_b R_1 + (\lambda_r - \lambda_b) R_2$   
 $Re_{ef}$  = Reynolds number, equation (16)  
 $Re_s$  = Reynolds number,  $\rho_{01} c_{01} h / \mu_{01}$   
 $S$  = length coordinate along downstream wall  
 $\Delta S = S_w - S_r$   
 $u$  = longitudinal velocity  
 $x$  = longitudinal coordinate  
 $y$  = transverse coordinate  
 $\tilde{\xi}_r = y/b_r$   
 $\gamma = c_p/c_v$   
 $\eta = \sigma y/x$   
 $\Lambda = T_0/T_{02}$   
 $\tilde{\Lambda} = T_0/T_{0r}$   
 $\lambda_b = T_b/T_{02}$   
 $\tilde{\lambda}_b = T_b/T_{0r}$   
 $\lambda_r = T_{0r}/T_{02}$   
 $\sigma$  = free layer spread rate parameter  
 $\varphi = u/u_2$   
 $\tilde{\varphi}_r = u/u_r$

## Subscripts

ad = adiabatic conditions  
 $b$  = zero velocity at cutoff station  
 $bw$  = wall adjacent to recirculating region  
 $j$  = dividing streamline in free shear layer  
 $L$  = lower edge of free layer where  $\varphi_L \approx 0$   
 $r$  = wall conditions at cutoff station  
 $w$  = dividing streamline reattachment point  
 $0$  = isentropic stagnation conditions  
 $1$  = freestream of approach flow  
 $2$  = freestream adjacent to free layer  
 $6$  = plane of backstep

## Superscript

( $\sim$ ) = reverse flow

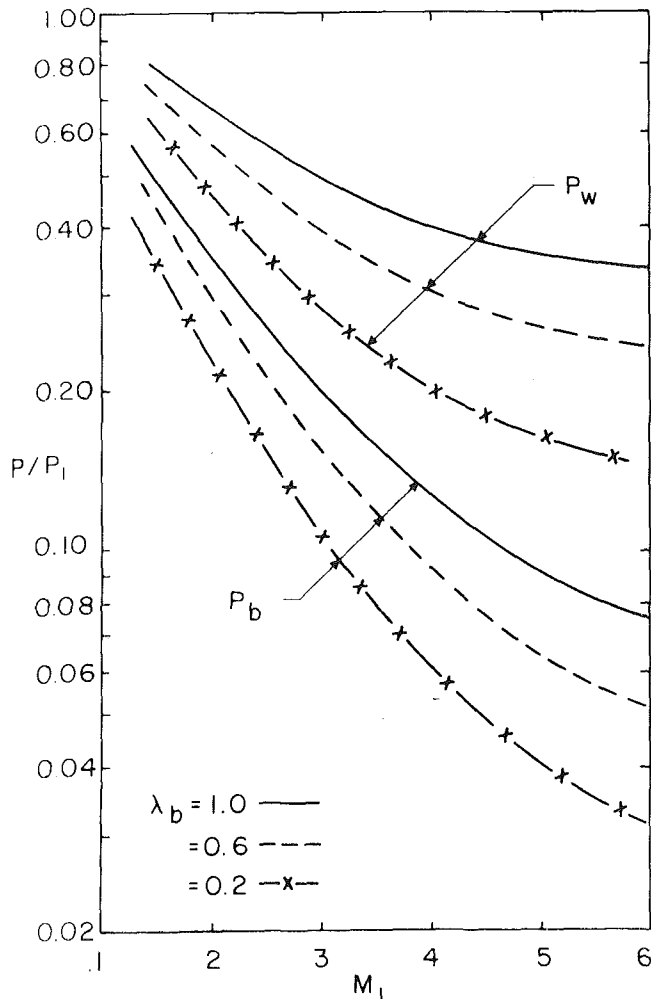


Fig. 3 Predicted variations of  $P_b$  and  $P_w$  with approach Mach number and  $\lambda_b$ .

The second condition, which must be satisfied at the cutoff station, is a continuity relation which may be expressed in terms of reference quantities and nondimensional integrals as

$$L[\rho u(T/T_0)I_{1j}/\sigma]_{M_2} = b_r[\rho u(T/T_0)R_1]_{M_r}$$

However, it may be shown that for an isobaric, diabatic flow  $\rho u(T/T_0) \propto C(T_0)^{1/2}$  so that the continuity relation becomes

$$C_2 L I_{1j} / \sigma = C_r b_r R_1 (\lambda_r)^{-1/2} \quad (3)$$

The integral  $R_1$  in the foregoing equation depends upon the stagnation temperature profile which can be related to the velocity profile via the Crocco integral of the energy equation for a turbulent Prandtl number of unity. The free layer profile is

$$\Lambda = T_0/T_{02} = \lambda_b + (1 - \lambda_b)\varphi \quad (4)$$

whereas, for the reverse flow, it is

$$\tilde{\Lambda} = T_0/T_{0r} = \tilde{\lambda}_b + (1 - \tilde{\lambda}_b)\tilde{\varphi}_r \quad (5)$$

where  $\lambda_b$  and  $\tilde{\lambda}_b$  are proportional to  $T_b$ , which is the temperature of the zero-velocity point at the cutoff station. This definition differs from that of [9] in which  $T_b$  is also denoted as a bulk temperature.

Writing the Crocco relation,  $T_0 = Au + B$  at  $u = u_r$  and  $u = u_2$ , and using the definition of Crocco number allows one to obtain the relation

$$C_r/C_2 = (\lambda_r)^{-1/2}(\lambda_r - \lambda_b)/(1 - \lambda_b) \quad (6)$$

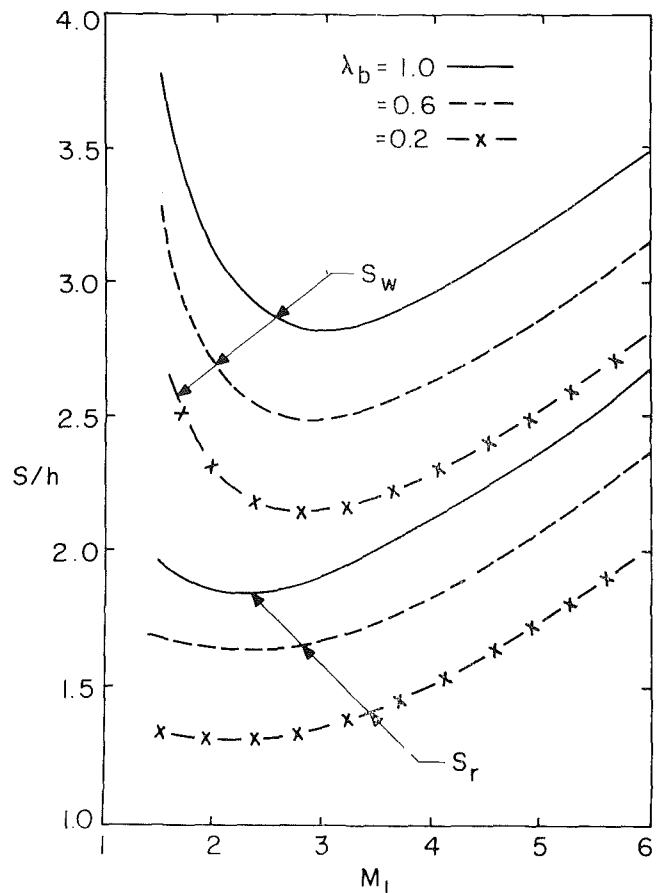


Fig. 4 Predicted variations of  $S_r$  and  $S_w$  with approach Mach number and  $\lambda_b$ .

This equation may be substituted into equation (3) to yield an expression of the form

$$F(C_2, C_r, L, \lambda_b) = 0 \quad (7)$$

Therefore, one must specify both  $C_2$  and  $\lambda_b$  at a given value of  $L$ , after which equation (7) becomes  $F(C_r) = 0$ . The correct root of this equation can then be found numerically with the Newton-Raphson technique and the constraint that  $0 < C_r < 1$ . The value of  $\lambda_r$  corresponding to the correct  $C_r$  is then determined from equation (6). It should be noted that the foregoing procedure only allows one to couple the free layer and reverse flows at an arbitrary cutoff station; the proper location of the cutoff point must also satisfy momentum considerations.

A solution to the reattachment problem is established by writing momentum balance relations in both longitudinal and transverse directions for the control volume shown in Fig. 2. In the original formulation [6] of the flow model, a number of recent experimental observations were employed; a discussion of these is omitted here for brevity.

The two momentum relations can be combined into the dimensionless form

$$(b_r/h)(1 + GC_r^2 R_2) - 1/2(1 + P_w/P_b)(\Delta S/h) \tan \psi + (L/h\sigma)(\eta_j - \eta_L + GC_2^2 I_{2j})(\cos \psi + \sin \psi \tan \tilde{\psi}) = 0 \quad (8)$$

where  $\tilde{\psi} = \psi - (\eta_m - \eta_j)/\sigma$  and  $G = 2\gamma/(\gamma - 1)$ .

Expressions for  $b_r$  and  $\Delta S$  can be obtained from geometric relationships so that the only unknowns in the momentum equation are the reattachment pressure ( $P_w$ ) and the length ( $L$ ) of the shear layer. The latter parameter determines  $C_r$  and  $\lambda_r$  from continuity considerations. A systematic search procedure was developed in [6] which determines the unique combination of  $P_w$  and  $L$ , satisfying equations (7) and (8).

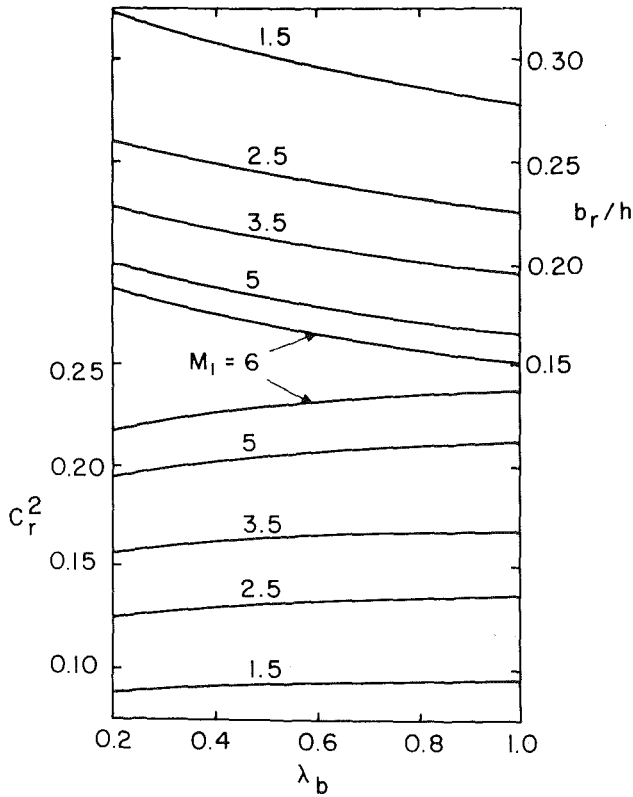


Fig. 5 Predicted variations of  $C_r$  and  $b_r$  with approach Mach number and  $\lambda_b$

It should be noted that the base pressure ( $P_b$ ) is considered to be known either from experiment or through various theoretical models. The present calculations were made using the well-known Korst analysis [9]. Knowledge of the base pressure enables one to determine the Mach number ( $M_2$ ) and the inviscid impingement angle ( $\psi$ ), as well as conditions at the dividing streamline. The search procedure of [6] completes the reattachment analysis, determining flow parameters in the reverse flow at the cutoff station.

No further flow field analysis is necessary for heat transfer predictions, because experiments have shown that the recirculating flow is essentially a constant-flux region. This is not unexpected in view of the similarity between the recirculating layer and a wall jet which is known [10] to exhibit a virtually constant flux near its origin. Thus, the heat transfer rate, which exists at the cutoff station, can be taken as characteristic of the entire recirculating zone.

Some predicted variations of flow field parameters are illustrated in Figs. 3, 4, and 5. The first graph indicates the variation of base pressure and dividing streamline impingement pressure with approach Mach number for various values of  $\lambda_b$ , while Fig. 4 shows the corresponding variations of the distances  $S_r$  and  $S_w$ . It is observed that the major effect of a higher freestream stagnation temperature (i.e., lower  $\lambda_b$ ) is to shift the adiabatic variations downward. Although the present analysis is valid for an arbitrary nonunit value of  $\lambda_b$ , typical predictions for flows with  $\lambda_b$  greater than one are not presented because of the limited occurrence of such situations in practice.

As shown in [6], data such as that in Figs. 3 and 4 can be employed to construct centerplane pressure distributions up to the impingement point, viz., the pressure is equal to  $P_b$  out to a distance  $S_r$  from the backstep and then increases linearly to  $P_w$  at a distance  $S_w$ . The relatively minor effect of heat transfer on the reverse flow parameters  $b_r$  and  $C_r$  is depicted in Fig. 5 which also indicates the large influence of compressibility.

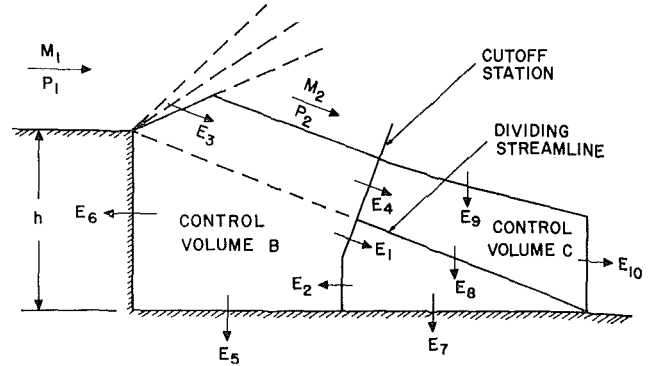


Fig. 6 Control volumes for energy balance

## Thermal Analysis

For the thermal analysis, the almost isobaric, near field is employed as a control volume as shown in Fig. 6. Using the foregoing flow field results, it is possible to specify the amount and direction of energy crossing each control surface. First, an energy balance for control volume (B) may be solved for the energy ( $E_5 + E_6$ ) which is transferred to or from the recirculating region. Therefore,

$$E_5 + E_6 = E_2 + E_3 - (E_1 + E_4) \quad (9)$$

where the energy ( $E_1 + E_4$ ), convected from the control volume by the free layer, is given by

$$\begin{aligned} E_1 + E_4 &= \int_{y_L}^{y_R} \rho u c_p T_0 dy \\ &= L[\rho u c_p T_0 (T/T_0) I_{3R}/\sigma]_{M_2} \end{aligned} \quad (10)$$

The energy ( $E_3$ ) which enters the control volume from the approach flow can be expressed as  $E_3 = \dot{m}_3 c_p T_{02}$  where the mass flow rate ( $\dot{m}_3$ ) is given by

$$\dot{m}_3 = \int_{y_1}^{y_R} \rho u dy = L[\rho u (T/T_0) (I_{1R} - I_{1j})/\sigma]_{M_2}$$

Therefore  $E_3$  may be written as

$$E_3 = L[\rho u c_p T_0 (T/T_0) (I_{1R} - I_{1j})/\sigma]_{M_2} \quad (11)$$

The rate of energy returned to the control volume via the reverse flow is

$$\begin{aligned} E_2 &= \int_0^{b_r} \rho \tilde{u} c_p T_0 d\tilde{y} \\ &= [\rho u c_p T_0 (T/T_0)]_{M_2} (\lambda_r)^{1/2} b_r R_3 C_r / C_2 \end{aligned} \quad (12)$$

Substitution of equations (10), (11), and (12) into equation (9) yields an expression for the total energy transferred from the recirculating region. After simplification, one obtains

$$E_5 + E_6 = [\rho u c_p T_0 (T/T_0)]_{M_2} F_6 \quad (13)$$

where  $F_6$  is given in the Nomenclature.

In view of the constant-flux character of the recirculating region, the average heat transfer rate ( $\dot{q}_{bw}$ ) in this zone is related to the total energy transferred by  $E_5 + E_6 = \dot{q}_{bw}(h + S_r)$ . Thus

$$\dot{q}_{bw} = [\rho u c_p T_0 (T/T_0)]_{M_2} (F_6/h) / (1 + S_r/h) \quad (14)$$

where  $S_r$  can be found from geometric relationships.

The wall temperature ( $T_{bw}$ ) associated with the foregoing heat transfer rate can be determined from the relation  $\dot{q}_{bw} = H_{bw}(T_{br} - T_{bw}) = H_{bw} T_{02}(\lambda_r - \lambda_{bw})$ . Therefore,

$$\lambda_{bw} = \lambda_r - \dot{q}_{bw}/H_{bw}T_{02} \quad (15)$$

where  $\lambda_r$  has been previously obtained in the reattachment analysis, equations (7) and (8).

The heat transfer coefficient in equation (15) can be estimated with the usual turbulent flow correlation of Stanton, Reynolds, and Prandtl numbers when written [11] for a flow with varying external velocity. It is thus necessary to evaluate, at the cutoff station, the relation

$$St = 0.0295(Pr)^{-0.4}(Re)_{ef}^{-0.2} \quad (16)$$

where the effective Reynolds number is  $(Re)_{ef} = (1/\mu) \int_0^x \rho u dx$ .

Inasmuch as the exponent of  $(Re)_{ef}$  is small, only a reasonable approximation of this parameter is necessary. It can be obtained by considering that part of the reverse flow which is accelerating along the wall between  $S_w$  and  $S_r$  (Fig. 2). As a first approximation, this reverse flow can be considered equivalent to that near a planar stagnation point so that  $\tilde{u} \approx (\tilde{u}_r/\Delta S)\tilde{x}$ , where  $\tilde{x} = 0$  at  $S_w$ . Furthermore, because compressibility effects are not large, one can write  $P_w \approx P + 1/2\rho\tilde{u}^2$  so that  $\rho\tilde{u} = (P_w - P)/(1/2\tilde{u})$ . However, in addition to the nearly linear relation between  $\tilde{u}$  and  $\tilde{x}$ , there is also a linear relation between  $P$  and  $\tilde{x}$  which was invoked in [6] during the development of equation (8). Thus, one finds that  $\rho\tilde{u} \approx \text{constant}$  and, therefore,  $(Re)_{ef} \approx (\rho u)_r \Delta S/\mu$ . The heat transfer coefficient can thus be expressed as

$$\begin{aligned} H_{bw} &= (\rho\tilde{u})_r c_p St \\ &= 0.0295(\rho\tilde{u})_r c_p (Pr)^{-0.4}(Re)_{ef}^{-0.2} \end{aligned} \quad (17)$$

Since the wall temperature ( $T_{bw}$ ) is considered to be a constant, the only remaining parameters of interest are those associated with the dividing streamline reattachment point. An energy balance for the wedge-shaped control volume of Figs. 2 and 6 gives the heat transferred to the wall in the reattachment region as

$$E_7 = E_1 - E_2 + E_3 \quad (18)$$

whereas a similar balance for control volume (C) of Fig. 6 yields the energy transferred across the dividing streamline in the reattachment zone as

$$E_8 = E_4 + E_9 - E_{10} \quad (19)$$

The initial attempt to determine  $E_7$  involved the estimation of  $E_8$  from equation (19) using approximate velocity and temperature profiles to evaluate  $E_{10}$  and assuming that  $E_9$  could be neglected. However, the resulting values of  $E_8$  were often negative even for  $\lambda_b < 1$ ; this meant that the corresponding values of  $E_7$  were too low. As a consequence, the predicted flux levels at reattachment were lower than those in the recirculating region which is quite unrealistic. Furthermore, modification of  $E_9$  to account for energy transfer from the inviscid flow (at the same rate as to the free layer) did not significantly alter the results.

This failure of the integral approach suggested that the value of  $E_8$  must be relatively small and thus quite sensitive to the profile assumptions. The former supposition was confirmed after estimates of  $E_8$  were obtained by integrating an approximate expression for the local flux:  $\dot{q}_8(x) = (\tau u)_j + k_t(dT/dy)_j$ . This calculation indicated that  $E_8$  is on the order of 5 to 8 percent of  $E_1$ . Thus, all current numerical results have been obtained from equation (18) with  $E_8 = 0$ .

The flux ( $\dot{q}_w$ ) at reattachment can be estimated from equation (18) by recalling that experiments have demonstrated a nearly linear variation of heat transfer rate in the reattachment region. Therefore,  $E_7 \approx 1/2\Delta S(\dot{q}_{bw} + \dot{q}_w)$  or  $\dot{q}_w = 2(E_1 - E_2)/\Delta S - \dot{q}_{bw}$ . After substitution of equation (12) and a relation similar to equation (10) for  $E_1$ , one obtains

$$\begin{aligned} \dot{q}_w &= [\rho u c_p T_0(T/T_0)]_{M_1} F_3/\Delta S \\ &\quad - [1 + 2(1 + S_r/h)/(\Delta S/h)]\dot{q}_{bw} \end{aligned} \quad (20)$$

Equations (14), (15), (17), and (20) allow one to determine values of  $\dot{q}_{bw}$ ,  $\dot{q}_w$ , and  $\lambda_{bw}$  using flow field information generated by the reattachment analysis.

## Discussion of Heat Transfer Results

Although the foregoing solution technique is formally complete, it is not in a readily usable form, because one cannot select a wall temperature and calculate the corresponding heat flux distribution. Instead, one must compute heat transfer rates and wall temperatures for selected values of the temperature ( $T_b$ ). These results may then be interpolated to obtain information for other wall temperatures. Because of this unattractive feature, as well as the complexity of the computation scheme, it is desirable to develop a general correlation of the predicted results in terms of useful parameters.

It is noted from equations (14) and (20) that the two heat fluxes of interest are independent of  $h$  for a fixed  $\lambda_b$ . Furthermore, it is observed that, for a given  $M_1$ , the terms  $\rho u c_p T_0(T/T_0)$  are proportional to  $P_0 T_0^{1/2}$ . Thus, one can define a dimensional heat transfer parameter [5] by

$$\bar{q} = \dot{q}/P_{01}(T_{01})^{1/2} \quad (21)$$

where the units are Btu, deg R, ft, lb<sub>f</sub>, and sec. The parameter ( $\bar{q}$ ) can also be related to a type of Stanton number of the form

$$St = \dot{q}/(\rho_{01} c_{01} T_{01}) = 4.52\bar{q}$$

The effect of absolute values of  $P_{01}$ ,  $T_{01}$ , and  $h$  on the wall temperature ( $\lambda_{bw}$ ) cannot be determined by inspection. To explore this point, a series of machine computations involving large variations (two orders of magnitude) in the three independent quantities was carried out for air using the variation of  $\sigma$  with  $C_2$  and  $\lambda_b$  given in [12]. These results showed that the predicted parameters could be correlated with a characteristic Reynolds number of the form  $Re_s = \rho_{01} c_{01} h/\mu_{01} = 0.286 P_{01} h/\mu_{01}(T_{01})^{1/2}$ , where  $c$  is the sonic velocity and the units are the same as those given for equation (21).

The proposed method of correlating the variation of wall heat transfer parameters with approach Mach number ( $M_1$ ) and the Reynolds number ( $Re_s$ ) involves the limiting case of absolute zero wall temperature. Expressing the heat flux as  $\dot{q} = HT_{01}(\lambda_r - \lambda_{bw})$  allows one to write

$$\bar{q} = H(T_{01})^{1/2}(P_{01})^{-1}(\lambda_r - \lambda_{bw}) \quad (22)$$

or, when  $\lambda_{bw} = 0$ ,

$$(\bar{q})_{\max} = H(T_{01})^{1/2}(P_{01})^{-1}(\lambda_r)_{\min} \quad (23)$$

which gives the heat transfer coefficient as

$$H(T_{01})^{1/2}/P_{01} = (\bar{q})_{\max}/(\lambda_r)_{\min} \quad (24)$$

Equations (22) and (23) can be combined to yield

$$\bar{q} = (\bar{q})_{\max}(\lambda_r - \lambda_{bw})/(\lambda_r)_{\min} \quad (25)$$

The present computations for  $\lambda_b < 1$  indicate that there is an essentially linear relationship between  $\lambda_{bw}$  and  $\lambda_r$  which can be expressed as

$$\lambda_r = (\lambda_r)_{\min} + \lambda_{bw}[1 - (\lambda_r)_{\min}/(\lambda_{bw})_{\text{ad}}] \quad (26)$$

where  $(\lambda_{bw})_{\text{ad}}$  represents the wall temperature for zero heat transfer, i.e.,  $(\lambda_{bw})_{\text{ad}} = \lambda_r$ . Combining equations (25) and (26), therefore, yields

$$\bar{q} = (\bar{q})_{\max}[1 - \lambda_{bw}/(\lambda_{bw})_{\text{ad}}] \quad (27)$$

Figs. 7 and 8 present the variations of  $(\bar{q}_{bw})_{\max}$  and  $(\bar{q}_w)_{\max}$

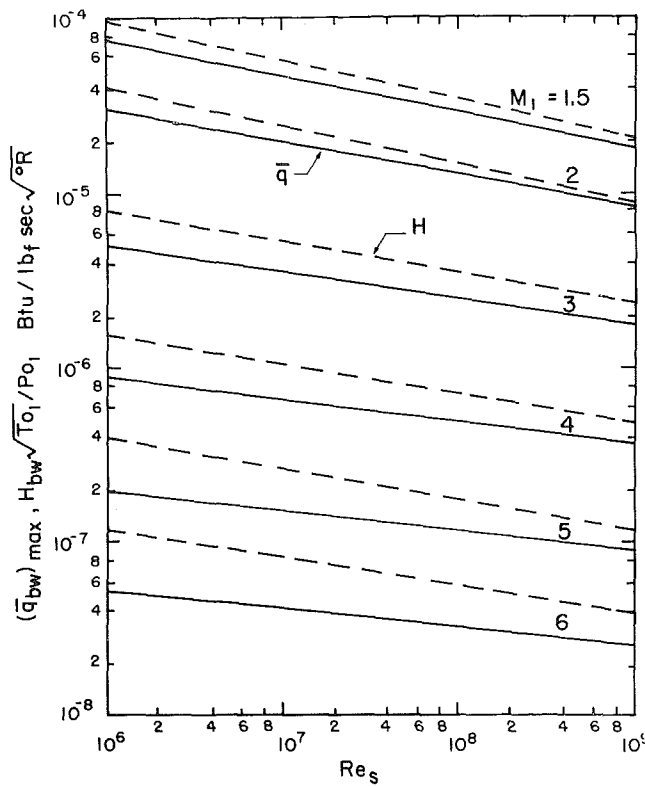


Fig. 7 Predicted variations of  $(\bar{q}_w)_{\max}$  and  $H_w$  with approach Mach number and characteristic Reynolds number

found from equation (23), along with the corresponding convective transfer coefficients determined from equation (24). It is observed that these parameters vary with  $Re_s$  in the usual power-law fashion. For ease in making rapid estimates of heat transfer using equation (27), Table 1 presents the variations with Mach number of the pertinent parameters for two extreme values of  $Re_s$ . These results indicate that the temperature ratio  $(\lambda_{bw})_{ad}$  is nearly independent of  $Re_s$ , although there is a slight semi-logarithmic variation, i.e.,  $(\lambda_{bw})_{ad} \propto \log(Re)_s$ . It is also observed that this ratio approaches unity for low supersonic Mach numbers.

One of the major uncertainties in any turbulent flow model is the level of turbulence which, in the current analysis, is characterized by the spread rate parameter ( $\sigma$ ). To ascertain how sensitive the present model was to changes in  $\sigma$ , a series of computations was made with  $\sigma$  fixed at 17.5, as opposed to a range between 14 and 30 predicted by [12].

This sensitivity study indicated that a given percentage change in  $\sigma$  leads to a corresponding change in wall temperature, while the heat flux changes are in the opposite direction, as equation (14) suggests, and somewhat greater in magnitude. The inherent difficulties in estimating  $\sigma$  from experimental data are

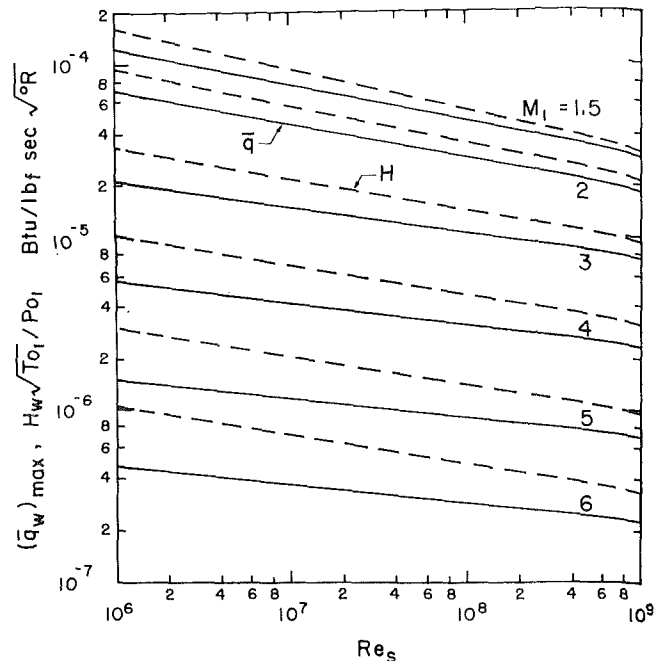


Fig. 8 Predicted variations of  $(\bar{q}_w)_{\max}$  and  $H_w$  with approach Mach number and characteristic Reynolds number

discussed in [12], where it is shown that uncertainties of 20 percent are not uncommon.

Although there have been reported a number of experimental investigations of heat transfer in turbulent separated regions, only four possess sufficient geometric similarity or present necessary peripheral information to allow quantitative comparison with the present predictions.

Naysmith [13] obtained heat transfer coefficients on a reattachment surface downstream of a 15-deg wedge which was located along the tunnel wall. The step height was approximately 1 in., while stagnation conditions were 75 psia and 570 deg R. The tunnel nominal Mach number of 4 resulted in an approach Mach number of 3.8 for a hypothetical backstep.

The hypersonic study of Holloway, Sterrett, and Creekmore [14] was carried out in a blowdown tunnel at a nominal Mach number of 6 with a backstep height of 0.25 in. and a wall temperature ratio  $(\lambda_{bw})$  of 0.53. Stagnation conditions were approximately 400 psia and 1000 deg R. Additional hypersonic tests were reported by Nestler, Saydah, and Auxer [15] for a 1-in. backstep with an approach Mach number of 6.3. The value of  $\lambda_{bw}$  was 0.3, while stagnation conditions were 1800 psia and 1900 deg R.

Sandford and Ginoux [16] have presented heat transfer coefficients downstream of a 6.8-mm (0.268-in.) step for an approach Mach number of 1.9. The values of  $P_{01}$  and  $T_{01}$  were 30 psia and 550 deg R, respectively. In this investigation the approaching

Table 1 Typical numerical results

$Re_s$	$M_1$	$(\lambda_{bw})_{ad}$	$(\bar{q}_w)_{\max}$	$H_w(T_{01})^{1/2}/P_{01}$	$(\bar{q}_w)_{\max}$	$H_w(T_{01})^{1/2}/P_{01}$
$10^6$	1.5	0.898	7.6 (-5)	9.7 (-5)	1.2 (-4)	1.5 (-4)
	2	0.884	3.1 (-5)	4.1 (-5)	7.0 (-5)	9.4 (-5)
	3	0.847	5.2 (-6)	8.2 (-6)	2.1 (-5)	3.3 (-5)
	4	0.823	9.0 (-7)	1.6 (-6)	5.6 (-6)	1.0 (-5)
	5	0.802	2.0 (-7)	4.1 (-7)	1.5 (-6)	3.0 (-6)
	6	0.787	5.4 (-8)	1.2 (-7)	4.7 (-7)	1.0 (-6)
$10^9$	1.5	0.925	1.8 (-5)	2.0 (-5)	2.8 (-5)	3.2 (-5)
	2	0.901	8.4 (-6)	9.0 (-6)	1.8 (-5)	2.1 (-5)
	3	0.866	1.8 (-6)	2.4 (-6)	7.6 (-6)	9.4 (-6)
	4	0.840	3.7 (-7)	4.9 (-7)	2.3 (-6)	3.1 (-6)
	5	0.821	9.1 (-8)	1.2 (-7)	6.9 (-7)	9.6 (-7)
	6	0.805	2.6 (-8)	4.0 (-8)	2.3 (-7)	3.3 (-7)

Note: 1.8 (-5) =  $1.8 \times 10^{-5}$



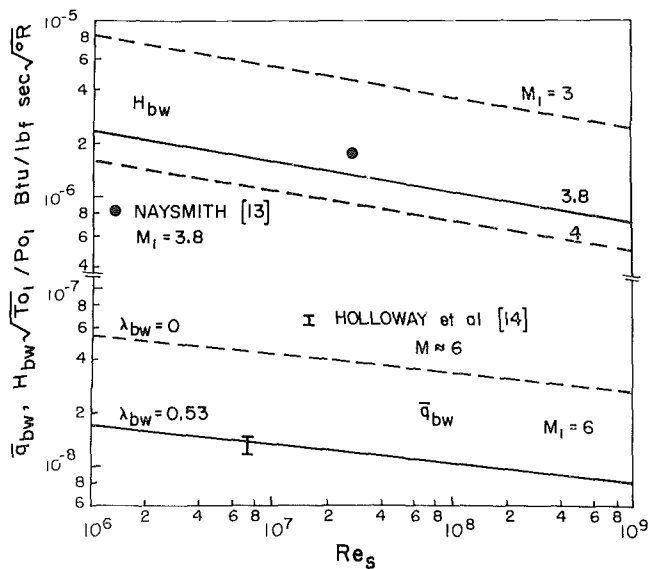


Fig. 9 Comparison of predictions with data of Naysmith and of Holloway et al.

boundary layer was made turbulent by tripping, whereas there was natural transition in the other studies. In all cases, the upstream viscous layers were relatively thin, i.e.,  $\delta/h \leq 0.3$ .

For both the Naysmith and Holloway data, there was a poor correlation with the current predictions of the distribution of heat transfer downstream of the step. In the former case, there was considerable scatter due to the use of relatively large heat meters, whereas for the latter investigation, the increase in heat flux near reattachment was more characteristic of a transitional than a turbulent flow. However, despite these differences, there was reasonably good agreement for heat transfer rates within the recirculating region. This is illustrated in Fig. 9 which depicts the heat transfer coefficients of Naysmith and the flux values of Holloway et al., along with the current predictions for similar flow conditions.

More detailed comparisons were possible for the data of Sandford and Ginoux and Nestler et al. In these cases, it is possible to present the longitudinal distribution of heat transfer on the reattachment surface as in Figs. 10 and 11. Although the present analysis does not permit computations downstream of the point of dividing streamline impingement, it is observed that one can estimate the heat transfer increase by extrapolating the variation which exists for the reattachment zone between  $S_r$  and  $S_w$ .

Furthermore, relatively crude estimates of the maximum heat transfer rate can be made from the aforementioned observation that wall pressures and heat transfer rates develop to their downstream maxima in a similar manner. Thus one can write  $H_{max} \approx H_{bw}(P_1/P_b)$  and  $\bar{q}_{max} \approx \bar{q}_{bw}(P_1/P_b)$  where  $P_b$  is the theoretical base pressure which, as was noted earlier, is determined with the method of Korst [2, 9]. For the pressure field the downstream maximum is substantially equivalent [6] to the upstream pressure ( $P_1$ ).

It is noted in Figs. 10 and 11 that the spatial orientation of the lower Mach number prediction is quite satisfactory, whereas there is considerable error in the hypersonic flow regime. This disagreement is attributed primarily<sup>2</sup> to the lip shock which is formed by the overexpansion of the boundary layer at the corner of the backstep [6] (Fig. 1). Although this is a very complex flow process [17], it is seen from Fig. 11 that its primary effect on the distribution of heat transfer (also wall pressure) is to reduce the effective step height ( $h$ ) and thus shift the predicted distributions to larger  $S/h$  values.

<sup>2</sup> Although other flow field parameters are undoubtedly involved their relative importance cannot be assessed without extensive experimental diagnostics.

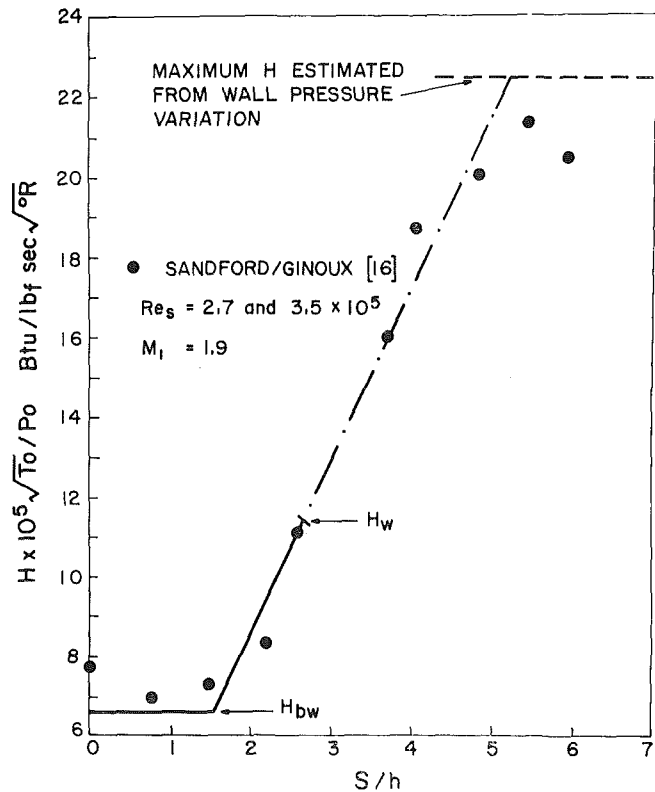


Fig. 10 Distribution of heat transfer coefficient downstream of backstep

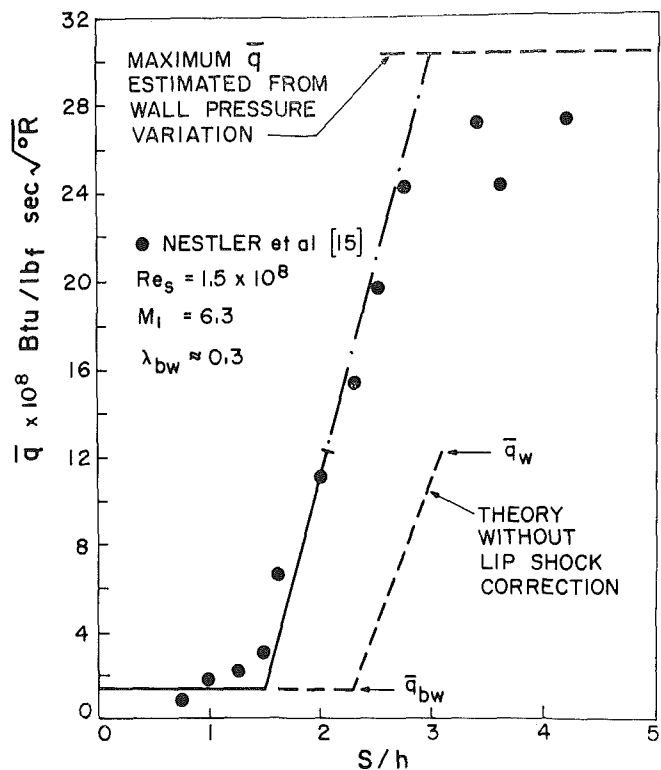


Fig. 11 Distribution of heat flux downstream of backstep

Examination of Figs. 10 and 11 along with corresponding comparisons of pressure predictions [6] and test results of Roshko and Thomke [18] and Hama [19], reveals that the amount of shift resulting from the lip shock is negligible below  $M_1 = 2$  but increases rapidly for higher Mach numbers. By comparing predicted and measured values of the distance ( $S_r/h$ ), one

can develop a simple empirical correction factor for the step height in the form  $(h - h_{th})/h = 0.295 \ln(M_1/2)$ , where the subscript  $th$  refers to the theoretical value. The predicted values of  $S_r/h$  and  $S_w/h$  can then be corrected according to the relation,  $S/h = (S/h)_{th} (h_{th}/h)$ . It is observed in Fig. 11 that this type of modification tends to rotate the predicted line slightly, so that the final slope is in reasonably good agreement with the measurements.

Because of the dearth of experimental heat transfer data, it is not possible to precisely ascertain the effect of an approach boundary layer on heat transfer rates in the separated region. The present theoretical model suggests that the effect of a non-zero  $\delta_i/h$  would be to reduce the energy flux  $E_3$  of equation (11). Furthermore, the resulting free layer profile would be slightly distorted [9] from the asymptotic form given in equation (2). This, in turn, would tend to reduce the energy flux  $E_1 + E_4$  of equation (10). Thus, the fact that the present analysis, which omits boundary layer effects, exhibits reasonably good agreement for a variety of test conditions suggests that all three of the foregoing flux values are reduced by similar amounts; therefore the resulting net flux  $E_5 + E_6 - E_2$  from equation (9) is substantially unaffected by the initial boundary layer. However, for extreme cases where  $\delta_i/h \geq 1$  the present formulation would not be applicable because of the significantly different flow fields in the two cases.

### Concluding Remarks

An engineering analysis has been presented for the diabatic, turbulent reattachment region downstream of a backward-facing step in supersonic flow. The base pressure was first determined by employing the dividing streamline escape criterion of Korst. Next a control volume analysis of the reattachment region yielded integral conservation equations which were solved by numerical search techniques for characteristic flow field parameters. The reverse flow portion of the reattachment zone was analyzed as a stagnation point region with the associated heat transfer coefficient being obtained from a variable freestream, turbulent boundary layer heat transfer correlation.

Overall energy balances were employed to determine the wall temperature and the distribution of heat transfer out to the point of dividing streamline impingement. Although the present analysis does not extend past this attachment point, it was illustrated that reasonable estimates of the maximum heat transfer can be obtained from the wall pressure variation, since experiments have confirmed the similarities of the two distributions.

Results of an extensive series of computations were shown to be correlated in terms of the approach Mach number and a Reynolds number based on approach flow stagnation conditions and the backstep height. Predictions of the present analysis were shown to compare reasonably well with data from four experimental investigations which cover the Mach number range of

2 to 6. For the hypersonic flows, a method was discussed for correcting the predicted heat transfer distribution to account for the effect of the lip shock which originates at the corner.

### References

- 1 Chapman, D. R., "A Theoretical Analysis of Heat Transfer in Regions of Separated Flow," NACA TN 3792, 1956.
- 2 Korst, H. H., "A Theory for Base Pressures in Transonic and Supersonic Flow," *Journal of Applied Mechanics*, TRANS. ASME, Vol. 78, No. 4, Dec. 1956, pp. 593-600.
- 3 Larson, H. K., "Heat Transfer in Separated Flows," *Journal of Aerospace Sciences*, Vol. 26, 1969, pp. 731-737.
- 4 Korst, H. H., "Dynamics and Thermodynamics of Separated Flows," *Proceedings of Symposium on Single and Multi-Component Flow Processes*, Rutgers Engineering Research Publication No. 45, 1965; also AGARD Conference Proceedings No. 4, *Separated Flows*, 1966.
- 5 Page, R. H., and Dixon, R. J., "Base Heat Transfer in a Turbulent Separated Flow," Fifth International Symposium of Space Technology, Tokyo, 1963.
- 6 Lamb, J. P., and Hood, C. G., "An Integral Analysis of Turbulent Reattachment Applied to Plane Supersonic Base Flows," *Journal of Engineering for Industry*, TRANS. ASME, Series B, Vol. 90, No. 4, Nov. 1968, pp. 553-560.
- 7 Lamb, J. P., Hood, C. G., and Johnson, M. G., "A Convective Transport Model for Turbulent Supersonic Planar Base Flows," ASME Paper 70-HT/SpT-35, Space Technology and Heat Transfer Conference, Los Angeles, Calif., 1970.
- 8 Schlichting, H., *Boundary Layer Theory*, 6th ed., McGraw-Hill, New York, 1968.
- 9 Korst, H. H., Chow, W. L., and Zumwalt, G. W., "Research on Transonic and Supersonic Flow of a Real Fluid at Abrupt Increases in Cross Section," University of Illinois, ME TN 392-5, 1959.
- 10 Myers, G. E., Schauer, J. J., and Eustis, R. H., "Heat Transfer to Plane Turbulent Wall Jets," *JOURNAL OF HEAT TRANSFER*, TRANS. ASME, Series C, Vol. 85, No. 3, Aug. 1963, pp. 209-214.
- 11 Kays, W. M., *Convective Heat and Mass Transfer*, McGraw-Hill, New York, 1966, p. 247.
- 12 Lamb, J. P., and Bass, R. L., "Some Correlations of Theory and Experiment for Developing Turbulent Free Shear Layers," *Journal of Basic Engineering*, TRANS. ASME, Series D, Vol. 90, No. 4, Dec. 1968, pp. 572-580.
- 13 Naysmith, A., "Heat Transfer and Boundary Layer Measurements in a Region of Supersonic Flow Separation and Attachment," TN Aero 2558, Royal Aircraft Establishment, England, May 1958.
- 14 Holloway, P. F., Sterrett, J. R., and Creekmore, H. S., "An Investigation of Heat Transfer within Regions of Separated Flow at a Mach Number of 6.0," NASA TN D-3074, 1965.
- 15 Nestler, D. E., Saydah, A. R., and Auxer, W. L., "Heat Transfer to Steps and Cavities in Hypersonic Turbulent Heat Flow," AIAA Paper 68-673, 1968.
- 16 Sandford, J., and Ginoux, J. J., "Laminar, Transitional, and Turbulent Heat Transfer Behind a Backward Facing Step in Supersonic Flow," Technical Note 38, von Karman Institute for Fluid Dynamics, Rhode-Saint-Genese, Belgium, Oct. 1968.
- 17 Weinbaum, S., "Rapid Expansion of a Supersonic Boundary Layer and Its Application to the Near Wake," *AIAA Journal*, Vol. 4, 1966, pp. 217-226.
- 18 Roshko, A., and Thomke, G. J., "Observations of Turbulent Reattachment Behind an Axisymmetric Downstream-Facing Step in Supersonic Flow," *AIAA Journal*, Vol. 4, 1966, pp. 975-980.
- 19 Hama, F. R., "Experimental Studies of the Lip Shock," *AIAA Journal*, Vol. 6, 1968, pp. 212-219.

# Measurement of Free Convection Velocity Field around the Periphery of a Horizontal Torus

T. AIHARA

Assistant Professor,  
Institute of High Speed Mechanics,  
Tohoku University,  
Sendai, Japan

E. SAITO

Assistant Professor,  
Department of Mechanical Engineering,  
Iwate University,  
Morioka, Japan

Free convection velocity fields around the peripheries of horizontal tori in air have been measured for diameter ratios of 0.5, 0.3, and 0 (a cylinder) by utilizing the trajectories of fine zinc stearate particles. The induced flow through the torus opening and the curvature of the great circle were found to influence the velocity profiles and the location of the upper and lower stagnation points. Experimental profiles for tori are compared with theoretical results for cylinders and spheres proposed by others.

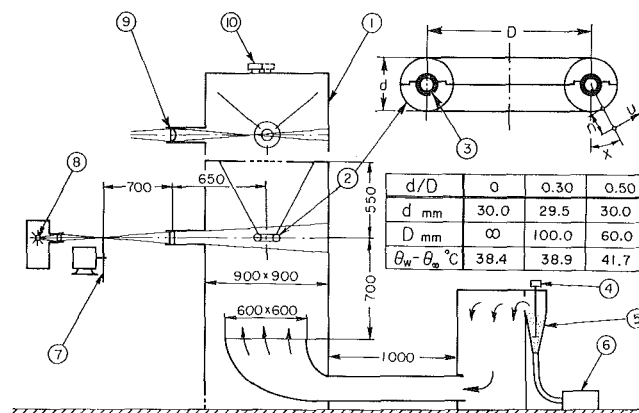
## Introduction

FREE CONVECTION heat transfer around tori has a number of interesting engineering applications. For example, heat transfer from heating and cooling coils, pipe bends, and electrical devices. In the present paper free convection flow around the periphery of an isothermal horizontal torus in air was investigated experimentally by utilizing the trajectories of fine particles [1].<sup>1</sup> An experiment on a horizontal circular cylinder corresponding to infinite great circle diameter was also carried out. The induced flow through the torus opening and the curvature of the great circle were observed to influence the velocity profiles and the location of the stagnation points. The possibility of the existence of similarity solutions for the velocity profiles is explored.

## Experimental Apparatus and Procedure

**Test Tori.** Test tori 2 were electrically heated by a nichrome heater 3 as shown in Fig. 1; the current and thermocouple leads were brought out through small holes in the upper surface. Each torus was suspended horizontally in air at the center of a free convection chamber 1 as shown in Fig. 1. The surface temperatures  $\theta_w$  were measured with 0.1-mm-dia copper-constantan thermocouples, and ambient temperatures  $\theta_\infty$  (about 20 deg C) with a 50- $\mu$ -dia copper-constantan thermocouple at a position 150 mm below the torus. A test circular cylinder 200 mm long was also constructed.

**Measurement of Velocity Field.** After thermal equilibrium was established, fine zinc stearate particles were suspended in air



- ① FREE-CONVECTION CHAMBER
- ② TEST TORUS
- ③ NICHROME HEATER
- ④ MOTOR FOR STIRRING
- ⑤ CONTINUOUS FLUIDIZED BED
- ⑥ BLOWER
- ⑦ ROTATING DISK-SHUTTER
- ⑧ SUPER HIGH PRESSURE MERCURY LAMP: ARC OF 0.25 mm DIA., BRIGHTNESS OF  $1.7 \times 10^5$  cd/cm<sup>2</sup>
- ⑨ CYLINDRICAL LENS
- ⑩ CAMERA

Fig. 1 Schematic diagram of experimental apparatus (units of dimensions, millimeters)

by a fluidized bed 5 and conducted into the convection chamber at a low velocity of 5 mm/sec for 10 to 15 min. The particles in the convection chamber were then left to settle naturally for 60 to 90 min. After this procedure, the sizes of the majority of the remaining particles were within 2 to 6  $\mu$ .

A light beam emitted by a mercury lamp 8 was intercepted at a rate of 50 or 100 times per sec by a rotating-disk shutter 7. This intermittent light beam was focused on a region about 4 mm thick near the torus 2 by a cylindrical lens 9. Photographs of the trajectories of particles passing through the high-intensity light beam were then taken on films with a speed of 400 A.S.A.

<sup>1</sup> Numbers in brackets designate References at end of paper.

Contributed by the Heat Transfer Division for publication (without presentation) in the JOURNAL OF HEAT TRANSFER. Manuscript received by the Heat Transfer Division December 29, 1970. Paper No. 71-HT-X.

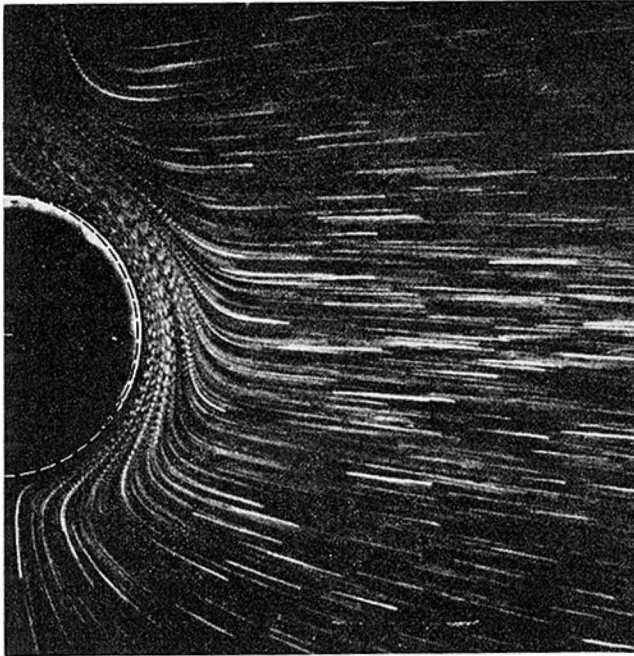


Fig. 2 Dust trajectories (streamlines) about a horizontal cylinder

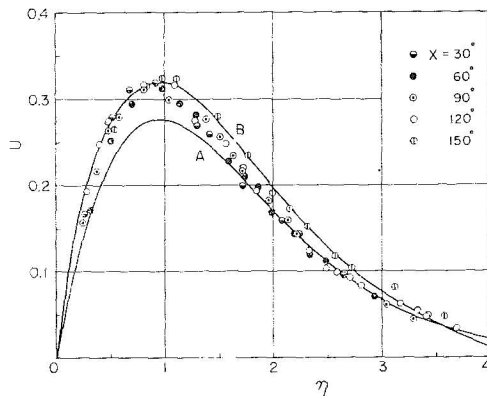


Fig. 3 Velocity profiles about a horizontal cylinder referred to Hermann's dimensionless coordinates ( $Gr_d = 10^5$ ,  $Pr = 0.72$ )

by using exposures of 0.5 sec for measuring velocity and of 1 to 5 sec for the flow pattern. Other procedures used were the same as those described by Eichhorn [1].

**Determination of Tangential Velocity.** The tangential velocity  $u$  at any point  $(x, n)$  in the boundary layer is determined by

$$u = ls/m(N - 1) \quad (1)$$

where  $l$  is the distance of  $N$  images of the same particle on a photograph,  $s$  the interception frequency of the disk shutter, and  $m$  the magnification of the photograph.

The accuracy of the present measurement may be affected by various factors. The authors have estimated the magnitudes of the following in addition to the factors discussed by Eichhorn [2]: centrifugal force, Schlieren, and thickness of the light beam. From these error analyses, it was predicted that the maximum indeterminate error for the present measurements

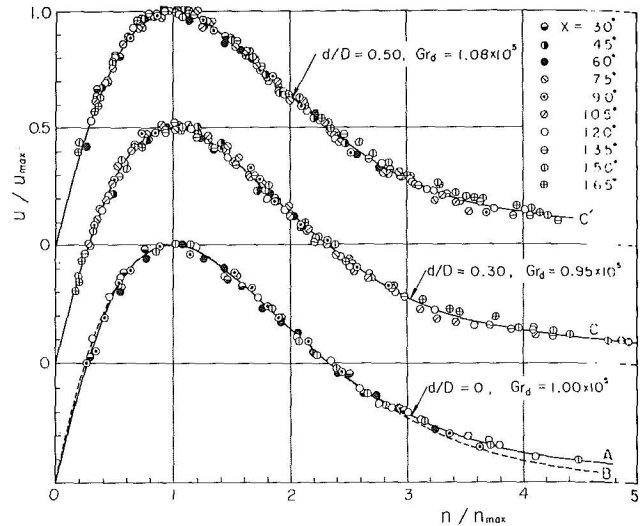


Fig. 4 Dimensionless velocity profiles

is of the order of  $\pm 4.1$  mm/sec in tangential velocity  $u$  and of  $\pm 0.19$  mm in normal distance  $n$ . However, since the average of the two to four measured values is used in the following analysis, experimental scatter was considered to be much smaller than the above-mentioned errors.

## Results and Discussion

**Velocity Field around the Cylinder.** Fig. 2 illustrates a typical velocity field observed around the horizontal cylinder. It may be seen from the figure that, unlike the usual theoretical assumption, the streamlines at a large distance are horizontal. In Fig. 3, the measured velocity profiles are shown in terms of the dimensionless velocity  $U$  and dimensionless distance  $\eta$  defined by Hermann [3]:

$$U = \frac{ud}{\nu} \left( \frac{2}{Gr_d} \right)^{1/2} / f(x)g(x) \quad (2)$$

$$\eta = \frac{n}{d} (2Gr_d)^{1/4} g(x) \quad (3)$$

where  $f(x)$  and  $g(x)$  are azimuth functions. The fluid properties are evaluated at the reference temperature [1]:  $\theta_r = \theta_w - 0.17(\theta_w - \theta_\infty)$ . Curve A is a plot of Ostrach's solution [4] which is identical to Hermann's result; curve B represents Akagi's perturbation solution [5]. The measured maximum velocities agree well with Akagi's theoretical predictions; however, the measured positions of the maximum velocity are somewhat smaller than his theoretical values. The latter tendency has also been observed in the experiment in water ( $Pr = 7$ ) by Sesonke [6].

The possibility of representing the velocity profiles in a dimensionless form based on the maximum velocity  $u_{max}$  and its position  $n_{max}$  was next investigated. The results, corresponding to  $d/D = 0$ , are shown in Fig. 4. An improved correlation was achieved. Curve A in Fig. 4 is the "average curve" representing the experimental data; curve B represents the similarity solution. Jodlbauer [7] also has measured the velocity profiles about a

## Nomenclature

$d$  = diameter of a small circle of a torus or that of a cylinder  
 $D$  = diameter of the great circle of a torus  
 $Gr_d$  = Grashof number based on  $d$   
 $n$  = normal distance from wall  
 $n_{max}$  = position of the maximum velocity

$Pr$  = Prandtl number  
 $u$  = tangential velocity  
 $u_{max}$  = maximum tangential velocity  
 $U$  = dimensionless velocity defined by equation (2)  
 $x$  = azimuth angle from the lower stagnation point

$x_0$  = lower stagnation point  
 $\eta$  = dimensionless distance defined by equation (3)  
 $\theta$  = temperature, deg C  
 $\nu$  = kinematic viscosity  
 $\xi = (x - x_0)/\pi$

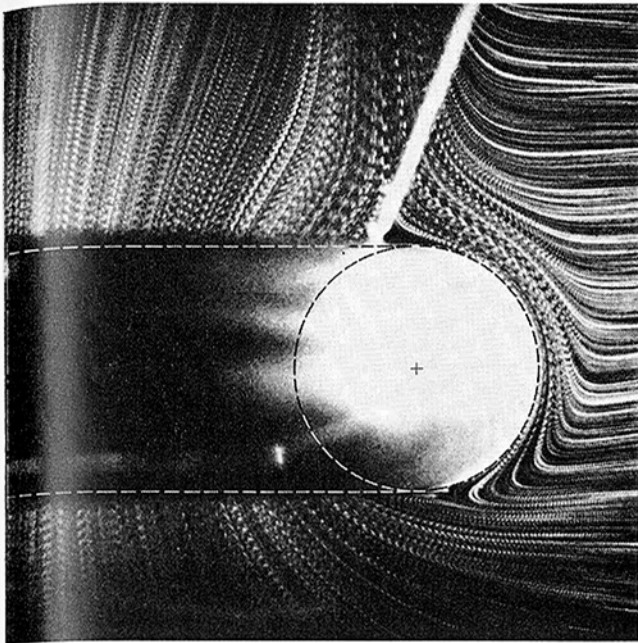


Fig. 5 Dust trajectories (streamlines) about a torus ( $d/D = 0.30$ )

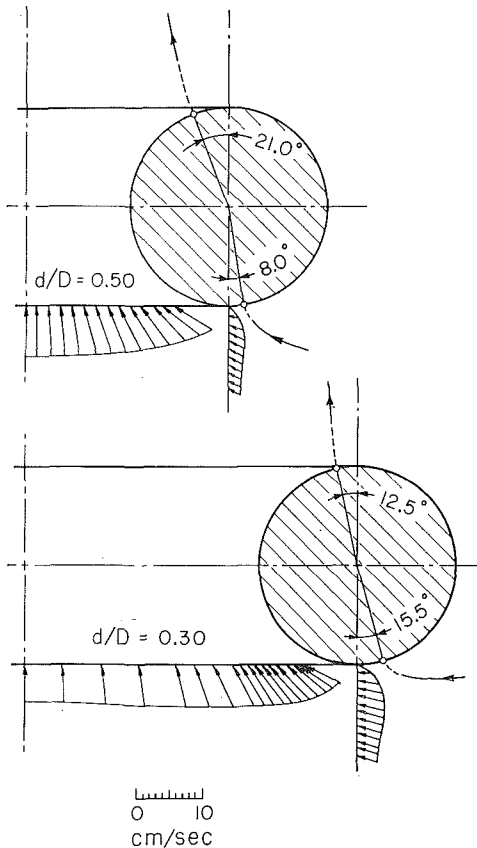


Fig. 6 Velocity distributions near the lower end and shift of stagnation points

horizontal cylinder in air; his experimental data agree comparatively well<sup>2</sup> with this average curve A.

**Velocity Field around a Torus.** The measured velocity profiles around the outer peripheries of the tori of  $d/D = 0.30$  and  $0.50$  are shown in Fig. 4. From these figures, it may be seen that both

<sup>2</sup> Details of the comparison will be presented in Reports of the Institute of High Speed Mechanics, Tohoku University, Japan.

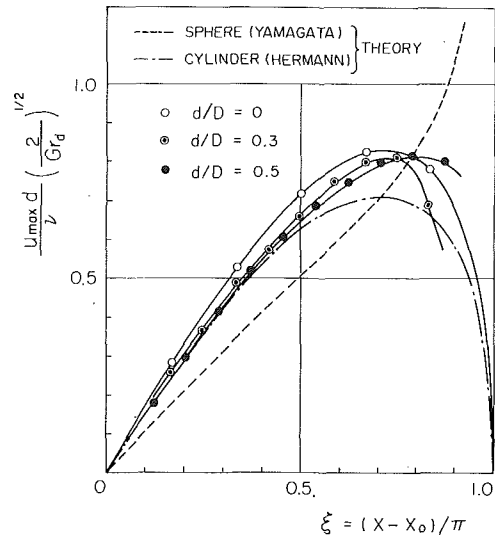


Fig. 7 Dimensionless maximum velocity for  $Pr = 0.72$

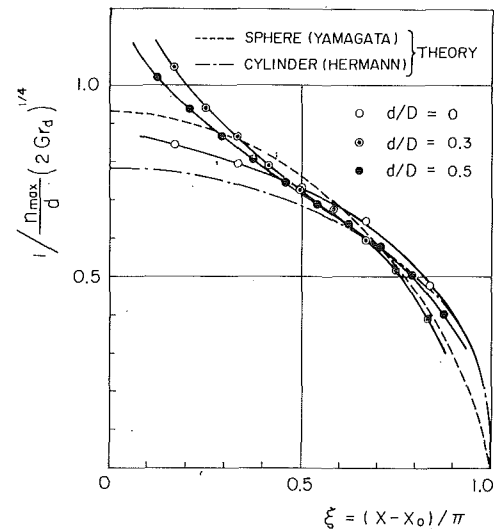


Fig. 8 Dimensionless distance of maximum velocity for  $Pr = 0.72$

velocity profiles can be successfully correlated by the respective single average curves C and C'. Therefore, for the range of  $n/n_{max} < 2.5$  and  $30 \text{ deg} < x < 165 \text{ deg}$ , it seems possible to assume a similarity solution as the zeroth-order approximation. These average curves C and C' agree with curve A within 1 percent of the maximum in the range  $n/n_{max} < 3$ .

Fig. 5 illustrates a typical photograph of the velocity field around a horizontal torus, from which the shift of the stagnation points can be observed. The shift of the lower stagnation point is caused by the induced flow at the torus opening which has an unexpectedly high velocity as illustrated in Fig. 6. The magnitude of the shift  $x_0$  increases with the diameter ratio  $d/D$ ; after reaching a maximum, it begins to decrease. The shift of the upper stagnation point is caused by the fact that the high-density fluid outside the torus tends to flow into the upper portion of the opening; accordingly, the magnitude of the shift increases monotonically with increasing  $d/D$ .

In Fig. 7 the data in terms of a dimensionless maximum velocity  $(u_{max} d / \nu) (2 / Gr_d)^{1/2}$  are plotted versus a modified azimuth angle  $\xi = (x - x_0) / \pi$ . With the use of these dimensionless groups, the effect of the diameter ratio  $d/D$  on the dimensionless maximum velocity almost disappears; the variation with  $\xi$  follows Hermann's similarity solution for a cylinder (chain curve). Yamagata's [8] similarity solution for a sphere corre-

sponding to the limiting case of  $d/D \rightarrow \infty$  is also plotted as a dashed curve in Fig. 7. As can be noted, no similarity appears to exist.

In Fig. 8 the dimensionless position of the maximum velocity  $(n_{\max}/d)(2Gr_d)^{1/4}$  is plotted; the greater the shift of the lower stagnation point, the nearer the maximum velocity approaches the wall. This is caused by the fact that the velocity profile near the lower stagnation point is of the dual-flow type, owing to the sudden inversion of the flow (see Fig. 5).

## Conclusions

The results obtained are summarized as follows:

1 The measured velocity profiles around a cylinder agree comparatively well with Akagi's perturbation solution; unlike the usual theoretical assumption, the streamlines at a large distance are horizontal.

2 The measured velocity profiles for the tori, non-dimensionalized on the basis of  $u_{\max}$  and  $n_{\max}$ , agree fairly well with those for the cylinder. For the range of  $n/n_{\max} < 2.5$  and  $30 \text{ deg} < x < 165 \text{ deg}$ , a similarity solution is applicable.

3 The induced flow through the torus opening leads to the shift of the lower stagnation point. The lower stagnation point first moves up and then down as  $d/D$  increases. The upper stagnation point also shifts widely with increasing  $d/D$ .

4 The variation of  $u_{\max}$  with the modified azimuth angle  $\xi$  follows Hermann's similarity solution closely; however, no similarity in  $u_{\max}$  between tori and spheres is observed.

The effect of the  $d/D$  value on  $n_{\max}$  is prominent in the region of small  $\xi$ ; the value of  $n_{\max}$  decreases as  $x_0$  increases.

## Acknowledgment

The authors wish to express their gratitude to Professor Emeritus T. Tsubouchi, Tohoku University, for his advice and encouragement during this work, and to Mr. S. Endo, a technician of the Institute of High Speed Mechanics, for his assistance in making the experiments.

## References

- 1 Eichhorn, R., "Measurement of Low Speed Gas Flows by Particle Trajectories: A New Determination of Free Convection Velocity Profiles," *International Journal of Heat and Mass Transfer*, Vol. 5, 1962, pp. 915-928.
- 2 Eichhorn, R., "An Analytical Investigation of Combined Free and Forced Convections and a New Method to Measure Free Convection Velocity Profiles," PhD thesis, University of Minnesota, 1959, pp. 86-97.
- 3 Hermann, R., "Wärmetübergang bei freier Strömung am waagerechten zylinder in zweiatomigen Gasen," *VDI Forschungsheft*, No. 379, 1936.
- 4 Ostrach, S., "An Analysis of Laminar Free-Convection Flow and Heat Transfer Around a Flat Plate Parallel to the Direction of the Generating Body Force," NACA Report No. 1111, 1953.
- 5 Akagi, S., "The Effect of Curvature on Free Convection Around a Horizontal Cylinder," *Transactions of the Japan Society of Mechanical Engineers*, Vol. 31, 1965, pp. 1327-1335 (in Japanese).
- 6 Sesonke, A., "Velocity and Temperature Distributions About a Horizontal Cylinder in Free Convection Heat Transfer," *AIChE Journal*, Vol. 7, 1961, pp. 352-353.
- 7 Jodlbauer, K., "Das Temperatur- und Geschwindigkeitsfeld um ein Geheiztes Rohr bei freier Konvektion," *Forschung auf dem Gebiete des Ingenieurwesens*, Vol. 4, 1933, pp. 158-172.
- 8 Yamagata, K., "Convective Heat Transfer from Sphere in Still Air," *Transactions of the Japan Society of Mechanical Engineers*, Vol. 9, 1943, pp. 11-132-138 (in Japanese).

ISMAILA ISA

Assistant Professor,  
Gannon College,  
Erie, Pa.

CHING-JEN CHEN

Associate Professor,  
Department of Mechanical Engineering,  
University of Iowa,  
Iowa City, Iowa.  
Mem. ASME

# Steady Two-Dimensional Forced Film Condensation with Pressure Gradients for Fluids of Small Prandtl Numbers<sup>1</sup>

*A laminar two-dimensional steady forced film condensation with pressure gradients on a nonisothermal surface with  $(T_{\text{sat}} - T_w)$  remaining constant is considered. The case of small Prandtl number has been solved. Body force and interface resistance effects have been neglected. Inertia effect for the liquid phase is assumed negligible. Three parameters govern the problem: the pressure gradient parameter  $\beta$ , the property parameter  $R = (\nu_w/\nu_l)^{1/2}$ , and the parameter  $B = h_{f0}\mu_w/\Delta TK_l$ . It is found that an increase in pressure parameter,  $\beta$ , results in the decrease of the average Nusselt number, the condensation rate, and the average skin friction coefficient. With or without pressure gradients, the condensation rate and the heat flux increase with the property parameter  $R$ . The average Nusselt number, however, decreases with the parameter  $B$  to a minimum and then rises again.*

## Introduction

DURING the past years, many investigations have been made both theoretically and experimentally to find heat transfer characteristics of forced film condensation on cooled surfaces. Cess [1]<sup>2</sup> considered forced film condensation over a flat plate by neglecting inertia forces, body forces, and convected energy in the governing liquid-flow equations. A similar problem was treated by Koh [2] but he included the inertia terms in the liquid layer equation. His results showed that the convective heat transfer is negligible for low  $N_{Pr}$  liquids but quite important for high  $N_{Pr}$  liquids. Rohsenow, Webber, and Ling [3] considered the condensation of pure vapor with a uniform velocity over a vertical plate with a constant shear at the interface. Body forces and inertia forces were neglected. Forced convection laminar film condensation over an isothermal flat plate has also been treated by Shekrladze and Gomelauri [4]. A linear temperature profile was shown for the condensate film.

Combined free and forced film condensation have been considered by Chung [5] and Jacobs [6]. Chung showed that the heat transfer and condensation rates did not depend explicitly on the  $N_{Pr}$  and that the effect of the body force was to decrease the heat transfer coefficient. Jacobs [6] showed that the heat

transfer coefficient decreased with increasing  $H$  (i.e.,  $C_p\Delta T/N_{Pr}h_{f0}$ ). In particular he showed that for  $\rho_l/\rho_v = 210.19$  and  $R = 4.496$ , both body and inertia forces are important for the range of Froude number 1.0 to 2000. The problem is purely that of forced convection above this, while natural convection dominates for cases of Froude number less than 1.0. Koh [7] showed that the heat transfer rate is decreased by the presence of noncondensables. Sparrow, Minkowycz, and Saddy [8] showed that interface resistance in forced condensation is negligible. Minkowycz and Sparrow [9] later showed that the effect of vapor superheating is negligible for the case of pure vapor but becomes significant in the presence of noncondensable gases. The present analysis considers the additional effect of pressure gradients on laminar forced film condensation for liquids of small  $N_{Pr}$ . The vapor flow is similar to Falkner-Skan flow.

## Problem Formulation

A physical model is depicted in Fig. 1 in the dimensionless coordinate  $(x, y)$  plane;  $x$  and  $y$  are coordinates along and normal to the surface respectively and  $U_\infty(x)$  is the free-stream vapor velocity at the edge of the vapor boundary layer. The vapor temperature is assumed at the saturated state which depends on the local pressure. This assumption may approximate an expansion process from a saturated state at the leading edge into a wet region downstream where the vapor temperature remains essentially at the saturated temperature at the given local pressure. The temperature on the wall is nonisothermal but is linearly proportional to the local vapor temperature. All vapor and liquid properties are considered constant. There is

<sup>1</sup> This research was partially supported by an Old Gold Faculty Fellowship from the University of Iowa for the second author.

<sup>2</sup> Numbers in brackets designate References at end of paper.

Contributed by the Heat Transfer Division for publication (without presentation) in the JOURNAL OF HEAT TRANSFER. Manuscript received by the Heat Transfer Division March 15, 1971. Paper No. 71-HT-Y.

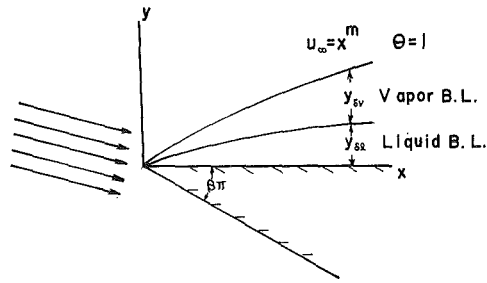


Fig. 1 Physical model in dimensionless coordinate plane

neither heat generation nor superheat. Body force and surface tensions are neglected. The condensate film layer is thin in comparison with the characteristic length  $L$  of the cooling surface so that the boundary layer approximations apply.

Governing equations are made dimensionless by defining:

$$\begin{aligned} x &= \frac{X}{L} & u_v &= \frac{U_v}{U_{1v}} \\ y &= \frac{Y}{\delta L} & v_v &= \frac{V_v}{U_{1v}} \\ u_l &= \frac{U_l}{U_r} & U_r &= \frac{\mu_v}{\mu_l} U_{1v} \\ v_l &= \frac{v_l}{U_r \delta} \\ \theta &= \frac{T_l - T_w}{T_{sat} - T_w} \end{aligned} \quad (1)$$

The potential vapor velocity distribution will be given by

$$\frac{U_{\infty}(x)}{U_{1v}} = x^m = u_{\infty}(x) \quad (2)$$

The known characteristics are  $U_{1v}$ ,  $(T_{sat} - T_w)$ , and  $L$ , where

$$N_{Rev} = \frac{U_{1v} L}{\nu_v} \quad \delta = \frac{1}{\sqrt{N_{Rev}}} \quad (3)$$

The following parameters appear in the normalized equations:  $1/\delta^2 = N_{Rev}$ , the vapor Reynolds number,  $R = (\nu_v/\nu_l)^{1/2}$ , the property ratio,  $m$ , the velocity exponent that measures the effect of the pressure gradient, and  $B = h_{fg}\mu_v/(T_{sat} - T_w)K_l$  which comes from the thermal boundary conditions. A term  $\rho_l\mu_v^2/\rho_v\mu_l^2$  appears as the coefficient of the liquid inertia term as a result of ordering analysis and is only a function of the vapor and liquid properties. Its magnitude is generally less than unity.

## Nomenclature

$B$  = thermal parameter =  $h_{fg}\mu_v/\Delta TK_l$   
 $c_f$  = friction coefficient  
 $F$  = transformed vapor stream function  
 $f$  = transformed liquid stream function  
 $h_{fg}$  = latent heat of condensation, Btu/lbm  
 $K$  = see equation (22)  
 $k$  = liquid thermal conductivity, Btu/ft-deg F-sec  
 $\dot{m}$  = condensation rate  
 $m$  = power index of vapor potential flow, see equation (2)

$N_{Re}$  = Reynolds number  
 $N_{Pr}$  = Prandtl number  
 $R$  =  $(\nu_v/\nu_l)^{1/2}$ , liquid-vapor kinematic viscosity ratio  
 $T$  = absolute temperature, deg R  
 $U, V$  = tangential and normal velocity at any point, ft/sec  
 $\alpha = \eta - \eta_{\delta}$   
 $\beta$  = pressure gradient parameter =  $2m/(m+1)$   
 $\delta$  = order of magnitude of boundary layer thickness, equation (3)  
 $\eta$  = similarity variable, equation (14)  
 $\theta = (T_l - T_w)/(T_{sat} - T_w)$   
 $\mu$  = viscosity, lbm/sec-ft  
 $\rho$  = density, lbm/ft<sup>3</sup>

$\phi$  = temperature function, see equation (14)  
 $\psi$  = stream function, see equation (14)

### Subscripts

$l$  = liquid  
 $v$  = vapor  
 $w$  = at wall  
 $\infty$  = vapor free stream  
 $sat$  = at saturated condition  
 $\delta$  = at edge of boundary layer  
 $i$  = vapor-liquid interface

### Superscript

$\bar{\phantom{x}}$  = mean

Thus the liquid inertia terms may be neglected. This confirms the calculations of Sparrow and Gregg [10] and of Shekrladze and Gomelaouri [4].

Neglecting terms involving small coefficients and assuming small liquid Prandtl number, we have the approximated governing equations:

### Liquid layer:

Continuity:

$$\frac{\partial u_l}{\partial x} + \frac{\partial v_l}{\partial y} = 0 \quad (4)$$

Momentum:

$$\frac{\partial^2 u_l}{\partial y^2} = -u_{\infty} \frac{du_{\infty}}{dx} \quad (5)$$

Energy:

$$\frac{\partial^2 \theta_l}{\partial y^2} = 0 \quad (6)$$

Boundary conditions:

$$\begin{aligned} \text{at } y = 0 & \quad u_l = v_l = 0 \\ & \quad \theta_l = 0 \\ \text{at } y = y_i & \quad \theta_l = 1 \end{aligned} \quad (7)$$

where subscript  $i$  denotes conditions at the interface.

### Vapor layer:

Continuity:

$$\frac{\partial u_v}{\partial x} + \frac{\partial v_v}{\partial y} = 0 \quad (8)$$

Momentum:

$$u_v \frac{\partial u_v}{\partial x} + v_v \frac{\partial v_v}{\partial y} = u_{\infty} \frac{du_{\infty}}{dx} + \frac{\partial^2 u_v}{\partial y^2} \quad (9)$$

Boundary conditions:

$$\begin{aligned} \text{at } y = y_i & \quad u_v = 0 \\ \text{as } y \rightarrow \infty & \quad u_v = u_{\infty} = x^m \end{aligned} \quad (10)$$

### Interface matching conditions at $y = y_i$ :

Shear:

$$\left. \frac{\partial u_l}{\partial y} \right|_i = \left. \frac{\partial u_v}{\partial y} \right|_i \quad (11)$$

Mass:

$$R^2 \left\{ v - u \frac{dy_i}{dx} \right\}_{l,i} = \left\{ v - u \frac{dy_i}{dx} \right\}_{v,i} \quad (12)$$

Energy:

$$R^2 B \left\{ u \frac{dy_i}{dx} - v \right\}_{v,i} = \left. \frac{\partial \theta_l}{\partial y} \right|_{l,i} \quad (13)$$



## Method of Solution

We define the stream function from the continuity equations as:

$$\begin{aligned}\psi_l &= [2u_\infty x / (m+1)]^{1/2} f(\eta) \\ \phi(\eta) &= \theta_l(x, y)\end{aligned}\quad (14)$$

and

$$\psi_v = [2u_\infty x / (m+1)]^{1/2} F(\eta)$$

where

$$\eta = y \{ [(m+1)/2] [u_\infty/x] \}^{1/2}$$

The resulting transformed equations are:

**Liquid boundary layer:**

$$f''' + \beta = 0 \quad (15)$$

$$\phi'' = 0 \quad (16)$$

with boundary conditions:

$$f(\eta = 0) = 0 \quad (17)$$

$$f'(\eta = 0) = 0$$

and

$$\phi(\eta = 0) = 0$$

$$\phi(\eta = \eta_\delta) = 1$$

where

$$\eta_\delta = y_l [(m+1)u_\infty/2x]^{1/2} \quad (18)$$

**Vapor boundary layer:**

$$F''' + FF'' + \beta(1 - F'^2) = 0 \quad (19)$$

with boundary conditions:

$$F'(\eta = \eta_\delta) = 0 \quad (20)$$

$$F'(\eta \rightarrow \infty) = 1$$

**Matching conditions:**

$$F''(\eta_\delta) = f''(\eta_\delta) \quad (21)$$

$$R^2 f(\eta_\delta) = F(\eta_\delta) = K \quad (22)$$

$$R^2 B = \frac{\phi(\eta_\delta)}{f(\eta_\delta)} \quad (23)$$

where

$$R^2 = \frac{\nu_v}{\nu_l}, \quad B = \frac{h_{fg}\mu_v}{\Delta T K_l}, \quad \text{and} \quad \beta = \frac{2m}{m+1}$$

To solve the vapor boundary layer equation, a transformation of  $F(\eta)$  to  $F(\alpha)$  is made by defining  $\alpha$  as

$$\alpha = \eta - \eta_\delta \quad (24)$$

Equation (19) remains the same with the prime denoting differentiation with respect to  $\alpha$ . The boundary conditions become:

$$F'(0) = 0$$

$$F'(\infty) = 1 \quad (25)$$

$$F(0) = K$$

Thus equation (19) can be solved independently of the liquid governing equation up to an unknown constant  $K$  in equation (25). This problem may be interpreted as a boundary layer flow with suction, which has been solved by Watson [11] and others. However, in order to match the liquid equation analytically we consider an integral method and integrate equation (19) as

$$\int_0^\infty \{ F''' + FF'' + \beta(1 - F'^2) \} d\alpha = 0 \quad (26)$$

that is

$$-F''(0) + F(\alpha_\delta) - (1 + \beta) \int_0^{\alpha_\delta} F'^2 d\alpha + \int_0^{\alpha_\delta} \beta d\alpha = 0 \quad (27)$$

We assume a polynomial function for  $F(\alpha)$  given by

$$F(\alpha) = K + \frac{\alpha^2}{\alpha_\delta} - \frac{1}{3} \frac{\alpha^3}{\alpha_\delta^2} \quad (28)$$

and substitute in equation (27) to solve for  $\alpha_\delta$ , the vapor boundary layer thickness. Thus we have

$$\alpha_\delta = \frac{15 \{ -K \pm [K^2 + (8/15)(2 + 7\beta)]^{1/2} \}}{(4 + 14\beta)} \quad (29)$$

where the positive sign is chosen to make  $\alpha_\delta$  positive. From equations (28) and (29) we have the interfacial shear,  $F''(\eta_\delta)$ , at  $\eta = \eta_\delta$  as

$$\begin{aligned}F''(\eta_\delta) &= f''(\eta_\delta) = F''(\alpha = 0) \\ &= \frac{(8 + 28\beta)}{15 \{ -K + [K^2 + (8/15)(2 + 7\beta)]^{1/2} \}} = \frac{2}{\alpha_\delta}\end{aligned}\quad (30)$$

or solving for  $K$  which is related to condensation rate,

$$K = F''(\eta_\delta) - \frac{(4 + 14\beta)}{15F''(\eta_\delta)} \quad (31)$$

With the value of  $F''(\eta_\delta)$  obtained from (31) and together with the boundary conditions (17), the liquid momentum and energy equations (15) and (16) can respectively be integrated to give

$$f(\eta) = 1/2 \left\{ -\frac{\beta}{3} \eta^3 + \{ F''(\alpha = 0) + \beta \eta_\delta \} \eta^2 \right\} \quad (32)$$

and

$$\phi(\eta) = \eta/\eta_\delta \quad (33)$$

$K$ ,  $\alpha_\delta$  or  $[F''(0)]$ , and  $\eta_\delta$  are yet unknown. They are solved from the three matching conditions (21), (22), and (23) with  $\beta$ ,  $R$ , and  $B$  as parameters. Equation (23) combined with (33) gives

$$KB = 1/\eta_\delta \quad (34)$$

while (22) with (31) gives

$$f(\eta_\delta) = \frac{K}{R^2} = \frac{\beta \eta_\delta^3}{3} + \frac{\eta_\delta^2 F''(\alpha = 0)}{2} \quad (35)$$

where  $F''(\alpha = 0)$  is given by either equation (30) or (31). Hence  $K$ ,  $\eta_\delta$ , and  $F''(\alpha = 0)$  may now be solved from (31), (34), and (35) in terms of  $\beta$ ,  $R$ , and  $B$ . Equation (34) together with (35) yields

$$B^3 - \left( \frac{F'' R^2}{2 C^3} \right) B - \frac{\beta R^2}{3 C^4} = 0 \quad (36)$$

where

$$C = F'' - \frac{1}{F''} \left( \frac{4 + 14\beta}{15} \right) \quad (37)$$

$F''(\alpha = 0)$  or  $f''(\eta_\delta)$ , shear force at the interface, are solved from equation (36) in terms of  $B$ ,  $R$ , and  $\beta$  parameters. Then  $K$  and  $\eta_\delta$  are obtained respectively from (31) and (34). These are given in Table I.

The local condensation rate per unit area is expressed in dimensionless form as:

**Table 1** General results of  $f''(\eta_\delta)$ ,  $f'(\eta_\delta)$ ,  $K$ , and  $\eta_\delta$  as functions of  $B$ ,  $R$ , and  $\beta$

$\beta = -0.1$					
$R$	$B$	$f''(\eta_\delta)$	$f'(\eta_\delta)$	$K$	$\eta_\delta$
2	30.7909	0.47	0.1457	0.1012	0.3209
	1.1266	1.45	0.9452	1.3305	0.6672
	0.1421	10.00	7.0236	9.9827	0.7048
	0.0141	100.00	70.6684	99.9983	0.7069
10	151.2616	0.47	0.0305	0.1012	0.0653
	11.3266	0.90	0.1115	0.7074	0.1248
	1.4304	5.00	0.7030	4.9653	0.1408
	0.1414	50.00	7.0692	49.9965	0.1414
0.0141	500.00	70.7090	499.9995	0.1414	
50	753.5286	0.47	0.0062	0.1012	0.0131
	27.7592	1.45	0.0392	1.3305	0.0271
	12.5824	2.90	0.0811	2.8402	0.0280
	1.7690	20.00	0.5655	19.9913	0.0283
	0.1179	300.00	8.4852	299.9993	0.0283
	0.0141	2500.00	70.7106	2499.9990	0.0283
$\beta = 0.0$					
2	32.6969	0.57	0.1706	0.1022	0.2994
	1.1954	1.45	0.9581	1.2661	0.6607
	0.1420	10.00	7.0616	9.9733	0.7062
	0.0141	100.00	70.7097	99.9973	0.7071
10	163.4846	0.57	0.0341	0.1022	0.0599
	11.2599	1.00	0.1211	0.7333	0.1211
	1.4371	5.00	0.7033	4.9467	0.1407
	0.1414	50.00	7.0707	49.9947	0.1414
0.0141	500.00	70.7106	499.9993	0.1414	
50	817.4231	0.57	0.0068	0.1022	0.0120
	29.8842	1.45	0.0383	1.2661	0.0264
	12.7952	2.90	0.0807	2.8080	0.0278
	1.7695	20.00	0.5655	19.9867	0.0283
	0.1179	300.00	8.4853	299.9990	0.0283
	0.0141	2500.00	70.7107	2499.9990	0.0283
$\beta = 0.5$					
2	51.6406	0.90	0.2175	0.0852	0.2273
	1.7196	1.45	0.9879	0.9443	0.6159
	0.1413	10.00	7.2575	9.9267	0.7130
	0.0141	100.00	70.9170	99.9927	0.7079
10	267.6101	0.90	0.0400	0.0852	0.0439
	9.1555	1.45	0.1711	0.9443	0.1157
	1.4719	5.00	0.7048	4.8533	0.1400
	0.1414	50.00	7.0784	49.9853	0.1415
0.0141	500.00	70.7189	499.9985	0.1414	
50	1346.8750	0.90	0.0079	0.0852	0.0087
	256.1174	1.00	0.0147	0.2667	0.0146
	13.9577	2.90	0.0787	2.6471	0.0271
	1.7722	20.00	0.5655	19.9633	0.0283
	0.1179	300.00	8.4856	299.9976	0.0283
	0.0141	2500.00	70.7110	2499.9990	0.0283
$\beta = 1.0$					
2	3.0131	1.45	0.9153	0.6224	0.5332
	0.7018	2.50	2.01231	2.0200	0.7056
	0.1405	10.00	7.4631	9.8800	0.7204
	0.0141	100.00	71.1252	99.9880	0.7087
10	16.9582	1.45	0.1419	0.6224	0.0947
	3.8265	2.50	0.3318	2.0200	0.1294
	1.5083	5.00	0.7061	4.7600	0.1393
	0.1414	50.00	7.0861	49.9760	0.1415
0.0141	500.00	70.7271	499.9976	0.1414	
50	86.3285	1.45	0.0272	0.6224	0.0186
	15.3120	2.90	0.0765	2.4862	0.0263
	1.7749	20.00	0.5655	19.9400	0.0283
	0.1178	300.00	8.4859	299.9958	0.0283
	0.0141	2500.00	70.7113	2499.9990	0.0283

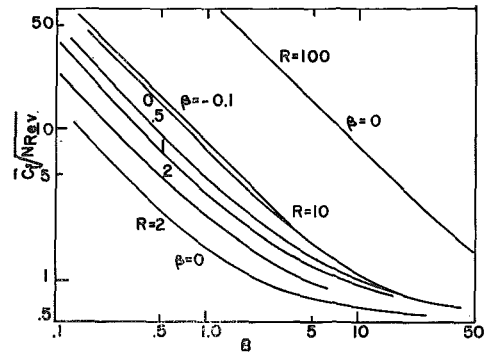


**Fig. 2** Average friction coefficient

$$\dot{m} = \frac{\dot{M}}{\delta U_{1v} \rho} = R^2 \left( \frac{\mu_v}{\mu_l} \right)^2 \frac{1}{(N_{Rev})^{1/2}} x^{\frac{m-1}{2}} f(\eta_\delta) \quad (38)$$

while the average value is given as

$$\dot{m} = \frac{K}{(N_{Rev})^{1/2}} \left( \frac{\mu_v}{\mu_l} \right)^2 (2 - \beta) f(\eta_\delta) \quad (39)$$

The local skin friction coefficient is equal to

$$C_f = \frac{\mu_l \frac{\alpha U_l}{\alpha Y} \Big|_0}{\rho U_{1v}} = \frac{1}{(N_{Rev})^{1/2}} \cdot \frac{1}{(2 - \beta)} x^{\frac{(2\beta-1)}{2-\beta}} f''(0) \quad (40)$$

and the average value is given as

$$\bar{C}_f = \frac{1}{(N_{Rev})^{1/2}} \cdot \frac{1}{(1 + \beta)} \{f''(\eta_\delta) + \beta \eta_\delta\} \quad (41)$$

The local Nusselt number is

$$Nu_x = \frac{h(x)L}{K_l} = (N_{Rev})^{1/2} \left( \frac{1}{2 - \beta} \right)^{1/2} X^{\frac{\beta-1}{2-\beta}} \phi'(0) \quad (42)$$

while the average value is given by

$$\bar{Nu} = [N_{Rev}(2 - \beta)]^{1/2} \phi'(0) \quad (43)$$

that is

$$\frac{\bar{Nu}}{(N_{Rev})^{1/2}} = \frac{(2 - \beta)^{1/2}}{\eta_\delta} \quad (44)$$

## Results and Discussion

Forced film condensation with pressure gradient is solved for liquids of small Prandtl number. Three parameters, namely,  $B$ ,  $R$ , and  $\beta$ , are involved. Quantities of major interest are given in Table 1, details of which can be found in reference [12]. Table 2 summarizes the general characteristics of the liquid thickness,  $\eta_\delta$ , interfacial liquid velocity,  $f'(\eta_\delta)$ , shear force,  $f''(\eta_\delta)$ , friction coefficient,  $\bar{C}_f$  ( $N_{Rev})^{1/2}$ , condensation rate,  $\dot{m}$ , and Nusselt number,  $\bar{Nu}$ , as functions of the thermal parameter,  $B$ , the kinematic viscosity ratio,  $R$ , and the pressure gradient parameter,  $\beta$ . Results are also plotted in Figs. 2-6.

**Effect of  $B$ .** For a given pressure gradient parameter  $\beta$  and the kinematic viscosity ratio  $R$ , the skin friction coefficient decreases with increasing  $B$  (see Fig. 2). Thus, for example, we will have

**Table 2** Summary of general characteristics

$R$	$B$	$\beta$	$\eta_\delta$	$f'(\eta_\delta)$	$f''(\eta_\delta)$	$\bar{C}_f(N_{Rev})^{1/2}$	$\dot{m}(N_{Rev})^{1/2} \times (\mu_l/\mu_v)^2$	$Nu/(N_{Rev})^{1/2}$
F	F	D	I	D	D	I	I	I
I	F	F	D	D	I	I	I	I
F	D	F	I	I	I	I	I	D

F = fixed, I = increase, D = decrease

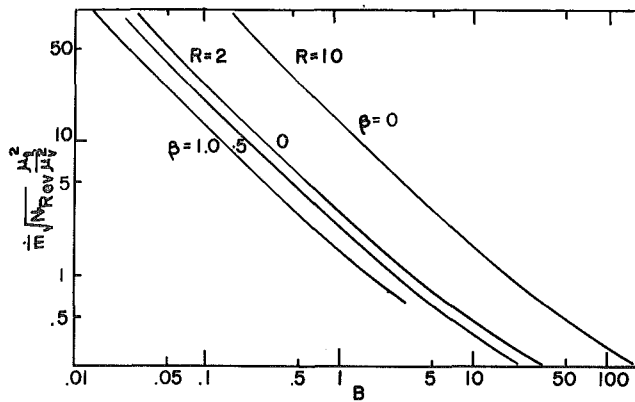


Fig. 3 Average rate of condensation

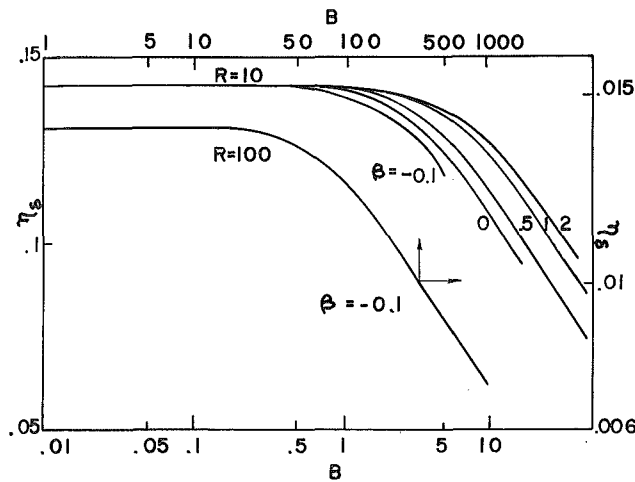


Fig. 4 Film thickness,  $\eta_\delta$

a small value of friction coefficient with small temperature difference. The friction coefficient approaches that of vapor fluid in the limit of large  $B$ . Both the condensate velocity at the interface,  $f'(\eta_\delta)$ , and the condensation rate (see Fig. 3), increase with a decrease of  $B$ . The film thickness  $\eta_\delta$  (Fig. 4) increases monotonically to a limit as  $B$  decreases for all  $R$  and  $\beta < 0$ . However, for  $\beta > 0$  and as  $B$  decreases,  $\eta_\delta$  first increases to a maximum and then slightly falls back to a constant value. Therefore, for example, an increase in the temperature difference between the wall and vapor can only increase the thickness of the condensate film to a limit. However, an increase in the temperature difference will always decrease heat transfer,  $\bar{Nu}$  (see Fig. 5).

**Effect of  $R$ .** The film thickness decreases with a liquid having larger  $R$ . The average friction coefficient (see Fig. 2) increases with  $R$  for a given value of  $\beta$  and thermal parameter  $B$ .

**Effect of  $\beta$ .** Given  $R$  and  $B$ , the average condensation rate  $\bar{m}$ , heat transfer, and the film thickness  $\eta_\delta$  increase with a decrease in  $\beta$  (see Figs. 3–5). For example, the average condensation rate for a stagnation point flow ( $\beta = 1$ ) is smaller than that for a flat plate ( $\beta = 0$ ). This is so because the vapor velocity component along the surface just outside the boundary layer must accelerate from zero at the stagnation point to some value, while the velocity is a constant for a flat plate.

**Comparison with Some Known Results.** The forced condensation over a flat plate ( $\beta = 0$ ) is a special case that may be compared with the results of the present work with pressure gradient  $\beta$  being arbitrary. In particular, comparison with the results of Cess [1] and Koh [2, 7] will be made. The present result for the vapor side agrees within one-half percent with those of Koh [2, 7]. Table 3 shows a comparison of the result for the flat-

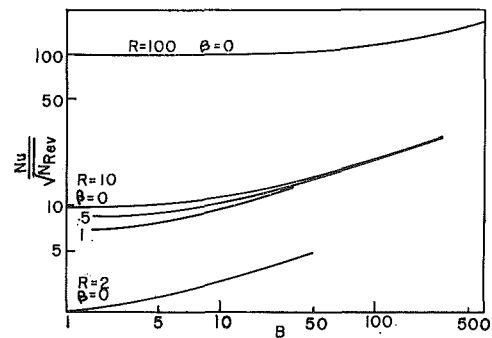


Fig. 5 Heat transfer

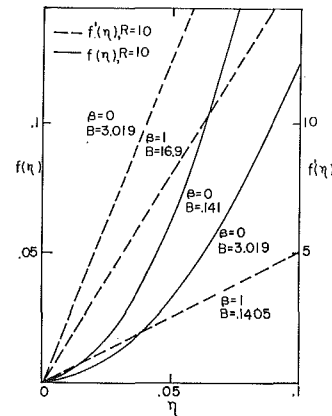


Fig. 6 Liquid velocity profiles

Table 3 Comparison of others' and present results for flat-plate case

$R = 10, B = 11.2599$					Source
$\eta_\delta$	$f(\eta_\delta)$	$f''(\eta = 0)$	$\phi'(\eta_\delta)$	$\phi'(\eta = 0)$	
0.1202	0.00790	1.0946	8.2874	8.3340	Koh
0.1211	0.00733	1.0000	8.2554	8.2572	present

$R = 2.12, B = 0.8661$

1.3941	Jacob
1.4689	Koh
1.499	Cess
1.499	present
1.5809	Chung

plate case,  $\beta = 0$ . It shows a good agreement for the primary functions  $f(\eta)$ ,  $f''(\eta)$ , and  $\phi'(\eta)$ , and consequently the condensation rate, the skin friction coefficient, and the heat transfer quantities respectively. Fig. 6 shows that for large  $B$ , the liquid velocity profiles are linear and this agrees well with the result of Koh [7] which he illustrates in his Fig. 2. The present results and those of Cess [1] and Koh [2, 7] show that  $\bar{Nu}/(N_{Re,v})^{1/2}$  is approximately independent of Prandtl number for thin films and increases as  $B$  increases. Koh [7] and the present work show that  $\bar{Nu}/(N_{Re,v})^{1/2}$  decreases with  $B$  to a minimum and then rises again (see Fig. 5).

## Summary and Conclusion

The two-phase boundary layer flow for laminar film condensation with constant  $(T_{sat} - T_w)$  is solved for liquids of small Prandtl number. The physical parameters involved are the kinematic viscosity ratio,  $R^2 = \nu_v/\nu_l$ , the thermal parameter  $B = h_{fg}\mu_v/\Delta TK_l$ , and the pressure gradient parameter  $\beta$ . The analysis shows that an increase in the pressure gradient or configuration parameter  $\beta$  results in the decrease of: the film thickness, the average rate of heat transfer, the average condensation rate, and the average skin friction coefficient. The average Nusselt number decreases to a minimum and then rises again with  $B$ . Comparison shows that the present results agree well with those of Cess [1] and Koh [7] for the flat-plate case of  $\beta = 0$ .

## References

- 1 Cess, R. D., "Laminar Film Condensation on a Flat Plate in the Absence of a Body Force," *Z. Angew. Math. Phys.*, Vol. 11, 1960, pp. 426-433.
- 2 Koh, J. C. Y., "Film Condensation in a Forced-Convection Boundary Layer Flow," *International Journal of Heat and Mass Transfer*, Vol. 5, 1962, pp. 941-954.
- 3 Rohsenow, W. M., Webber, J. H., and Ling, A. T., "Effect of Vapor Velocity on Laminar and Turbulent-Film Condensation," *TRANS. ASME*, Vol. 78, 1956, pp. 1637-1643.
- 4 Shekrladze, I. G., and Gomelauro, V. I., "Theoretical Study of Laminar Film Condensation of Flowing Vapor," *International Journal of Heat and Mass Transfer*, Vol. 9, 1966, pp. 581-591.
- 5 Chung, P. M., "Film Condensation With and Without Body Force in a Boundary Layer Flow of Vapor Over a Flat Plate," NASA TND-790, 1961.
- 6 Jacobs, H. R., "An Integral Treatment of Combined Body Force and Forced Convection Film Condensation," *International Journal of Heat and Mass Transfer*, Vol. 9, 1966, pp. 637-648.
- 7 Koh, J. C. Y., "Laminar Film Condensation of Condensable Gases and Mixtures on a Flat Plate," *Proceedings of the Fourth National Congress of Applied Mechanics*, 1962, pp. 1327-1336.
- 8 Sparrow, E. M., Minkowycz, W. J., and Saddy, M., "Forced Convection Condensation in the Presence of Noncondensables and Interfacial Resistance," *International Journal of Heat and Mass Transfer*, Vol. 10, 1967, pp. 1829-1845.
- 9 Minkowycz, W. J., and Sparrow, E. M., "Condensation Heat Transfer in the Presence of Noncondensables, Interfacial Resistance, Superheating, Variable Properties, and Diffusion," *International Journal of Heat and Mass Transfer*, Vol. 9, 1966, pp. 1125-1145.
- 10 Sparrow, E. M., and Gregg, J. L., "A Boundary Layer Treatment of Laminar Film Condensation," *International Journal of Heat and Mass Transfer*, Feb. 1959, pp. 13-18.
- 11 Watson, E. J., "The Asymptotic Theory of Boundary Layer Flow with Suction," Aeronautical Research Council Reports and Memoranda No. 2619, Sept. 1945, Table 4, p. 11.
- 12 Isa, I., "Steady, Two-Dimensional Forced Film Condensation with Pressure Gradient," MS thesis, Department of Mechanical Engineering, University of Iowa, Iowa City, Iowa, Feb. 1969.

## BENJAMIN T. F. CHUNG

Assistant Professor,  
Mechanical Engineering Department,  
University of Akron,  
Akron, Ohio.  
Assoc. Mem. ASME

## L. T. FAN

Professor and Chairman,  
Chemical Engineering Department,  
Kansas State University,  
Manhattan, Kan.

## C. L. HWANG

Associate Professor,  
Industrial Engineering Department,  
Kansas State University,  
Manhattan, Kan.

# A Model of Heat Transfer in Fluidized Beds

*An expression for estimating the heat transfer coefficient in a fluidized bed has been developed based on the surface renewal and penetration concept. The predicted heat transfer coefficients between walls and beds agree well with experimental results. The result of this analysis shows that, in general, the effect of thermal conductivity of particle on heat transfer is insignificant. The maximum possible Nusselt number for the gas fluidized system is determined theoretically as 13.5. This value appears to be reasonable in light of the majority of available experimental data.*

## Introduction

ONE OF the important characteristics of a fluidized bed is the uniformity of temperature throughout the system and the high rate of heat transfer to the heating and cooling surface. The thermal resistance appears to exist only in the vicinity of the heat exchange surface. Measurement of coefficients of the heat transfer between a fluidized bed and the boundary surface has been carried out by many investigators and extensive data are available in the literature. The discrepancy among the results by different workers was illustrated by Wen and Leva [1]<sup>1</sup> as well as by Van Heerden [2]; they have shown that the dense-phase heat transfer correlations by different investigators can be varied by sixtyfold. It appears that the understanding of the mechanism of heat transfer in a fluidized bed is still in a primitive stage.

One of the early theories of heat transfer in fluidized beds was provided by Levenspiel and Walton [3] based on the film concept. Mickley and Fairbanks [4] proposed that the transport process between the bed and the wall is controlled by unsteady conduction of heat from the surface into packets (a group or assembly of particles). Baskakov [5] extended this model by considering the additional surface resistance. Botterill et al. [6] applied the same concept and used the step-by-step variation of the relaxation method to determine the heat transfer between a spherical particle in contact with a plane of heat transfer surface. Ziegler et al. [7] derived a model by considering an unsteady-state heat absorption of the particles from the hot gas near the wall.

<sup>1</sup> Numbers in brackets designate References at end of paper.

Contributed by the Heat Transfer Division for publication (without presentation) in the JOURNAL OF HEAT TRANSFER. Manuscript received by the Heat Transfer Division March 4, 1970. Paper No. 71-HT-Z.

However, their analysis is based on the assumption that the conductivity of the solid,  $k$ , is independent of the heat transfer coefficient in a fluidized bed. Their model is limited to the case where the ratio between the conductivities of gas and solid,  $k_g/k$ , is less than 0.2. The present analysis may be considered as a modification of Ziegler's work, since the same basic mechanism is employed essentially.

Besides Ziegler, several authors [8, 9] concluded from their experimental data that the conductivity of particles has little effect on the heat transfer in a fluidized bed. This proposition so far has not been satisfactorily verified theoretically. On the other hand, Earnest [10] claimed that the thermal conductivity of the solid is more important than that of the gas in fluidized beds.

The purposes of this paper are to develop an expression for the wall heat transfer coefficient in a fluidized bed based on the renewal-penetration concept and to clarify the effects of the thermal conductivity of particles on the heat transfer coefficient between beds and the wall.

The surface renewal and penetration theory was first proposed by Higbie [36] and modified by Danckwerts [37]. The basic notion of this theory may be stated as follows [37, 38]: Consider a transport system as being composed of elements of fluid which are initially completely mixed and at bulk concentration. Due to the turbulence in the bulk stream numerous extremely small fluid elements are constantly brought to the interface. While those elements in one phase under consideration are exposed to the other phase at the interface, each element will absorb matter (or heat) by unsteady-state diffusion. The amount of matter (or heat) which will have been absorbed at any instant depends on the contact time of the fluid element on the interface. After certain lengths of time, each element on the interface is displaced from the surface by a new element or elements in the bulk stream. In

this way, the surface at that particular location is renewed. Equations which describe the rate of mass transfer process based on the renewal-penetration theory are the unsteady-state diffusion (or conduction) coupled with some statistical age distribution function. While this theory appears to be sufficiently flexible for treating a variety of transport processes its applications have been restricted mainly to certain classes of mass transfer processes. Comparatively little work has been done to extend the theory to heat transfer. Furthermore, the majority of the applications have been restricted to the use of the basic form of the theory as derived from Higbie's or Danckwerts' model. In this work, the theory is applied to the heat transfer process in a fluidized bed and a more realistic contact time distribution is employed.

### Proposed Equation for Heat Transfer between Wall and Bed

According to the renewal-penetration theory, it can be considered that the fluidized particles with bulk temperature  $T_b$  are swept to the surface of the heater by the fluid bubbles and absorb heat from the surrounding fluid adjacent to the heating surface of temperature  $T_0$ . After a certain length of time, the particles are swept back to the bulk of the fluidized medium.

The unsteady-state temperature profile of a spherical solid particle during the transient heat conduction which takes place when a fluidized particle is in the surrounding fluid adjacent to the heating surface may be written as

$$\frac{\partial T}{\partial \theta} = \frac{\alpha}{r^2} \frac{\partial}{\partial r} \left( r^2 \frac{\partial T}{\partial r} \right), \quad 0 \leq r \leq R \quad (1)$$

The initial and boundary conditions are

$$T = T_b \quad \text{for} \quad 0 \leq r \leq R, \quad \theta = 0 \quad (2)$$

$$k \frac{\partial T}{\partial r} = h_s(T_0 - T) \quad \text{for} \quad r = R, \quad \theta > 0 \quad (3)$$

$$T = \text{finite} \quad \text{for} \quad r = 0, \quad \theta \geq 0 \quad (4)$$

where  $\theta$  is the contact time of a particle near or at the surface of the heater,  $k$  is the thermal conductivity of particles,  $r$  is the distance from the center of a particle, and  $\alpha$  is the solid thermal diffusivity.

The instantaneous rate of local heat absorption into the surface of a particle depends on its contact time (or age) only, that is,

$$q_i(\theta) = k \left. \frac{\partial T}{\partial r} \right|_{r=R} \quad (5)$$

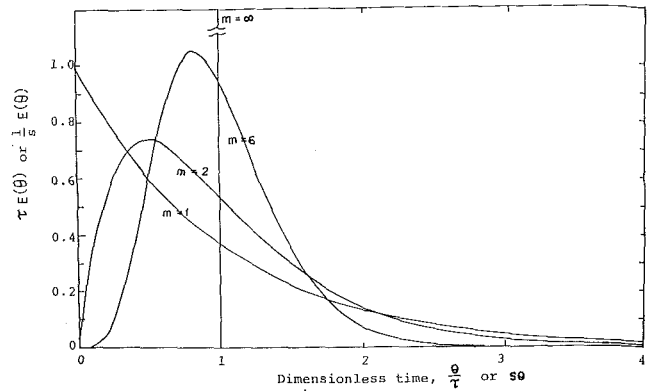


Fig. 1 Multiple capacitance residence time distribution curves for various values of the parameter  $m$

The average rate of local heat absorption per unit transfer area of the particle can be expressed as the summation of individual contributions of particles of all ages as

$$q = \int_0^{\infty} \phi(\theta) q_i(\theta) d\theta \quad (6)$$

where  $\phi(\theta)$  is defined as the contact time (or age) distribution function. The following so-called multiple capacitance contact time distribution proposed by Perlmutter [12] will be introduced here:

$$\begin{aligned} \phi(\theta) &= \frac{1}{\tau} e^{-\frac{m\theta}{\tau}} \sum_{j=0}^{m-1} \frac{1}{j!} \left( \frac{m\theta}{\tau} \right)^j \\ &= s \left\{ e^{-ms\theta} \sum_{j=0}^{m-1} \frac{1}{j!} (ms\theta)^j \right\} \end{aligned} \quad (7)$$

where  $m$  is the number of capacitances (or capacitors),  $\tau$  is the mean residence time of particles on the heating surface, and  $s$  is defined as the mean frequency of surface renewal and, hence, equals  $1/\tau$ . When  $m$  equals unity, equation (7) reduces to random age distribution and, when  $m$  approaches infinity, equation (7) becomes the uniform distribution function. Hence the multiple capacitance distribution functions with different values of  $m$  may be considered as successive degree compromise between Higbie's uniform distribution function and Danckwerts' random distribution function. A realistic contact time distribution should be a monotonic non-increasing function, because, at any instant, the

### Nomenclature

$A_w$  = area of the heating surface  
 $b = \frac{d}{\sqrt{2\alpha\tau}} \coth \frac{d}{\sqrt{2\alpha\tau}} - 1$   
 $c_p$  = specific heat of solid particles  
 $d$  = diameter of fluidized particles  
 $h$  = heat transfer coefficient between walls and beds  
 $h_s$  = inverse of surface resistance  
 $k$  = thermal conductivity of fluidized particles  
 $k_g$  = thermal conductivity of fluidizing gas  
 $L_h$  = length of heater  
 $m$  = number of capacitances or decapacitors in multiple capacitance contact time distribution  
 $N_p$  = number of particles in contact with unit area of heating surface

$Nu$  = Nusselt number =  $hd/k_g$   
 $Nu' = h_s d/k_g$   
 $q$  = average local heat transfer rate per unit transfer area of the particle  
 $q_i$  = instantaneous local heat transfer rate per unit area of particles  
 $Q$  = heat transfer rate from wall to beds  
 $R$  = radius of spherical particle  
 $Re$  = Reynolds number  
 $s$  = fractional rate of surface renewal  
 $T$  = temperature of fluidized particles  
 $\bar{u}$  = average downward velocity of solid past a vertical surface  
 $x = \frac{d}{\sqrt{2\alpha\tau}}$

$\alpha$  = thermal diffusivity of fluidized particle  
 $\gamma = \frac{h_s}{k}$   
 $\epsilon$  = void fraction  
 $\theta$  = contact time or age  
 $\mu$  = viscosity  
 $\rho$  = density of particles  
 $\tau$  = mean residence time  
 $\phi$  = contact time (or age) distribution function

#### Subscripts

$b$  = quantity evaluated at bulk stream  
 $g$  = fluidizing gas  
 $0$  = quantity evaluated at interface  
 $\max$  = maximum or upper bound

amount of particles on the heating surface with ages between  $\theta$  and  $\theta + d\theta$  can never exceed that of ages between  $\theta - d\theta$  and  $\theta$ . It can be seen that equation (7) satisfies the condition of being monotonic non-increasing functions. Equation (7) becomes increasingly complicated as the number of capacitances  $m$  increases. That  $m$  equals to unity in equation (7) implies that the highest probability for contact or residence time of particles on the wall is in the vicinity of zero. It is very unlikely for any particle to have zero residence time because of the interactions among particles. However, due to the high elastic property of solid particles, the value of  $m$  is expected to close to unity. Hence that  $m$  of 2 would probably best represent the contact time distribution of particles in the vicinity of the heating surface. Numerical computations show that the values of  $\phi(\theta)$  do not differ much when  $m$  is greater than 3. Fig. 1 shows a dimensionless plot of the multiple capacitance residence time distribution with different values of parameter  $m$ . Replacing  $m$  by 2 and  $s$  by  $1/\tau$  and solving equations (1)–(7) simultaneously, one obtains [13]

$$q = (T_0 - T_b)h_s \left[ \frac{4b^2 + \gamma R \left( b^2 + 5b - \frac{d^2}{2\alpha\tau} \right)}{4(b + \gamma R)^2} \right] \quad (8)$$

where

$$b = \frac{d}{\sqrt{2\alpha\tau}} \coth \frac{d}{\sqrt{2\alpha\tau}} - 1 \quad (9)$$

If  $N_p$  is the number of particles in contact with a unit area of the heating surface, the rate of heat transfer from the unit area of heater,  $Q/A_w$  is

$$\begin{aligned} \frac{Q}{A_w} &= \pi d^2 N_p q \\ &= \pi d^2 N_p (T_0 - T_b) h_s \left[ \frac{4b^2 + \gamma R \left( b^2 + 5b - \frac{d^2}{2\alpha\tau} \right)}{4(b + \gamma R)^2} \right] \end{aligned} \quad (10)$$

where  $Q$  is the rate of heat transfer from the wall to the bed and  $A_w$  is the area of the heating surface. Adopting Ziegler's [7] assumption that the heater wall is completely coated with particles which come into contact with the wall at any instant in hexagonal packing, one can write

$$N_p = \frac{2\sqrt{3}}{3d^2} \quad (11)$$

In equation (10),  $\gamma$  is defined as

$$\gamma \equiv \frac{h_s}{k} = \frac{h_s d}{k_g} \frac{k_g}{kd} = \text{Nu}' \frac{k_g}{kd} \quad (12)$$

and

$$\text{Nu}' = \frac{h_s d}{k_g} \quad (13)$$

where  $\text{Nu}'$  is the Nusselt number for fluid to particle convection heat transfer.

In the vicinity of the wall, the velocity of fluid around the particle is small. Harriott and Barnstone [15] indicated that the minimum Nusselt number for transfer from solid to gas,  $\text{Nu}'$ , is greater than 2 (a limiting value of  $\text{Nu}'$  in the Frössling [16] expression) if the particle is confined in an enclosure. Kramers [17] obtained the same conclusion from his experiments. According to his correlation, the minimum Nusselt number for heat transfer between solid and gas is given by [17]

$$\text{Nu}' = 3.2 \quad (14)$$

This value will be employed in the present analysis.

Shirai et al. [19] showed experimentally that 88 percent of the heat transfer in fluidized beds is by way of particle transport.

With this fact in mind and combining equations (10), (11), (12), (14), and (1), one obtains the equation for the Nusselt number of heat transfer between wall and beds as

$$\text{Nu} = \frac{hd}{k_g} = \frac{Qd}{A_w(T_0 - T_b)k_g} \quad (15)$$

or

$$\begin{aligned} \text{Nu} &= \frac{2\pi \text{Nu}'}{\sqrt{3} \times 0.88} \left[ \frac{b^2 + \text{Nu}' \frac{k_g}{8k} \left( b^2 + 5b - \frac{d^2}{2\alpha\tau} \right)}{\left( b + \text{Nu}' \frac{k_g}{2k} \right)^2} \right] \\ &= 13.5 \left[ \frac{b^2 + 0.4 \frac{k_g}{k} \left( b^2 + 5b - \frac{d^2}{2\alpha\tau} \right)}{\left( b + 1.6 \frac{k_g}{k} \right)^2} \right] \end{aligned} \quad (16)$$

and

$$h = \frac{13.5 k_g \left[ b^2 + 0.4 \frac{k_g}{k} \left( b^2 + 5b - \frac{d^2}{2\alpha\tau} \right) \right]}{d \left( b + 1.6 \frac{k_g}{k} \right)} \quad (16a)$$

where  $b$  is given by equation (9).

## Effects of Thermal Conductivity of Particles

Most frequently, the value of  $d/\sqrt{2\alpha\tau}$  is less than unity for the usual laboratory fluidized bed, because the average diameter of particles  $d$  is small (usually around  $10^{-3}$  ft or less, see Table 2) and the value of  $\tau$  can not be too small; its lower bound is limited by the velocity of fluid. Note that  $\tau$  decreases as the velocity of the fluid increases; very high velocity would cause "slugging."

When the value of  $d/\sqrt{2\alpha\tau}$  is less than unity, from equation (9)

$$b \doteq \frac{x^2}{3} \quad (17)$$

where

$$x = \frac{d}{\sqrt{2\alpha\tau}} \quad (18)$$

Substituting equation (17) into equation (16), one obtains

$$\text{Nu} = \frac{13.5 \left[ \frac{x^4}{9} + 0.4 \frac{k_g}{k} \left( \frac{2}{3} x^2 + \frac{x^4}{9} \right) \right]}{\left( \frac{x^2}{3} + 1.6 \frac{k_g}{k} \right)} \quad (19)$$

When  $d/\sqrt{2\alpha\tau}$  or  $x$  is less than 1, the second term,  $x^4/9$ , inside the parentheses may be neglected in the above expression in comparison with the lower-order terms. It follows that

$$\text{Nu} \doteq \frac{13.5 \left( \frac{x^4}{9} + \frac{0.8 k_g x^2}{3 k} \right)}{\left( \frac{x^2}{3} + 1.6 \frac{k_g}{k} \right)} \quad (20)$$

Numerical computation has shown that equation (20) holds not only for  $x < 1$  but also approximately for  $x > 1$  when  $x$  is not far from 1.

Introducing equation (18) into equation (20) and cancelling  $k$  in the denominator and the numerator, one obtains

$$\text{Nu} = \frac{13.5 \left( 1 + \frac{4.8\tau k_g}{d^2 \rho c_p} \right)}{\left( 1 + \frac{9.6\tau k_g}{d^2 \rho c_p} \right)} \quad (21)$$

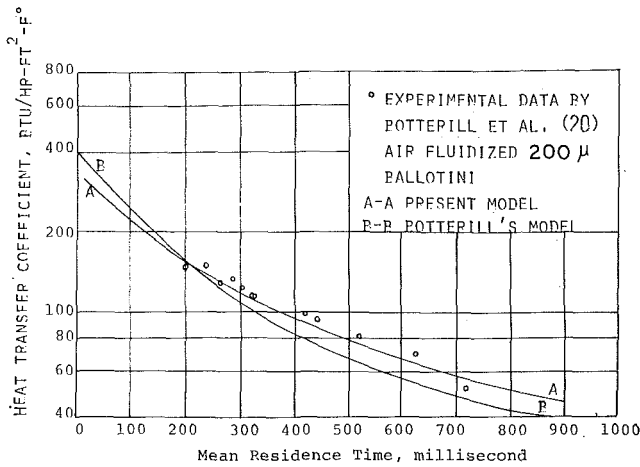


Fig. 2 Comparison of present model with Botterill's model and experimental data

or

$$h = \frac{13.5k_p \left(1 + \frac{4.87k_p}{d^2\rho c_p}\right)}{d \left(1 + \frac{9.67k_g}{\rho c_p d^2}\right)^2} \quad (22)$$

Note that equations (21) and (22) do not involve the conductivity of the solid spheres. These equations show that the heat transfer coefficient in fluidized beds can be independent of the thermal conductivity of particles based on the present model.

If the Fourier modulus,  $\alpha\tau/d^2$ , is very small, which implies that  $x$  or  $b$  is extremely large, the Nusselt number becomes independent of any properties of particles as can be seen from the limiting value of Nu derived from equation (21).

$$\lim_{x \rightarrow \infty} \text{Nu} = \lim_{x \rightarrow \infty} \frac{13.5 \left[ (x \coth x - 1)^2 + 0.4 \frac{k_g}{k} [(x \coth x - 1)^2 + 5(x \coth x - 1) - x^2] \right]}{\left( x \coth x + 1.6 \frac{k_g}{k} \right)^2} = 13.5 \quad (23)$$

The only instance when the thermal conductivity of the solid may have influence on the heat transfer coefficient is when  $d/\sqrt{2\alpha\tau}$  and  $k_g/k$  are both very large. For example, when  $d/\sqrt{2\alpha\tau} = 10$  and  $k_g/k = 1$ , the results obtained from equation (20) deviate from the exact solution of equation (16) by 25 percent.

The mean residence time of particles in the vicinity of the wall, in general, decreases as the velocity of the fluidizing gas increases. This relation has been shown in reference [6]. Mickley and Fairbanks [4] suggested the following approximate expression for estimating the mean residence time

$$\tau = \frac{L_h}{\bar{u}} \quad (24)$$

where  $L_h$  is the length of the heater and  $\bar{u}$  is the average downward velocity of the solid past a vertical surface. Assuming that the initial velocity is zero and the acceleration is due to purely gravitational force, it can be shown from equation (24) that

$$\tau = \frac{L_h}{4} \quad (25)$$

Here the unit of  $\tau$  is sec and of  $L_h$  is ft. Obviously, the above equation is a very approximate estimation; it neglects the resistance of the fluid, frictional force between the wall and the particle, and the delay time due to collision with other particles. Therefore, equation (25) at best can only be considered as a rough estimation of the mean residence time.

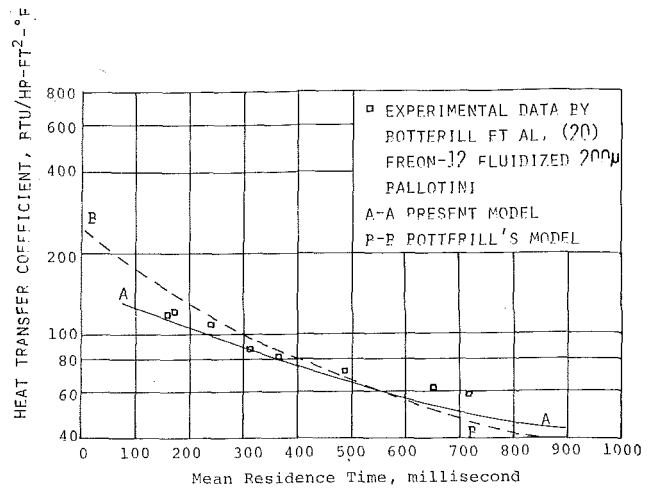


Fig. 3 Comparison of present model with Botterill's model and experimental data

Ziegler et al. [7] measured the heat transfer data in air fluidized beds. Copper, nickel, and solder (50 percent Pb, 50 percent Sn) were chosen as particle material since they have a wide variation in thermal conductivity, twofold variation in specific heat, and almost no variation in density. The heat transfer rate from the wall to beds was found to be independent of the thermal conductivity of particles from their experiments. This can be interpreted mathematically by the present model as follows: Let a wide range of mean residence time, say, ranging from 0.1 to 2.1 sec, be chosen. Numerical calculations show the values of  $d/\sqrt{2\alpha\tau}$  fall between 0.054 and 0.0118 for copper, 0.119 and 0.026 for nickel, and 0.117 and 0.026 for solder. Clearly, the heat transfer coefficients are independent of the thermal conductivity because of

the low values of  $d/\sqrt{2\alpha\tau}$  (less than 1) according to the analysis just presented, equation (21). The length of heater in Ziegler's experiments was 0.208 ft; equation (25) gives an approximate value of  $\tau$  of 0.114 sec.

Reed and Fenske [9] also concluded that the thermal conductivity of particles is not an important factor in determining the heat transfer rate. The same maximum heat transfer coefficient of 150 Btu/ft<sup>2</sup>-hr-deg F was obtained from their experiments by fluidizing nickel powder and copper powder, while the thermal conductivities of these two types of material show sevenfold variations. This result can be explained satisfactorily by the present model with the same argument as in the previous case, i.e., the values of  $d/\sqrt{2\alpha\tau}$  in their experiments are always less than unity.

### Comparison of the Present Model with Experimental Results

Botterill et al. [6, 20] conducted a series of experiments by employing a stirred annular fluidized bed heat exchanger. The contact time of particles with the surface of the heat exchanger was controlled by moving the stirrer through the fluidized bed of particles at various speeds. Figs. 2, 3, and 4 show their experimental data, the predicted heat transfer coefficients by their theoretical model, and those by the present model as characterized by equation (16a). The thermal properties of the gas were evaluated at 200 deg F in the calculations. It can be seen that the present model agrees well with Botterill's experimental data especially for the case of 200- $\mu$  size particles.



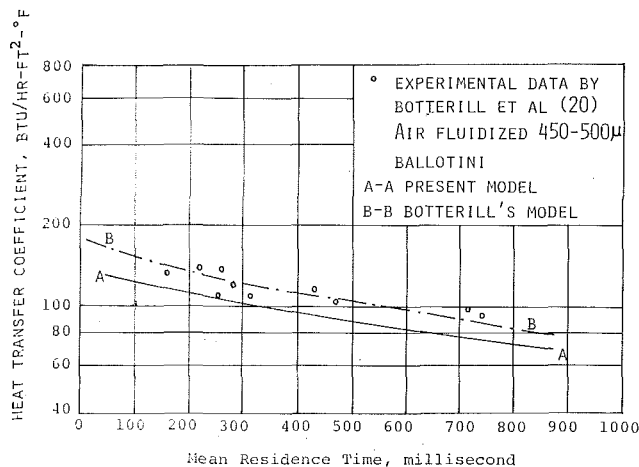


Fig. 4 Comparison of present model with Botterill's model and experimental data

Table 1 Comparison between the experimental result by Dow and Jakob and the results from present model

	Experiments	Present Model
$d$	0.000253, 0.000344, 0.000513	0.000253, 0.000344, 0.000513
$\rho$	121	121
$c_p$	0.223	0.223
$L_h$	0.38 ~ 1.1	
$\tau$		0.2 ~ 0.5
$h$	30 ~ 121	34 ~ 138

Dow and Jakob [8] conducted 191 experiments with three kinds of solid particles to determine the heat transfer coefficients from a vertical tube of a fluidized air-solid mixture. The conditions and results of their experiments for the air-coke system including both small and large heating units are summarized on the left-hand side of Table 1. The calculated results based on the present model with the mean residence time from 0.2 to 0.5 sec are shown in the right column of Table 1. The calculations are based on equation (16a). Since the length of the heater employed in Dow and Jakob's experiments is in the range of 0.38 to 1.1 ft, from equation (25)  $\tau$  is approximately in the range of 0.15 to 0.26 sec. Hence, the mean residence times employed in the present calculation (0.2 and 0.5 sec) are in the right order of magnitude. It may be concluded that the experimental data of Dow and Jakob appear to provide some support to the present model.

### Maximum Nusselt Number of Heat Transfer between Beds and Wall for the Gas Fluidized Systems

The appearance of a maximum and a minimum in the experimental heat transfer coefficients in a fluidized bed is very common. A theoretical maximum value can be estimated from equation (21) by letting  $\tau$  approach zero or can be observed directly from equation (23). This model yields the maximum Nusselt number for any gas fluidized systems as

$$Nu_{\max} = 13.5$$

in contrast to 7.2 predicted by Ziegler et al. [7]. In reviewing the experimental data, it has been found that Jacob and Osberg [14] obtained the highest heat transfer coefficient by using a very small heat exchange surface. The maximum value they were able to observe was 12. As a matter of fact, the observed Nusselt number should be appreciably below the theoretical maximum Nusselt number because it is impossible to achieve the zero mean residence time of particles in a fluidized system. Table 2 shows values of the maximum observed Nusselt number measured by different investigators. Data are obtained from the work by Ziegler et al. [7] and others. It can be seen that the observed values of the Nusselt number are all below the predicted maxi-

Table 2 Maximum values of the observed Nusselt number for heat transfer in fluidized beds

Investigators	Solid Particles	$d \times 10^4$ (ft)	Maximum Nusselt $\left(\frac{hd}{k_g}\right)_{\max}$
Mickley [21]	Scotchlite beads	1.5	3.9
Mickley [21]	Scotchlite beads	1.5	2.3
Levenspiel [22]	coal	38.6	4.5
Leva [23]	iron catalyst	3.6	1.7
Baerg [24]	round sand	28.8	8.1
Vreedenberg [25]	sharp mass sand	11.6	2.6
Dow [8]	spheroidal catalyst	5.6	4.7
Van Heerden [26]	carborundum	7.4	3.0
Van Heerden [2]	sharp silver sand	7.1	3.7
Olin [27]	Ottawa sand	3.9	3.0
Toomey [28]	Scotchlite beads	12.3	5.1
Wicke [29]	river sand	1.0	4.6
Muchlenov [30]	aluminum-nickel catalyst	11.5	5.0
Miller [31]	silicon carbide	8.2	3.6
Brotz [32]	quartz sand	14.7	6.7
Mickley [33]	Scotchlite beads	10.5	5.6
Botterill [34]	lead glass	6.6	3.5
Ziegler [7]	nickel sphere	8.4	6.2
Jacob [14]	glass bead	9.6	12.0
Bartholomew [35]	sand	8.0	1.8
Reed [9]	microsphere	2.0	1.4
Yamazaki [40]	limestone	10.1	4.72
Yamazaki [40]	molding sand	6.9	4.2
Yamazaki [40]	alumina	3.7	2.94
Gel'perin [41]	glass sphere	36.0	7.9
Gel'perin [41]	glass sphere	14.5	5.4
Heertjes [42]	silica gel	36.0	7.9
Agrawal [39]	Scotchlite beads	18.4	5.15

imum Nusselt number based on the present model. It should also be of interest to note that the recent work by Agrawal and Ziegler [39] indicates that the calculated  $Nu_{\max}$  is 4.19 in contrast to the experimental  $Nu_{\max}$  of 5.15 based on Brazelton's data [39].

### Conclusions

An expression for the heat transfer coefficient in a fluidized bed has been proposed. The predicted heat transfer coefficients between walls and beds agree well with the experimental results of Botterill et al. [20]. The thermal conductivity of solid particles has little effect on the transfer rate if the value of  $d/\sqrt{2\alpha\tau}$  is less than unity. The only condition under which the conductivity of particles may have influence on the heat transfer coefficient is when both  $d/\sqrt{2\alpha\tau}$  and  $k/k_g$  are large. The upper bound of the Nusselt number for the gas fluidized system has been derived from equation (16) as 13.5. This value appears to be reasonable in light of the majority of available experimental data.

### References

- 1 Wen, C. Y., and Leva, M., "Fluidized Bed Heat Transfer; A Generalized Dense Phase Correlation," *AIChE Journal*, Vol. 2, 1956, pp. 482-488.
- 2 Van Heerden, C., "Some Fundamental Characteristics of the Fluidized State," *Journal of Applied Chemistry*, Vol. 2, Sup. 1, 1952, pp. 7-17.
- 3 Levenspiel, O., and Walton, J. S., *Proceedings of the Heat Transfer and Fluid Mechanics Institute*, ASME, New York, 1949, pp. 139-146.
- 4 Mickley, H. S., and Fairbanks, D. F., "Mechanism of Heat Transfer to Fluidized Beds," *AIChE Journal*, Vol. 1, 1955, p. 374.
- 5 Baskakov, A. P., "The Mechanism of Heat Transfer between a Fluidized Bed and a Surface," *International Chemical Engineering*, Vol. 4, 1964, pp. 320-323.
- 6 Botterill, J. S. M., Redish, K. A., Ross, D. K., and Williams, J. R., "The Mechanism of Heat Transfer to Fluidized Beds," *Institution of Chemical Engineers Symposium*, London, 1962, pp. 183-189.
- 7 Ziegler, E. N., Koppel, L. B., and Brazelton, W. T., "Effects of Solid Thermal Properties on Heat Transfer to Gas Fluidized Beds," *I & EC, Fundamentals*, Vol. 3, 1964, pp. 304-328.
- 8 Dow, W. M., and Jakob, M., "Heat Transfer between a Vertical Tube and a Fluidized Air-Solid Flow," *Chem. Eng. Prog. Symp. Ser.*, Vol. 47, 1951, pp. 637-648.

- 9 Reed, T. M., and Fenske, R. M., "Effect of Agitation on Gas Fluidization of Solids," *I & EC*, Vol. 47, 1955, pp. 275-282.
- 10 Earnest, R., "Der Mechanismus des Wärmeüberganges an Wärmeaustauscher in Fließbetten," *Chem. Ing. Tech.*, Vol. 31, 1959, pp. 166-173.
- 11 Baddour, R. F., and Young, C. Y., "Local Radial Effective Conductivity and Wall Effect in Packed Beds," *Chem. Eng. Prog. Symp. Ser.*, Vol. 57, 1961, pp. 35-50.
- 12 Perlmutter, D. D., "Surface Renewal Model in Mass Transfer," *Chem. Eng. Sci.*, Vol. 16, 1961, pp. 287-296.
- 13 Chung, B. T. F., "Models of Some Transport Processes Based on the Surface Renewal and Penetration Concept," PhD thesis, Kansas State University, Manhattan, Kan., 1968.
- 14 Jacob, A., and Osberg, L. G., "Effect of Gas Thermal Conductivity on Local Heat Transfer in a Fluidized Bed," *Canadian Journal of Chemical Engineering*, Vol. 35, 1957, pp. 5-9.
- 15 Harriott, P., and Barnstone, L. A., "Heat Transfer in Fluidized Beds," *I & EC*, Vol. 59, 1967, pp. 55-58.
- 16 Frössling, N., *Gerlands Beitr. Geophys.*, Vol. 52, 1938, p. 170.
- 17 Kramers, H., "Heat Transfer from Spheres to Flowing Media," *Physica*, Vol. 12, 1946, p. 61.
- 18 Ziegler, E. N., and Brazelton, W. F., "Effects of Solid Thermal Properties on Heat Transfer to Gas Fluidized Beds," *I & EC, Fundamentals*, Vol. 3, 1964, pp. 324-328.
- 19 Shirai, T., Yashitome, H., Shaji, Y., Tanaka, S., Hojo, K., and Yoshida, S., "Heat and Mass Transfer on the Surface of Solid Spheres Fixed with Fluidized Beds," *Kagaku Kogaku (Chem. Eng., Japan)*, Vol. 29, 1965, pp. 880-884.
- 20 Botterill, J. S. M., Cain, G. L., Brundrett, G. W., and Elliott, D. E., "Heat Transfer to Gas Fluidized Beds," paper presented at the Symposium on Developments in Fluid-Particle Technology, *Transactions of the Institution of Chemical Engineers*, London, 1964.
- 21 Mickley, H. S., and Trilling, C. H., "Heat Transfer Characteristics of Fluidized Beds," *I & EC*, Vol. 41, 1949, pp. 1135-1147.
- 22 Levenspiel, O., and Walton, S. J., "Bed Wall Heat Transfer in Fluidized System," *Chem. Eng. Prog. Ser.*, Vol. 50, 1954, pp. 1-13.
- 23 Leva, M., Weintraub, M., and Grummer, M., "Heat Transmission Through Fluidized Beds of Fine Particles," *Chem. Eng. Prog.*, Vol. 45, 1949, pp. 563-573.
- 24 Baerg, A., Klassen, J., and Gishler, P. E., "Heat Transfer in a Fluidized Solids Bed," *Canadian Journal of Research*, Vol. 28F, 1950, pp. 287-307.
- 25 Vreedenberg, H. A., paper presented at general discussion of heat transfer, Institution of Mechanical Engineers, London, 1951.
- 26 Van Heerden, C., Nobel, A. P., and van Krevelen, D., "Mechanism on Heat Transfer in Fluidized Beds," *I & EC*, Vol. 45, 1953, pp. 1237-1242.
- 27 Olin, H. L., and Dean, O. C., "Heat Transfer and Fouling of Fluidized Beds," *Petroleum Engineering*, Vol. 25, 1955, p. C-23.
- 28 Toomey, R. D., and Johnstone, H. F., "Heat Transfer Between Beds of Fluidized Solids and the Walls of the Container," *Chem. Eng. Prog. Symp. Ser.*, Vol. 49, 1953, pp. 51-63.
- 29 Wicke, E., and Fitting, F., "Wärmeübertragung in Gaswerbelschichten," *Chem. Ing. Tech.*, Vol. 26, 1954, pp. 301-309.
- 30 Muchlenov, I. P., Traber, D. G., and Sarkits, B. U., "Heat Transfer Between Suspended Beds of Granular Materials and Heat Transfer Surfaces," *Zhur. Priklad. Khim.*, Vol. 33, 1960, pp. 2206-2212.
- 31 Miller, C. O., and Logwinuk, A. K., "Fluidization Studies of Solid Particles," *I & EC*, Vol. 43, 1951, pp. 1220-1226.
- 32 Brotz, W., "Untersuchungen über Transportvorgänge in Durchstromten Gekörntem Gut," *Chem. Ing. Tech.*, Vol. 28, 1956, pp. 165-174.
- 33 Mickley, H. S., Fairbanks, F. D., and Hawthorne, D. R., "The Relation between the Transfer Coefficient and Thermal Fluctuations in Fluidized-Bed Heat Transfer," *Chem. Eng. Prog. Symp. Ser.*, Vol. 57, 1961, pp. 51-56.
- 34 Botterill, J. S. M., and William, J. R., "The Mechanism of Heat Transfer to Gas-Fluidized Beds," *Transactions of the Institution of Chemical Engineers*, Vol. 41, 1963, pp. 217-230.
- 35 Bartholomew, R. N., and Katz, D. L., "Heat Transfer from the Wall of a Tube to the Fluidized Bed," *Chem. Eng. Prog. Symp. Ser.*, Vol. 48, 1952, pp. 3-10.
- 36 Higbie, R., "The Rate of Absorption of a Pure Gas into a Still Liquid During Short Period of Exposure," *AIChE Transactions*, Vol. 31, 1935, pp. 365-389.
- 37 Danckwerts, P. V., "Significance of Liquid-Film Coefficients in Gas Absorption," *I & EC*, Vol. 43, 1951, pp. 1460-1467.
- 38 Chung, B. T. F., Fan, L. T., and Hwang, C. L., "General Mathematical Models of Transport Processes With and Without Chemical Reactions," *Canadian Journal of Chemical Engineering*, Vol. 49, 1971, pp. 340-345.
- 39 Agrawal, S., and Ziegler, E. N., "On the Optimum Transfer Coefficient at an Exchange Surface in a Gas-Fluidized Bed," *Chem. Eng. Sci.*, Vol. 24, 1969, pp. 1235-1240.
- 40 Yamazaki, R., and Jimbo, G., "Heat Transfer Between Fluidized Beds and Heated Surfaces," *J. of Chem. Eng. of Japan*, Vol. 3, 1970, pp. 44-48.
- 41 Gel'perin, N. I., Lebedev, P. D., Napalkov, G. N., and Ainshtein, V. G., "Heat and Mass Transfer in a Fluidized Bed and other Disperse System," *Int. Chem. Eng.*, Vol. 6, 1966, pp. 4-15.
- 42 Heertjes, P. M., and McKibbins, S. W., "The Partial Coefficient of Heat Transfer in a Drying Fluidized Bed," *Chem. Eng. Sci.*, Vol. 5, 1956, pp. 161-167.

**W. H. THIELBAHR**

Naval Weapons Center,  
China Lake, Calif.

**W. M. KAYS**

Professor.  
Mem. ASME

**R. J. MOFFAT**

Associate Professor.  
Assoc. Mem. ASME

Department of Mechanical Engineering,  
Stanford University,  
Stanford, Calif.

# The Turbulent Boundary Layer on a Porous Plate: Experimental Heat Transfer with Uniform Blowing and Suction, with Moderately Strong Acceleration

*Experimental data are presented for heat transfer to the turbulent boundary layer subjected to transpiration and acceleration at constant values of the acceleration parameter  $K = (\nu/U_\infty^2)(dU_\infty/dx)$  of approximately  $1.45 \times 10^{-6}$ . This is a moderately strong acceleration, but not so strong as to result in laminarization of the boundary layer. The results for transpiration fractions  $F$  of  $-0.002$ ,  $0.0$ , and  $+0.0058$  are presented in detail in tabular form, and in graphs of Stanton number versus enthalpy thickness Reynolds number. In addition, temperature profiles at several stations are presented. Stanton number results for  $F = -0.004$ ,  $+0.002$ , and  $+0.004$  are also presented, but in graphical form only. The data were obtained using air as both the free-stream and the transpired fluid, at relatively low velocities, and with temperature differences sufficiently low (approximately 40 deg F) that the influence of temperature-dependent fluid properties is minimal. All data were obtained with the surface maintained at a temperature invariant in the direction of flow.*

## Introduction and Objectives

THIS PAPER is one of a series on momentum and heat transfer processes involving the turbulent boundary layer with fluid transpired through a porous plate. All of these papers are based on data obtained as part of a systematic experimental investigation employing the Stanford Heat and Mass Transfer Apparatus.

The first two papers in this series, Moffat and Kays [1]<sup>1</sup> and Simpson, Moffat, and Kays [2], covered the heat transfer and hydrodynamics for constant free-stream velocity, and constant surface temperature, with a range of constant blowing and suction fractions from "blow-off" to asymptotic suction. Whitten, Moffat, and Kays [3] again considered heat transfer using a constant free-stream velocity, but included the influence of both blowing fraction and surface temperature varying in the main flow direction. Simpson, Whitten, and Moffat [4] is a study of turbulent Prandtl numbers extracted from the data of the first two papers.

A second phase of the program has been concerned with the influence of free-stream acceleration on both the momentum and heat transfer characteristics of the transpired turbulent boundary layer. The first paper in this phase, Kays, Moffat, and Thielbahr [5], is specifically concerned with the phenomenon described as "laminarization" in an accelerated transpired turbulent boundary layer, and also with a finite-difference prediction technique that adequately predicts the effects of strong accelerations, and predicts virtually all of the results in the preceding papers. Kays, Moffat, and Thielbahr [5] contains samples of the experimental data obtained during the acceleration phase of the program, but since these data are only used to support a discussion and analysis of the "laminarization" phenomenon, they are not presented in sufficient detail to be useful to other workers. The primary objective of the present paper, as well as that of a companion paper, Julien, Kays, and Moffat [6], is to present and document some selected experimental data, obtained under a moderately strong free-stream acceleration, in sufficient detail and with all of the experimental conditions sufficiently described, so that other workers can make meaningful comparisons with data and theoretical prediction techniques. Julien, Kays, and Moffat [6] is confined to the momentum boundary layer alone, while the present paper is concerned with the development of the thermal boundary layer. No theoretical analysis is presented in either case; the purpose of these papers is to present facts and data that can be used to test the validity of new theories.

<sup>1</sup> Numbers in brackets designate References at end of paper.

Contributed by the Heat Transfer Division for publication (without presentation) in the JOURNAL OF HEAT TRANSFER. Manuscript received by the Heat Transfer Division May 14, 1971. Paper No. 71-HT-BB.

Specifically, the objectives of the present paper are:

1 To present Stanton number data taken under conditions of constant surface temperature, for three transpiration rates ( $F = -0.002, 0.0,$  and  $+0.0058$ ) for one case of moderately strong constant  $K$  acceleration,  $K = 1.47 \times 10^{-6}$ , including the constant velocity recovery region following the acceleration, and the constant velocity region before acceleration.

2 To present a series of temperature profiles taken simultaneously with the Stanton number data, covering the same range of conditions.

## Asymptotic Boundary Layer

The acceleration parameter  $K$  [ $K = (\nu/U_\infty^2)(dU_\infty/dx)$ ] is a convenient measure of the strength of an imposed pressure gradient. This parameter appears explicitly in a particular form of the two-dimensional integral momentum equation,

$$\frac{dRe_M}{dRe_x} = \frac{c_f}{2} - Re_M(1 + H)K + F \quad (1)$$

Examination of equation (1) reveals that if  $K$  is positive and constant, and  $F$  constant, the term  $dRe_M/dRe_x$  can vanish if  $c_f$ ,  $Re_M$ , and  $H$  reach appropriate values. A boundary layer having a constant momentum thickness Reynolds number will be called an "asymptotic" boundary layer. This particular type of boundary layer is characterized by constant  $Re_M$ ,  $K$  (positive), and  $F$ . Furthermore, if the hydrodynamic profiles were completely similar, then  $H$  and  $c_f$  would also be constant. Under these conditions, the important inner region variables  $P^+$  and  $v_w^+$  remain constant.

Exact solutions to the asymptotic laminar boundary layer are available [7]. Townsend [8] considered an exactly self-preserving turbulent boundary layer with constant positive  $K$ , and showed it possessing a constant  $Re_M$ . Launder and Stinchcombe [9] established a turbulent boundary layer at a constant value of  $K$ , and obtained near-constant  $Re_M$ ,  $c_f$ , and  $H$ .

Because so many parameters remain constant, the asymptotic boundary layer provides a particularly convenient configuration for study of accelerated boundary layers. Although the overall experimental program covered a range of values of  $K$ , the present paper is restricted to  $K \approx 1.45 \times 10^{-6}$ . In addition, all runs were restricted to constant blowing fraction ( $F$ ) and constant surface temperature ( $t_s$ ) boundary conditions. The blowing fraction ranges from  $-0.004 \leq F \leq +0.006$ . This range of  $F$  is

of practical interest since the upper limit is near blow-off ( $F \approx +0.010$ ), and asymptotic suction conditions (where  $St = -F$ ) are rapidly approached at  $F = -0.004$ .

## Experimental Apparatus

All data were taken on the Stanford Heat and Mass Transfer Apparatus. This apparatus provides the capability of accurately evaluating heat transfer coefficients along a flat surface in the presence of (1) arbitrary free-stream velocity distribution, (2) arbitrary surface transpiration (blowing or suction), and (3) arbitrary surface temperature distribution. The working fluid is air.

A detailed description of the apparatus can be found in reference [1]. Briefly, the test section is a rectangular flow duct 8 ft long by 20 in. wide by 6 in. high (at the air free-stream entrance). Twenty-four porous bronze plates form the lower surface, two stationary plexiglass walls form the sides, and a flexible plexiglass top provides the means to produce any desired variation in free-stream velocity. All data were taken on the center 6-in. span of each porous segment. The main air system is supplied by a 2000-scfm blower which can produce up to 44-fps free-stream velocity at the duct entrance. The transpiration air system provides individual control of flow through each of the 24 porous plates. The plates are electrically heated so the system can operate with no surface mass transfer. The transpiration system also has the capability for simultaneous blowing and suction through different plates.

Each porous plate is 0.25 in. thick, sintered together from spherical bronze particles (0.002 to 0.007 in. diameter). The surface has an rms roughness of 50–200  $\mu\text{in.}$  (measured with 0.0005-in-radius stylus), and the plate is uniformly porous ( $\pm 6$  percent) over the center 6-in. span. Each plate is heated individually by electrical energy dissipated from 0.012-in-dia wires glued into grooves on the back of the plate. The spacing of the wires was selected to yield negligible temperature variation across the plate surface. Each plate's surface temperature is determined from an average of 5 iron-constantan thermocouples embedded in the plate at a depth of 0.040 in. from the free-stream surface.

Acceleration of the main stream is necessarily accompanied by a gradient in static pressure in the flow direction. This gradient acts to cause the transpiration flow through each segment to be higher than average on the downstream edge and lower than average on the upstream edge. The maximum disturbance in transpiration flow necessarily occurs on the last plate in the

## Nomenclature

$c_f$ = friction coefficient ( $c_f/2 = g_c \tau_w / \rho_\infty U_\infty^2$ )	$Re_M$ = momentum thickness Reynolds number ( $Re_M = \delta_2 U_\infty \rho_\infty / \mu_\infty$ )	$y$ = distance measured normal to flow
$c_p$ = specific heat at constant pressure	$Re_x$ = integrated $x$ Reynolds number	$y^+$ = nondimensional distance from wall ( $y^+ = y U_\infty \sqrt{c_f/2} / \nu$ )
$F$ = blowing fraction [ $F = \dot{m}'' / (U_\infty \rho_\infty)$ ]	$\left[ Re_x = \int_0^x (U_\infty \rho_\infty / \mu_\infty) dx \right]$	$\delta_2$ = momentum thickness of boundary layer
$g_c$ = proportionality factor in Newton's second law	$St$ = Stanton number [see equation (5)]	$\Delta_2$ = enthalpy thickness of boundary layer [see equation (3)]
$H$ = velocity profile shape factor	$t$ = temperature	$\nu$ = kinematic viscosity ( $\nu = \mu/\rho$ )
$i_s$ = stagnation enthalpy	$T$ = absolute temperature	$\mu$ = dynamic viscosity
$K$ = acceleration parameter [ $K = (\nu/U_\infty^2)(dU_\infty/dx)$ ]	$\bar{l}$ = temperature difference ratio [ $\bar{l} = (t - t_\infty)/(t_w - t_\infty)$ ]	$\rho$ = fluid density
$\dot{m}''$ = mass flux through wall (positive if flow is into the boundary layer)	$t^+$ = nondimensional temperature ( $t^+ = \bar{l} \sqrt{c_f/2} / St$ )	$\tau$ = shear stress
$P$ = pressure	$U_\infty$ = free-stream velocity	<b>Subscripts</b>
$P^+$ = nondimensional pressure-gradient parameter [ $P^+ = -K/(c_f/2)^{3/2}$ ]	$u$ = velocity component in $x$ direction	w = refers to evaluation at the wall, or wall state
$\dot{q}''$ = heat flux normal to free-stream flow direction	$u^+$ = nondimensional velocity [ $u^+ = u/(u_\infty \sqrt{c_f/2})$ ]	$\infty$ = refers to evaluation in the free stream
$Re_H$ = enthalpy thickness Reynolds number ( $Re_H = \Delta_2 U_\infty \rho_\infty / \mu_\infty$ )	$v_w^+$ = a blowing parameter ( $v_w^+ = F/\sqrt{c_f/2}$ )	s = refers to stagnation condition
	$x$ = distance measured in direction of flow	$T$ = refers to the state of the transpired fluid before passing through surface plate

accelerating region, where the local value of  $dP/dx$  is largest. The combination of strong acceleration (high  $K$ ) and low blowing fraction produces the largest percent variations in the transpired flow. Under these conditions ( $K = 1.45 \times 10^{-6}$ ,  $F = +0.001$ ) the transpiration flow at the upstream and downstream edges of the worst plate differed by 5 percent.

The streamwise static pressure distribution along the test section was obtained from 48 equally spaced pressure taps located on one of the side walls. Free-stream velocity distribution and the axial distribution of  $K$  were calculated from Bernoulli's equation. It was confirmed experimentally that wall static pressure taps located 1 in. above the porous plates adequately measure the local static pressure in the center of the duct, i.e., there were no significant lateral or vertical gradients in static pressure in the potential core for  $0 \leq K \leq 1.45 \times 10^{-6}$  in the region of the boundary layer.

All stagnation pressures were measured with flattened-mouth pitot probes, approximately 0.015 in. high by 0.040 in. wide. A description of these probes and application of the appropriate corrections can be found in references [2 and 11]. The boundary layer temperature probe consisted of an iron-constantan thermocouple with the junction flattened to a height of 0.009 in. Electrical continuity was used to establish the location of contact between wall and probe. A 1-in.-displacement micrometer, having a least count of 0.001 in., provided the means of measuring vertical displacement.

A uniform hydrodynamic and energy potential flow core existed on all test runs. Tests with a constant temperature hot-wire anemometer established a maximum turbulence intensity of 1.2 percent at an entrance free-stream velocity of 44 fps. For the tests at entrance velocity of 25 fps, the lowest free-stream velocity used, the free-stream turbulence intensity was reduced to 0.8 percent with the addition of a special set of flow screens.

To achieve constant  $K$  flow at  $F = 0$ , the flexible upper wall was bent downward at a constant slope. When uniform blowing is present, a constant slope upper wall still provides a reasonably constant  $K$  flow.

For a fixed inlet velocity, large values of  $K$  are achieved at the expense of testing length. Thirty-two inches of test surface was exposed to the maximum  $K$  achieved in this study ( $1.45 \times 10^{-6}$ ).  $K$  varied from its initial level ( $K = 0$ ) to its maximum in about 1.4 ft, and after acceleration recovered to  $K = 0$  in about 1.0 ft.

When  $Re_M$  at the start of acceleration was approximately equal to the anticipated asymptotic  $Re_M$ , the flow adjusted to its asymptotic condition in a relatively small distance. It was not always possible to achieve this condition; the largest percent deviations from the asymptotic condition were associated with the higher suction runs.

## Wall Heat Flux and Qualification Tests

The surface heat flux  $\dot{q}_w''$  was calculated from an energy balance performed on a control volume covering the center 6 in. of porous plate. Applying the first law of thermodynamics to the control volume yields

$$\dot{q}_w'' = \text{electric power} - \text{losses} - \dot{m}''(i_{s,w} - i_T) \quad (2)$$

Description of the various losses can be found in reference [1].

To qualify the test rig, a series of energy balance tests were performed before and after these tests. These tests are routinely conducted every six months to confirm the validity of the thermal model. The test procedures are documented in reference [1]. The energy balance tests do not utilize mainstream flow; the top cover is removed so as to provide one-dimensional flow of transpired fluid. Under these conditions  $\dot{q}_w'' = 0$  thus enabling the individual energy transfer mechanisms in equation (2) to be properly evaluated for each plate. Upon completion of these tests, it was concluded that no significant change in the characteristics of the apparatus had occurred during the course of these tests.

Based on the method of Kline and McClintock [10], the calculated uncertainty in Stanton number was  $\pm 0.0001$  for all but the high suction runs ( $F = -0.002$  and  $-0.004$ ). At these higher suction fractions, the St uncertainty interval rose to  $\pm 0.0002$ . The uncertainty in enthalpy thickness Reynolds number (calculated from the two-dimensional energy integral equation) averaged approximately 2 percent of the reported value for all but the higher suction runs. Uncertainties in the acceleration parameter  $K$  ranged from 8 to 17 percent of the reported values. For a discussion of the uncertainties in  $c_f$ , see references [6 or 11].

## Roughness and Two-Dimensionality

The rms roughness of the plate surfaces varied between 50 and 200  $\mu\text{in.}$ , measured with a  $\frac{1}{2}$ -mil stylus. Roughness effects on  $c_f/2$  and St can probably be discounted if this roughness is small compared to the thickness of the effective laminar sublayer.

Assuming the sublayer for an impermeable flat-plate flow to extend to  $y^+ = 5$ , this represents a physical thickness of 0.0015 in. when  $Re_M = 500$  and  $U_\infty = 125$  fps, well beyond the 0.0002-in. maximum roughness. All impermeable flat-plate data reported here are for conditions which are conservative compared to these conditions.

The effects of surface roughness have not been established for blown and sucked layers, but Simpson et al. [2] and others have shown that the sublayer thickness decreases with blowing while the data reported here show that acceleration tends to thicken the sublayer. The most critical conditions, therefore, would be those in the recovery region, i.e., with no acceleration, with a high blowing fraction, and with a high free-stream velocity.

Data were taken at  $F = +0.006$  and  $U_\infty = 75$  fps in the recovery region following a strong acceleration. Even under these conditions the value of skin friction was such that the viscous sublayer extended at least to  $y = 0.001$  (assuming a critical  $y^+ = 1.0$ ) which again seems safe.

Velocity profile and heat transfer data were taken at constant free-stream velocities of 42, 86, and 126 fps with no blowing. The resulting values of friction factor and Stanton number, and the  $u^+$ ,  $y^+$  profiles agreed with accepted standards for the 42- and 86-fps data. The friction factor was about 8 percent high for the 126-fps data, and the  $u^+ - y^+$  profiles showed a shift to a lower value of the constant (to a value of 4.0). All of the tabular data reported here are for velocities less than 75 fps and, consequently, are felt to be free of roughness effects.

Two-dimensionality of a boundary layer flow can be established only by elaborate and precise traversing of the boundary layer. This was not done in the present tests, but there is strong secondary evidence that the flow was acceptably two-dimensional. First, the spanwise variation of momentum thickness, across the center 6-in. span, was on the order of 6-8 percent which precludes any major crossflows. Second, and most important, is the evidence available from energy balance considerations applied to the boundary layer.

The local enthalpy thickness,  $\Delta_2$ , was calculated from its definition

$$\Delta_2 = \frac{\int_0^x \rho u (i_s - i_{s,\infty}) dy}{\rho_\infty U_\infty (i_{s,w} - i_{s,\infty})} \quad (3)$$

and from the two-dimensional energy integral equation with constant surface temperature

$$St + F = \frac{d\Delta_2}{dx} + \Delta_2 \left( \frac{1}{U_\infty} \frac{dU_\infty}{dx} + \frac{1}{\rho_\infty} \frac{d\rho_\infty}{dx} \right) \quad (4)$$

The velocity profiles of Julien [11] (also summarized in Julien, Kays, and Moffat [6]) taken under identical free-stream and blowing fraction operating conditions on the same apparatus, and the measured temperature profiles, were used to calculate

$\Delta_2$  from equation (3). Experimental  $St$ ,  $U_\infty$ , and  $F$  were utilized in equation (4) to calculate  $\Delta_2$ .

The uncertainty in  $\Delta_2$  from equation (3) ranged from 3 to 8 percent for  $F \geq -0.001$ . Uncertainty in  $\Delta_2$  from equation (4) ranged from 2 to 6 percent for  $F \geq -0.001$ . It was concluded for  $F \geq -0.001$  that when  $\Delta_2$  from equation (3) was within 8 percent of  $\Delta_2$  calculated from equation (4), the boundary layer development along the test surface was sufficiently two-dimensional. Excluding the first temperature profile, that being in the constant  $U_\infty$  region preceding acceleration, all data for  $F \geq -0.001$  met this two-dimensionality criterion.

The uncertainty in  $\Delta_2$  from equations (3) and (4) became greater than 10 percent for  $F = -0.002$ . This large uncertainty means that this method is unsatisfactory for checking two-dimensionality for those conditions. All zero pressure gradient, flat-plate skin friction, and heat transfer data corresponding to  $F = -0.002$  agreed with the two-dimensional data of references [1, 2].

Conclusions regarding two-dimensionality of the flow are as follows:

1 The pressure gradient and recovery section data describe the characteristics of a nearly two-dimensional turbulent boundary layer.

2 Prior to acceleration, the experimental Stanton numbers obeyed an accepted smooth wall, two-dimensional correlation within  $\pm 5$  percent.

### Determination of Boundary Layer Integral Descriptors

Boundary layer enthalpy thicknesses were calculated from temperature and velocity profile data as well as from integration of the two-dimensional energy integral equation along the plate surface. Neither a radiation nor a turbulent fluctuation correction was applied to the indicated probe temperatures. Errors induced as a result of "wall effects" were assumed negligible. The length of bare thermocouple wire exposed to the flow was selected to reduce the conduction loss from the junction. It was assumed that the indicated probe temperature corresponded to the  $y$  position of the probe's half-height. The uncertainty in  $y$  position was assumed to be  $\pm 0.001$  in. Local velocities were low enough so as to yield no significant difference between local "adiabatic probe" and stagnation temperatures.

In the wall dominated region of the boundary layer,  $t^+$ ,  $y^+$  coordinates are appropriate. The  $t^+$  and  $y^+$  variables were evaluated using free-stream fluid properties. The Stanton number contained in the definition of  $t^+$  was corrected to constant properties, employing the assumption that the heat transfer coefficient varies as the negative 0.4 power of  $(T_w/T_\infty)$ . The skin friction coefficient, obtained from reference [11], corresponds to approximately the same free-stream conditions.

The velocity profile data were taken in separate isothermal tests, see references [6 or 11], and not during the heat transfer tests. An experimental and analytical study was undertaken to find the most accurate method of combining isothermal hydrodynamic profile data with temperature profile data from the heat transfer case so as to calculate local  $\delta_2$  and  $\Delta_2$  [12]. From this study it was concluded that if the free-stream conditions are similar for the isothermal and nonisothermal cases, a good approximation to apply in calculating  $\delta_2$  with heat transfer is  $(u/U_\infty)_H = (u/U_\infty)_I$ , where  $( )_H$  and  $( )_I$  subscript notations designate heat transfer and isothermal situations respectively. This same relationship can also be used in the evaluation of  $\Delta_2$ . These results apply when  $0.95 \leq (T_\infty/T_w) \leq 1.05$ , and were verified by experiments conducted with blowing and favorable pressure gradient. For the range of experimental conditions reported in this paper, the error in  $\delta_2$  and  $\Delta_2$  resulting from this approximation is on the order of 1 percent.

Local Stanton number was calculated from its definition

$$St = \frac{\dot{q}_w''}{\rho_\infty U_\infty (i_{s,w} - i_{s,\infty})} \quad (5)$$

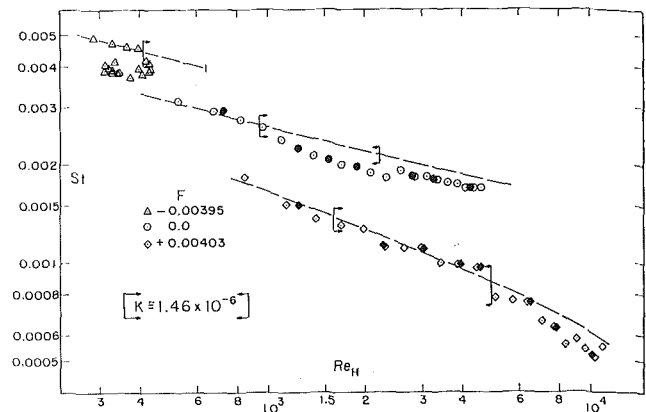


Fig. 1 Local heat transfer results for transpiration and acceleration

As presented in the tables, it has *not* been corrected for the influence of the 35–40 deg F temperature differences existing between the free stream and the wall surfaces.

The reported values of  $Re_H$  were calculated by integration of the two-dimensional energy integral equation (constant  $t_0$ ),

$$\frac{dRe_H}{dRe_x} = St + F \quad (6)$$

starting with an estimate of the enthalpy thickness at the beginning of the heated plate. An exception to this procedure is at the points where temperature and velocity traverses were made, and where equation (3) was used to evaluate  $\Delta_2$ . Thus an idea of the uncertainty in the reported values of  $Re_H$  can be had by comparing the results of two completely independent procedures.

### Experimental Results

The heat transfer data reported here are taken from the larger program reported by Thielbahr [12] covering accelerations at  $K = 0.55, 0.75$ , and  $1.45 \times 10^{-6}$ . The tabular and graphical results presented here should suffice to describe the principal effects of acceleration within this range.

The experimental results for one value of the acceleration parameter,  $K \approx 1.45 \times 10^{-6}$ , and three values of the blowing fraction,  $F = -0.002, 0.0$ , and  $+0.0058$ , are presented in tabular form in Tables 1 and 2. The same data are shown graphically in Figs. 1–5, but in addition Stanton number data is presented in Figs. 1 and 2 for  $F = +0.004, +0.002$ , and  $-0.004$ .

In Table 1, Stanton numbers are presented for each of the three runs considered, as a function of axial position along the test plate beginning with plate #3. The Stanton numbers are averages over a 4-in. plate, but are presented as local Stanton numbers at  $x$  distances which are measured from the beginning of the first plate to the centerline of the indicated plate. An exception to this rule is the case of the positions for which  $c_t/2$  is indicated. These are positions at which temperature and velocity profiles have been taken, and the local Stanton number for each of these positions has been estimated by interpolating on a smooth curve through the data at the plate centerlines.

For each of the three tabulated runs, there is an approach section for which  $K = 0$ , and the first of the velocity and temperature profiles are taken in this section. Three (and in one case four) profiles are taken in the acceleration region, and then three (or two) in the recovery region following acceleration. The enthalpy thickness Reynolds numbers,  $Re_H$ , obtained from the temperature and velocity profiles are indicated by (\*); all other values of  $Re_H$  are obtained by integration of equation (6). A comparison of the values of  $Re_H$  obtained by the two methods provides an indication of the uncertainty in Reynolds number.

Note that the momentum thickness Reynolds numbers,  $Re_{\theta}$ , appear to approach a constant value in the accelerated region, as

**Table 1 Stanton number results and integral parameters**

Run No. 080668-1  
 $K = 1.47 \times 10^{-6}$  nominal  
 $F = -0.002 \pm 0.00003$   
 $t_{\infty} = 66.7 \pm 0.5^{\circ}\text{F}$ ,  $t_w = 102.2 \pm 0.8^{\circ}\text{F}$   
 $P = 29.85$  in. Hg at exit

X, in.	$U_{\infty}$ , fps	$K \times 10^6$	$Re_H$	$Re_M$	$c_f/2$	St
10	25.0	-0.03	396			0.00384
13.78	24.9	0.00	543*	656	0.00353	0.00369
14	24.9	-0.02	487			0.00369
18	25.0	0.37	570			0.00355
22	25.9	0.92	648			0.00345
26	27.7	1.38	721			0.00319
29.67	29.9	1.41	811*	600	0.00340	0.00304
30	30.2	1.44	787			0.00303
34	33.2	1.56	848			0.00284
37.69	36.7	1.42	963*	486	0.00330	0.00271
38	36.9	1.40	902			0.00270
42	41.5	1.51	955			0.00260
45.64	46.9	1.53	1056*	392	0.00323	0.00246
46	47.5	1.52	1000			0.00245
49.63	54.9	1.51	1073*	349	0.00310	0.00242
50	55.7	1.48	1050			0.00242
54	66.0	0.80	1080			0.00222
58	67.8	0.00	1110			0.00216
61.77	67.7	0.01	1116*	421	0.00315	0.00252
62	67.7	-0.01	1160			0.00251
66	67.8	0.01	1250			0.00282
69.70	67.8	0.01	1293*	661	0.00330	0.00301
70	67.8	-0.01	1380			0.00302
74	67.8	-0.01	1520			0.00292
78	67.7	0.00	1650			0.00290
82	67.7	0.00	1770			0.00282
85.78	67.7	0.00	1675*	1130	0.00290	0.00282
86	67.7	0.00	1880			0.00282
90	67.7	0.02	2000			0.00281

Run No. 072968-1  
 $K = 1.47 \times 10^{-6}$  nominal  
 $F = 0.0$   
 $t_{\infty} = 66.8 \pm 0.5^{\circ}\text{F}$ ,  $t_w = 109.8 \pm 0.6^{\circ}\text{F}$   
 $P = 29.82$  in. Hg at exit

X, in.	$U_{\infty}$ , fps	$K \times 10^6$	$Re_H$	$Re_M$	$c_f/2$	St
10	24.8	-0.11	525			0.00313
13.78	24.7	0.02	727*	881	0.00230	0.00293
14	24.7	0.04	678			0.00292
18	24.9	0.43	822			0.00276
22	26.0	1.14	961			0.00260
26	28.0	1.47	1100			0.00238
29.67	30.3	1.38	1243*	905	0.00245	0.00224
30	30.5	1.47	1240			0.00224
34	33.7	1.51	1380			0.00213
37.69	37.2	1.44	1537*	796	0.00252	0.00206
38	37.5	1.47	1530			0.00206
42	42.2	1.47	1690			0.00200
45.64	47.8	1.45	1898*	747	0.00248	0.00197
46	48.4	1.51	1880			0.00197
50	57.0	1.49	2080			0.00188
54	67.8	0.80	2320			0.00182
58	69.6	-0.01	2580			0.00191
61.77	69.6	0.01	2795*	1234	0.00222	0.00183
62	69.6	-0.01	2850			0.00183
66	69.6	0.02	3110			0.00183
69.70	69.7	0.00	3280*	1793	0.00191	0.00178
70	69.7	0.00	3360			0.00179
74	69.8	0.00	3610			0.00175
78	69.8	0.01	3860			0.00173
82	70.0	0.02	4100			0.00169
85.78	70.1	0.00	4266*	2760	0.00175	0.00169
86	70.1	0.00	4350			0.00169
90	70.1	0.00	4590			0.00169

Run No. 082768-1  
 $K = 1.45 \times 10^{-6}$  nominal  
 $F = +0.0058 \pm 0.00006$   
 $t_{\infty} = 67.6 \pm 0.8^{\circ}\text{F}$ ,  $t_w = 98.8 \pm 1.3^{\circ}\text{F}$   
 $P = 30.87$  in. Hg at exit

X, in.	$U_{\infty}$ , fps	$K \times 10^6$	$Re_H$	$Re_M$	$c_f/2$	St
10	25.0	0.00	1050			0.00122
13.78	25.0	0.06	1481*	1676	0.00082	0.00104
14	25.0	0.11	1420			0.00103
18	25.4	0.47	1780			0.00088
22	26.4	1.02	2140			0.00083
26	28.4	1.34	2530			0.00093
29.67	30.8	1.39	2924*	2019	0.00102	0.00074
30	30.9	1.43	2950			0.00074
34	34.3	1.52	3400			0.00073
37.69	38.2	1.42	3952*	2045	0.00105	0.00071
38	38.2	1.39	3900			0.00071
42	43.1	1.42	4460			0.00067
45.64	49.4	1.45	5152*	2020	0.00107	0.00063
46	49.4	1.44	5090			0.00063
50	58.3	1.42	5820			0.00062
54	69.2	0.73	6670			0.00047
58	71.0	0.00	7590			0.00044
62	71.1	0.00	8520			0.00049
66	71.1	0.00	9450			0.00038
69.70	71.1	0.00	10062*	5538	0.00035	0.00033
70	71.1	-0.01	10400			0.00033
74	71.1	0.00	11300			0.00031
78	71.1	0.00	12200			0.00032
82	71.1	0.00	13100			0.00028
85.78	71.1	0.00	13711*	9187	0.00028	0.00031
86	71.1	-0.01	14000			0.00031
90	71.0	0.00	14900			0.00029

\* Evaluated from temperature and velocity profiles. All others from integral energy equation.

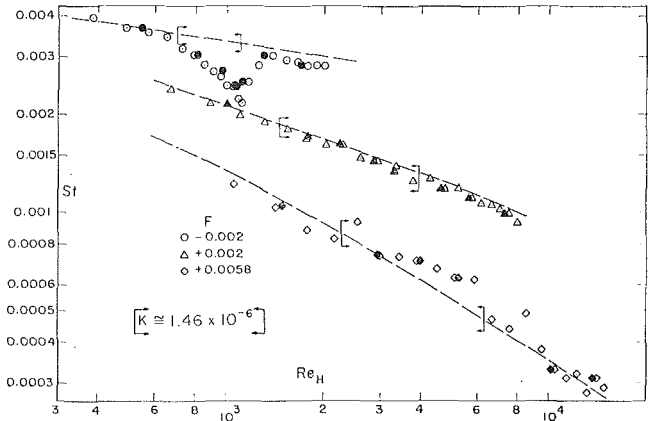


**Fig. 2 Local heat transfer results for transpiration and acceleration**

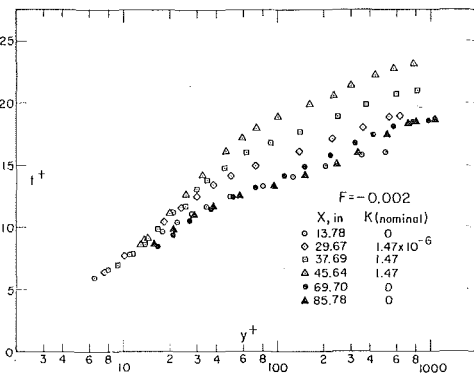


**Fig. 3 Temperature profiles for  $F = -0.002$**

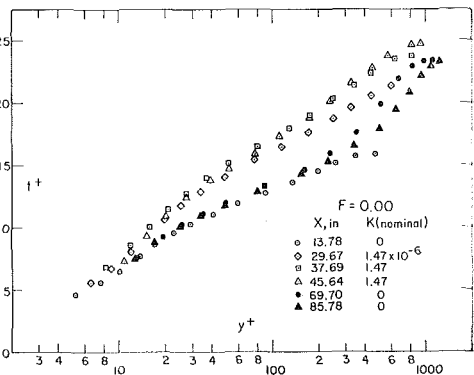


**Fig. 4 Temperature profiles for  $F = 0.0$**

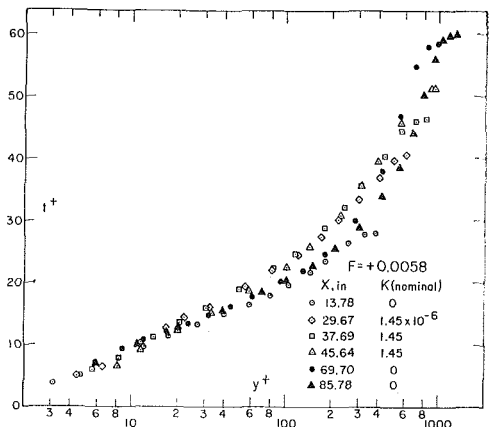


**Fig. 5 Temperature profiles for  $F = +0.0058$**

**Table 2 Temperature profiles**

Run 080668-1

X = 13.78 in.					X = 29.67 in.			X = 37.69 in.		
y, in.	y <sup>+</sup>	t <sup>+</sup>	u/U <sub>∞</sub>	l	y, in.	y <sup>+</sup>	t <sup>+</sup>	y, in.	y <sup>+</sup>	t <sup>+</sup>
0.0085	6.42	5.97	0.346	0.372	0.0085	7.57	6.36	0.0085	9.14	6.90
0.0105	7.93	6.66	0.386	0.415	0.0115	10.2	7.72	0.0105	11.3	7.78
0.0145	11.0	7.81	0.473	0.486	0.0155	13.8	8.98	0.0125	13.4	8.64
0.0185	14.0	8.73	0.539	0.544	0.0205	18.3	10.4	0.0155	16.7	9.84
0.0235	17.8	9.66	0.600	0.602	0.0265	23.6	11.6	0.0195	21.0	11.2
0.0295	22.3	10.4	0.646	0.650	0.0335	29.8	12.5	0.0235	25.3	12.2
0.0365	27.6	11.1	0.672	0.693	0.0425	37.8	13.4	0.0275	29.6	13.1
0.0455	34.4	11.7	0.708	0.726	0.0555	49.4	14.1	0.0325	34.9	13.8
0.0655	49.5	12.4	0.749	0.774	0.0805	71.7	14.9	0.0415	44.6	14.8
0.1055	79.7	13.3	0.792	0.828	0.1555	138.0	16.2	0.0585	62.9	16.0
0.1655	125.0	14.1	0.837	0.878	0.2555	227.0	17.2	0.0835	89.8	16.8
0.2705	204.0	15.0	0.903	0.931	0.4055	361.0	18.1	0.1285	138.0	17.7
0.4705	355.0	15.8	0.987	0.984	0.6055	539.0	18.9	0.2285	246.0	18.9
0.6705	507.0	16.1	1.000	1.000	0.7055	628.0	19.0	0.3535	380.0	19.9
								0.5535	595.0	20.8
								0.7535	810.0	21.0

X = 45.64 in.			X = 69.70 in.			X = 85.78 in.		
y, in.	y <sup>+</sup>	t <sup>+</sup>	y, in.	y <sup>+</sup>	t <sup>+</sup>	y, in.	y <sup>+</sup>	t <sup>+</sup>
0.0085	11.6	8.12	0.0085	16.9	8.50	0.0085	15.8	8.64
0.0105	14.3	9.16	0.0105	20.9	9.39	0.0115	21.3	9.86
0.0145	19.7	11.2	0.0135	26.8	10.5	0.0155	28.7	11.0
0.0185	25.2	12.7	0.0185	36.8	11.5	0.0205	38.0	11.7
0.0235	32.0	14.2	0.0255	50.7	12.4	0.0305	56.6	12.5
0.0335	45.6	16.1	0.0355	70.6	13.2	0.0505	93.6	13.3
0.0435	59.2	17.2	0.0555	110.0	14.2	0.0805	149.0	14.2
0.0535	72.8	18.0	0.0755	150.0	14.9	0.1305	242.0	15.1
0.0735	100.0	18.9	0.1105	220.0	15.8	0.1805	335.0	16.0
0.1185	161.0	19.9	0.1605	319.0	16.8	0.2805	520.0	17.5
0.1685	229.0	20.7	0.2105	418.0	17.5	0.3805	705.0	18.4
0.2185	297.0	21.4	0.2855	568.0	18.2	0.4305	798.0	18.6
0.3185	433.0	22.3	0.3855	766.0	18.5	0.5805	1076.0	18.7
0.4185	569.0	22.8	0.4855	965.0	18.6			
0.5685	773.0	23.2	0.5355	1064.0	18.7			
0.6685	910.0	23.3						

Run 072968-1

X = 13.78 in.					X = 29.67 in.			X = 37.69 in.		
y, in.	y <sup>+</sup>	t <sup>+</sup>	u/U <sub>∞</sub>	l	y, in.	y <sup>+</sup>	t <sup>+</sup>	y, in.	y <sup>+</sup>	t <sup>+</sup>
0.0085	5.13	4.61	0.276	0.288	0.0085	6.48	5.65	0.0085	8.07	6.82
0.0125	7.54	5.63	0.365	0.352	0.0115	8.77	6.79	0.0125	11.9	8.58
0.0165	9.95	6.49	0.433	0.406	0.0155	11.8	8.14	0.0165	15.7	10.1
0.0225	13.6	7.72	0.498	0.482	0.0195	14.9	9.31	0.0215	20.4	11.5
0.0285	17.2	8.70	0.541	0.543	0.0255	19.5	10.7	0.0285	27.1	12.8
0.0375	22.6	9.63	0.593	0.601	0.0325	24.8	11.8	0.0385	36.6	14.1
0.0475	28.7	10.3	0.625	0.640	0.0435	33.2	12.9	0.0535	50.8	15.2
0.0675	40.7	11.1	0.662	0.694	0.0635	48.4	14.1	0.0835	79.3	16.5
0.0975	58.8	11.9	0.704	0.745	0.0985	75.1	15.4	0.1335	127.0	18.0
0.1475	89.0	12.8	0.752	0.799	0.1485	113.0	16.5	0.1835	174.0	19.1
0.2225	134.0	13.7	0.811	0.856	0.2235	171.0	17.7	0.2585	245.0	20.3
0.3225	195.0	14.6	0.876	0.912	0.3235	247.0	18.8	0.3585	340.0	21.4
0.4225	255.0	15.2	0.938	0.951	0.4235	323.0	19.7	0.4585	435.0	22.4
0.5725	345.0	15.8	0.990	0.986	0.5735	438.0	20.7	0.6586	625.0	23.6
0.7725	466.0	16.0	1.000	0.998	0.7735	590.0	21.4	0.8585	815.0	23.8
0.8725	526.0	16.0	1.000	1.000						

X = 45.64 in.			X = 69.70 in.			X = 85.78 in.		
y, in.	y <sup>+</sup>	t <sup>+</sup>	y, in.	y <sup>+</sup>	t <sup>+</sup>	y, in.	y <sup>+</sup>	t <sup>+</sup>
0.0085	10.3	7.39	0.0085	13.2	7.55	0.0085	12.7	7.53
0.0125	15.2	9.26	0.0125	19.4	9.34	0.0115	17.2	8.81
0.0165	20.0	10.9	0.0165	25.6	10.3	0.0165	24.7	10.1
0.0225	27.3	12.4	0.0225	35.0	11.2	0.0225	33.6	11.0
0.0325	39.4	13.8	0.0315	49.0	12.0	0.0325	48.6	11.9
0.0425	51.5	14.7	0.0565	87.8	13.3	0.0525	78.5	12.9
0.0625	75.8	15.9	0.1015	158.0	14.7	0.1025	153.0	14.3
0.0925	112.0	17.3	0.1515	235.0	16.0	0.1525	228.0	15.3
0.1425	173.0	18.8	0.2265	352.0	17.7	0.2275	340.0	16.6
0.1925	233.0	20.1	0.3265	507.0	19.9	0.3275	490.0	18.0
0.2675	324.0	21.6	0.4265	663.0	22.0	0.4275	639.0	19.5
0.3675	445.0	22.9	0.5265	818.0	23.0	0.5275	789.0	20.9
0.4675	567.0	23.8	0.6265	973.0	23.4	0.6275	938.0	22.3
0.6675	809.0	24.7	0.7265	1129.0	23.5	0.7275	1088.0	23.1
0.7675	930.0	24.8				0.8275	1237.0	23.4



Table 2 (cont.)

Run 082768-1

X = 13.78 in.				X = 29.67 in.			X = 37.69 in.			
y, in.	y <sup>+</sup>	t <sup>+</sup>	u/U <sub>∞</sub>	y, in.	y <sup>+</sup>	t <sup>+</sup>	y, in.	y <sup>+</sup>	t <sup>+</sup>	
0.0085	3.21	3.83	0.151	0.137	0.0085	4.41	4.94	0.0085	5.54	5.97
0.0125	4.71	5.10	0.229	0.183	0.0125	6.48	6.69	0.0125	8.15	7.93
0.0215	8.11	7.72	0.278	0.277	0.0225	11.7	10.4	0.0215	14.0	11.2
0.0315	11.9	9.66	0.346	0.347	0.0325	16.9	12.6	0.0315	20.5	13.5
0.0465	17.5	11.4	0.381	0.408	0.0425	22.0	14.3	0.0465	30.3	15.8
0.0715	27.0	13.2	0.437	0.473	0.0625	32.4	16.2	0.0765	49.9	18.9
0.1065	40.2	14.8	0.487	0.530	0.1075	55.7	19.3	0.1265	82.5	22.1
0.1565	59.0	16.4	0.536	0.589	0.1575	81.6	21.8	0.1765	115.0	24.6
0.2065	77.9	17.8	0.586	0.639	0.2325	121.0	24.3	0.2765	180.0	28.7
0.2815	106.0	19.7	0.655	0.707	0.3325	172.0	27.4	0.3765	245.0	32.2
0.3815	144.0	21.6	0.741	0.776	0.4325	224.0	29.9	0.4765	311.0	35.4
0.4815	182.0	23.4	0.813	0.839	0.5825	302.0	33.2	0.6765	441.0	40.2
0.6815	257.0	26.3	0.945	0.943	0.7825	406.0	36.7	0.8765	572.0	44.1
0.8815	332.0	27.7	0.994	0.994	0.9825	509.0	39.5	1.0765	702.0	45.9
1.0315	389.0	27.9	1.000	1.000	1.1825	613.0	40.5	1.2765	832.0	46.3

X = 45.64 in.			X = 69.70 in.			X = 85.78 in.		
y, in.	y <sup>+</sup>	t <sup>+</sup>	y, in.	y <sup>+</sup>	t <sup>+</sup>	y, in.	y <sup>+</sup>	t <sup>+</sup>
0.0095	8.08	6.55	0.0085	5.93	7.34	0.0095	5.92	6.97
0.0135	11.5	9.06	0.0125	8.72	9.30	0.0175	10.9	10.0
0.0235	20.0	12.3	0.0175	12.2	10.7	0.0325	20.3	12.8
0.0385	32.8	15.1	0.0245	17.1	12.2	0.0625	39.0	15.5
0.0685	58.3	18.6	0.0335	23.4	13.5	0.1125	70.2	18.5
0.1185	101.0	22.5	0.0455	31.7	14.8	0.1625	101.0	20.4
0.1685	143.0	25.7	0.0635	44.3	16.2	0.2375	148.0	22.7
0.2685	228.0	30.7	0.0885	61.7	17.7	0.3375	210.0	25.5
0.3685	313.0	35.4	0.1335	93.1	20.1	0.4875	304.0	28.8
0.4685	399.0	39.4	0.1835	128.0	21.9	0.6875	429.0	33.7
0.6685	569.0	45.6	0.2585	180.0	24.7	0.8875	553.0	38.5
0.8685	739.0	49.6	0.4085	285.0	29.9	1.0875	678.0	43.9
1.0685	909.0	51.0	0.6085	424.0	37.8	1.2875	803.0	50.0
1.1185	951.0	51.1	0.8085	564.0	46.6	1.4875	928.0	55.8
			1.0085	703.0	54.7	1.6875	1052.0	58.8
			1.2085	843.0	57.8	1.8875	1177.0	59.7
			1.4085	982.0	58.4	2.0875	1302.0	59.8

is suggested by equation (1). This is particularly noticed in the run for  $F = +0.0058$ , where the anticipated asymptotic Reynolds number is closely approached just before acceleration starts. For the other two runs, the approach Reynolds number considerably exceeds the apparent asymptotic value, with the result that there is a continuous decrease in Reynolds number during acceleration. After acceleration,  $Re_M$  in all cases increases. Note that  $Re_H$  continuously increases in all cases before, during, and after acceleration. This is consistent with equation (6), which unlike the analogous equation (1), does not contain an explicit acceleration term. However, equation (6) does indicate the possibility of a constant  $Re_H$  boundary layer when  $F$  is negative (suction) so that  $St = -F$ . An example of this, which will occur whether there is acceleration or not, will be shown in the figures.

In Table 2, all of the temperature profiles indicated in Table 1 are presented in detail. At each position the normal distance  $y$  is given, along with the nondimensional  $y^+$  and  $t^+$ . Additionally, at the first station for each run,  $x = 13.78$  in.,  $u/U_\infty$  and  $t$  are given so that those desiring to test theoretical models in thermal boundary layer prediction schemes have all of the necessary data to start calculations at  $x = 13.78$  in.

Figs. 1 and 2 show plots of Stanton number as a function of  $Re_H$  for six different values of  $F$ , including the three values of  $F$  given in the tables. The open data points are those for which  $Re_H$  has been evaluated by integration of equation (6); the filled-in data points differ only in that  $Re_H$  is evaluated from the temperature and velocity profiles, and equation (3). The dashed lines are the results of Moffat and Kays [1] for transpiration with constant free-stream velocity.

Most of the heat transfer characteristics of the transpired and accelerated turbulent boundary layer can be seen in the data in these figures. For  $F = 0$ , Fig. 1, acceleration causes a decrease in Stanton number below the expected value for constant  $U_\infty$ . This decrease is caused primarily by an increase in the viscous sublayer thickness, as is discussed in reference [5]. Higher

values of  $K$  cause a more pronounced decrease, and if  $K$  is sufficiently high, the boundary layer will apparently revert to a completely laminar one. However, at  $K = 1.45 \times 10^{-6}$  there is no evidence of "laminarization."

Following acceleration, there is an abrupt increase in Stanton number as the sublayer returns to its zero pressure gradient condition, but now the thermal layer is thicker than the momentum boundary layer (see comparison of  $Re_H$  and  $Re_M$  in Table 1), and the return to the constant  $U_\infty$  value of Stanton number is not complete. The recovery is rather slow, but this is predictable from the integral equation, equations (1) and (6). Recovery will not be complete until  $Re_M$  has closely approached its usual relationship to  $Re_H$ .

The results for blowing,  $F = +0.004$  in Fig. 1, and  $F = +0.002$  and  $+0.0058$  in Fig. 2, do not show a dip in Stanton number with acceleration; in fact for  $F = +0.0058$  there is actually an increase in Stanton number when acceleration is applied. Blowing alone causes a very substantial drop in friction coefficient, and in Stanton number, caused primarily by the influence of transpiration on the shear stress and heat flux distribution in the region near the wall. The effect of blowing can be readily seen if the region near the wall is approximated as a Couette flow, and the resulting equations for shear stress and heat flux are examined.

$$\tau/\tau_w = 1 + v_w^+ u^+ + P^+ y^+ \quad (7)$$

$$\dot{q}''/\dot{q}_w'' = 1 + v_w^+ u^+ \quad (8)$$

In the center of the boundary layer the shear stress and heat flux behavior are relatively independent of what is occurring near the wall. However, equations (7) and (8) show that blowing (positive  $v_w^+$ ) causes both the shear stress and heat flux to be lower at the wall than farther out in the boundary layer. Physically this simply means that at and near the wall the transpired fluid absorbs part of the momentum and thermal energy that would otherwise arrive at the wall as shear stress and heat flux.

Blowing also causes a decrease in the viscous sublayer thickness, but this is much more than offset by the shear stress and heat flux effect. Acceleration causes an opposite effect on shear stress distribution from that caused by blowing (note in equation (7) that acceleration corresponds to negative  $P^+$ ), resulting in an increase in friction coefficient (see Table 1 for  $F = +0.0058$ ). There is no directly analogous effect on heat flux distribution, see equation (8), but heat flux distribution is indirectly affected by the newly established velocity distribution. The result is that Stanton number responds as does the friction coefficient, although not so markedly, and partly regains what it has lost as a result of blowing alone. Acceleration also causes an increase in the viscous sublayer thickness, as is the case for no transpiration, but this effect is evidently more than offset by the shear stress effect when the blowing fraction is large.

Suction alone results in an increase in Stanton number and friction coefficient, due again to the influence of transpiration on the heat flux and shear stress distribution. In this case, however, acceleration has a very strong effect on Stanton number, see Fig. 2 for example, while the effect on  $c_f/2$  is slight, see Table 1. Suction causes a thickening of the viscous sublayer, and acceleration further thickens it, instead of opposing, as is the case for blowing and acceleration. The substantial decrease in Stanton number caused by acceleration of a sucked boundary layer is believed to be primarily the viscous sublayer effect.

It is interesting to note the limitation imposed by the energy integral equation, equation (6), on the suction heat transfer behavior. If the sucked gas is at plate temperature when it reaches the plate surface, the suction limit is reached so that  $St = -F$ . For the case of  $F = -0.002$  in Fig. 2, the suction limit is almost reached in the accelerated region. For the case of  $F = -0.00395$  in Fig. 1, the suction limit is actually attained, and the cluster of data points around  $St = 0.004$  is an indication of a constant value of  $Re_H$  and  $St$  and the random experimental uncertainty. It appears that  $Re_H$  is decreasing in the accelerated region, but since  $Re_H$  is determined by integration of equation (6), the error in  $Re_H$  is cumulative. Temperature profiles were not taken for this run. It is apparent that the suction limit for this run would have been reached without acceleration at about  $Re_H = 640$ . Acceleration, by decreasing Stanton number, merely hastens the attainment of the suction limit.

The temperature profiles, Figs. 3, 4, and 5, substantially corroborate the explanation given above in connection with the Stanton number behavior. The various effects are probably seen most clearly in Fig. 4 for  $F = 0.0$ . In the inner region,  $y^+ < 100$ , the  $t^+$ ,  $y^+$  behavior is virtually identical both before and after acceleration. During acceleration the inner region data is again virtually identical out to  $y^+ = 30$  or 40, but  $t^+$  in this region is very substantially higher than for no acceleration. This, along with the same behavior in  $u^+$ ,  $y^+$  plots, can be discussed in terms of a thicker sublayer during acceleration. It can also be seen on this plot that the behavior in the recovery region following acceleration is almost entirely an outer region effect, the inner region having quickly recovered.

In the strongly blown run, Fig. 5, similar viscous sublayer effects are present, but they make a relatively smaller contribution to overall behavior. Quite the reverse is true for suction, Fig. 3.

## Summary and Conclusions

In this paper experimental data have been presented for heat transfer to turbulent boundary layers subjected to transpiration and moderately strong accelerations, and in which the acceleration parameter  $K$  has been maintained approximately constant at a value of  $1.45 \times 10^{-6}$ . Various constant transpiration fractions from  $-0.004$  to  $+0.0058$  have been considered. All data were obtained with a uniform surface temperature in the flow direction. Sufficient documentation has been provided to establish the

precision of the data, and to allow meaningful comparisons with boundary layer prediction techniques.

It has been shown that acceleration can be interpreted as causing an increase in the viscous sublayer thickness, which has a very substantial influence on heat transfer behavior for suction, a moderate effect for no transpiration, and very little effect for strong blowing. The boundary layers remained turbulent in character for the acceleration considered,  $K = 1.45 \times 10^{-6}$ .

For suction, and for no blowing, acceleration causes a decrease in Stanton number below the value which would obtain at the same enthalpy thickness Reynolds number without acceleration. With blowing, however, this decrease is not noted, and in fact acceleration of a highly blown boundary layer will actually cause an increase in Stanton number. A qualitative explanation for this behavior is presented.

In the region following an acceleration, the inner region (i.e., the viscous sublayer) recovers rapidly to its equilibrium conditions for no pressure gradient, but the outer region recovers rather slowly, apparently because during acceleration the thermal boundary layer has grown substantially relative to the momentum boundary layer.

## Acknowledgments

This work was made possible by support of the National Aeronautics and Space Administration, NASA Grant NGL 05-020-134, and the National Science Foundation, NSF GK-2201. The continued interest of Dr. Royal E. Rostenbach of NSF and Dr. Robert W. Graham of NASA Lewis Laboratories is greatly appreciated.

## References

- Moffat, R. J., and Kays, W. M., "The Turbulent Boundary Layer on a Porous Plate: Experimental Heat Transfer With Uniform Blowing and Suction," *International Journal of Heat and Mass Transfer*, Vol. 11, No. 10, 1968, pp. 1547-1566.
- Simpson, R. L., Moffat, R. J., and Kays, W. M., "The Turbulent Boundary Layer on a Porous Plate: Experimental Skin Friction With Variable Injection and Suction," *International Journal of Heat and Mass Transfer*, Vol. 12, No. 7, 1969, pp. 771-789.
- Whitten, D. G., Moffat, R. J., and Kays, W. M., "Heat Transfer to a Turbulent Boundary Layer With Non-Uniform Blowing and Surface Temperature," ASME Paper No. 69-IC-168. Presented at Fourth International Heat Transfer Conference, Paris, France, Aug. 31-Sept. 5, 1970.
- Simpson, R. L., Whitten, D. G., and Moffat, R. J., "An Experimental Study of the Turbulent Prandtl Number of Air With Injection and Suction," *International Journal of Heat and Mass Transfer*, Vol. 13, No. 1, 1970, pp. 125-143.
- Kays, W. M., Moffat, R. J., and Thielbahr, W. H., "Heat Transfer to the Highly Accelerated Turbulent Boundary Layer With and Without Mass Addition," *JOURNAL OF HEAT TRANSFER*, TRANS. ASME, Series C, Vol. 92, No. 3, Aug. 1970, pp. 499-505.
- Julien, H. L., Kays, W. M., and Moffat, R. J., "Experimental Hydrodynamics of the Accelerated Turbulent Boundary Layer With and Without Mass Injection," Department of Mechanical Engineering, Stanford University, Stanford, Calif., 1970.
- Schlichting, H., *Boundary Layer Theory*, McGraw-Hill, New York, N. Y., 1960.
- Townsend, A. A., *The Structure of Turbulent Shear Flow*, Cambridge University Press, Cambridge, England, 1956.
- Launder, B. E., and Stinecombe, H. S., "Non-Normal Similar Turbulent Boundary Layers," Report TWF/TN/21, Mechanical Engineering Department, Imperial College of Science and Technology, London, England, 1967.
- Kline, S. J., and McClintock, F. A., "Describing Uncertainties in Single-Sample Experiments," *Mechanical Engineering*, Vol. 75, No. 1, Jan. 1953, pp. 3-8.
- Julien, H. L., "The Turbulent Boundary Layer on a Porous Plate: Experimental Study of the Effects of a Favorable Pressure Gradient," PhD thesis, Department of Mechanical Engineering, Stanford University, Stanford, Calif., 1969; available from University Microfilms, Ann Arbor, Mich.
- Thielbahr, W. H., "The Turbulent Boundary Layer: Experimental Heat Transfer With Blowing, Suction, and Favorable Pressure Gradient," PhD thesis, Department of Mechanical Engineering, Stanford University, Stanford, Calif., 1969; available from University Microfilms, Ann Arbor, Mich.

**L. H. BACK**  
Member Technical Staff,  
Mem. ASME

**P. F. MASSIER**  
Group Supervisor.

**E. J. ROSCHKE**  
Member Technical Staff.

Jet Propulsion Laboratory,  
California Institute of Technology,  
Pasadena, Calif.

# Partially Ionized Gas Flow and Heat Transfer in the Separation, Reattachment, and Redevelopment Regions Downstream of an Abrupt Circular Channel Expansion<sup>1</sup>

Heat transfer and pressure measurements obtained in the separation, reattachment, and redevelopment regions along a tube and nozzle located downstream of an abrupt channel expansion are presented for a very high enthalpy flow of argon. The ionization energy fraction extended up to 0.6 at the tube inlet just downstream of the arc heater. Reattachment resulted from the growth of an instability in the vortex sheet-like shear layer between the central jet that discharged into the tube and the reverse flow along the wall at the lower Reynolds numbers, as indicated by water flow visualization studies which were found to dynamically model the high-temperature gas flow. A reasonably good prediction of the heat transfer in the reattachment region where the highest heat transfer occurred and in the redevelopment region downstream can be made by using existing laminar boundary layer theory for a partially ionized gas. In the experiments as much as 90 percent of the inlet energy was lost by heat transfer to the tube and the nozzle wall.

## I Introduction

HEAT TRANSFER measurements in internal subsonic flows where changes in cross-sectional area cause separation have usually been made at moderate temperatures and pressures and at Reynolds numbers that are high enough so that the flow is turbulent. Examples of experimental results for essentially constant-property turbulent flows appear in [1-9],<sup>2</sup> and for variable-property turbulent flows in [10]. High-temperature gas flows, however, such as those heated by means of an arc heater, are often laminar because of the correspondingly lower Reynolds numbers. Separation and reattachment of such flows have not been investigated to any great extent. The results of the present investigation are a contribution to the understanding of high-temperature flows of this type.

<sup>1</sup> This paper presents the results of one phase of research carried out in the Propulsion Research and Advanced Concepts Section at the Jet Propulsion Laboratory, California Institute of Technology, under Contract No. NAS7-100, sponsored by the National Aeronautics and Space Administration.

<sup>2</sup> Numbers in brackets designate References at end of paper.

Contributed by the Heat Transfer Division for publication (without presentation) in the JOURNAL OF HEAT TRANSFER. Manuscript received by the Heat Transfer Division February 24, 1971. Paper No. 71-HT-DD.

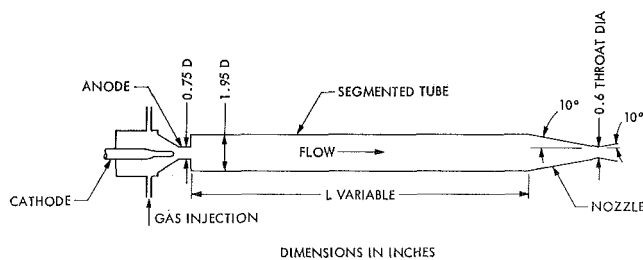


Fig. 1 Test apparatus

Local heat transfer and wall pressure measurements were obtained along a tube and a convergent-divergent nozzle located downstream of an arc heater (Fig. 1). The fluid consisted of argon which was heated by means of an electrical discharge. An abrupt increase in diameter from 0.75 in. to 1.95 in. existed between the arc heater and the tube to confine the arc attachment. The step increase in flow cross-sectional area caused the flow to separate in the entrance region of the tube. The flow reattached along the tube and subsequent redevelopment occurred downstream. Two lengths of tube were used, the longer one was 9.7 diameters long and the shorter one was 3.1 diameters long. The nozzle, which was operated in the choked condition, had a comparatively large contraction area ratio which provided

low-speed flow through the tube, the Mach number being 0.11 in the tube inlet region. Data were obtained with both radial and tangential injection of the flow upstream of the arc heater. The swirling flow was introduced to help stabilize the arc discharge.

At the tube inlet average enthalpies ranged from 2400 to 7900 Btu/lb, average temperatures from 16,600 to 21,600 deg R (9,200 to 12,000 deg K), and static pressures from 1.5 to 4.3 psia. Because of the relatively high temperatures there was a significant amount of ionization at the tube inlet, the ionization energy fraction extended up to about 0.6. The Reynolds number based on the tube diameter and the viscosity at the tube inlet ranged from 210 to 450.

There have been other heat transfer measurements made in plasma flows through channels [11-13] but only the measurements by Johnson, Choksi, and Eubank [12] are directly related to the measurements herein since they were also obtained downstream of an abrupt increase in channel cross-sectional area. The measurements by Johnson et al. were obtained with helium, argon, and nitrogen at temperatures up to 12,600 deg R; however, there were only five coolant passages along the tube that was 6 diameters long so that the separated and reattachment regions could not be resolved from the heat transfer measurements.

In the present investigation it was possible to obtain information on the flow phenomena that are believed to occur in the hot-gas experiments by visual observations in a lucite half-scale model through which water flowed and dye was injected to reveal flow patterns. In the Reynolds number range of the hot-gas experiments, the location of reattachment in the model studies was found to depend strongly on the growth of an instability in the vortex sheet-like shear layer between the central jet that discharged into the tube and the outer slower-moving reverse flow along the tube wall. This observation has an important bearing on the determination of heat transfer in separated flow regions since it is in the reattachment region where the heat transfer is a maximum. This in turn establishes the kind of heat transfer distribution along the rest of the tube, i.e., downstream of reattachment in the redevelopment region and upstream in the separated flow region.

## II Test Apparatus and Instrumentation

A diagram of the test apparatus is shown in Fig. 1. Argon at approximately ambient temperature was introduced either radially or tangentially through four 0.25-in-dia holes into an upstream chamber. The gas flowed through the arc heater, acquiring energy from the arc discharge, and then into the larger-diameter tube. The step height at the tube inlet is 0.6 in., and the ratio of diameters between the tube and the anode is 2.6. The tube consisted of segments so that its length could be

changed. From the tube the gas flowed through a supersonic nozzle and discharged into a vacuum system where it was cooled to approximately 200 deg F by flowing through a coiled-tube heat exchanger. Only the test section of interest in this investigation is shown in Fig. 1. The test section was fabricated from stainless steel.

The entire test section through which the hot gas flowed, i.e., the arc heater, the tube, and the nozzle, was cooled externally. The circumferential coolant passages ranged in axial width from about 0.3 in. to 1.0 in., there being 26 passages in the larger tube. Each coolant passage was instrumented with a rotameter and three pairs of series-connected thermocouple junctions formed by resistance-welding the ends of chromel and constantan wires. The longitudinal distribution of heat flux was then determined from the coolant water flow rates, water temperature rises, and surface areas of the coolant passages. The gas side wall temperatures which are virtually negligible compared to the very high gas temperatures were calculated by using the average coolant water temperature, a calculated water side heat transfer coefficient, and the measured heat flux in conjunction with the heat conduction equation for the wall. The longitudinal distribution of the average enthalpy of the gas was determined by an energy balance between the applied electrical power and the total heat transferred to the cooled sections up to each measuring station. The total gas flow rate needed to perform these calculations was obtained from readings of a rotameter located in the gas feedline. Applied electrical power was computed from voltage and current measurements. The ratio of the total heat transferred to the individual coolant passages along the entire test section to applied power was near 1.0 for all tests, thus establishing confidence in the measurements.

There were 35 wall pressure taps spaced along the longer cooled tube. These taps were connected to manometers that contained silicone oil (specific gravity 0.93). These readings were accurate to pressure differences of approximately 0.001 psi.

The half-scale lucite model of the upstream chamber, simulated arc heater, tube, and nozzle used in the water flow studies were instrumented with small holes through which light-absorbent dye (specific gravity near 1) could be metered. Water flow rates were measured with a calibrated rotameter and water temperature was measured by insertion of a thermometer in the water discharge.

## III Flow and Transport Property Evaluation

Conditions at which the hot-gas experiments were conducted are tabulated in Table 1. From the measured mass flow rate and wall static pressure, and the average total enthalpy in the flow obtained from an energy balance, it was possible to calculate

## Nomenclature

$A$ = channel cross-sectional area	$q$ = wall heat flux: $q_c$ , convective; $q_r$ , radiative; $q_A$ , atomic	<b>Subscripts</b>
$C_p$ = pressure coefficient	$Q$ = nondimensional heat flux or Nusselt number	$a$ = condition upstream of step at arc heater
$\bar{c}_p$ = specific heat, $\frac{5}{2}R(1 + \alpha)$	$r$ = channel radius	$A$ = atomic or non-ionized gas value
$D$ = channel diameter	$R$ = gas constant	$b$ = base flow condition
$D_{am}$ = ambipolar diffusion coefficient	$Re_D$ = Reynolds number, $\dot{m}D/A\mu$	$e$ = condition at free stream of boundary layer
$F$ = function defined in equation (1)	$s$ = step height	$i$ = tube inlet condition
$G_w'$ = heat transfer parameter, values given in [48]	$T$ = temperature	$0$ = reservoir condition
$H$ = static enthalpy	$u$ = axial velocity	$R$ = reattachment
$H_t$ = total enthalpy	$v$ = swirl velocity	$t$ = stagnation condition
$I$ = first ionization potential	$V$ = velocity in the separation region	$w$ = wall condition
$k$ = thermal conductivity (translational value)	$x$ = length along surface	
$L$ = tube length	$z$ = axial distance	
$Le$ = Lewis number, $\rho D_{am}\bar{c}_p/k$	$\alpha$ = ionization fraction	
$\dot{m}$ = mass flow rate	$\mu$ = viscosity	<b>Superscript</b>
$p$ = pressure	$\nu$ = kinematic viscosity	$j = 0, 1$ for plane and axisymmetric flow
$Pr$ = Prandtl number, $\mu\bar{c}_p/k$	$\rho$ = density	

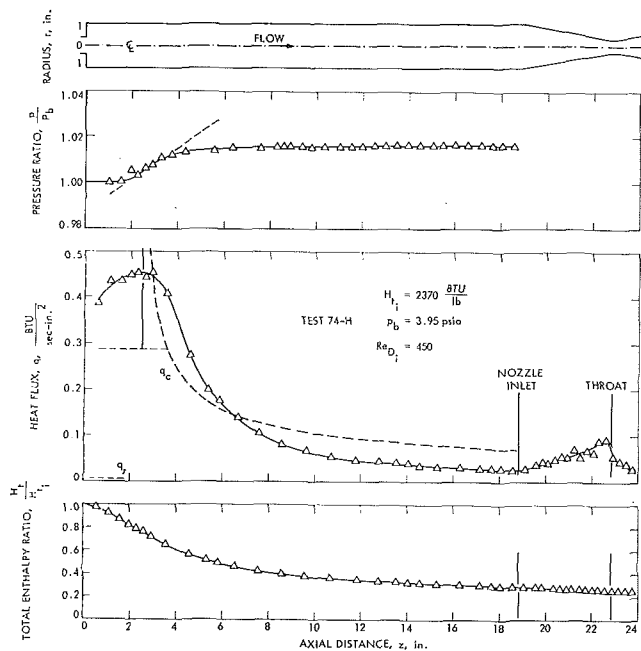


Fig. 2 Measurements along the tube and nozzle with radial injection; test 74-H, long tube  $L/D = 9.7$

other average quantities across the flow from the following relations for partially ionized argon in equilibrium.

$$\text{mass flow rate: } \dot{m} = \rho u A$$

$$\text{equation of state: } p = (1 + \alpha)\rho RT$$

$$\text{total enthalpy: } H_t = H + \frac{u^2}{2}$$

$$\text{enthalpy: } H = \frac{5}{2}R(1 + \alpha)T + \alpha I$$

$$\text{Saha equation:}$$

$$\frac{\alpha^2}{1 - \alpha^2} = \frac{2.23 \times 10^{-8} (4 + 2\epsilon \frac{3710}{T}) T^{5/2} \epsilon \frac{329,000}{T}}{p}$$

where  $p$  is in psia and  $T$  in deg R. See [14, Appendix A] for the form of the enthalpy relation and the Saha equation: For argon the first ionization potential  $I$  is 16,400 Btu/lb. The quantities  $T$ ,  $\alpha$ ,  $H$ ,  $u$ , and  $p$  were calculated from the preceding five relations.

A more detailed description of internal flow quantities and their variations across the tube in the separated flow region downstream of the step (inlet of the tube) where conditions are denoted by  $i$  was not possible because of the nature of the flow investigated. Important in this regard is that arc heating probably also occurred in the inlet section of the tube because of the interaction of the flow with the arc discharge, and also that the gas may not have been in equilibrium just downstream of the arc discharge. These effects, however, are expected to be confined to a relatively short region downstream of the inlet. For the moderately high pressures at which measurements were made, electron number densities were on the order of  $10^{16} \text{ cm}^{-3}$  in the inlet flow.

Transport properties, needed to calculate the Reynolds number and the Prandtl and Lewis numbers related to subsequent heat transfer predictions, were evaluated from the equilibrium calculations of de Voto [15, 16]. These transport property calculations, obtained from Chapman-Enskog theory, do follow the trends indicated by measurements that have been made for argon [17-24] at temperatures (up to 25,000 deg R) where ionization is significant, and also agree fairly well in magnitude with the measurements. In partially ionized gases the thermal conductivity (translational value) exceeds the atomic value  $k_A$  because of the contribution of the electrons; also, the viscosity is less than the atomic value  $\mu_A$  apparently because of the larger ion-atom collision cross sections than for atom-atom collisions, e.g., see [14, Appendix C]. Table 1 contains the predicted values of  $k$  and  $\mu$  relative to the atomic (non-ionized) values along with the Prandtl number which is correspondingly less than the atomic value of  $2/3$ . The atomic values of  $k_A$  and  $\mu_A$  were obtained from the calculations of Amdur and Mason [25] which are approximated closely by a  $3/4$ -power dependence on temperature. For the thermal conductivity  $k_A$ , the  $3/4$ -power dependence was supported earlier by end wall heat transfer measurements in a shock tube for atomic argon up to extremely high temperatures of 135,000 deg R before the ionization relaxation time [26] and by more recent measurements [27-29]. Other measurements [30-33], however, have indicated a weaker power dependence of 0.65 to 0.70. Ultrasonic absorption measurements [34] up to temperatures of 15,000 deg R were found to be in agreement with Amdur and Mason's values for the atomic viscosity  $\mu_A$ .

## IV Hot Gas Results

The experimental results obtained with radial and tangential injection of the gas upstream of the arc heater (Table 1) are described in this section and estimates of the heat transfer that were made and are shown in the figures are discussed later in Section V.

Longitudinal distributions of pressure, heat flux, and total enthalpy are shown in Figs. 2-5 for radial injection upstream. The figure sequence corresponds to increasing values of the inlet total enthalpy and therefore, usually, decreasing values of the Reynolds number. In general, the heat flux to the wall rises in the inlet region of the tube, reaches a maximum, and then decreases farther downstream in a similar manner to that observed in low-temperature investigations of abrupt channel expansions. The maximum heat flux occurs in the compression region where the shear layer between the central jet that discharges into the tube and the reverse flow along the wall impinges on the wall. Downstream of reattachment the heat flux decreases because of subsequent flow development, a situation that is also found upstream as the reverse flow develops along the wall.

A distinctive feature of the results shown in Figs. 2-5 is the reattachment location. At the highest Reynolds number (Fig. 2) reattachment occurs a short distance downstream of the tube inlet (about 4 step heights, i.e.,  $z_R/s$ ). As the Reynolds number decreases (Figs. 3-5) reattachment occurs farther downstream as seen more clearly in Fig. 6, but in a way opposite to that expected if the shear layer between the central jet and reverse flow along

Table 1 Experimental conditions

Injection	$\frac{L}{D}$	Test	$H_{ti}$ Btu/lb	$P_{ti}$ psia	$\dot{m}$ lb/sec	$T_{ti}$ deg R	$\alpha_i$	$\frac{\alpha_i I}{H_{ti}}$	$Re_{Di}$	$Pr_i$	$\frac{k_i}{k_A}$	$\frac{\mu_i}{\mu_A}$	$\frac{q}{q_A}$	$\frac{z_R}{s}$
Radial	9.7	74-H	2370	4.02	0.0103	16,600	0.016	0.11	450	0.32	1.9	0.89	1.10	4.2
		75-H	4280	2.11	0.00480	19,100	0.10	0.39	250	0.22	2.3	0.69	0.89	8.3
		72-H	5220	1.60	0.00344	19,600	0.15	0.46	210	0.18	2.4	0.56	0.80	12.5
		73-H	5610	1.83	0.00389	20,000	0.17	0.48	260	0.17	2.5	0.55	0.81	10.8
Tangential	9.7	69-H	2610	4.27	0.00952	17,300	0.025	0.16	420	0.30	2.0	0.88	1.09	5.0
		70-H	5140	2.52	0.00542	20,000	0.14	0.45	330	0.18	2.5	0.60	0.85	8.3
		71-H	7910	1.46	0.00307	20,900	0.28	0.58	290	0.13	2.6	0.39	0.67	15.8
Tangential	3.1	78-H	3230	3.62	0.00725	18,400	0.051	0.26	350	0.24	2.3	0.78	1.03	4.6
		81-H	5620	2.96	0.00488	20,500	0.16	0.47	340	0.14	2.7	0.50	0.81	6.3
		84-H	7820	2.69	0.00430	21,600	0.27	0.56	390	0.11	2.8	0.37	0.69	7.9

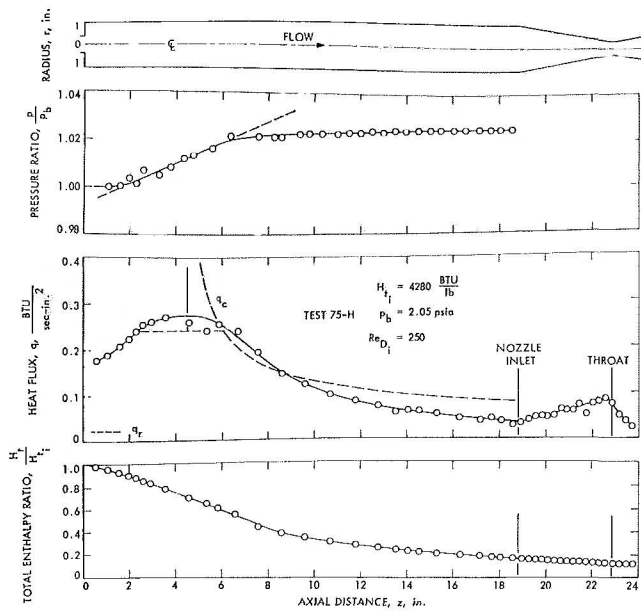


Fig. 3 Measurements along the tube and nozzle with radial injection; test 75-H, long tube  $L/D = 9.7$

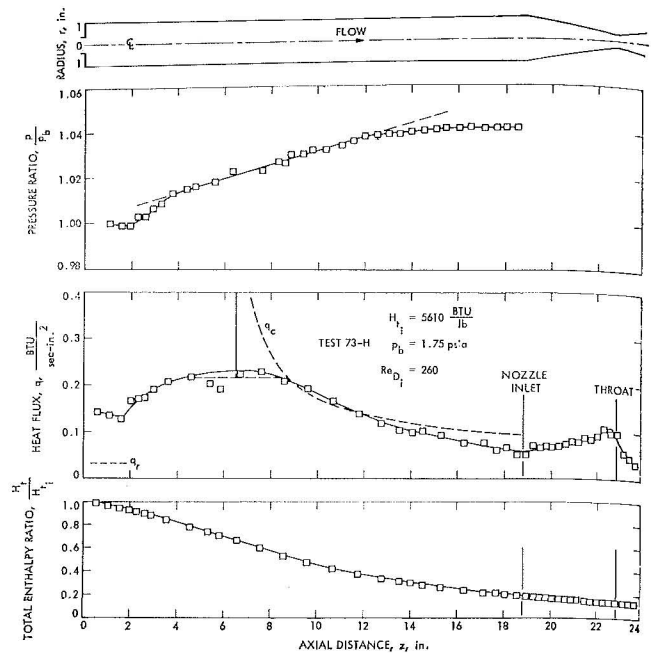


Fig. 5 Measurements along the tube and nozzle with radial injection; test 73-H, long tube  $L/D = 9.7$

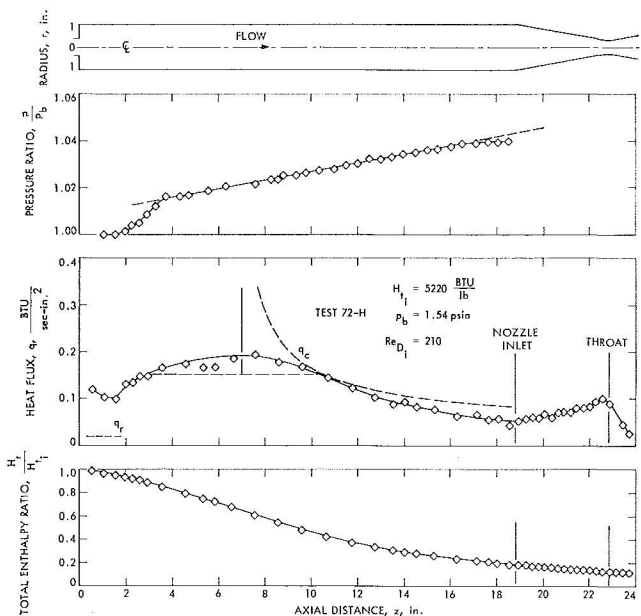


Fig. 4 Measurements along the tube and nozzle with radial injection; test 72-H, long tube  $L/D = 9.7$

the wall grew by diffusion of momentum. For example, for constant-property laminar mixing of a stream which has a uniform velocity  $u_a$ , with a fluid at rest, the velocity profiles depend upon a similarity variable and thus the half-width of the shear layer  $b$  is given by

$$\frac{b}{z} \sqrt{\frac{u_a z}{\nu}} = c$$

where  $c = \text{const}$ . This relation can be used to estimate the dependence of reattachment location on Reynolds number by taking  $b$  equal to the step height  $s$  at the reattachment point  $z = z_R$  to give

$$\frac{z_R}{s} = \frac{1}{c^2} \left( \frac{u_a s}{\nu} \right) = \frac{1}{c^2} \left( \frac{s}{D} \right) \left( \frac{u_a D}{\nu} \right)$$

Whereas simple mixing theory indicates a linear variation of re-

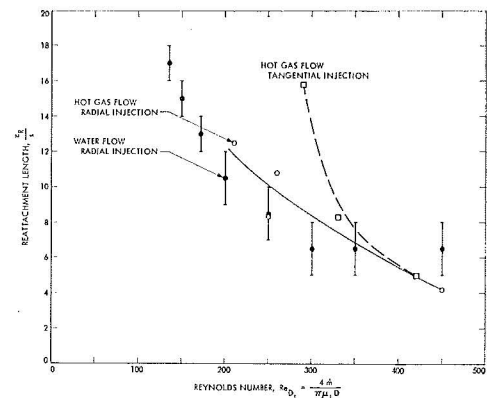


Fig. 6 Reattachment location: hot gas and water flow measurements, long tube  $L/D = 9.7$  (the average curves represent the hot-gas flow data)

attachment location with Reynolds number, the experimental data indicate an opposite trend. This behavior is believed to be associated with an instability in the vortex sheet-like shear layer which grows in amplitude more rapidly as the inertia forces become larger compared to the viscous forces, i.e., as the Reynolds number is increased. Therefore reattachment occurs nearer the step. In Section VI this phenomenon is discussed in connection with the flow visualization studies.

When reattachment occurs farther downstream in the tube as it does at the lower Reynolds number (Figs. 2-5), the region along which the pressure rises increases in length and therefore the reattachment compression process takes place over a greater portion of the tube. The pressure increases linearly in this region. The overall pressure rise from the pressure at the base of the step to the recovery pressure in the tube downstream is shown in Fig. 7 in terms of a pressure coefficient. This pressure coefficient is defined in terms of the dynamic pressure  $\frac{1}{2} \rho_a u_a^2$  upstream of the step at the arc heater outlet.

$$C_{p_{\max}} = \frac{p_{\max} - p_b}{\frac{1}{2} \rho_a u_a^2}$$

When the flow reattaches near the step (about 4 to 5 step heights downstream) the value of  $C_{p_{\max}}$  is about 0.05. However, the

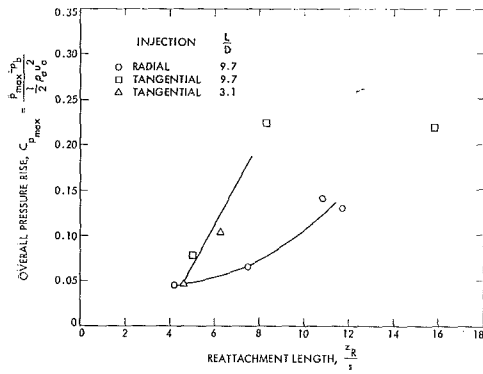


Fig. 7 Hot-gas pressure rise

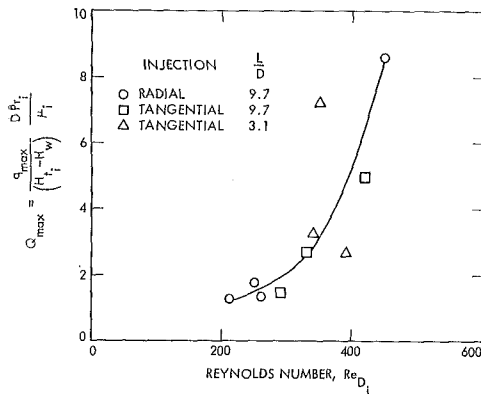


Fig. 8 Reattachment heat transfer correlation

pressure coefficient becomes substantially larger when reattachment occurs farther downstream and this is believed to be related to the rather large transverse undulations in the shear layer that develop along the tube as the instability grows in amplitude (Section VI). Apparently this enhanced lateral momentum transport leads to larger time-averaged recovery pressures. Of note is that the pressure coefficients shown in Fig. 7 are relatively low compared to those based on a more appropriate dynamic pressure descriptive of the reattaching flow,  $\frac{1}{2}\rho_e u_e^2$

$$\tilde{C}_{p_{max}} = \frac{p_{max} - p_b}{\frac{1}{2}\rho_e u_e^2}$$

Measurements in both laminar [35] and turbulent [36, 37] separated flows have indicated a value of  $\tilde{C}_{p_{max}}$  of about 0.34, which is also in good agreement with that calculated by taking the recovery pressure equal to the stagnation pressure along the dividing streamline of a low-speed flow (Chapman-Korst criterion, e.g., see [38]). In the representation herein values of  $C_{p_{max}}$  are expected to lie below  $\tilde{C}_{p_{max}}$  because of the lower velocities  $u_e$  in the reattachment region relative to those upstream of the step  $u_a$ , i.e.,

$$C_{p_{max}} = \tilde{C}_{p_{max}} \left( \frac{u_e}{u_a} \right)^2$$

The shape of the heat flux distribution in the reattachment region is seen in Figs. 2-5 to become relatively flat when reattachment occurs farther downstream in the tube. The reattachment location shown as a vertical line was taken to coincide with the peak heat flux. This peak heat flux is shown in Fig. 8 in nondimensional form (Nusselt number). The Nusselt number increases with Reynolds number as one would expect, but the increase of the Nusselt number with Reynolds number is greater than that found in most laminar flows where the increase is less than linear.

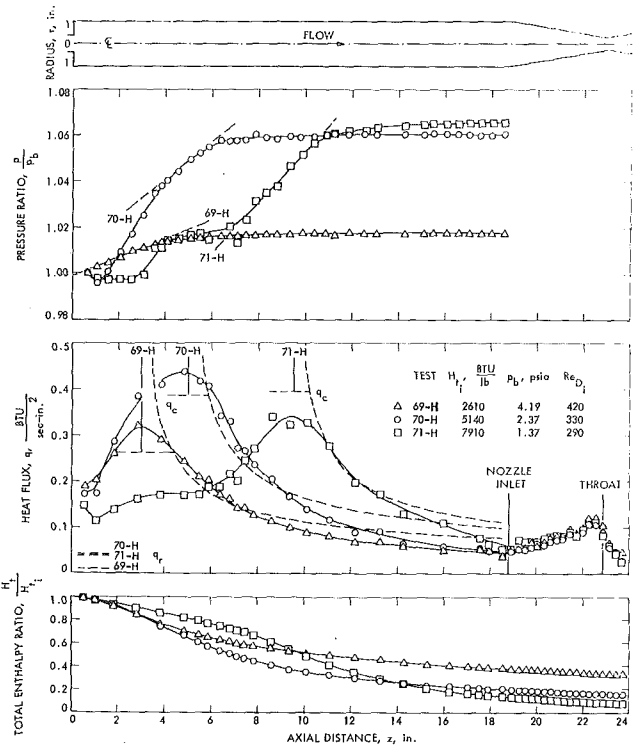


Fig. 9 Measurements along the tube and nozzle with tangential injection; long tube  $L/D = 9.7$

There is an appreciable loss of energy from the flow as indicated by the fraction of the total enthalpy remaining in the flow relative to the value at the tube inlet as seen in Figs. 2-5. When reattachment occurs farther along the tube, the energy loss along the entire tube is 80 percent of the inlet energy since the total enthalpy fraction is 0.2 at the end of the tube. Clearly, the largest energy loss occurs in the tube. Even though the heat flux does increase along the convergent section of the nozzle, the surface area there is smaller and consequently less energy is lost in the nozzle than in an equivalent length of tube upstream of the throat. The peak heat flux in the nozzle is found upstream of the throat. The heat flux then decreases along the divergent section of the nozzle so that the overall variation of the heat flux along the nozzle is similar to that found for turbulent boundary layer flows (e.g., [39-41]) and laminar boundary layer flows, but at higher Reynolds numbers [42]. However, the relative increase in the heat flux is less along the convergent section for a laminar than for a turbulent flow primarily because of the weaker dependence of the heat flux on mass flux, i.e.,  $q_w(\rho_e u_e)^n$ , where  $n = 0.5$  for a laminar boundary layer and  $n = 0.75$  or  $0.80$  for a turbulent boundary layer. This difference in behavior between laminar and turbulent boundary layers is vividly illustrated in [40, 41] which contain heat transfer measurements in a turbulent flow where laminarization occurred along the convergent section because of flow acceleration. Consequently, the heat flux increased less along the convergent section when the boundary layer became laminar-like near the wall than when the boundary layer remained turbulent. Discussion of heat transfer in the nozzle for a situation where the entering flow and thermal distributions were known and the ionization energy was negligible appears in [43].

Since the heat flux is highest in the reattachment region in the tube, an important aspect of these relatively low Reynolds number separated flows is the location of reattachment and a method by which the reattachment heat flux can be estimated. Information related to the reattachment location is described in Section VI and an estimate of the reattachment heat flux is made in Section V.

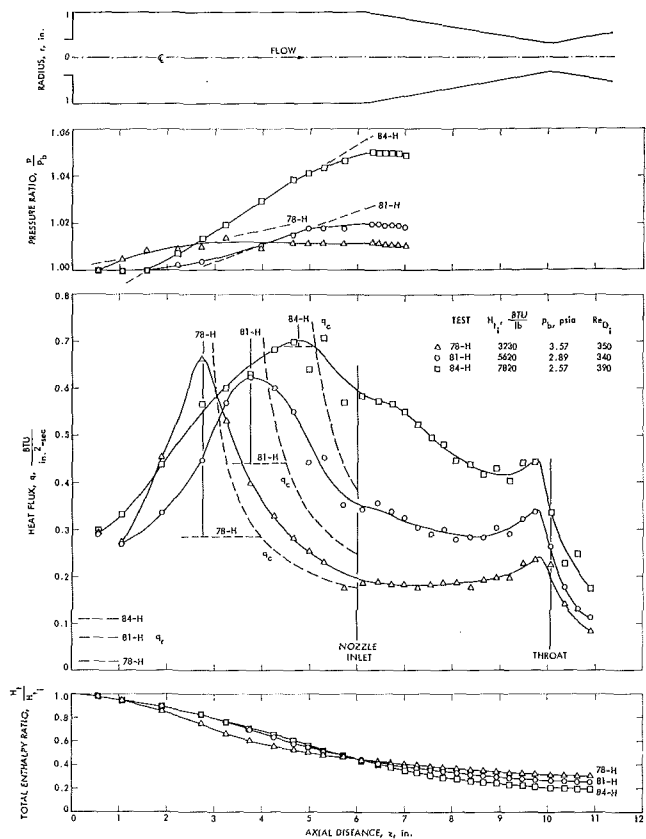


Fig. 10 Measurements along the tube and nozzle with tangential injection; short tube  $L/D = 3.1$

Results obtained with tangential injection upstream of the tube are shown in Fig. 9 for a tube the same length as was used for the radial injection results, i.e.,  $L/D = 9.7$ . An important parameter for flows with a tangential velocity component (swirl) is the magnitude of the swirl velocity,  $v$ , relative to the axial velocity,  $u$ . The ratio  $v/u$  could be estimated since the anode of the arc heater melted during one of the relatively high-current and high-pressure tests leaving a deposit of copper particles in a helical pattern around the tube. The swirl velocity was found to be smaller than the axial velocity, the ratio  $v/u$  being about 0.5. This ratio also agreed in relative magnitude with that calculated from the known tangential injection velocity at the chamber upstream of the arc heater and assuming that  $vr = \text{const.}$ , thereby ignoring tangential momentum losses between the injection chamber and the tube, to calculate the swirl velocity in the tube. Thus the tangential velocity could be estimated for the other tests at lower pressures for which the ratio  $v/u$  was found to be less than 0.5.

With tangential injection the heat flux becomes more peaked at reattachment and the pressure rises more steeply in the reattachment region than with radial injection. The reattachment location moves downstream with decreasing Reynolds number as before, as can be seen in Fig. 6. At a given Reynolds number, reattachment occurs farther downstream than with radial injection. The overall pressure rise in the reattachment region is also greater with tangential injection (Fig. 7). Of note in this respect is the pressure plateau before the final compression that is evident in Fig. 9 for the lowest Reynolds number test.

Whereas the shape of the peak heat flux in the reattachment region is changed, the magnitude is virtually the same as found with radial injection (Fig. 8). This correspondence in peak heating for radial and tangential injection is believed to be associated with the negligible influence of swirl on heat transfer when the swirl velocity is of about the same magnitude as the

axial velocity. This was indicated by the laminar boundary layer predictions in [44] when applied to swirling flow through a conical convergent nozzle where the heat transfer was found not to be influenced at all for equal swirl and axial velocities at the nozzle inlet. As observed before, the energy loss from the flow is greatest when the flow reattaches farther downstream and the higher heat flux in the reattachment region appears to establish a higher overall level for the tube, i.e., the total enthalpy remaining in the flow at the end of the tube is least for the highest inlet enthalpy test. The heat flux distribution in the nozzle is similar to that found with radial injection and this is consistent with that expected because of the relatively small amount of swirl in the flow.

Results were also obtained with tangential injection, but with a shorter tube so that  $L/D = 3.1$ . These results shown in Fig. 10 are generally similar to those observed with the longer tube. However, when reattachment occurs near the end of the tube, the heat flux decreases along the redevelopment region in the convergent section of the nozzle rather than increase as it does when reattachment occurs farther upstream. Correspondingly, the local maximum heat flux in the nozzle just upstream of the throat is not as much below the value at reattachment. Because of the shorter tube, the energy loss in the flow is less, e.g., the total enthalpy ratio is 0.45 at the end of the tube. Even though the reattachment heat fluxes are higher than with the longer tube, the nondimensional heat fluxes (Fig. 8) are about the same.

## V Heat Transfer Estimates

Having observed the thermal nature of the flow, attention is now directed toward making predictions of the wall heat flux, which in general is comprised of contributions from radiation, conduction, and diffusive energy transfer associated with partially ionized argon. Emphasis will be placed on the reattachment and redevelopment regions, and in particular the reattachment region which is the location of the peak heat flux.

An estimate of the radiation contribution to the wall heat flux was made in the inlet portion of the tube by calculating the radiation radially from the volume of gas contained in the circular jet that discharges into the tube. The volume radiation was estimated based on the measurements of Evans and Tankin [45] with argon that were made at pressures of  $1/2$ , 1, and 2 atm and which at 1 atm agree well with the earlier measurements by Yos [17] and more recent measurements by Abu-Romia and Blair [46]. Other measurements by Emmons [20] and Krey and Morris [47] are somewhat higher. Evans and Tankin's measurements were extrapolated to the lower pressures of this investigation. In making the radiation estimate the surrounding cooler gas that flows in the reverse direction along the tube wall was taken to be nonabsorbing, and all of the incident irradiation of the tube wall was assumed to be absorbed; in addition, radiation from the arc heater was not taken into account. The estimated radiative heat flux  $q_r$  that is shown in Figs. 2-5, 9, and 10 is seen to be rather small compared to the measured wall heat flux. The magnitude of the contribution, which is shown only in the inlet region, would also diminish along the tube as the gas cools. Clearly, the heat transfer in the tube is convection (conduction and diffusion) dominated and this observation is compatible with the distribution of the heat flux in the separated, reattachment, and redevelopment regions which is similar in shape to that which has been found in low-temperature investigations.

To calculate the convective heat flux the following laminar boundary layer prediction was used for a partially ionized monatomic gas

$$\frac{q_c}{(H_{10} - H_w)\rho_e u_e} \left( \frac{\rho_e u_e x}{\mu_e} \right)^{1/2} = F \quad (1)$$

where



$$F = \frac{0.87G_w'}{\text{Pr}_e^{1/3}} \left[ 1 + \left( \frac{1 - \frac{\alpha_w}{\alpha_e}}{1 - \frac{H_w}{H_{i0}}} \right) \left( \frac{\alpha_e I}{H_{i0}} \right) (\text{Le}_e^{0.63} - 1) \right]$$

$$\bar{x} = \frac{\int_0^x \rho_e \mu_e u_e r^{2i} dx}{\rho_e \mu_e u_e r^{2i}}$$

This relationship was found in [48] to be a good approximation of the calculations by Finson and Kemp [49]. Two conditions were considered: (1) Ambipolar diffusion by ion-electron pairs was assumed to be larger than the net ion production rate (frozen flow), and (2) local equilibrium existed. Transport properties were evaluated in [48] by using the Fay mixture rule [50, 14] which yields values in fair agreement with the more exact calculations of de Voto [15] over the temperature range of this investigation. Even though equilibration between the electron and heavy-particle temperatures, as assumed in the calculations, probably does not persist through the shear layer adjacent to the highly cooled wall because of the relatively small collisional energy loss by the lighter, more-mobile electrons to the heavier particles, inclusion of non-equilibrium effects has been found to change the predicted heat transfer by only a small amount (Camac and Kemp [51]). This is primarily because the electrons contribute little to the heat flux unless there is current flow to the surface such as at electrodes, e.g., [52, 53]. In the calculations a value of 0.2 was used for the Lewis number,  $\text{Le}$ . This relatively low value results from higher thermal conductivities and lower ambipolar diffusion coefficients for partially ionized argon than for non-ionized argon, e.g., see [48]. Because the Lewis number is less than unity, the contribution of the diffusive energy flux is less than the conductive heat flux and their sum (the total convective heat flux) would be less than that for a non-ionized gas if it were not for the lower Prandtl numbers associated with an ionized gas. The net effect is that values of the function  $F$  for an ionized gas exceed those for a non-ionized gas, and for the measurements herein the predicted percentage increase in  $F$  amounts to 7 to 16 percent, which is not large. The value of  $F$  for a non-ionized gas flow over a highly cooled wall with no external flow variation is 0.48, from the recent exact calculations in [54], and is very close to the value of 0.47 obtained from the approximate relation, equation (1).

Predicted values of the convective heat flux  $q_c$  from equation (1) are shown in Figs. 2-5, 9, and 10 by the dashed curves, the prediction being initiated at the reattachment location in a similar way as was done earlier by Seban, Emery, and Levy [55] in applying a turbulent boundary layer prediction to their low-temperature, turbulent air flow measurements downstream of a backward-facing step. In the prediction herein, the thermal boundary layer was taken to be thin relative to the tube radius so that the enthalpy driving potential  $H_{i0} - H_w$  was chosen as the value at the tube inlet ( $H_{i1} - H_w$ ). Furthermore, any external flow variation was not accounted for (i.e.,  $\bar{x} = x$ , the axial distance from reattachment) and  $G_w' = 0.47$ . The prediction is seen generally to be in fairly good agreement with the measured heat flux not too far downstream of reattachment in the redevelopment region, especially when reattachment occurs farther downstream in the tube as it does at the lower Reynolds numbers. However, at greater distances, the predicted heat flux exceeds the measured values obtained with the long tubes.

The reason for the overestimate of the heat flux farther downstream in the redevelopment region is believed to be primarily associated with using an enthalpy driving potential that no longer is descriptive of the central jet flow. For example, recent calculations of very high-temperature gas flow through cooled tubes [56] indicate that both the velocity and thermal boundary layers grow to the centerline a few diameters downstream of the tube inlet when the Reynolds numbers are rela-

tively low as they are in this investigation. The core flow then becomes nonadiabatic and consequently the driving potential for heat transfer is less. It is clear that a more appropriate heat transfer prediction in this region as well as in the nozzle downstream would require numerically solving the viscous heat-conducting laminar-flow equations, e.g., as in [43] for the situation where the ionization energy is negligible.

An estimate of the heat transfer is still possible in the reattachment region by using the corresponding properties descriptive of the flow at the inlet of the tube and the enthalpy driving potential  $H_{i1} - H_w$ . The reattachment heat transfer was calculated by applying equation (1) in the stagnation region for a plane flow ( $G_w' = 0.50$ ) to give

$$q_c = (H_{i1} - H_w)(\rho_i \mu_i V')^{1/2} [(2)^{1/2} F] \quad (2)$$

As in all stagnation-region heat transfer predictions, the velocity gradient  $V'$  needs to be specified. This was done by applying the inviscid form of the momentum equation along the tube wall in a direction upstream of reattachment.  $V'$  is then given in terms of the pressure gradient  $p'$  which, in the experiments, could be calculated from the pressure measurements as shown by the dashed lines in Figs. 2-5, 9, and 10, and the velocity  $V$ , characteristic of the reverse flow, by

$$\rho V V' = -p'$$

Originally it was thought that the reverse flow velocity  $V$  might be estimated from the water flow studies (Section VI). However, it was not possible to measure average reverse flow velocities at Reynolds numbers as large as in the hot-gas flow investigation. Inference from the water flow studies and the measurements by Seban [57] downstream of a backward-facing step in a low-temperature, high Reynolds number, turbulent air flow investigation indicate a reverse flow velocity from 0.15 to 0.2 of the velocity  $u_a$  upstream of the step. In the calculation herein a value of  $V/u_a$  of 0.15 was used which coincidentally is essentially the average velocity in the tube, i.e., from conservation of mass  $u = (A_a/A)u_a = 0.15 u_a$  because of the particular expansion area ratio of the channel investigated.

The reattachment heat transfer calculations are shown as a horizontal dashed curve in Figs. 2-5, 9, and 10. Considering the approximate nature of the prediction, the correspondence with the measured reattachment heat transfer is fairly good, especially when reattachment occurs farther downstream in the tube. Together with the streamwise predictions previously discussed, it does appear possible to make a meaningful estimate of the heat transfer in the reattachment and redevelopment regions.

As a final observation, some additional remarks are in order with regard to the question of the influence of ionization on heat transfer. For the lower enthalpy tests (Table 1) the predicted heat flux for an ionized gas is larger than that predicted by ignoring ionization and using the transport properties for atomic argon. This can be observed in Table 1 where values of  $q/q_A$  are shown. The predicted increase in  $q$  above the value for atomic argon  $q_A$  is associated with the larger values of the function  $F$  for an ionized gas which offset the lower predicted viscosities since  $q_c \propto (\mu_e)^{1/2} F$ . However, for the higher enthalpy tests (Table 1) the significantly lower predicted viscosities predominate in the heat transfer relation, and the predicted values of  $q$  are less than the values for atomic argon. Although there is difficulty in isolating the effect of ionization on heat transfer because of the nature of the flow investigated, the fairly good agreement between the predictions from existing theory and the measurements indicates that reasonable estimates of heat transfer can be made in very high enthalpy flows such as the ones considered herein where the ionization energy fraction extended up to about 0.6. This finding is in accord with the fair agreement found between stagnation region heat transfer predictions and measurements in partially ionized monatomic gases. It can be observed, for example, in Finson and Kemp's comparison [49] of their

prediction with the data of Rutowski and Bershader [58] and Reilly [59]. Another relevant study is Park [60] whose theoretical calculations based on choosing the binary mixture as that of heavy particles, i.e., atoms and ions, and electrons, agree with his data.

## VI Water Flow Studies

A study was made of the flow regimes and reattachment lengths in a water flow through a half-scale lucite model of the hot-gas test apparatus. A salient feature of the study was that the hot-gas flow where velocities through the tube ranged from 520 to 780 fps could be dynamically modeled by a relatively slow water flow where velocities extended down to 0.027 fps; for example, in 1 min the average flow displacement was 1.6 ft. This advantageous situation from a flow observation point of view arises because for the same ratio of inertia to viscous forces, i.e., Reynolds number in the gas and water flows, the significantly lower kinematic viscosity of water compared to high-temperature argon permits operation at relatively low water velocities.

Reattachment locations were determined by metering dye through small holes along the tube and observing which way the dye moved, toward the step in the reverse-flow region, or downstream in the reattachment region. With radial injection the reattachment location was found to move back toward the step with increasing Reynolds number similar to that observed in the hot-gas flow (Fig. 6). At Reynolds numbers where the hot-gas and water flow results overlapped each other, the reattachment lengths corresponded fairly well with each other. It should be noted that modeling of rotating gas flows with rotating liquid flows are usually not successful because of the radial variation in density of gas flows.

Dye could also be metered into the flow at locations in the upstream chamber, at the tip of the assimilated cathode and along the assimilated anode, as well as at the numerous locations along the tube. Flow observations revealed that the shear layer between the central jet and the reverse flow along the wall became unstable as the Reynolds number was increased and reattachment was determined when the lateral extent of the undulating motion of this vortex sheet-like region extended to the wall. At the lowest Reynolds number of about 200 corresponding to the hot-gas results, these undulations began to lose definition and to form eddies of random behavior. At a larger Reynolds number of about 450 the shear layer exhibited a more-random, fluctuating behavior. Pictures revealing these regimes are shown in [61] where the water flow results are presented. These measurements not only encompassed the Reynolds number range of the hot-gas flow investigation, but also extended down to Reynolds numbers based on the diameter upstream of the abrupt channel expansion of 20 and up to 4200. In the nomenclature used in [61]  $Re_{D_0} = (1.95/0.75) Re_{D_i} = 2.6 Re_{D_i}$ . At lower Reynolds numbers reattachment lengths were found to increase linearly with increasing Reynolds number as indeed might be expected for growth of the laminar shear layer by diffusion (Section IV).

## VII Summary and Conclusions

Measured distributions of pressure and heat flux were presented in the separation, reattachment, and redevelopment regions along a tube and a supersonic nozzle located downstream of an abrupt channel expansion. Argon, which was heated and partially ionized by an electric arc, was used as the fluid. The location of reattachment was found to depend upon the growth of an instability in the vortex sheet-like shear layer between the central jet that discharged into the tube and the outer, slower-moving reverse flow along the wall. The reattachment location moved upstream toward the step at the tube inlet as the ratio of inertia forces compared to the viscous forces became larger, i.e., as the Reynolds number was increased. As this occurred the instability grew more rapidly in amplitude and extended to

the tube wall. For radial injection it was possible to dynamically model the very high-temperature gas flow by a water flow. In the water flow experiments visual observations revealed the nature of the flow and indicated reattachment locations in terms of step heights that were in good agreement with the gas flow results at the same Reynolds number.

The highest heat transfer occurred in the reattachment region in the tube and established the kind of heat transfer distribution that is believed to be convection-dominated along the rest of the tube. The loss of energy from the flow as indicated by the fraction of the total enthalpy remaining in the flow relative to the value at the tube inlet was generally larger when the flow reattached farther along the tube as was the case at the lower Reynolds numbers. It was possible to make a meaningful estimate of the heat transfer at reattachment from a stagnation region, boundary layer prediction for a partially ionized gas flow. In the redevelopment region downstream of reattachment the level of heat transfer could also be estimated from a laminar boundary layer prediction initiated at reattachment, although the prediction eventually failed farther along the tube because the core flow is believed to have become nonadiabatic. Although there is difficulty in separately appraising the effect of ionization on heat transfer because of the kind of flow investigated, the fairly good agreement between predictions from existing theory and measurements does indicate that reasonable estimates of heat transfer can be made in very high enthalpy flows such as the ones considered herein where the ionization energy fraction extended up to about 0.6. The energy loss in these relatively low Reynolds number flows with externally cooled walls is appreciable; as much as 90 percent of the inlet energy was lost by heat transfer to the tube and nozzle wall. The largest amount of energy that was transferred occurred in the tube because of the reattachment process and the larger enthalpy driving potential there.

## Acknowledgment

The authors express their gratitude to Mr. M. Noel, Mr. S. Kikkert, and Mr. F. Slover for operation of the system and acquisition and reduction of the experimental data.

## References

- Boelter, L. M. K., Young, G., and Iversen, H. W., "An Investigation of Aircraft Heaters XXVII—Distribution of Heat-Transfer Rate in the Entrance Section of a Circular Tube," NACA TN-1451, July 1948.
- Ede, A. J., Hislop, C. I., and Morris, R., "Effect on the Local Heat Transfer Coefficient in a Pipe of an Abrupt Disturbance of the Fluid Flow: Abrupt Convergence and Divergence of Diameter Ratio 2/1," *IME Proceedings*, No. 38, 1956.
- Ede, A. J., "Effect of an Abrupt Disturbance of the Flow on the Local Heat-Transfer Coefficient in a Pipe: Progress Report," NEL Report Heat 164, National Engineering Laboratory, East Kilbride, Glasgow, Scotland, Jan. 1959.
- Ede, A. J., Morris, R., and Birch, E. S., "The Effect of Abrupt Changes of Diameter on Heat Transfer in Pipes," NEL Report No. 73, National Engineering Laboratory, East Kilbride, Glasgow, 1962.
- Emerson, W. H., "Heat Transfer in a Duct in Regions of Separated Flow," *Proceedings 3rd International Heat Transfer Conference*, AIChE, Vol. 1, Aug. 1966, pp. 267-275.
- Kralj, K. M., and Sparrow, E. M., "Turbulent Heat Transfer in the Separated, Reattached, and Redevelopment Regions of a Circular Tube," *JOURNAL OF HEAT TRANSFER*, TRANS. ASME, Series C, Vol. 88, No. 1, Feb. 1966, pp. 131-136.
- VanSant, J. H., and Larson, M. B., "Convection Heat Transfer for Turbulent Flow in Subsonic Diffusers," *JOURNAL OF HEAT TRANSFER*, TRANS. ASME, Series C, Vol. 88, No. 4, Nov. 1966, pp. 391-398.
- Filetti, E. G., and Kays, W. M., "Heat Transfer in Separated, Reattached, and Redevelopment Regions Behind a Double Step at Entrance to a Flat Duct," *JOURNAL OF HEAT TRANSFER*, TRANS. ASME, Series C, Vol. 89, No. 2, May 1967, pp. 163-168.
- Zemanick, P. P., and Dougall, R. S., "Local Heat Transfer Downstream of Abrupt Circular Channel Expansion," *JOURNAL OF HEAT TRANSFER*, TRANS. ASME, Series C, Vol. 92, No. 1, Feb. 1970, pp. 53-60.
- Back, L. H., Massier, P. F., and Cuffel, R. F., "Flow and Heat

Transfer Measurements in Subsonic Air Flow Through a Contraction Section," *International Journal of Heat and Mass Transfer*, Vol. 12, Jan. 1969, pp. 1-13.

11 Skrivan, J. F., and von Jaskowsky, W., "Heat Transfer from Plasmas to Water-Cooled Tubes," *Industrial and Engineering Chemistry Process Design and Development*, Vol. 4, No. 4, Oct. 1965, pp. 371-379.

12 Johnson, J. R., Choksi, N. M., Eubank, P. T., "Entrance Heat Transfer from a Plasma Stream in a Circular Tube," *Industrial and Engineering Chemistry Process Design and Development*, Vol. 7, No. 1, Jan. 1968, pp. 34-41.

13 Schmidt, P. S., and Leppert, G., "Heat Transfer From Plasma in Tube Flow," *JOURNAL OF HEAT TRANSFER*, TRANS. ASME, Series C, Vol. 92, No. 3, Aug. 1970, pp. 483-489.

14 Back, L. H., "Laminar Boundary-Layer Heat Transfer From a Partially-Ionized Monatomic Gas by the Similarity Approach," Technical Report No. 32-867, Jet Propulsion Laboratory, Pasadena, Calif., 1966.

15 de Voto, R. S., "Argon Plasma Transport Properties," SUDAER No. 217, Department of Aeronautics and Astronautics, Stanford University, Feb. 1965. (Tables recently prepared by de Voto under NASA Grant NGR 05-020-091 replace SUDAER No. 217.)

16 de Voto, R. S., "Transport Coefficients of Partially Ionized Argon," *Physics of Fluids*, Vol. 10, No. 2, Feb. 1967, pp. 354-364.

17 Yos, J. M., "Theoretical and Experimental Studies of High Temperature Gas Transport Properties," Final Report, AVCO/RAD Technical Report RAD-TR-65-7, Research and Advanced Development Div., Avco Corp., Wilmington, Mass., May 1965.

18 Knopp, C. F., and Cambel, A. B., "Experimental Determination of the Thermal Conductivity of Atmospheric Argon Plasma," *Physics of Fluids*, Vol. 9, No. 5, May 1966, pp. 989-996.

19 Bues, I., Patt, H. J., and Richter, J., "Über die Elektrische Leitfähigkeit und die Wärmeleitfähigkeit des Argons bei hohen Temperaturen," *Z. Angew. Phys.*, Vol. 22, Part 4, March 1967, pp. 345-350.

20 Emmons, H. W., "Arc Measurement of High Temperature Gas Transport Properties," *Physics of Fluids*, Vol. 10, No. 6, June 1967, pp. 1125-1136.

21 Morris, J. C., Rudis, R. P., and Yos, J. M., "Measurements of Electrical and Thermal Conductivity of Hydrogen, Nitrogen and Argon at High Temperatures," *Physics of Fluids*, Vol. 13, No. 3, March 1970, pp. 608-617.

22 Kanzawa, A., and Kimura, I., "Measurements of Viscosity and Thermal Conductivity of Partially Ionized Argon Plasmas," *AIAA Journal*, Vol. 5, No. 7, July 1967, pp. 1315-1319.

23 Schreiber, P. W., Hunter, A. M., II, and Benedetto, K. R., "Argon Plasma Viscosity Measurements," AIAA Paper No. 70-775, June 1970.

24 Aeschliman, D. P., and Cambel, A. B., "Measurement of the Viscosity of Atmospheric Argon from 3500 to 8500°K," *Physics of Fluids*, Vol. 13, No. 10, Oct. 1970, pp. 2466-2477.

25 Amdur, I., and Mason, E. A., "Properties of Gases of Very High Temperatures," *Physics of Fluids*, Vol. 1, No. 5, Sept.-Oct. 1958, pp. 370-383.

26 Camac, M., and Feinberg, R. M., "Thermal Conductivity of Argon at High Temperatures," *Journal of Fluid Mechanics*, Vol. 21, Part 4, April 1965, pp. 673-688.

27 Fay, J. A., and Arnoldi, D., "High Temperature Thermal Conductivity of Argon," *Physics of Fluids*, Vol. 11, No. 5, May 1968, pp. 983-985.

28 Kuiper, R. A., "Interferometric Study of the End-Wall Thermal Layer in Ionizing Argon," AIAA Paper No. 69-694, 1969.

29 Willeke, K., and Bershader, D., "Thermal Transport and Relaxation Processes in Shock-Heated Argon," *AIAA Journal*, Vol. 7, No. 11, Nov. 1969, pp. 2172-2174.

30 Lauver, M. R., "Evaluation of Shock-Tube Heat-Transfer Experiments to Measure Thermal Conductivity of Argon from 700° to 8600°K," NASA TN D-2117, Feb. 1964.

31 Collins, D. J., and Menard, W. A., "Measurement of the Thermal Conductivity of Noble Gases in the Temperature Range 1500 to 5000 Deg Kelvin," *JOURNAL OF HEAT TRANSFER*, TRANS. ASME, Series C, Vol. 88, No. 1, Feb. 1966, pp. 52-56.

32 Matula, R. A., "High Temperature Thermal Conductivity of Rare Gases and Gas Mixtures," *JOURNAL OF HEAT TRANSFER*, TRANS. ASME, Series C, Vol. 90, No. 3, Aug. 1968, pp. 319-327.

33 Bunting, J. O., de Voto, R. S., and Bershader, D., "Thermal Conductivity of Shock-Heated Argon," *Shock Tube Symposium, Physics of Fluids Supplement I*, 1969, pp. I-85-88.

34 Carey, C. A., Carnevale, E. H., and Marshall, T., "Experimental Determination of the Transport Properties of Gases. Part II, Heat Transfer and Ultrasonic Measurements," Contract AF33-(615)-1325, Proj. AF-7360, Task 736001, AFML TR-65-141-Pt. s, Sept. 1966 (AD-804604).

35 Roshko, A., "On the Drag and Shedding Frequency of Two-Dimensional Bluff Bodies," NACA TN 3169, 1954.

36 Roshko, A., and Lau, J. C., "Some Observations on Transition and Reattachment of a Free Shear Layer in Incompressible Flow,"

*Heat Transfer and Fluid Mechanics Institute*, 1965, pp. 157-167.

37 Seban, R. A., "The Effect of Suction and Injection on the Heat Transfer and Flow in a Turbulent Separated Airflow," *JOURNAL OF HEAT TRANSFER*, TRANS. ASME, Series C, Vol. 88, No. 3, Aug. 1966, pp. 276-284.

38 Chapman, D. R., Kuehn, D. M., and Larson, H. K., "Investigation of Separated Flows in Supersonic and Subsonic Streams with Emphasis on the Effect of Transition," NACA R-1356, 1958.

39 Bartz, D. R., "Turbulent Boundary-Layer Heat Transfer from Rapidly Accelerating Flow of Rocket Combustion Gases and Heated Air," in: *Advances in Heat Transfer*, Vol. 2, (Irvine, T. F., and Hartnett, J. P., eds.), Academic Press, New York, N. Y., 1965.

40 Back, L. H., Massier, P. F., and Cuffel, R. F., "Flow Phenomena and Convective Heat Transfer in a Conical Supersonic Nozzle," *J. Spacecraft Rockets*, Vol. 4, No. 8, Aug. 1967, pp. 1040-1047.

41 Back, L. H., Cuffel, R. F., and Massier, P. F., "Laminarization of a Turbulent Boundary Layer in Nozzle Flow—Boundary Layer and Heat Transfer Measurements With Wall Cooling," *JOURNAL OF HEAT TRANSFER*, TRANS. ASME, Series C, Vol. 92, No. 3, Aug. 1970, pp. 333-344.

42 Back, L. H., Massier, P. F., and Cuffel, R. F., "Effect of Inlet Boundary Layer Thickness and Structure on Heat Transfer in a Supersonic Nozzle," *J. Spacecraft Rockets*, Vol. 5, No. 1, Jan. 1968, pp. 121-123.

43 Back, L. H., and Massier, P. F., "Viscous, Non-Adiabatic Laminar Flow Through a Supersonic Nozzle—Numerical Calculations and Experimental Results," to be published in *JOURNAL OF HEAT TRANSFER*.

44 Back, L. H., "Flow and Heat Transfer in Laminar Boundary Layers with Swirl," *AIAA Journal*, Vol. 7, No. 9, Sept. 1969, pp. 1781-1789.

45 Evans, D. L., and Tankin, R. S., "Measurement of Emission and Absorption of Radiation by an Argon Plasma," *Physics of Fluids*, Vol. 10, No. 6, June 1967, pp. 1137-1144.

46 Abu-Romia, M. M., Blair, D. W., "Experimental Determination of the Radiative Properties of High-Temperature Plasmas," AIAA Paper No. 69-601, June 1969.

47 Krey, R. U., and Morris, J. C., "Experimental Total and Total Line Radiation of Nitrogen, Oxygen, and Argon Plasmas," *Physics of Fluids*, Vol. 13, No. 6, June 1970, pp. 1483-1487.

48 Back, L. H., "Laminar Boundary Layer Heat Transfer From a Partially Ionized Monatomic Gas," *Physics of Fluids*, Vol. 10, No. 4, April 1967, pp. 807-819.

49 Finson, M. L., and Kemp, N. H., "Theory of Stagnation-Point Heat Transfer in Ionized Monatomic Gases," *Physics of Fluids*, Vol. 8, No. 1, Jan. 1965, pp. 201-204.

50 Fay, J. A., "Hypersonic Heat Transfer in the Air Laminar Boundary Layer," in: *High Temperature Aspects of Hypersonic Flow* (Nelson, W. C., ed.), Macmillan, New York, N. Y., 1964, pp. 583-605.

51 Camac, M., and Kemp, N. H., "A Multi-temperature Boundary Layer," AIAA Paper No. 63-460, 1963; also Research Rept. 184, Aug. 1964, AVCO Everett Research Lab.

52 Eckert, E. R. G., and Pfender, E., "Plasma Energy Transfer to a Surface with and without Electric Current," *Welding Journal*, Oct. 1967, pp. 471-S-480-S.

53 Bose, T. K., "Anode Heat Transfer for a Flowing Argon Plasma at Elevated Electron Temperature," to be published in *International Journal of Heat and Mass Transfer*.

54 Back, L. H., "Effects of Severe Surface Cooling and Heating on the Structure of Low-Speed Laminar Boundary-Layer Gas Flows With Constant Free-Stream Velocity," Technical Report No. 32-1301, Jet Propulsion Laboratory, Pasadena, Calif., 1968.

55 Seban, R. A., Emery, A., and Levy, A., "Heat Transfer to Separated and Reattached Subsonic Turbulent Flows Obtained Downstream of a Surface Step," *J. of the Aero/Space Sciences*, Vol. 26, No. 12, Dec. 1959, pp. 809-814.

56 Back, L. H., "Very High Temperature Laminar Flow of a Gas Through the Entrance Region of a Cooled Tube—Numerical Calculations and Experimental Results," to be published in *International Journal of Heat and Mass Transfer*.

57 Seban, R. A., "Heat Transfer to the Turbulent Separated Flow of Air Downstream of a Step in the Surface of a Plate," *JOURNAL OF HEAT TRANSFER*, TRANS. ASME, Series C, Vol. 86, No. 2, May 1964, pp. 259-264.

58 Rutowski, R. W., and Bershader, D., "Shock Tube Studies of Radiative Transport in an Argon Plasma," *Physics of Fluids*, Vol. 7, No. 4, April 1964, pp. 568-577.

59 Reilly, J. A., "Stagnation-Point Heating in Ionized Monatomic Gases," *Physics of Fluids*, Vol. 7, No. 12, Dec. 1964, pp. 1905-1912.

60 Park, C., "Heat Transfer from Nonequilibrium Ionized Argon Gas," *AIAA Journal*, Vol. 2, No. 1, Jan. 1964, pp. 169-171.

61 Back, L. H., and Roschke, E. J., "Shear Layer Flow Regimes and Wave Instabilities and Reattachment Lengths Downstream of an Abrupt Circular Channel Expansion," to be published in *Journal of Applied Mechanics*, TRANS. ASME.